Thermodynamics, constitution and kinetics in the Mo-Si-Ti system

Zur Erlangung des akademischen Grades eines

DOKTORS DER INGENIEURWISSENSCHAFTEN (DR.-ING.)

von der KIT-Fakultät für
Maschinenbau
des Karlsruher Instituts für Technologie (KIT)

genehmigte

DISSERTATION

von

M.Sc. Andreas Klaus Czerny
geb. in München

Tag der mündlichen Prüfung:	02.12.2024
Hauptreferent:	Prof. Dr. rer. nat. Hans Jürgen Seifert
Korreferentin:	Prof. Dr. rer. nat. Britta Nestler

"Anything can happen, in spite of what you’re pretty sure should happen."
Richard Feynman

Abstract

Engineering materials in the Mo-Si-Ti system are promising candidates for applications at high temperatures and in extreme environments such as gas turbines. Several alloys have shown suitable properties in terms of mechanical parameters as well as corrosion and oxidation resistance. However, alloy design in this system is challenging due to the presence of highly brittle detrimental phases and the fact that many beneficial phases are prone to catastrophic oxidation. Therefore, the constituent phases of potential materials, as well as their compositions and phase fractions, must be carefully tailored. The CALPHAD approach can be used for this purpose. While a thermodynamic dataset exists for the Mo-Si-Ti system, the analysis of annealed samples has shown the need to refine it for the conditions most relevant to gas turbine applications, i.e. temperatures between 1300 and 1600 K and Si concentrations below 37.5 at.%.

Therefore, the metal-rich region of the Mo-Si-Ti system was experimentally investigated. Samples were prepared by vacuum arc melting and analyzed by scanning electron microscopy, energy dispersive X-ray spectroscopy, electron probe microanalysis, X-ray diffraction, inductively coupled plasma optical emission spectroscopy, and carrier gas hot extraction. A novel type of furnace was developed and tested for annealing and subsequent quenching. Care has been taken to ensure that the risk of contamination of the samples was as low as possible. The samples were investigated both in the as-cast state and after annealing for 330 h at 1573 K. In the as-cast state, the objective was to evaluate the accuracy of the liquidus projection and Scheil solidification calculations performed with the existing dataset. It was found that the agreement between experiments and calculations was generally quite high and most of the microstructure evolution could be accurately predicted. Some samples showed deviations from the predicted microstructures, but in most cases this was not due to major problems in the dataset. Rather, it was due to slight shifts in ternary reaction temperatures or the position of maxima at the edges of double saturation which, for example, led to an underestimation of the phase fractions of certain phases. In a few cases, however, the microstructures showed features that cannot be calculated with the dataset, suggesting that other reactions than those calculated may occur in certain regions.

The effect of the cooling rate on Mo-Si-Ti samples was investigated. This was done by annealing samples in a two-step process. First, the samples were annealed and then furnace cooled. These samples were analyzed before being annealed again at the same temperature. This time the

samples were quenched in water. By comparing the microstructure and phase composition of the same samples in both states, it could be concluded that the cooling rate is quite insignificant for Mo-Si-Ti samples, likely due to the slow diffusion in the system.
Analysis of the annealed samples revealed that the composition of the phase Mo_3Si was consistently off-stoichiometric with an average Si content of 23 at.%. Since this cannot be corrected without changing the model in the underlying binary dataset, it was decided after a thorough literature search to reassess the Mo-Si system. The phase Mo_3Si was modeled either as a stoichiometric phase with the experimentally observed composition, or with a sublattice model representing the defect structure and allowing for a homogeneity range. In addition, the model of Mo_5Si_3 was chosen to represent the crystallography of the phase as accurately as possible. Furthermore, heat capacity data were used for the first time to optimize the system. It was shown that all reliable experimental data from the literature could be well represented by the calculations with the new dataset.
Examination of the isothermal section of the ternary system at 1573 K revealed that many of the samples were not in thermodynamic equilibrium after heat treatment for 330 h. This was especially the case when the microstructure after solidification consisted of many small grains or when many non-equilibrium phases were formed during solidification. Sometimes the non-equilibrium state was obvious from the presence of more than three phases, but sometimes XRD analysis was required to determine that non-equilibrium stable phases were present. In some cases, the microstructures did not change at all. Nevertheless, many other equilibria in the system were confirmed and their exact locations were in some cases more precisely defined than previously described in the literature. The off-stoichiometry of Mo_3Si could be confirmed for the ternary system, and it was found that the β phase dissolves significantly more Si than previously assumed. The latter finding is particularly promising for future alloy development, since the concentration of Si dissolved in β has a significant influence on the corrosion resistance of the alloys.
Based on the experimental results, the reassessment of the Mo-Si system and a thorough analysis of the available literature on the ternary system, a new modeling in the Mo-Si-Ti system was performed. The reassessment was limited to the metal-rich region, since Si contents higher than 37.5 at.% are irrelevant to the research question of this dissertation. It could be shown that the newly developed dataset reflects the reliable experimental results, namely the isothermal sections at 1573 and 1873 K, very well. Likewise, the invariant reactions in this region of the system, although never directly experimentally investigated, seem very reasonable as calculated. The liquidus projection is also reasonable, and it has been shown that Scheil solidification calculations are capable of predicting the microstructures of alloys produced by vacuum arc melting. Thus, the reassessed dataset can be used to design alloys in the metal-rich region of the system with high accuracy.

Kurzfassung

Werkstoffe im System Mo-Si-Ti sind vielversprechende Kandidaten für Anwendungen bei hohen Temperaturen und in extremen Umgebungen wie etwa Gasturbinen. Mehrere Legierungen haben geeignete Eigenschaften in Bezug auf die mechanischen Parameter sowie die Korrosions- und Oxidationsbeständigkeit gezeigt. Die Entwicklung von Legierungen in diesem System ist jedoch eine anspruchsvolle Aufgabe, da sie oft schädliche, extrem spröde Phasen beinhalten und viele der nützlichen Phasen anfällig für katastrophale Oxidation sind. Daher müssen die Phasen, welche die potenziellen Werkstoffe aufbauen, sowie ihre Zusammensetzungen und Phasenanteile sorgfältig aufeinander abgestimmt werden. Zu diesem Zweck kann die CALPHAD-Methode verwendet werden. Zwar gibt es einen thermodynamischen Datensatz für das System Mo-Si-Ti, doch hat die Analyse wärmebehandelter Proben gezeigt, dass er für die für Gasturbinenanwendungen wichtigsten Bedingungen, d. h. Temperaturen zwischen 1300 und 1600 K und Si-Konzentrationen unter 37,5 at.%, optimiert werden sollte.

Aus diesem Grund wurde in dieser Arbeit der metallreiche Bereich des Mo-Si-Ti-Systems experimentell untersucht. Die Proben wurden durch Vakuumlichtbogenschmelzen hergestellt und mittels Rasterelektronenmikroskopie, energiedispersiver Röntgenspektroskopie, Elektronenstrahlmikroanalyse, Röntgenbeugung, optischer Emissionsspektroskopie mit induktiv gekoppeltem Plasma und Trägergasheißextraktion analysiert. Für das Tempern und anschließende Abschrecken wurde ein neuartiger Ofen entwickelt und erprobt. Es wurde darauf geachtet, dass das Risiko einer Verunreinigung der Proben so gering wie möglich ist. Die Proben wurden sowohl im Gusszustand als auch nach 330 h Glühen bei 1573 K untersucht. Im gegossenen Zustand bestand das Ziel darin, die Genauigkeit der Liquidusprojektion und der Scheil-Erstarrungsberechnungen zu bewerten, die mit dem vorhandenen Datensatz durchgeführt wurden. Es zeigte sich, dass die Übereinstimmung zwischen Experimenten und Berechnungen im Allgemeinen recht hoch war und die meisten Mikrostrukturentwicklungen genau vorhergesagt werden konnten. Einige Proben wiesen Abweichungen von den vorhergesagten Mikrostrukturen auf, was jedoch in den meisten Fällen nicht auf größere Probleme im Datensatz zurückzuführen war. Vielmehr handelte es sich um leichte Verschiebungen der ternären Reaktionstemperaturen oder der Position der Maxima an den Kanten doppelter Sättigung, die beispielsweise zu einer Unterschätzung der Phasenanteile bestimmter Phasen führten. In einigen wenigen Fällen wiesen die Mikrostrukturen jedoch Merkmale auf, die mit dem Datensatz nicht berechnet werden können, was darauf hindeutet, dass

in bestimmten Regionen andere Reaktionen als die berechneten ablaufen könnten.
Die Auswirkung der Abkühlgeschwindigkeit auf Mo-Si-Ti-Proben wurde untersucht. Dazu wurden die Proben in einem zweistufigen Verfahren geglüht. Zunächst wurden die Proben wärmebehandelt und dann im Ofen abgekühlt. Diese Proben wurden analysiert, bevor sie erneut bei der gleichen Temperatur geglüht wurden. Dieses Mal wurden die Proben in Wasser abgeschreckt. Ein Vergleich der Mikrostruktur und der Phasenzusammensetzung derselben Proben in beiden Zuständen ergab, dass die Abkühlungsgeschwindigkeit für Mo-Si-Ti-Proben relativ unbedeutend ist, was vermutlich auf die langsame Diffusion im System zurückzuführen ist.
Die Analyse der wärmebehandelten Proben ergab, dass die Zusammensetzung der Phase Mo_3Si mit einem durchschnittlichen Si-Gehalt von 23 at.% durchweg unterstöchiometrisch ist. Da dies nicht korrigiert werden kann, ohne das Modell des zugrunde liegenden binären Datensatzes zu ändern, wurde nach einer gründlichen Literaturrecherche beschlossen, das Mo-Si-System neu zu optimieren. Die Phase Mo_3Si wurde sowohl als stöchiometrische Phase mit der experimentell beobachteten Zusammensetzung als auch mit einem Untergittermodell modelliert, welches die tatsächliche Defektstruktur repräsentiert und einen Homogenitätsbereich zulässt. Darüber hinaus wurde das Modell von Mo_5Si_3 so gewählt, dass die Kristallographie der Phase so korrekt wie möglich dargestellt wird. Des Weiteren wurden zum ersten Mal Wärmekapazitätsdaten verwendet, um das System zu optimieren. Es wurde gezeigt, dass alle zuverlässigen experimentellen Daten aus der Literatur durch die Berechnungen mit dem neuen Datensatz gut repräsentiert werden konnten.
Die Untersuchung des isothermen Schnittes des ternären Systems bei 1573 K zeigte, dass sich viele Proben nach 330 h wärmebehandeln nicht im thermodynamischen Gleichgewicht befanden. Dies war insbesondere dann der Fall, wenn das Gefüge nach der Erstarrung aus vielen kleinen Körnern bestand oder wenn sich während der Erstarrung viele Nicht-Gleichgewichtsphasen gebildet hatten. In manchen Fällen war der Nichtgleichgewichtszustand durch das Vorhandensein von mehr als drei Phasen offensichtlich, aber in einigen Fällen war eine XRD-Analyse erforderlich, um festzustellen, dass Nichtgleichgewichtsphasen vorhanden waren. In einigen Fällen änderte sich das Gefüge auch nach 330 h nicht. Dennoch wurden viele andere Phasengleichgewichte in dem System bestätigt, und ihre genaue Lage wurde in einigen Fällen präziser definiert als zuvor in der Literatur beschrieben. Die Stöchiometrieabweichung von Mo_3Si konnte für das ternäre System bestätigt werden, und es wurde festgestellt, dass die β-Phase deutlich mehr Si löst als bisher angenommen. Letztere Erkenntnis ist besonders vielversprechend für die künftige Legierungsentwicklung, da die Konzentration des in β gelösten Si einen erheblichen Einfluss auf die Korrosionsbeständigkeit der Legierungen hat.
Auf der Grundlage der experimentellen Ergebnisse, der Neuoptimierung des Mo-Si-Systems und einer gründlichen Analyse der verfügbaren Literatur über das ternäre System wurde eine neue Modellierung im Mo-Si-Ti-System durchgeführt. Die Neuoptimierung beschränkte sich

auf den metallreichen Bereich, da Si-Gehalte von mehr als 37,5 at.% für die Fragestellung dieser Dissertation irrelevant sind. Es konnte gezeigt werden, dass der neu entwickelte Datensatz die zuverlässigen experimentellen Ergebnisse, namentlich die isothermen Schnitte bei 1573 und 1873 K, sehr gut wiedergibt. Ebenso scheinen die invarianten Reaktionen in diesem Bereich des Systems, obwohl nie direkt experimentell untersucht, sehr plausibel berechnet. Die Liquidusprojektion ist ebenfalls akzeptabel, und es hat sich gezeigt, dass die Scheil-Erstarrungsberechnungen in der Lage sind, die Mikrostrukturen von Legierungen vorherzusagen, die durch Vakuumlichtbogenschmelzen hergestellt werden. Somit kann der neu optimierte Datensatz verwendet werden, um Legierungen im metallreichen Bereich des Systems mit hoher Genauigkeit zu entwickeln.

Acknowledgement

I would like to thank everyone who made this work possible. First and foremost, I would like to thank Prof. Hans Seifert for supervising my thesis, as well as for our many discussions, the feedback throughout, and his genuine interest in me and my topic.
I would also like to thank Dr. Magnus Rohde for his co-supervision and the opportunity to discuss whatever was on our minds during our group meetings.
My thanks go to Dr. Peter Franke for our discussions, especially on all things related to the optimization of the Mo-Si system, and for his support in the publication on this topic.
I would like to thank Prof. Yong Du for kindly providing us with the Mo-Si-Ti dataset and for giving me the opportunity to present my work at the Sino-German meeting in Changsha and Guilin in 2023.
My gratitude goes to Dr. Thomas Bergfeldt for the chemical analysis of my samples and his patience to discuss them whenever necessary, and to Kolja Erbes for the EPMA measurements.
Special thanks to all my colleagues in the Thermophysics and Thermodynamics group of the IAM-AWP. To Judith Jung, Christoph Gebert and Robin Markert, not only for their invaluable support with just about everything I did in the labs (and beyond), but also for many a nice discussion. To Clemens Hausner, who not only got things started on Mo-Si-Ti at the IAM-AWP, but who was still interested enough in the topic to discuss it endlessly and deeply, even long after he had moved on to new topics. To Julian Gebauer, who was very involved and helpful when we had to set up (and occasionally fix) the new quenching furnace, and who was always open to discussing ideas, CALPHAD and beyond. And Wenhao Ma, who not only showed me the ropes of CALPHAD optimization and without whom the Mo-Si reassessment would not have been what it is now, but who was also always open to talk about things that might not be so work-related during the breaks. You all made my work here not only successful, but also a lot of fun.
Then of course there are colleagues from other groups I would like to thank. Alexandra Meyer, Aycan Kutlu and Karsten Geuder for the occasional topical discussions, but especially for all the discussions that were usually not so topical and often involved a cup of coffee.
I would also like to thank my colleagues from RTG 2561 for all the great opportunities and cooperation over the years. I am also grateful to the German Research Foundation for funding the project.

Finally, I would also like to thank my family and all my friends who are not specifically listed here for their support in a variety of roles and ways. Without all of you, this work would not have been the same.

Contents

List of abbreviations and symbols

Elements

Mo	Molybdenum
Si	Silicon
Ti	Titanium
B	Boron
W	Tungsten
Al	Aluminium
Nb	Niobium
Cu	Copper
Pt	Platinum
Rh	Rhodium

Abbreviations

KIT	Karlsruhe Institute of Technology
CALPHAD	Calculation of phase diagrams
CEF	Compound energy formalism
VAM	Vacuum arc melting
OPS	Oxidic polishing suspension
SEM	Scanning electron microscope
SE	Secondary electrons

BSE	Backscattered electrons
EDX	Energy dispersive X-ray spectroscopy
EPMA	Electron probe microanalysis
XRD	X-ray diffraction
ICP – OES	Inductively coupled plasma optical emission spectroscopy
CGHE	Carrier gas hot extraction
CCD	Charge Coupled Device
EMF	Electromotive Force
DFT	Density functional theory
slm	Standard liters per minute

Symbols

$\mathbf{H}$	Enthalpy
$\mathbf{G}$	Gibbs energy
$\mathbf{T}$	Temperature
$\mathbf{p}$	Pressure
$\mathbf{S}$	Entropy
$\mathbf{c_P}$	Specific heat capacity
$\mathbf{c_x}$	Concentration of the element x
$\mathbf{c_{x,St}}$	Concentration of the element x in the standard
$\mathbf{P_x}$	Intensity of the characteristic X-rays of the element x in the sample
$\mathbf{P_{x,St}}$	Intensity of the characteristic X-rays of the element x in the standard
$\mathbf{I}$	Beam current used for the sample
$\mathbf{I_{St}}$	Beam current used for the sample
$\mathbf{N_0}$	Avogadro's constant
ρ	Density

$\mathbf{A_x}$	Atomic weight of the element x
$\mathbf{Q_x(E)}$	Cross sectional area
$\mathbf{w}$	Quantum efficiency
$\mathbf{ds}$	Differential distance
$\mathbf{E_c}$	Ionization energy
$\mathbf{E_0}$	Incidence energy
$\mathbf{P_0}$	Incidental intensity
μ	Absorption coefficient
ϕ	Take-off angle
$\mathbf{d}$	Distance of the lattice plane
θ	Angle of incidence between the X-ray and the sample
$\mathbf{n}$	Order of the diffraction peak
λ	Wavelength of the incident X-ray

1. Motivation

Changing energy supply infrastructure and environmental concerns are driving significant new requirements for gas turbines and their materials. Not only are higher combustion temperatures desired to increase turbine efficiency [1], but future turbines must be able to withstand higher demands on their load flexibility as their use case will shift towards auxiliary power generation and to absorb peaks in power consumption [2]. In addition, the fuels will change from fossil fuels to renewables and possibly pure hydrogen [3]. All of these requirements are highly challenging for gas turbines, requiring entirely new concepts and materials beyond the Ni-based superalloys currently used as airfoil materials [4].

Materials based on the Mo-Si system are promising candidates for high-temperature alloys in extreme conditions due to their high melting point and good oxidation and corrosion resistance [5, 6, 7, 8]. The disadvantages are mainly poor mechanical properties due to the brittleness of the silicides and a relatively high density (ρ_{Mo} = 10.2 g/cm^3). To improve the properties, alloys in higher order systems such as Mo-Si-B [9, 10], Mo-Si-Ti-B [11], and, particularly in more recent years, Mo-Si-Ti [12, 13, 14] are being developed.

To guide efficient alloy development, the CALPHAD approach [15] is used. For the Mo-Si-Ti system, a CALPHAD dataset was developed and published by Yang et al. in 2003 [16]. Citing the need to develop Mo-Si-Ti-B alloys that are both reasonably ductile and corrosion resistant, they focused their experimental investigations on the region of the phase diagram with a Si content between 10 and 63 at.%. The specimens were analyzed in the cast state and after annealing at 1698 and 1873 K for 300 and 150 h, respectively. Two three-phase regions were reported in the metal-rich region of the system: β+Mo_5Si_3+Ti_5Si_3 and β+Mo_3Si+Mo_5Si_3. Furthermore, two-phase equilibria exist between β+Ti_5Si_3, β+Mo_5Si_3, β+Mo_3Si and Mo_3Si+Mo_5Si_3. A liquidus projection has been proposed based on the binary systems, the isothermal regions of the ternary system, and an isopleth, respectively. However, the publication by Yang et al. has several shortcomings. First, there are competing data from a publication by Svechnikov et al. [17], who also studied the isothermal section of the system at 1698 K. While they studied only the range between 37.5 and 66.7 at.% Si, which is of limited interest for contemporary gas turbine applications, the two publications show considerable differences in the solubility ranges of the two 5-3 silicides $(Mo,Ti)_5Si_3$ and $(Ti,Mo)_5Si_3$. Both publications have no obvious errors, so it is unclear which data are more reliable. Since these two phases are of major practical

importance due to their presence in all but one equilibrium in the metal-rich region, further investigation of this subject is warranted. It must be noted that Yang et al. does not show micrographs of annealed samples or X-ray diffractograms. Likewise, phase compositions are not listed but only indicated in the diagrams of the isothermal section. Therefore, it is difficult to fully rely on the data provided by this paper due to the lack of irrefutable evidence that data was not overlooked. Another issue is related to the Scheil solidification calculations presented by Yang et al. Several samples were prepared and experimental micrographs were compared with calculations of their solidification paths. Of the three specimens discussed, two proposed solidification paths are thermodynamically impossible. Therefore, a critical examination of the microstructures of cast samples is required to determine the validity of the proposed liquidus projection. Finally, further experimental investigations have provided new information on the crystallography of several phases. As these reports were published after the publication of Yang et al. they are of course not included in this dataset. Most importantly, it was discovered that the phase Mo_3Si is not stoichiometric, but consistently Si deficient. This is expected to affect the location of the two-phase and three-phase regions containing this phase, which in turn affects the usability of the dataset to accurately design alloys. In addition, the model used by Yang et al. for the Mo_5Si_3 phase, while not incorrect, is quite simplified; crystallographic data allow for an improved description of this phase as well.

A commercial Pandat database based on this dataset was used by Schliephake et al. [12] to develop alloys that combine oxidation resistance with good mechanical properties. The oxidation resistance was achieved by tailoring the Si content to enable formation of a protective oxide scale on the entire material, while the mechanical properties were derived from a fine-grained microstructure. One of the results of this work was the development of an alloy with the composition 45Mo-21Si-34Ti (all values in at.%), which was expected to decompose entirely into fine β and $(Mo,Ti)_5Si_3$ grains after annealing at 1573 K according to the dataset. While the as cast microstructure could be accurately predicted with Scheil solidification calculations, the annealed sample unexpectedly showed the presence of a third phase, Ti_5Si_3. These results indicate that while the dataset is an excellent starting point for alloy development, further investigations of the phase equilibria at 1573 K are necessary to develop novel turbine material.

The objective of this work is the investigation of the thermodynamics, constitution and kinetics of the Mo-Si-Ti system for the areas most relevant to gas turbine materials. The development of Mo-Si-Ti alloys and suitable protective coatings is ongoing in the German Research Foundation-funded Research Training Group RTG2561: Materials Compounds from Composite Materials for Applications in Extreme Conditions (MATCOM-COMMAT), of which this work is a part. This limits the Si content to 37.5 at.%, beyond which there is no equilibrium with the ductile β phase, and temperatures slightly above the current maximum application limit of gas turbine materials of about 1400 K. Since the investigations of Schliephake et al. showed discrepancies between experiment and calculation for 1573 K, this temperature was chosen as the annealing

temperature for this work. A major research question will be the phase equilibria under these parameters. As explained above, the publication by Yang et al., while a very good starting point, is not without issues. Therefore, and in light of conflicting reports from other sources such as Svechnikov et al., a dedicated, detailed analysis of the equilibria and phase compositions in the metal-rich region of the system at 1573 K is in order. For this purpose, samples will be prepared by vacuum arc melting and subsequently annealed. Their microstructure will then be studied by scanning electron microscopy. The compositions of the phases will be analyzed by electron probe microanalysis and energy dispersive X-ray spectroscopy. X-ray diffraction will be used to identify the phases present in the samples. Another crucial issue concerns the kinetics in the system. So far, there are no data on diffusion in the system. However, a detailed investigation, e.g. using diffusion couples or multiples, would be a complete topic for a Ph.D. thesis and therefore cannot be part of this work. Instead, the influence of the cooling rate on the microstructure of the samples is investigated. By analyzing the samples both after furnace cooling and after quenching, qualitative information about the diffusion rate in the system can be obtained. Although no quantitative values are determined, it can be assumed that practical information on the extent to which the structure of the samples is influenced by slow or fast cooling rates can be obtained. Another research question is the solidification of samples after casting in a vacuum arc melter. As mentioned above, a liquidus projection and the corresponding Scheil reaction scheme has been proposed by Yang et al. However, their applicability is unclear due to the fact that the microstructural evolution described in this publication is not always thermodynamically possible. Therefore, different samples will be prepared and their as-cast microstructure will be compared with the predictions made with the dataset. Depending on the results of these experiments, a decision can be made whether the liquidus projection can be accepted, needs to be refined, or even needs to be completely remodeled.

Furthermore, the binary system Mo-Si will be examined. As mentioned above, the models of Mo_3Si and Mo_5Si_3 can no longer be considered ideal and should be updated to reflect new experimental observations. The off-stoichiometry of Mo_3Si in particular is expected to affect several equilibria in the ternary system. Furthermore, no previous evaluation of this binary system has taken into account the heat capacities of the intermetallic phases, despite the existence of experimental data and their considerable relevance for high-temperature materials. Therefore, binary samples will be prepared and studied as described above in order to obtain more information about the phase Mo_3Si. These data, together with all reliable data from the literature, will then be used for a complete thermodynamic reassessment of this system.

Finally, the thermodynamic dataset of the Mo-Si-Ti system will be reassessed using the reassessed binary Mo-Si system as well as the experimental data obtained in this work. Following the binary reassessment, the best possible models for all phases will be used to ensure that the crystallography is reflected as accurately as possible. With the results of the ternary system investigations, the model parameters will be optimized to allow even better calculation of the phase equilibria in the

system. In addition, the liquidus projection will be refined as necessary to enable the prediction of microstructures under Scheil conditions.

2. The CALPHAD method

Originally, the term CALPHAD stood for "Calculation of Phase Diagrams". Since its inception, however, the method has been continuously developed into a powerful tool capable of calculating much more than just phase diagrams, and is now used to calculate and extrapolate all kinds of thermodynamic, thermophysical, and thermochemical properties of materials. Therefore, a more appropriate descriptor for the CALPHAD method is "computer coupling of phase diagrams and thermochemistry". The following section provides an introduction to the CALPHAD method itself, followed by the models and underlying mathematical descriptions most relevant to this work. Finally, the process of numerical optimization of the dataset is explained. Due to the complexity of the topic, further specialized literature, such as the book by Lukas, Fries and Sundmann [18], should be consulted for a more detailed explanation of certain topics. Regarding the history of the method, the paper by Spencer [19] gives a good overview, especially for the early development.

2.1. Introduction to the CALPHAD method

The core of the CALPHAD method is the development of databases that store analytical descriptions of the Gibbs energy of all phases in the system of interest. While the calculation of phase diagrams from Gibbs energy models was reported as early as 1908 by van Laar [20, 21], the CALPHAD method was substantially shaped and developed by Kaufman and Bernstein with the publication of a book [15] that sparked considerable scientific interest in the subject. A schematic process diagram of the modern CALPHAD method was published by Seifert and Aldinger [22] and is shown in Figure 2.1. The diagram shows well that the CALPHAD method consists of two principal parts, optimization and equilibrium calculations, whose "building blocks" are interrelated. For example, both theoretical data and experimental results inform the phase models. In practice, this means that the chosen model must match the physical and chemical properties of the phase, such as crystal structure, bond type, and order-disorder transformations. The models have adjustable parameters, explained in more detail later, which in turn are based on and determined by experimental information. Once these parameters have been correctly set, they are used to calculate thermodynamic functions such as the Gibbs energy G, the entropy S or the heat capacity c_p. These functions are stored in databases or datasets that are used in

thermodynamic calculations. These datasets are in practice often called "tdb files", named after their file extension in the computer operating system.

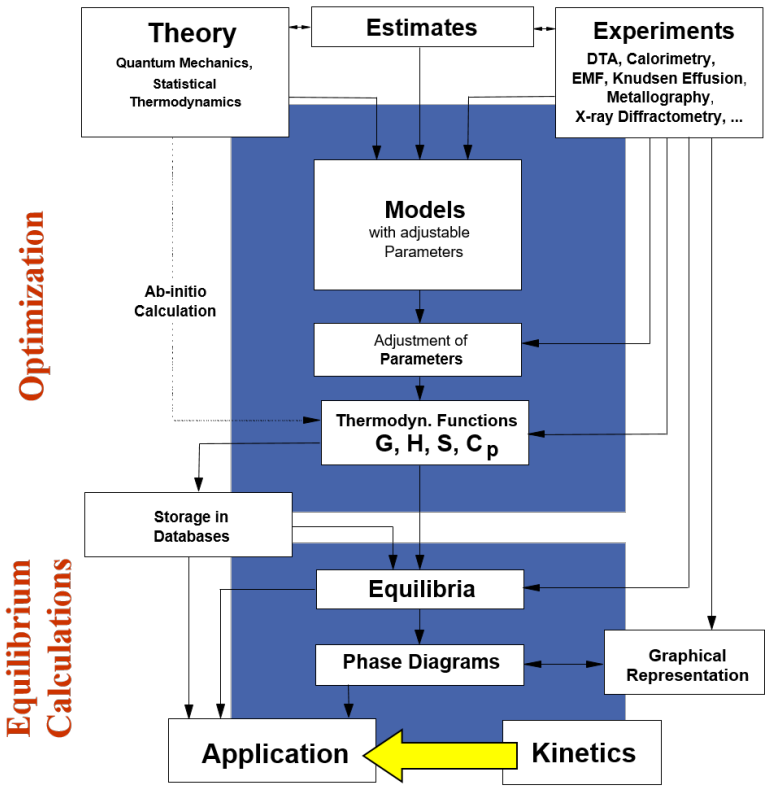

Figure 2.1.: Process diagram of the CALPHAD method, after [22].

Typically, the Gibbs energy G of the phases is chosen as the function stored in the databases. While in principle any other state function is equally suitable, the Gibbs energy is convenient because its characteristic state variables (temperature T, pressure p, and amount of component i N_i) are readily available in experiments. Other state functions can be derived from the Gibbs energy, for example by the following equations:

$$H = G - T(\frac{\delta G}{\delta T})_{P,N_i} \tag{2.1}$$

$$S = -(\frac{\delta G}{\delta T})_{P,N_i} \tag{2.2}$$

$$c_p = -T(\frac{\delta^2 G}{\delta T^2})_{P,N_i} = T(\frac{\delta S}{\delta T})_{P,N_i} \tag{2.3}$$

These equations can also be used to show how different experimental data directly correlate with the model parameters. For example, to describe the specific heat capacity of a material, the empirical approach by Maier and Kelley is often used. For a pure elemental component, the following equation is used:

$$c_p = -c - 2dT - 2eT^{-2} + ... \tag{2.4}$$

If this equation is terminated after the third term, the three parameters c, d and e can be fitted to the experimental values of c_p. By using the relationship between c_P and S from equation 2.3, the equation

$$\Delta S = -b - c\ln(T) - 2dT - eT^{-2} \tag{2.5}$$

is obtained. The parameter b describes the entropy at the lower integration limit. Likewise, ΔH can be expressed by the equation

$$\Delta H = a - cT - dT^2 + 2eT^{-1} \tag{2.6}$$

where the parameter a describes the enthalpy at the lower integration limit. Finally, for the Gibbs energy, the following form can be used:

$$\Delta G = a + bT + cT \cdot \ln(T) + dT^2 + eT^{-1} \tag{2.7}$$

This equation contains all parameters of the previous state equations, which highlights the versatility of the Gibbs energy and its suitability as the "default" function for thermodynamic datasets. With the information how the parameters influence the different functions, one can derive what kind of experimental data can be used in the optimization. Aside from phase equilibria and compositions, which are ultimately what a phase diagram shows, data from calorimetry, thermal analysis, electromotive force measurements and similar methods can be used to fit the parameters of the models. Likewise, theoretical data, such as ab initio calculations, can often be used in the optimization.

2.2. Analytical models for the Gibbs energy

As mentioned in the previous section, analytical models for the Gibbs energy of each phase of a system are at the core of the CALPHAD method. A good way to describe the total Gibbs energy of a phase θ is to express it as the sum of different influences and develop equations to calculate them separately. Thus the Gibbs energy can be described by the equation

$$G_m^\theta = {}^{srf}G_m^\theta + {}^{phys}G_m^\theta - T \cdot {}^{cnf}S_m^\theta + {}^{E}G_m^\theta. \tag{2.8}$$

Here ${}^{srf}G_m^\theta$ describes the Gibbs energy of the unreacted mixture of the components (the prefix srf stands for "surface of reference"). The term ${}^{phys}G_m^\theta$ accounts for contributions to the Gibbs energy from physical models such as magnetic transitions and can often be neglected for many materials. The third term, $T \cdot {}^{cnf}S_m^\theta$, represents the contributions to the Gibbs energy by the configurational entropy, i.e. the different possible arrangements of the atoms at the Wyckoff positions. Finally, the last term, ${}^{E}G_m^\theta$, represents the excess Gibbs energy and accounts for all contributions not represented by any of the other terms.
The equations in section 2.1 can be used to describe pure single component phases. In the following, models for different multicomponent phases will be explained.

2.2.1. Stoichiometric phases

Since stoichiometric phases by definition do not vary in composition, the Gibbs energy depends only on temperature (and pressure, which is usually negligible). Thus the analytic function is very similar to that for pure elements (Eq. 2.7). For a stoichiometric compound A_qB_p the equation becomes

$$G_{A_qB_p}(T) - q \cdot {}^0H_A^{SER} - p \cdot {}^0H_B^{SER} = a + bT + cT \cdot \ln(T) + dT^2 + fT^{-1} + ... \tag{2.9}$$

where ${}^0H_A^{SER}$ and ${}^0H_B^{SER}$ are the enthalpies of the pure elements A and B in their reference states at 298.15 K and 1 bar, respectively. For compounds consisting of more than two elements, the equation 2.9 can be generalized as

$$G_\theta(T) - \sum_{i=1}^{n} x_i \cdot H_i^{SER} = a + bT + cT \cdot \ln(T) + dT^2 + fT^{-1} + ... \tag{2.10}$$

2.2.2. Solid solution phases

In solid solutions the Gibbs energy depends not only on the temperature but also on the composition of the phase. Therefore Equation 2.8 can be applied. The first term can be written as

$$^{srf}G_m^\theta = \sum_i^n x_i \, {}^0G_i^\theta \tag{2.11}$$

where x_i is the concentration of component i in the solution and ${}^0G_i^\theta$ is the molar Gibbs energy of the pure component i at temperature T. The term derived from the configurational entropy, also called the Gibbs energy of the ideal solution ${}^{id}G_m^\theta$, is expressed as

$$^{id}G_m^\theta = -T \cdot {}^{cnf}S_m^\theta = RT \sum_i^n x_i \cdot \ln x_i. \tag{2.12}$$

However, ideal solutions are very rare in practice due to interactions between species. As a result of such effects, real compounds may show tendencies to form miscibility gaps, for example. As mentioned earlier, the excess Gibbs energy is the term that takes into account all such effects that are not represented by any other term. While several different models exist to describe the excess Gibbs energy analytically, one of the most common models is the Redlich-Kister excess model [23]. Here the excess Gibbs energy is expressed as

$$^{E}G_m^\theta = x_i x_j \sum_{\nu=0}^{n} (x_i - x_j)^\nu \cdot {}^\nu L_{ij}^\theta \tag{2.13}$$

where ${}^\nu L_{ij}^\theta$ are the so-called Redlich-Kister parameters of the order ν = 0,1,2,... The Redlich-Kister parameter itself is often described with a temperature dependence by the equation

$${}^\nu L_{ij}^\theta = {}^\nu a_{ij}^\theta + {}^\nu b_{ij}^\theta T + ..., \tag{2.14}$$

which is typically truncated after the linear term. Figure 2.2 shows the influence of the first five terms of the Redlich-Kister polynomial on the enthalpy. It can be seen that in order to describe asymmetrical effects, at least a first order Redlich-Kister term is necessary.

It should be noted that often the same models are applied to the liquid phase that are used to describe solid solution phases. This is because their behavior is very similar, unless special conditions are required, such as in the case of ionic liquids.

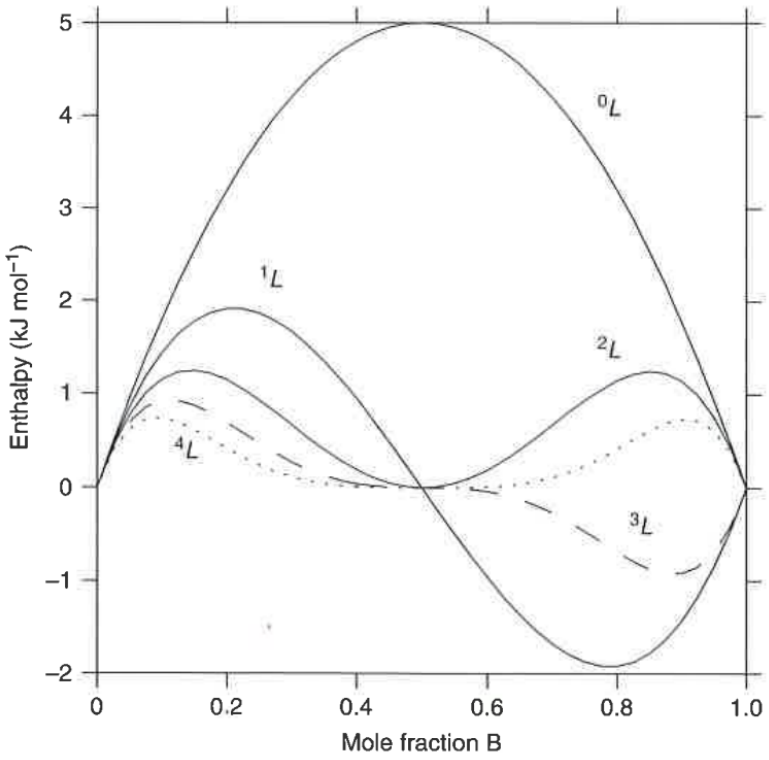

Figure 2.2.: The influence of 0th to 4th order Redlich-Kister parameters on the excess enthalpy. Image taken from [18].

2.2.3. Compounds with sublattices

Solid solutions with at least two sublattices that allow for a homogeneity range can be described by the Compound Energy Formalism (CEF) [24]. While the name was coined by Sundman and Ågren [25] its origins can be traced back to the sublattice model by Hillert and Staffanson [26]. A simple example of a compound with two sublattices is

$$(A, B)_p(C, D)_q \tag{2.15}$$

where the components A and B are located on one sublattice and the components C and D are located on the other. A and B can substitute each other, but they cannot occupy the second sublattice. The same is true for C and D on the second sublattice. The indices p and q are the stoichiometric coefficients of the respective sublattices. Note that the components are not necessarily atoms, but can be ions, vacancies, or even compounds. In the CEF, the mathematical model is similar to that of solid solution phases and Equation 2.8 can be applied again. However, instead of the mole fraction of an element (which could be distributed over different sublattices),

the site fraction y_i^S is used. It describes the occupancy of a sublattice by the component and is defined as

$$y_i^S = \frac{n_i^S}{\sum_j n_j^S} = \frac{n_i^S}{n^S} \tag{2.16}$$

where n_i^S is the amount of component i on the sublattice S and n^S is the total number of all positions on the sublattice. By definition, the equations

$$\sum_i y_i^S = 1 \tag{2.17}$$

and

$$\sum_S n^S = n \tag{2.18}$$

apply, where n is the total number of positions on all sublattices. With this, the mole fraction can be expressed by the equation

$$x_i = \frac{\sum_S n^S y_i^S}{\sum_S n^S (1 - y_{Va}^S)} \tag{2.19}$$

where y_{Va}^S is the amount of positions of the sublattice occupied by vacancies.
The final concept to be introduced before attempting to analytically describe the Gibbs energy is that of end members. This is simply the term for compounds where each sublattice is completely occupied by one component. In the example compound there are four end members: A_pC_q, A_pD_q, B_pC_q, and B_pD_q. Each of these compounds, whether experimentally stable or not, has a corresponding Gibbs energy called ${}^0G_{A:C}$, ${}^0G_{A:D}$, ${}^0G_{B:C}$, and ${}^0G_{B:D}$. When these Gibbs energies are plotted over the compositions in a 3-dimensional diagram, the Gibbs energies of each compound can be estimated by linear approximation. This is shown graphically in Figure 2.3, which is taken from the publication of Hillert [24]. The resulting surface is the reference surface of the Gibbs energy of the phase. This means that the first term of the equation 2.8 for the CEF can be described mathematically by the equation

$${}^{srf}G_m^\theta = y_A^1 y_C^2 \cdot {}^0G_{A:C} + y_A^1 y_D^2 \cdot {}^0G_{A:D} + y_B^1 y_C^2 \cdot {}^0G_{B:C} + y_B^1 y_D^2 \cdot {}^0G_{B:D} \tag{2.20}$$

for two sublattices. The superscript numbers 1 and 2 are not exponents, but denote the respective sublattices. In case of more sublattices, appropriate terms for the additional sublattices and components must be added. A generalized expression is

$${}^{srf}G_m^\theta = \sum_I P_I(Y)\, {}^0G_I \tag{2.21}$$

where I is a component array specifying one constituent in each sublattice, $P_I(Y)$ is the product of the constituent fractions, and ${}^0G_I$ is the Gibbs energy of the compound I.

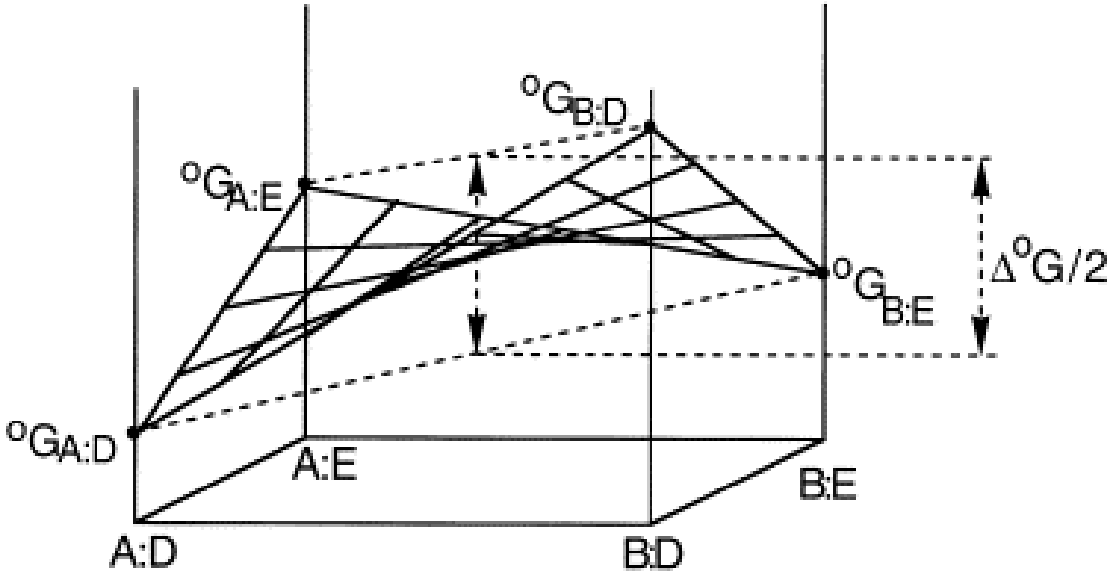

Figure 2.3.: The Gibbs energy surface of reference of the phase (A,B)(C,D). Image taken from [24].

The second term, specific physical effects, is again often negligible. For the third term, corresponding to the configurational entropy, ideal mixing is assumed, but restricted to the respective sublattices. The term can be expressed by the equation

$$ {}^{id}G_m^\theta = -T \cdot {}^{cnf}S_m^\theta = RT \cdot [p(y_A^1 \ln y_A^1 + y_B^1 \ln y_B^1) + q(y_C^2 \ln y_C^2 + y_D^2 \ln y_D^2)] \tag{2.22} $$

where the superscript numbers 1 and 2 again denote the respective sublattices and the appropriate terms need to be added in the case of more than two sublattices. The generalized expression is

$$ {}^{id}G_m^\theta = -T \cdot {}^{cnf}S_m^\theta = RT \sum_S a^S \sum_i y_i^S \ln y_i^S \tag{2.23} $$

where a^S is the number of sublattice sites and y_i^S is the constituent fraction of the component on that sublattice.

The definition of the excess Gibbs energy is similar to that for solid solution phases and Redlich-Kister polynomials are used for the analytical description. In the case of a compound with two sublattices, the equation

$$^{E}G_m^{\theta} = y_A^1 y_B^1 [y_C^2 L_{A,B:C} + y_D^2 L_{A,B:D}] + y_C^2 y_D^2 [y_A^1 L_(A:C,D) + y_B^1 L_{B:C,D}] \quad (2.24)$$

can be used. The parameter $L_{A,B:C}$ describes the interaction when the first sublattice is occupied by components A and B, while the second sublattice contains only component C. The other Redlich-Kister parameters are defined analogously. Again, Equation 2.24 is only valid for two sublattices each containing two components. The generalized equation is

$$^{E}G_m^{\theta} = \sum_{Z>0} \sum_{IZ} P_{IZ}(Y) L_{IZ} \quad (2.25)$$

where P_{IZ} is the product of the site fractions and Z is the order of the parameter.

2.3. Thermodynamic optimization

The objective of thermodynamic optimization is to adjust the coefficients of the model functions so that the discrepancy between calculated values of properties (e.g. phase equilibria, enthalpies of formation, and heat capacities) and experimental data is minimized. The experimental data are presented in a machine-readable and human-understandable format in the form of so-called pop files (named after their file extension in the operating system). This file defines the experimental conditions and the values of the relevant properties. During the optimization process, the CALPHAD software calculates the values with the current parameters of the dataset and compares the result with the values from the pop file. If the difference between the calculated and experimental values exceeds a specified threshold, the parameters are adjusted and the values are recalculated and compared again. By repeating this process for a sufficient amount of time, it is possible to identify a set of parameters that provide the best fit between calculations and experiments. Most optimizers, including the PARROT module used in this study, apply the method of least squares to evaluate the quality of the fit. This method is described in detail in section 2.3.1.

Although the computer performs the iteration, the user must exert significant effort to ensure that the optimization yields satisfactory and realistic outcomes. This begins with the seemingly simple task of compiling the pop file. Any error made here, from simple typos to incorrect definitions of elemental reference states, may lead to optimization errors that can be very difficult to notice and eventually correct. In addition, the user must identify an initial set of model parameters that are sufficiently accurate to ensure that the final equilibria are at least qualitatively correct. Otherwise, the calculation may fail entirely. Similarly, the user must make certain decisions, such as how to weigh the different experiments in the pop file or the amount and type of parameters to optimize

simultaneously at any given time. These decisions will affect the outcome of the optimizations. For the majority of these questions, no definitive guidelines can be provided. Instead, the user must rely on their experience and, on occasion, their "intuition" when optimizing a system. In certain instances, it is necessary to define hypothetical experiments in a pop file. This is the case when data is available for which no experimental evidence exists, but which must be included to correct unrealistic behaviors introduced by the software. A typical example of this is, when unrealistic miscibility gaps open during the optimization process, where it is numerically possible, but thermodynamically extremely unlikely. This occurs with some regularity, as the software prioritizes a satisfactory fit between the data from the pop file and the calculations. If an agreement is attainable with a set of parameters that leads to unrealistic behaviors in other, less well-defined areas, the software will accept these parameters. Further optimization with the same set of experiments will, in such cases, usually not lead to different results. In the aforementioned example, it may be necessary to define an experiment that prohibits the miscibility gap. This could be achieved by defining the driving force of the phases that are expected to be present, despite the lack of actual experimental data at the current stage. While this method is effective, it should be used with great caution and only in exceptional circumstances. It may restrict the parameters in a way that leads to a dataset that replicates the experimental data well but has limited capability to predict new, previously unexplored areas of the system.

2.3.1. Least-squares method

The least-squares method is a mathematical method for estimating a set of m parameters C_j in a given set of equations to minimize the difference between the "true" values L_i (that is, the experimental or theoretical value) and the result obtained by the calculation, W_i. W_i is a function of the parameters and independent variables $x_{k,i}$, such as the temperature, concentration or pressure:

$$W_i = F_i(C_j, x_{k,i}) \tag{2.26}$$

where $i = 1, ..., n$ is the consecutive number of the experiment, $j = 1, ..., m$ is the consecutive number of the parameter and k distinguishes between the independent variables.
The difference between the calculated result and the "true" value, sometimes multiplied with a weighing factor p_i, is referred to as the error v_i:

$$(W_i - L_i) \cdot p_i = v_i \tag{2.27}$$

The objective of the optimization is to identify the set of parameters that minimizes the sum of the squares of the errors:

$$\sum_{i=1}^{n} v_i^2 = min \tag{2.28}$$

This condition leads to the following equation for the parameters C_j:

$$\sum_{i=1}^{n} v_i \cdot \frac{\delta v_i}{\delta C_j} = 0 \tag{2.29}$$

A Taylor series expansion, terminated after the linear expression, yields the following equation:

$$v_i(C_j, x_{ki}) \approx v_i^0(C_j^0, x_{ki}) + \sum_{l=1}^{m} \frac{\delta v_i}{\delta C_l} \cdot \Delta C_l \tag{2.30}$$

where ΔC_l are corrections to the coefficients C_l. To calculate these corrections, the last two equations are inserted into each other to give

$$\sum_{l=1}^{m} (\sum_{i=1}^{n} \frac{\delta v_i}{\delta C_j} \cdot \frac{\delta v_i}{\delta C_l}) \Delta C_l = -\sum_{i=1}^{n} v_i^0 \cdot \frac{\delta v_i}{\delta C_j} \tag{2.31}$$

with $j = 1, ..., m$. Given an initial set of parameters C_l^0, this equation is solved for the corrections, which are used to calculate new parameters. This process is repeated until the corrections are below a defined threshold. The quality of the parameter fit can be determined by the mean square error MSE, which is defined as

$$MSE = \sum_{i=1}^{n} \frac{v_i^2}{n - m}. \tag{2.32}$$

The method of least-squares often fails when the parameters C_j are non-linear. This is understandable because in equation 2.30, the Taylor series is truncated after the linear term and is therefore not suitable for higher order dependencies. Also, initial values for the parameters that are very far from the "final" values are problematic for the least-squares method because the calculation may not converge. In such cases, other methods, such as the Marquardt algorithm [27], may be more suitable.

3. Materials and Experimental Methods

In order to investigate the thermodynamics of the Mo-Si-Ti system, samples were prepared and subsequently analyzed using a variety of different methods. While the majority of the samples were annealed and studied in equilibrium, some of the characterization methods were applied to samples in the as-cast state, either to obtain information on the state of the samples prior to heat treatment (e.g., their chemical composition) or to investigate the solidification behavior of the alloys. The following section describes the experimental methods used in this work. It is not the aim of this thesis to provide a comprehensive discussion of the techniques, but a fairly brief overview in the context most relevant to the challenges of the Mo-Si-Ti system. Where appropriate, references are given for more detailed explanations.

3.1. Sample preparation

All samples in this thesis were produced by Vacuum Arc Melting (VAM). In this process, an electric current is used to ignite a plasma arc between an electrode and a grounded crucible. This arc is used to melt the material. The equipment is operated in an argon atmosphere at a slight vacuum. Since the temperature of the arc can reach several thousand Kelvin, the crucible is typically a water-cooled copper plate. The electrode can be either consumable or non-consumable.

The materials used in this work were molybdenum foil of 0.025 mm thickness (99.95 % purity, Alfa Aesar), silicon granulate (99.99 % purity, Goodfellow GmbH), and two sample types of titanium. One was coarse Ti granules about 3-5 mm in diameter (99.6+ % purity, Goodfellow GmbH) and the other was Ti foil 0.127 mm thick (99.7 % purity, Merck KGaA). The foil was typically used when either the amount of Ti in an alloy was so high that Mo could not fully envelop all materials (see below), or when the granules were so coarse that the desired mass could not be satisfactorily achieved. Button ingots of 500 to 2000 mg (depending on the intended use of the specimen) were prepared using a non-consumable tungsten electrode. The device was a MAM-1 compact arc furnace from Edmund Bühler GmbH. To keep the atmosphere free of oxygen and nitrogen, the equipment was housed in a glove box. Both the arc furnace itself and the glove box were operated with high purity argon (99.9999 % purity, Alfa Aesar). Prior to arc melting, the materials were carefully weighed to ensure accurate sample composition. Due

to the large difference in melting points of the elements (Mo: 2896 K, Si: 1687 K, Ti: 1941 K), the Mo foil was wrapped around the other elements so that the molten Mo would trap any Si and Ti that might evaporate. In cases where this was not possible due to low Mo concentration in the alloy, the Si was wrapped in Ti foil instead, with the Mo foil placed on top to best achieve the same effect. The materials were melted on a flat copper crucible to form button-shaped ingots. Each sample was remelted five times to promote complete mixing of the elements. Before each step, a Ti getter was melted and allowed to solidify to reduce the partial pressure of oxygen in the melting chamber. After melting, all samples were reweighed to determine any mass loss during melting.

3.1.1. Heat treatments

The majority of the samples for this work were heat treated to achieve the equilibrium conditions necessary to obtain the relevant thermodynamic and compositional data for the CALPHAD method. However, many alloys in the Mo-Si-Ti system are highly susceptible to oxidation, with Ti being a common oxygen getter and Mo forming volatile oxides. Only for specific compositions protective layers of titanium oxide and silicon oxide duplex layers can be formed in this system [13]; however, when studying the phase diagram of the system, these conditions are usually not met, as all equilibria must be examined. Encapsulation of the samples in containers is also not feasible as this prevents effective quenching of the samples, which in turn may affect the phase composition of the sample. Furthermore, Mo and Ti tend to react with commonly used container materials such as Zr and W.
For the above reasons, a new quenching furnace was developed in collaboration with HTM Reetz GmbH specifically for this project. It is a tube furnace that can be tilted by 90° so that the samples fall out of the tube into another compartment containing the quenching medium. The furnace is designed so that the quenching medium is added to a separate compartment of the furnace just before quenching. In this way the samples were not exposed to the environment until they were quenched, minimizing the possible content of contaminants. The device and its development is explained in more detail in section 6.1.
The furnace operates with a flowing high-purity argon atmosphere (99.9999 %, 0.2 slm flow rate). The gas was additionally purified in an OxiClear - DGP-R1-3000B Purifier by LabClear Inc. before it was led into the furnace. The O_2 concentration of the effluent gas was monitored with an oxygen sensor (E2010 by Zirox GmbH). An Al_2O_3 tube forms the heating chamber of the furnace. To prevent reactions between the specimens and the tube, the samples were placed in an Al_2O_3 crucible lined with Mo foil. The heating elements of the furnace are made of metallic molybdenum to withstand the mechanical stresses of tilting the furnace during quenching. To prevent this material from degradation by oxidation, it is embedded in a getter material, the

composition of which has not been disclosed by the manufacturer for compliance reasons. The quenching medium used in this work was purified water. The annealing temperatures chosen in this work will be listed in the appropriate experimental sections.

3.1.2. Metallographic preparation

To prepare the samples for various analytical methods, they were sectioned to expose the internal areas, followed by grinding and polishing to achieve a surface quality suitable for electron microscopy. All specimens were bisected using a diamond blade (DiaCut 007 from Cloeren Technology GmbH) in a precision cutting machine (Brillant 220 from ATM Qness GmbH). One half of each sample was then hot mounted in a conductive medium (WEM REM from Cloeren Technology GmbH, the mounting press was a CitoPress-10 from Struers GmbH), while the other half was used for sample composition analysis (see section 3.2.3). The sectioning was done before embedding the samples, as residues of the medium could stick to the sample surfaces and affect the measurement of carbon in the sample. The conductive embedding medium was chosen because it allowed the sample to be examined in the SEM without the need to sputter the surface with gold or use conductive paste. The mounted specimens were then ground and polished according to the recipe given in the Table 3.1. The force used remained the same in each step, but depended on the composition of the sample. Generally, the more intermetallic phases an alloy contains, the higher the force needed to be due to the high hardness of these phases. In this work the forces used ranged from 4-20 N per sample in the sample holder. The first polishing steps were carried out with diamond suspensions and the last step with colloidal silica suspensions (all polishing media from Cloeren Technology GmbH). For the first two polishing steps, diamond suspension was added at the beginning and at half the total time. In between, a mixture of ethanol, water and detergent was used for lubrication as required. For the final step, water or polishing solution was added alternately every 30 seconds. As the silica suspension dries very quickly and then adheres to the surfaces thoroughly, the polishing cloth needs to be prepared to work properly. For this reason, it was rinsed with water in one polishing machine while the samples were polished in another machine for the first two steps. After the last step, the cloth and samples were rinsed with water for 5 min to prevent the solution from drying on the sample surface. The samples were then ultrasonicated in detergent for 5 minutes and rinsed in isopropanol.

Table 3.1.: The parameters used for grinding and polishing the samples. The chosen load was always 4-20 N per sample, the rotational speed was 100 rpm for the sample carrier and 150 rpm for the disk, respectively.

Surface	Abrasive size	Relative rotation	Time / min
SiC paper	#320	Same	Until level
SiC paper	#320	Same	1:00
SiC paper	#500	Opposite	1:00
SiC paper	#1000	Same	1:00
Silk	6 µm	Opposite	10:00
Cotton	3 µm	Same	8:00
Polychloroprene	0.04 µm	Opposite	6:00

3.2. Characterization methods

3.2.1. Electron optical methods combined with chemical phase analysis

Two methods of electron optical characterization using scanning electron microscopy (SEM) were utilized in this work: energy dispersive X-ray spectroscopy (EDX) and electron probe microanalysis (WDX/EPMA). Both methods are very similar in principle and are typically used to obtain the same information, but have unique strengths and weaknesses. The following sections briefly describe the two techniques, followed by a section on correction factors and error estimation for both methods. Electron optical methods are among the most versatile imaging techniques available. As such, there are numerous books that give an excellent description of the methods, such as those by Zhou et al. [28], Dunlap and Adaskaveg [29], or by Schmidt et al. [30]. The purpose of this section is therefore not to explain electron microscopy in detail, but rather to give a brief overview of the most important aspects of the technique as they relate to this work.

3.2.1.1. Scanning electon microscopy (SEM) and energy dispersive X-ray spectroscopy (EDX)

Scanning electron microscopy is similar in principle to optical microscopy, but instead of light, a beam of electrons is used to scan the surface of a sample. The electrons are typically generated by thermionic or field emission, accelerated, and focused into a narrow beam by a series of electromagnetic lenses. When the electron beam strikes the surface of the sample, a variety of signals are produced, see Figure 3.1. The most important of these signals are the secondary electrons (SE), the backscattered electrons (BSE) and the characteristic X-rays. Secondary

electrons are produced by inelastic scattering when the incident beam ionizes sample atoms and electrons are emitted from their outer shells. These electrons typically have a relatively low energy (a broad definition of secondary electrons is any electron with an energy below 50 eV [28]). Therefore, this signal is emitted only from the surface of the sample, providing excellent topographical information about the sample. Backscattered electrons, on the other hand, result from the elastic scattering of the incident electrons by the nuclei of the sample. In principle, the electron beam is deflected by the nuclei, loses some of its energy and is emitted from the sample. These electrons then reach the detector and a signal is detected. Not only does this signal come from electrons of much higher energy (and therefore potentially deeper in the sample), but the amount of elastic scattering depends on the nuclear mass of the atoms in the sample. Therefore, the heavier the element interacting with the electron at a given position, the more backscattered electrons will be produced and detected. This results in a compositional contrast in the image, with areas of heavier elements appearing brighter and areas of lighter elements appearing darker. Characteristic X-rays are emitted when high-energy electrons from the beam interact with inner-shell electrons in the sample. With sufficient energy, these electrons leave the atom and electrons from the outer shells fill the vacancies. The excess energy is emitted in the form of X-rays and the exact value of the energy is unique for each transfer. By using a detector to measure the energy of the X-rays, a quantitative analysis of the sample composition can be performed. This signal is used in the energy dispersive X-ray spectroscopy (EDX). This is one of the most widely used techniques in materials science because it is a fast and reliable method for obtaining information about most elements in a sample and their concentration. Limitations of this technique are light elements (elements lighter than boron cannot be detected at all by this method, and heavier elements tend to give more reliable quantification results), sample compositions containing elements with overlapping characteristic X-ray energies, and low elemental concentrations, as the error increases sharply with concentrations below 1 at.%. In these cases, electron probe microanalysis (EPMA) is often the better choice of characterization method.

The SEM used in this work was a Philips XL 30 SFEG scanning electron microscope. Typically, an acceleration voltage of 15 kV was used. The working distance was always set to 10 mm.

3.2.1.2. Electron probe microanalysis (EPMA)

Electron probe microanalysis is similar in principle to EDX analysis, but diffraction on crystals is used to split the X-ray spectrum into distinct wavelengths. Thus, instead of measuring a continuous spectrum as in EDX, one wavelength is measured at a time, which is why this technique is called wavelength dispersive X-ray analysis (WDX). The advantage of this method is that spectral resolution is greatly increased and overlapping peaks of different elements can

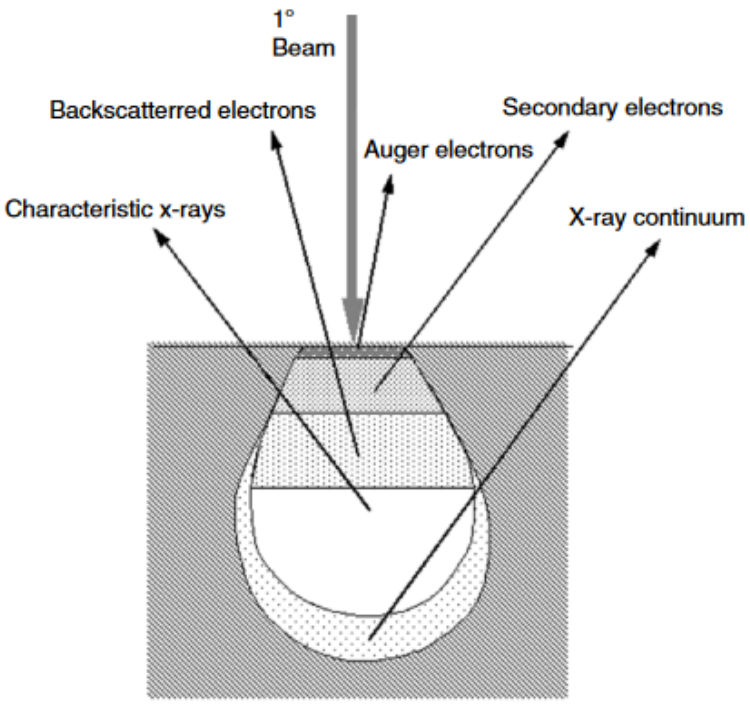

Figure 3.1.: An overview of the signals generated when the electron beam of a SEM interacts with a sample. Image taken from [28].

Table 3.2.: The energies of the characteristic X-rays of the elements relevant to this work.

Element	**Kα energy / eV**	**Lα energy / eV**	**M energy / eV**
Mo	17.481	2.293	0.192
Si	1.740	0.092	-
Ti	4.510	0.452	-

be reliably distinguished. It also avoids the common problems of EDX, such as a relatively high signal-to-noise ratio and false peaks. The main disadvantages are the increased measurement time, which scales with the number of elements analyzed, and the need for the experimenter to know which elements to look for.

Taking all this information into account, both EDX and WDX offer certain advantages and disadvantages. When measuring the Mo-Si-Ti system, peak overlap is not an issue, see Table 3.2 for the energies of the relevant peaks. However, for certain alloys EPMA can be expected to give quantitatively more reliable results. For this reason, many of the samples in this work have been measured by EPMA in addition to EDX.

The apparatus used in this work was a Cameca SX100 electron microprobe. An acceleration voltage of 15 kV was used.

3.2.1.3. Correction factors and error estimation

Under ideal conditions, the concentration of an element is directly proportional to the intensity of its characteristic X-ray radiation and the beam current:

$$c_x = c_{x,st} \cdot (P_x/P_{x,st}) \cdot (I/I_{st}) \tag{3.1}$$

with c_X: concentration of the element x in the sample, $c_{X,st}$: concentration of the element x in the standard, P_x: intensity of the characteristic X-rays of the element x in the sample, $P_{X,st}$: intensity of the characteristic X-rays of the element x in the standard, I: beam current used for the sample, I_{st}: beam current used for the measurement of the standard.

However, under real conditions, several factors affect P_x, making it only approximately proportional to the concentration. These factors must be taken into account for a quantitative analysis to be valid. The most common method to account for such effects is the so-called ZAF correction. Here, *Z* stands for the effect of the atomic number of the elements analysed, *A* stands for the absorption effect and *F* for the fluorescence excitation effect. The magnitude of each effect is estimated or, if possible, directly measured, and quantified as a factor which is multiplied with the aforementioned equation:

$$c_x = c_{x,st} \cdot (P_x/P_{x,st}) \cdot (I/I_{st}) \cdot F_Z \cdot F_A \cdot F_F \tag{3.2}$$

with F_Z, F_A, F_F: the correction factors for the atomic number effect, the absorption effect and the fluorescence effect, respectively. The following section explains each of these effects.

Atomic number (Z) effect: The number of photons dN_x generated from an element x by an electron inside the specimen can be expressed by the equation

$$dN_x = (N_0\rho/A_x) \cdot c_x \cdot Q_x(E) \cdot w \cdot ds \tag{3.3}$$

with N_0: Avogadro's constant, ρ: density of the material, A_x: atomic weight of the element x, $Q_x(E)$: cross-section, w: quantum efficiency, ds: differential distance.

Since the energy of the electron E decreases with the distance traveled, the total number of photons can be calculated by integration:

$$N_x = const \cdot \int_{E_c}^{E_0} Q_x/(dE/ds)\, dE \tag{3.4}$$

with E_c: ionisation energy and E_0: incidence energy. The loss of energy per distance traveled depends on the atomic number Z of the element:

$$dE/ds = const \cdot (1/E) \cdot (Z/A) \cdot \ln(E/11.5 \cdot Z)) \tag{3.5}$$

For samples consisting of several different elements, the effects are simply additive:

$$dE/ds = \sum c_i (dE/ds)_i \tag{3.6}$$

with c_i: the concentration of the respective element and $(dE/ds)_i$ the energy loss per distance traveled corresponding to the respective element alone. Therefore, the Z correction can account for the concentration difference of the different atoms of a specimen compared to the known standard.

Absorption (A) effect: Photons which are generated within the specimen can be absorbed by it, as well. Thus, the intensity of the radiation P decreases exponentially with the distance d travelled by the photon within the sample:

$$P = P_0 \cdot exp(-\mu d) \tag{3.7}$$

with P_0: incidental intensity, μ: absorption coefficient.

The magnitude of the absorption is expressed as the quotient of the amount of photons which reach the detector and the total amount of photons generated within the sample and is called $f(\chi)$. χ itself is a combined variable which takes into account the absorption coefficient (which is dependant on the material and the energy of the incident beam), the density of the material ρ and the take-off angle of the X-ray detector Φ:

$$\chi = \mu/(\rho \cdot sin(\Phi) \tag{3.8}$$

When the amount of photons n generated at depth z is $dn/d(z \cdot \rho)$, $f(\chi)$ can be expressed as

$$f(\chi) = \frac{\int (dn/dz \cdot \rho) \cdot exp(-\chi t)\, dt}{\int (dn/dz \cdot \rho)\, dt} \tag{3.9}$$

In practice, the A correction is typically the most significant influence of the ZAF correction. This is especially true for samples containing a high concentration of very light elements, whose photons have a high tendency to be absorbed by heavy elements.

Fluorescence excitation (F) correction: The fluorescence excitation correction is similar to the absorption correction in that both correct for the loss of photons due to absorption by the sample. However, the F-correction specifically addresses the case where the energy of the absorbed photon is sufficient to ionize another atom in the sample, which then emits another photon. This effect is particularly strong when the excitation energies of two elements in the sample are very close. In such cases, the radiation produced by the ionization of one element can be readily reabsorbed by the other element, which in turn becomes excited and emits characteristic X-rays. The detrimental effects of this are twofold: First, the concentration of the element with the slightly lower excitation energy is overestimated at the expense of the concentration of the element with the higher excitation energy. Second, due to the propagation of radiation in this way, the excitation volume can far exceed the excitation volume of the primary radiation. As a consequence, any quantification result will be significantly affected and the spatial resolution will also decline.

Another widespread, far simpler correction is the so-called **P/B correction**. The ratio of the intensity of the characteristic radiation of an element, P_x and its background intensity, B_x is nearly independent from the absorption in the sample. Thus, if the quotient P_x/B_x is used for quantification, no Z- or A- correction is necessary. The only remaining source of error is fluorescence excitation, which is negligible for most materials. This correction method is widely used for EDX measurements, which, unlike EPMA, allows for standardless measurements with fairly little effort. The reason why standardless measurements work for EDX but not EPMA is that the spherical angle of the detector is constant for all elements and the absorption of all components are measurable. However, for EPMA, only discrete wavelenghts are measured at any given time, which affect the reflectivity of the crystal, and the spherical angle of the detector is variable. Thus, the equations which link the intensity of the radiation with the concentration of the elements are significantly simpler for EDX measurements and are simplified even further when P_x/B_x is used instead of P_x. Therefore, most EDX systems use this standardless method and no further corrections. While this is simple and viable for most samples, materials which do exhibit significant fluorescence excitation will have large errors when measured with EDX. In addition, the fact that the background intensity is used for quantification means that a great effort has to be made to get a good and reliable signal from the background, which is less critical for EPMA measurements.

Table 3.3.: Estimated size of the relative error of EDX and EPMA depending on the concentration of the analysed element in the sample, according to Schmidt et al. [30].

Concentration / wt.%	Relative error / %
100 - 10	1 - 5
10 - 1	3 - 20
< 1	> 10

Another topic of considerable importance is the determination of systematic deviations and errors. According to the book by Schmidt et al. [30], the estimated error roughly corresponds to the concentration of the analyzed element in the sample, as shown in Table 3.3.

Several aspects contribute to the total error, which are briefly explained in the following section. For a more detailed explanation, the aforementioned book by Schmidt et al. is recommended.
Counting statistics: The error F is proportional to the square root of the number of impulses n counted by the detector, $F \propto \sqrt{n}$. This means that longer measurement times are generally favorable. In addition, this error is smaller for EPMA than for EDX because their detectors have higher counting rates and thus inherently better statistics.
Background correction: The user must ensure that the background is defined in regions of the spectrum where there are no peaks and that the signal quality is sufficient. This is especially important for EDX measurements where the background signal is used directly for element quantification by the P/B method.
Incident energy: The incident energy must be sufficient to ionize the elements in the sample. Typically, a beam voltage should be chosen that is twice as high as the highest energy of the characteristic X-rays to be analyzed. Related to this, the sample must be conductive in order to avoid charge buildup and thus beam deflection and the corresponding loss of not only spatial resolution but also incident energy.
Sample geometry: Several geometrical aspects of the sample can affect the measurement error. As discussed above, the absorption of photons by the sample depends on the take-off angle of the detector and thus on the geometry of the sample (both due to tilt and changing working distance with roughness, for example). This effect is generally negligible for EDX measurements because absorption effects are negligible when a P/B correction is used.
Element list: The user needs to know which elements are expected to be present in the analyzed sample. Both blind trust in the software and omission of relevant elements lead to errors. Often the software interprets background noise as peaks and adds extraneous elements, albeit in small amounts. It is up to the user to decide whether the elements in question are likely to be present due to contamination or whether this is an error and should be ignored. On the other hand, some samples may contain unexpected contaminants such as oxide or nitride layers, in which case prematurely omitting elements will lead to errors.

Normalization: In the case of EPMA, the analysis software calculates the concentrations of the elements from the signal by comparing them to (typically elemental) standards. If the calculated total composition deviates significantly from 100 %, it is an indication that either the normalization of the results was incorrect, for example because a relevant element was not considered, or the beam current fluctuated. Since EDX uses standardless measurements, the results are always normalized to 100 % and such errors are harder to detect.
Stability: The sample must be stable under the electron beam. This includes not only sufficient conductivity to avoid charge accumulation as mentioned above, but also chemical stability. Some species evaporate under an electron beam, which not only greatly affects the analysis, but also contaminates the entire instrument. A virtually unavoidable problem is the deposition of C on the sample surface due to ambient dust particles, etc.
Standards: The standards must be of very high quality because the quantification result is directly related to them. Any error in the standard measurement will accumulate in later quantifications. This means that the actual composition of the sample must be known exactly. The standard must be virtually free of oxides, etc., homogeneous and stable under the electron beam. The beam current must be precisely measured for the standard measurement.

3.2.2. X-ray diffraction (XRD)

X-ray diffraction is a very powerful technique for characterising the crystallographic properties of materials. As could be expected, many good explanations of this method exist in literature, such as the book by Zolotoyabko [31] or the one by Waseda et al. [32]. Therefore, only the very basics necessary to understand this work will be explained in the following section.
In this method, X-rays of a known wavelength are generated and used to irradiate the sample. If the sample is crystalline and the X-rays scatter elastically off the atoms of the sample, they are diffracted and the outgoing waves interfere with each other. While most of the waves interfere destructively, a certain number of them, which obey Bragg's law (Equation 3.10), interfere constructively:

$$2dsin(\theta) = n\lambda \tag{3.10}$$

By measuring the resulting pattern and the intensity of each peak with a suitable detector, a variety of information about the sample can be obtained. By comparing the pattern with data from databases, the phases present in the samples can be analyzed. In addition, information about the lattice parameters of the phases, grain orientation, phase fractions and more can be obtained.
In this work, samples were pulverized with an agate pistill and mortar before analysis to increase

signal intensity. Before pulverizing heat treated samples, the outer layer of the entire sample was mechanically abraded to prevent any remnants of an oxide layer or mounting medium from influencing the measurement. No attempt was made to determine the particle size of the powder. The instrument used was an Empyrean X-ray diffractometer (Malvern Panalytical GmbH) with a PIXCEL3D Medipix3 1x1 detector. The measurement was performed in Bragg-Brentano geometry. The radiation source was a copper cathode ($CuK_{\alpha 1}$ radiation) with a monochromator. The step size of the diffractometer was 0.013°.

3.2.3. Chemical analysis

In this work, two different methods were used to characterize the chemical composition of the samples: Inductively Coupled Plasma Optical Emission Spectroscopy (ICP-OES) and Carrier Gas Hot Extraction (CGHE). The former was used to determine the composition of the alloys, measuring the elements Mo, Si and Ti. The latter was used to analyze the content of impurities, i.e. O and C. Both techniques are briefly explained in the following sections.

3.2.3.1. Inductively Coupled Plasma Optical Emission Spectroscopy (ICP-OES)

As the name implies, ICP-OES uses a plasma, typically Ar, to ionize the sample material and measure the characteristic optical emission spectrum of the elements. The sample is first digested in an acid using a graphite furnace. The liquefied sample is then vaporized and fed into the Ar plasma. Here, the bonds of all compounds are broken and the atoms are completely ionized. Due to the high temperature in the plasma (typically around 6000 - 12000 K), the ions are put into an excited state. As they return to the ground state, the excess energy is emitted in the form of electromagnetic radiation with a wavelength characteristic of each atom. This radiation is detected, typically using a Charge Coupled Device (CCD), and the concentration of the elements can be calculated by comparing the intensity of the radiation with previously measured standards. The instrument used in this work was an ICAP 7600 DUO from Thermo Scientific. To obtain reliable results, three digestions per sample were analyzed, with a typical sample mass of at least 10 mg each.

3.2.3.2. Carrier Gas Hot Extraction (CGHE)

In Carrier Gas Hot Extraction, the sample is melted in a graphite crucible and a carrier gas is used to transport the species formed to the detectors. Different methods are used depending on the elements of interest. For oxygen and nitrogen, an inert gas, typically helium, is used to carry the species formed to the appropriate detectors. A thermal conductivity detector is used to measure

oxygen and nitrogen. In the case of carbon, the carrier gas is oxygen instead of an inert gas. In this way, the carbon reacts to CO_2, which is detected by an IR detector.
The instruments used in this work were a TC600 and a CS600 (both from LECO Instrumente GmbH) for O and C, respectively. The total sample mass required for a reliable analysis of the impurity content was about 550 mg.

4. Evaluation of binary and ternary system literature data

In this section, all available relevant literature on the Mo-Si-Ti system and its constituent binary systems is reviewed. Where previous assessments are available, their respective advantages and shortcomings are discussed. Where there are competing assessments, reasons are given as to which assessment has been accepted, if any. In the case of the Mo-Si system, a re-evaluation has been published in the course of this work, see [33] and chapter 7.1. Section 4.1 summarises the literature review published in that paper. In addition, an MSIT system report has been published in the course of this work [34].

4.1. The Mo-Si system

The Mo-Si system has been extensively investigated over the years because of the outstanding properties of $MoSi_2$ and its alloys for various applications such as gas turbines, aerospace applications, heating elements and structural materials in extreme environments [5, 6, 7, 8]. As a result, many of the properties of the system relevant to thermodynamic modeling, such as crystal structures, formation enthalpies, and heat capacities, are well investigated. The system consists of five solid phases: a bcc solid solution derived from Mo (often called β phase), pure Si (with no significant solubility for Mo), and the three intermetallic phases Mo_3Si, Mo_5Si_3, and $MoSi_2$. Table 4.1 lists the crystallographic information of these phases. The following sections give an overview of all available relevant information on the system from the literature. In addition, previous CALPHAD evaluations are discussed and explanations are given as to why the evaluations could not be accepted for this work.

4.1.1. Phase diagram data

A list of all experimental studies yielding phase diagram data is given in Table 4.2. In 1951, Ham studied the solubility of Si in the Mo-derived bcc crystal [35]. A year later, Kieffer and Cerwenka [36] presented liquidus temperatures of 22 samples within the system, covering the entire compositional range. In this paper the intermetallic phases are referred to as Mo_3Si,

Table 4.1.: Crystallographic information about the solid phases in the Mo-Si system.

Phase	Pearson symbol	Space group	Prototype
Mo	cI2	Im$\overline{3}$m, #229	W
Si	cF8	Fd$\overline{3}$m, #227	Diamond
Mo_3Si	cP8	(Pm$\overline{3}$n, #223)	Cr_3Si
Mo_5Si_3	tI32	I4/mcm, #140	W_5Si_3
$MoSi_2$	tI6	I4/mmm, #139	$MoSi_2$

Mo_3Si_2 and $MoSi_2$. However, in a study published in 1971 by Svechnikov et al. [37] it was found that the phase labeled Mo_3Si_2 by Kieffer and Cerwenka is instead Mo_5Si_3. In 1964, Cherniack and Elliot [38] studied the high temperature behavior of the phases Mo_5Si_3 and $MoSi_2$. In this publication, they reported the melting points of Mo_5Si_3 and $MoSi_2$ to be 2358 K and 2253 K, respectively, and the eutectic temperature of the reaction $L \rightleftarrows Mo_5Si_3 + MoSi_2$ to be 2173 K. However, they reported experimental problems in this study, such as significant evaporation of Si in the $MoSi_2$-containing samples, which affected the measurements. In the aforementioned paper by Svechniknov et al. they provide a detailed study of the phase equilibria of the system. Reaction temperatures and composition data for all invariant reactions are presented, along with liquidus and solidus temperatures for the entire system and Si solubilities in Mo and Mo_5Si_3. The phase Mo_5Si_3 was reported to have a homogeneity range from about 36.5 at.% to 39 at.%. The data published by Svechnikov et al. show significant differences compared to those published by Kieffer and Cerwenka. According to Svechnikov et al. the eutectic reaction $L \rightleftarrows Mo_3Si + Mo_5Si_3$ occurs at 2293 K and 26.4 at.% (composition of the liquid phase), while Kieffer and Cerwenka reported a temperature almost 100 K lower (2200 K) and a significantly higher Si concentration in the liquid phase (32.4 at.%). In addition, the solubility of Si in the bcc phase is almost twice as high according to Svechniknov et al. As Gokhale and Abbaschian point out in an evaluation of the system [39], the data of Svechniknov are more reliable due to more extensive experiments and better experimental equipment. Svechnikov et al. also included a polymorphic transformation of the phase $MoSi_2$ at 2173 K, from a tetragonal $C11_b$ structure to a hexagonal C40 structure (notation according to the *Strukturbericht*). In 1998, Frankwicz and Perepezko [40] studied the phase stability of $MoSi_2$ at high temperatures and showed that the hexagonal structure is metastable. Thus, it must not be included in the phase diagram of the system. In recent years, the focus of research has shifted to the phase Mo_3Si. In 2000, Rosales and Schneibel [41] reported that this phase is not stoichiometric at 25 at.% Si, but has a lower Si concentration "near 24 at.%". They studied a sample heat treated at 1873 K. In 2016, Gulec et al. [42] confirmed the Si deficiency of this phase. However, the samples observed in this study were analyzed without annealing prior to analysis. In 2020, Gnesin and Gnesin [43] studied the composition of several Mo-Mo_3Si samples prepared by sintering in one or more steps and

Table 4.2.: Experimental phase diagram data of the Mo-Si system.

Literature, Year	Method	Equilibria	Temperature / K	at. % Si
Gnesin and Gnesin, 2020 [43]	Metallography, EDX, X-ray	Composition of Mo_3Si	1753 - 1973	25
Gulec et al., 2016 [42]	Z-contrast imaging, electron diffraction, APT	Composition and structure of Mo_3Si	(cast sample not annealed)	25
Rosales and Schneibel, 2000 [41]	Metallography, EDX, X-ray	Composition of Mo_3Si	1600	22 - 28
Frankwicz and Perepezko, 1998 [40]	Metallography, EDX, X-ray	Phase equilibria and stability of $MoSi_2$	RT - 2173	55, 60, 67
Svechnikov et al., 1971 [37]	DTA, X-ray, metallography	Liquidus, Eutectics, Peritectic, Solidus, Si-solubility in Mo and Mo_5Si_3	1673 - ca. 2600	0 -100
Cherniak and Elliot, 1964 [38]	X-ray, Pyrometry, Metallography	$MoSi_2$, Mo_5Si_3	1973 - 2273	66.7
Kieffer and Cerwenka, 1952 [36]	Pyrometry, Metallography, X-ray	Liquidus	1673 - 2873	0 - 100
Ham, 1951 [35]	X-ray	Si-solubility in Mo	1588 - 1700	0.8 - 2.7

levitation melting with and without annealing. They consistently found that the Si concentration of the A15 phase is about 23 at.%.

4.1.2. Thermodynamic and thermophysical data

Experimental investigations on thermodynamic and thermophysical data of the Mo-Si system are listed in Table 4.3. Calculated data, both from first-principles calculations and from more traditional methods, are listed in Table 4.4. The following section gives an overview of the studies published in the literature.

Table 4.3.: Experimental thermodynamic investigations of the Mo-Si system.

Literature, Year	Method	Type of data	Temperature / K	at. % Si
Fujiwara and Ueda, 2007 [44]	EMF	Enthalpies and entropies of formation of Mo_3Si, Mo_5Si_3, $MoSi_2$	1305 - 1507	25, 37.5, 66.7
Meschel and Kleppa, 1998 [45]	Direct synthesis calorimetry	Enthalpies of formation of Mo_5Si_3, $MoSi_2$	1473	37.5, 66.7
Tomaskiewicz et al., 1997 [46]	Combustion calorimetry	Enthalpy of formation of Mo_5Si_3	298	37.5
Callanan et al., 1997 [47]	Adiabatic calorimetry	Heat capacity	7 - 392	66.7
Tomaskiewicz et al., 1996 [48]	Combustion calorimetry	Enthalpy of formation of Mo_3Si	298	25
O'Hare, 1993 [49]	Combustion calorimetry	Enthalpy of formation of $MoSi_2$	298	66.7
Arpaci and Frohberg, 1985 [50]	Pyrometry	Integral enthalpy of mixing (liquid phase)	3087	0 - 40
Ohmori et al., 1982 [51]	EMF	Standard Gibbs energies of formation of Mo_3Si, Mo_5Si_3	1150 - 1450	25, 37.5
Maslov et al., 1978 [52]	Direct synthesis calorimetry	Enthalpy of formation of $MoSi_2$	No temperature is given in this paper.	66.7

Chart, 1974 [53]	Knudsen effusion	Gibbs energies, enthalpies and entropies of formation and heat capacities of Mo_3Si, Mo_5Si_3, $MoSi_2$	1410 - 1675	20, 35, 60
Bondarenko et al., 1973 [54]	Calorimetry (displacement method)	Enthalpy	1200 - 2200	25, 37.5, 66.7
Bondarenko et al., 1972 [55]	Adiabatic calorimetry	Heat capacity	400 - 1200	25, 37.5, 66.7
Searcy and Tharp, 1960 [56]	Knudsen effusion	Enthalpies of formation of Mo_3Si, Mo_5Si_3, $MoSi_2$	1926 - 2261	25, 37.5, 66.7
King and Christensen, 1958 [57]	Calorimetry	Heat capacity, enthalpy	51 - 289 (Heat capacity), 400 - 1451 (Enthalpy)	25
Walker et al., 1956 [58]	Drop calorimetry	Heat capacity	303 - 1173	66.7
Robins and Jenkins, 1955 [59]	Combustion calorimetry	Enthalpy of formation of $MoSi_2$	298	66.7
Douglas and Logan, 1954 [60]	Ice calorimetry	Heat capacity	273 - 1173	66.7

4.1.2.1. Enthalpy of formation

In 1955, Robins and Jenkins [59] published results for the enthalpies of formation of Mo_5Si_3 (which at that time was still thought to be Mo_3Si_2) and $MoSi_2$ from combustion calorimetry. Due to impure raw materials, these measurements are not considered reliable. In 1960, Searcy and Tharp [56] measured the dissociation pressures and enthalpies of formation of all three intermetallic compounds of the Mo-Si system by Knudsen effusion. However, these

Table 4.4.: Calculated thermodynamic data of the Mo-Si system.

Literature, Year	Method	Type of data
Pan, 2019 [61]	First-principles calculations	Debye temperature, heat capacity (C_V) of Mo_5Si_3
Zhong et al., 2016 [62]	First-principles calculations	Debye temperature, heat capacity (C_V), thermal expansion of Mo_3Si
Gulec et al., 2016 [42]	First-principles calculations	Enthalpies of formation of Mo-silicides
Colinet and Tedenac, 2016 [63]	First-principles calculations	Enthalpies of formation of Mo_3Si, Mo_5Si_3, $MoSi_2$
Bhaduri et al., 1994 [64]	Calculation	Enthalpies of formation of Mo_5Si_3, $MoSi_2$
Birnie et al., 1982 [65]	Pair potential calculations	Enthalpies of formation of the Mo-Si solid solution
Niessen and de Boer, 1981 [66]	Miedema	Enthalpies of formation of Mo_3Si, $MoSi_2$
Machlin, 1981 [67]	Modified Miedema	Enthalpy of formation of Mo_3Si
Kaufman, 1979 [68]	Prediction	Enthalpies of formation of Mo_3Si, Mo_5Si_3, $MoSi_2$

measurements are also considered unreliable because of sample interaction with the sample vessel, sintering of the sample, and, as noted by Chandrasekharaihah et al. [69], a high probability that the samples were not in equilibrium under the experimental conditions. In 1974, Chart [53] published an investigation of the enthalpies of formation of the three Mo silicides measured with Knudsen effusion. The difficulties of the previous studies were taken into account, and the values reported by Chart are still considered trustworthy. However, in the aforementioned paper, Chandrasekharaih et al. recommend assigning larger uncertainties to the results obtained by Chart. The vast majority of measurements since then, for example the three related papers by O'Hare [49] for $MoSi_2$ and Tomaszkiewicz et al. for Mo_3Si [48] and Mo_5Si_3 [46] (all using combustion calorimetry) and Fujiwara and Ueda [44] (using electromotive force (EMF) measurements) agree well with each other. In all cases, the values obtained are within the measurement uncertainty given by Chart.

Calculations of the enthalpies of formation in Mo-Si vary considerably depending on the method used. Predictions with the Miedema model [70] for this system are highly unreliable, as reported in 1981 by Niessen and de Boer [66]. Bhaduri et al. [64] calculated the enthalpies of formation of Mo_5Si_3 and $MoSi_2$ using the values of the heat capacities (taken as listed by Barin [71]).

They obtained results quite close to the experimental values. For first-principles calculations of formation enthalpies in the Mo-Si system, three papers are available. In 2016, Zhong et al. [62] published results on structural, elastic, and thermodynamic properties calculated by density functional theory (DFT) for Mo_3Si. The reported enthalpies of formation differed significantly from the experimental results, both for the generalized gradient approximation and for the local density approximation. In the same year, Colinet and Tedenac [63] published enthalpies of formation of several transition metal compounds calculated by DFT. For the Mo silicides, these calculations agreed very well with the experimental results. Gulec et al. [42] used DFT to calculate the enthalpies of formation of Mo-silicides as a way to investigate the Si deficiency of the phase Mo_3Si. Uniquely, they computed values for hypothetical compounds and compositions as opposed to only the stoichiometric compositions. In 2019, Pan [61] used DFT to calculate the enthalpy of formation of Mo_5Si_3 and reported a result similar to the value of Chart [53].

4.1.2.2. Entropy of formation

Experimental data on the entropies of formation of the intermetallic phases in the Mo-Si system are scarce. In 1974, Chart [53] reported these data directly, derived from the same Knudsen effusion studies which were described in section 4.1.2.1. With the publication of Fujiwara and Ueda [44], the entropies of formation can be calculated from the data presented. While the enthalpies of formation reported by the two authors are very close to each other, there are considerable discrepancies between the two publications in the values of the entropies of formation of all three intermetallic compounds. Chart lists the entropies of formation at 298 K as 0.42 $\pm$ 1.3 $Jmol^{-1}K^{-1}$ for Mo_3Si, 1.0 $\pm$ 1.3 $Jmol^{-1}K^{-1}$ for Mo_5Si_3 and -0.42 $\pm$ 1.3 $Jmol^{-1}K^{-1}$ for $MoSi_2$, respectively. From the data of Fujiwara and Ueda on the other hand, the values -0.76 $Jmol^{-1}K^{-1}$ for Mo_3Si, 0.55 $Jmol^{-1}K^{-1}$ for Mo_5Si_3 and 8.54 $Jmol^{-1}K^{-1}$ for $MoSi_2$ can be derived. Another method of obtaining values for the entropies of formation of the intermetallic compounds is to calculate them from the reported entropies of the phases and the unary data provided by Dinsdale [72]. For the Mo-Si system, this is possible from the data of Callanan et al. [73] for $MoSi_2$ and King and Christensen [57] for Mo_3Si. The derived formation entropies at 298 K (with respect to 1 mole of atoms) are 0.446 $Jmol^{-1}K^{-1}$ for Mo_3Si and -1.57 $Jmol^{-1}K^{-1}$ for $MoSi_2$.

The immense differences in entropies of formation between otherwise reliable sources show that it is questionable to use these data for a CALPHAD evaluation of the system. None of the data mentioned can be considered as definitive values to be used in optimizing the system, as it is unclear which are the most reliable.

4.1.2.3. Enthalpy of mixing

In 1985, Arpaci and Frohberg [50] published an investigation of the mixing enthalpy of the liquid phase in the Mo-Si system. The experiment was performed using a levitation apparatus in which molten Mo was kept in a suspended state and Si was dropped from a revolver magazine. The experimental temperature was maintained at a mean value of 3087 K, scattering from 2960 to 3224 K, the Si concentrations ranged from 0 to 40 at.%. The enthalpy of mixing was derived from the resulting temperature change measured with a pyrometer. The calculation required an estimate of the heat capacity, which was obtained using the Kopp-Neumann approach. For the temperature measurement, the spectral emissivity of pure Mo was used due to the unavailability of data for Mo-Si alloys. Thus, the authors recognized the inherent cumulative error associated with the progressive addition of Si and made the decision to accept it. The total systematic error of the experiment is reported to be within $\pm 12\%$ for the enthalpy of mixing.
In the same year, Sudavtsova et al. [74] published measurements of the enthalpies of mixing in several binary Si-metal melts, including Mo-Si. The maximum Mo concentration studied was 8 at.%. The values were determined experimentally using a calorimeter, and the temperature chosen for the Mo-Si samples was 1870 K. Little other information about the purity of the components, experimental techniques, or possible errors is given in the paper. Therefore, the reliability of the data is considered questionable.

4.1.2.4. Heat capacity

Douglas and Logan [60], Callanan et al. [47] and Walker et al. [58] determined the heat capacity of $MoSi_2$. Mezaki et al. [75] published enthalpy increment values for the same compound. King and Christensen [57] published heat capacity and enthalpy increment data of Mo_3Si. Bondarenko et al. [55, 54] reported enthalpy increment values and heat capacity data for all three Mo silicides. In 1972 they reported data from 400 to 1200 K and in 1973 data from 1200 to 2200 K were published. There are considerable discrepancies in the data between the two publications, as well as between the "1972 data" and measurements by other authors. However, the "1973 data" are in fairly good agreement with data published by other authors. For this reason, the "1972 data" are not considered reliable today.

4.1.3. Thermodynamic assessments

Several thermodynamic assessments of the Mo-Si system were published over the years. The following section discusses the characteristics, advantages and disadvantages of each of them. It is explained why none of the assessments is fully satisfying and the decision was made to

re-assess the system in this work.

In a 1989 paper, Vahlas et al. [76] published several Si-component binary system assessments, including Mo-Si. This was the first publication to use the CALPHAD method on this system. As such, a set of optimised parameters was developed and published to calculate the Gibbs energies of all phases. However, the dataset had two major problems. Firstly, many of the invariant reactions, primarily in the Mo-rich region of the system, that are proposed in the evaluation are not observed experimentally. In addition, at high Si contents, the liquid phase exhibited a miscibility gap at high temperatures, which is an artefact of the dataset.

A highly regarded thermodynamic assessment of the Mo-Si system was presented by Gokhale and Abbaschian [39] in 1991. The paper provides a detailed review of the literature up to that year. The authors explained that the phase diagram data of Svechnikov et al. [37] was considered more reliable than that of Kieffer and Cerwenka [36] due to the more advanced experimental techniques of the former. The phase diagram in this work thus included the homogeneity range of the phase Mo_5Si_3, as it was observed by Svechniknov et al. However, the authors also included the alleged polymorphic transformation of $\alpha MoSi_2$ to $\beta MoSi_2$ at 2173 K. As explained in section 4.1.1, the hexagonal $\beta MoSi_2$ is metastable and should therefore not be included in the phase diagram.

In 1994, Costa e Silva [77] published an assessment of the Mo-Si system in his dissertation. The thesis was concerned with synthesizing $MoSi_2$ composites. The author stated that a re-evaluation of the system was necessary mainly because of the miscibility gap mentioned in Vahlas' work. The experimental data of Chart [78] and Arpaci and Froberg [50] were accepted, as were the assessments of Brewer and Lamoreaux [79] and Gokhale and Abbaschian. There are two concerns with the resulting dataset. Firstly, all intermetallic phases were treated as line compounds with ideal stoichiometric compositions. While the Si deficiency of Mo_3Si was not known at the time and therefore could not be included, this also means that Mo_5Si_3 was simplified with a composition of strictly 37.5 at.% Si. In addition, several invariant reactions proposed by Costa e Silva are no longer supported by experimental evidence.

In 2000, Liu et al. [80] evaluated the ternary system Al-Mo-Si. They also re-assessed Mo-Si in this course. Although the resulting data set is in fairly good agreement with most of the experimental information known at the time, it still has some shortcomings. For one, the temperatures of the invariant reactions are significantly lower than the experimental data reported by Svechnikov. In addition, the homogeneity range of the phase Mo_5Si_3 shows rather unrealistic behaviour at high temperatures. However, this last point is rather insignificant as there is no experimental data on the homogeneity range of the phase at very high temperatures close to its melting point.

In 2010, Geng et al. [81] evaluated the ternary system Nb-Mo-Si and, in the process, re-evaluated the Mo-Si system. At that time the Si deficiency of Mo_3Si was well known. However, it was omitted without comment in this paper. One of the main objectives of the evaluation was to make

the description of the isostructural phases Nb_5Si_3 and Mo_5Si_3 consistent, because these form a continuous solid solution in the ternary system. Therefore, the authors modelled the phase Mo_5Si_3 with three sublattices, accepting the model of Nb_5Si_3 by Fernandes et al. [82]. However, as Fernandes et al. note, this simplification is only applicable if there are no defects in the Si positions, which is valid for Nb_5Si_3 but invalid for Mo_5Si_3. Thus the phase should be described in four sublattices, one for each of the Wyckoff positions.
The assessment of Geng et al. was largely accepted by Guo et al. [83] in 2012, when they reassessed the Al-Mo-Si system. While the same models were used in this assessment, the authors re-optimised the parameters of the binary system Mo-Si. This led to a significant deviation of the enthalpy of formation of the phase $MoSi_2$ calculated by this dataset from the experimental values.
To conclude, all previous assessments of the Mo-Si binary system share two common issues. For once, the Si deficiency of the phase Mo_3Si is not included in any assessment, even the ones that were published after Rosales and Schneibels publication of 2000. Secondly, none of the assessments are very suitable to model the heat capacities of the silicides, even though this data is available since the 1970s at the latest. As both of those properties are highly relevant in the practical application of the system, none of the presented assessments was accepted and the decision was made to re-assess the system as part of this thesis.
Figure 4.1 shows the phase diagrams of the assessments by Liu et al. and Guo et al., two of the three most recent assessments of the binary system. The results of Geng et al. are not shown because the phase diagram is virtually identical to that of Guo et al. The experimental data obtained in this study will be discussed in detail in section 6.3.

4.2. The Ti-Si system

Like the Mo-Si system, Ti-Si system alloys are highly suitable for high temperature applications in extreme conditions. Other applications include the manufacture of heat and oxidation resistant alloys in the steel industry and for contacts in very large scale integrated circuits. The relevant thermodynamic properties are therefore largely well understood. The system consists of 8 solid phases: the solid solutions αTi and βTi, pure Si with no significant solubility for Ti and the intermetallic phases Ti_3Si, Ti_5Si_3, Ti_5Si_4, TiSi and $TiSi_2$. The crystallographic data of the phases are listed in Table 4.5. The following section summarises the available literature data for both experimental investigations and CALPHAD assessments.

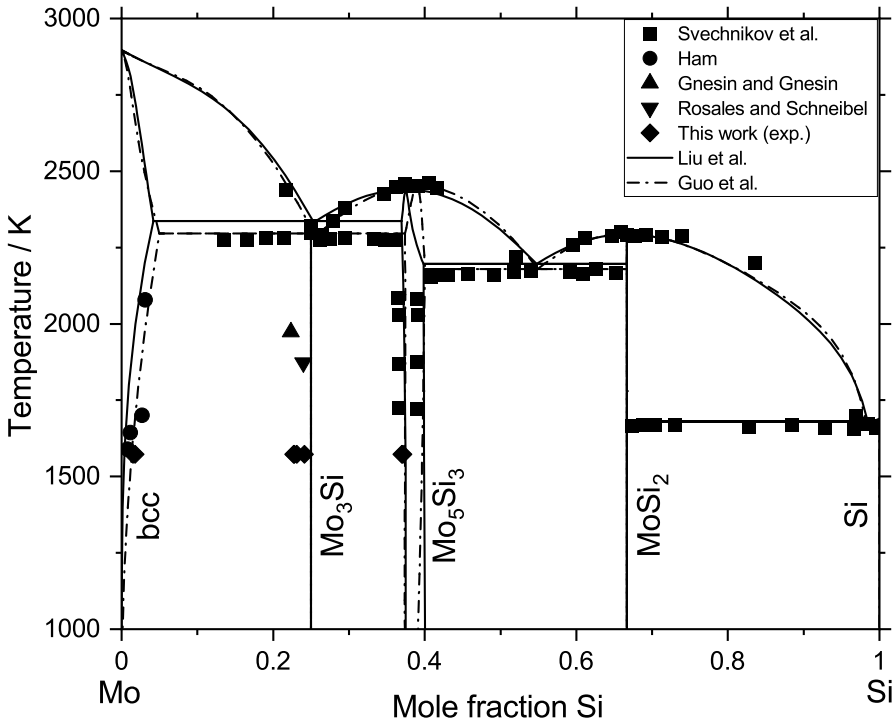

Figure 4.1.: The Mo-Si phase diagrams as calculated from the datasets of Liu et al. [80] and Guo et al. [83], together with the experimental datapoints from Svechnikov et al. [37], Ham [35], Gnesin and Gnesin [43], Rosales and Schneibel [41] and Czerny et al. [33]. Image re-printed from [33].

Table 4.5.: Crystallographic information about the solid phases in the Ti-Si system.

Phase	Pearson symbol	Space group	Prototype
αTi	hP2	$P6_3/mmc$, #194	Mg
βTi	cI2	$Im\bar{3}m$, #229	W
Si	cF8	$Fd\bar{3}m$, #227	Diamond
Ti_3Si	tP32	$P4_2/n$, #86	PTi_3
Ti_5Si_3	hP16	$P6_3/mcm$, #193	Mn_5Si_3
Ti_5Si_4	tP36	$P4_12_12$, #92	Si_4Zr_5
TiSi	oP8	Pmm2, #25	SiTi
$TiSi_2$	oF24	Fddd, #70	Si_2Ti

4.2.1. Phase diagram data

The phase diagram data available for the system Ti-Si are presented in Table 4.6. There are two comprehensive publications that have investigated the most relevant data, such as the liquidus line, invariant reactions as well as homogeneity ranges of the phases in the system. The first was published in 1952 by Hansen et al. [84] who used metallographic and X-ray methods as well as DTA to study the whole compositional range at temperatures from 1273 - 2393 K. In 1970, Svechniknov et al. [85] used similar techniques to study the same equilibria over a temperature range of 1073 - 2403 K. While some data, such as Si solubility and certain invariant reactions, are in good agreement, the two publications differ greatly in the intermetallic phases reported. In addition to Ti_5Si_3, TiSi and $TiSi_2$, Svechnikov et al. found Ti_3Si and Ti_5Si_4. In the years following this paper there was some controversy as to whether the newly discovered phases were stable or metastable, but several authors, such as Wakelkamp et al. [86], have since confirmed their stability. The reason why Ti_3Si was not found in the previous publication was due to the presence of impurities such as O and C, which cause the phase to decompose rapidly. As the experiments of Svechnikov et al. used high purity samples, the critical phases remained stable and could be observed for the first time. Corresponding to the presence of these phases, different invariant reactions were postulated by Svechnikov et al., for example the eutectoid reaction βTi $\rightleftarrows$ αTi + Ti_3Si instead of the reaction βTi $\rightleftarrows$ αTi + Ti_5Si_3 proposed by Hansen et al. Both publications agree that the only phases with a discernible homogeneity range are the Ti solid solution (specifically βTi) and Ti_5Si_3. The former has been the subject of investigations by Sutcliffe [87] and Pylaeva and Volkova [88], who studied Si solubility in Ti from 923 - 1372 K and 873 - 1123 K respectively. The maximum solubility for Si in βTi was found to be 5 at.% at 1613 K, while the homogeneity range of Ti_5Si_3 is from 38.5 - 36.2 at.% Si at room temperature to 40 - 37 at.% Si at 2193 K. The liquidus line of the system is still not reliably determined due to reactions of the samples with the crucible in both the investigations of Hansen et al. and Svechnikov et al. and the fact that no attempt was made to study these properties in subsequent publications. A list of all invariant reactions of the system is shown in Table 4.7.

4.2.2. Thermodynamic and thermophysical data

The thermodynamic and thermophysical data of the system Ti-Si are relatively well studied. This is particularly true for the data most relevant to CALPHAD-type assessments, such as the enthalpies of formation of the intermetallic phases and the enthalpy of mixing of the liquid phase. These studies are summarised in Table 4.8. The following section discusses particularly relevant papers or aspects thereof.

Table 4.6.: Experimental phase diagram data of the Ti-Si system.

Literature, Year	Method	Equilibria	Temperature / K	at. % Si
Svechnikov et al., 1970 [85]	Metallography, DTA, X-ray	Liquidus, Eutectics, Peritectics, Si-solubility in Ti	1073 - 2403	0 - 100
Pylaeva and Volkova, 1962 [88]	Metallography	Si-solubility in Ti	873 - 1123	0 - 1.4
Sutcliffe, 1954 [87]	Metallography, Chemical analysis	Si-solubility in Ti	923 - 1373	0 - 4
Hansen et al., 1952 [84]	Metallography, DTA, X-ray	Liquidus, Eutectics, Peritectics, Si-solubility in Ti	1273 - 2393	0 - 100

Table 4.7.: A list of the invariant equilibria in the system Ti-Si as reported by Svechnikov et al. [85].

Reaction	Temperature / K	x(Si) of liquid
$\beta Ti \rightleftarrows \alpha Ti + Ti_3Si$	1133	0.011
$\beta Ti + Ti_5Si_3 \rightleftarrows Ti_3Si$	1443	0.04
$L \rightleftarrows \beta Ti + Ti_5Si_3$	1613	0.137
$L \rightleftarrows Ti_5Si_3$	2403	0.375
$L + Ti_5Si_3 \rightleftarrows Ti_5Si_4$	2193	0.48
$L + Ti_5Si_4 \rightleftarrows TiSi$	1843	0.6
$L \rightleftarrows TiSi + TiSi_2$	1743	0.641
$L \rightleftarrows TiSi_2$	1773	0.6666
$L \rightleftarrows TiSi_2 + Si$	1603	0.86

Table 4.8.: Experimental thermodynamic investigations of the Mo-Si system.

Literature, Year	Method	Type of data	Temperature / K	at. % Si
Meschel and Kleppa, 1998 [89]	Direct synthesis calorimetry	Enthalpies of formation of Ti_5Si_3, Ti_3Si, Ti_5Si_4, TiSi and $TiSi_2$	1473	25, 37.5, 44.4, 50, 66.7
Sylla et al., 1994 [90]	Differential scanning calorimetry	Heat capacity of $TiSi_2$	100 - 500	66.7
Topor and Kleppa, 1986 [91]	Solution calorimetry	Enthalpy of formation of $TiSi_2$	298	66.7
Sudavtsova et al., 1985 [92]	Mixing calorimetry	Enthalpy of mixing	1795 - 1900	74 - 100
Yusin et al., 1981 [93]	Mixing calorimetry	Enthalpy of mixing	2000	58 - 100
Sychev et al., 1980 [94]	Differential scanning calorimetry	Heat capacity of Ti_5Si_3	13 - 300	37.5
Maslov et al., 1978 [52]	Reaction calorimetry	Enthalpy of formation of Ti_5Si_3	298	37.5
Bondarenko et al., 1973 [95]	Drop calorimetry	Heat content of Ti_5Si_3	1250 - 1749	37.5
Savin, 1973 [96]	Reaction calorimetry	Enthalpies of formation of Ti_5Si_3, TiSi and $TiSi_2$	298	37.5, 50, 66.7
Polyachenok et al., 1972 [97]	Reaction calorimetry	Enthalpy of formation of Ti_5Si_3	298	37.5
Yuck and Block, 1965 [98]	Mixing calorimetry	Enthalpy of mixing	1848	80 - 100

Gel'd and Gertman, 1960 [99]	Mixing calorimetry	Partial enthalpy of mixing	1773 - 1823	> 99.9
Golutvin, 1959 [100]	Drop calorimetry	Heat content of Ti_5Si_3, TiSi and $TiSi_2$	378 - 1352	37.5, 50, 66.7
Golutvin, 1956 [101]	Combustion calorimetry	Enthalpies of formation of Ti_5Si_3, TiSi and $TiSi_2$	298	37.5, 50, 66.7
Robins and Jenkins, 1955 [59]	Reaction calorimetry	Enthalpies of formation of Ti_5Si_3, TiSi and $TiSi_2$	298	37.5, 50, 66.7
Kematick and Myers, 1955 [59]	Knudsen effusion mass spectrometry	Enthalpies of formation of Ti_5Si_3, Ti_5Si_4, TiSi and $TiSi_2$	1700 - 2050	37.5, 44.4, 50, 66.7

4.2.2.1. Enthalpy of formation

There are several publications on the enthalpies of formation of the intermetallic compounds. In 1955, Robins and Jenkins [59] used direct reaction calorimetry to measure this quantity for TiSi and $TiSi_2$. A year later, Golutvin [101] used combustion calorimetry to measure the same property. In 1972, Polyachenok et al. [97] measured the enthalpy of formation of Ti_5Si_3 by reduction of Ti chlorides. Savin studied the reduction of Ti chlorides with Na to TiSi and $TiSi_2$ by calorimetry and derived the enthalpies of formation of these compounds. Maslov et al. [52] used self-combustion high temperature synthesis of Ti+Si powder mixtures and reported the enthalpies of formation of Ti_5Si_3. Topor and Kleppa [91] used high temperature solution calorimetry to investigate the enthalpy of formation of $TiSi_2$. In 1996, Kematick and Myers used Knudsen effusion mass spectrometry to investigate the enthalpies of formation of Ti_5Si_3, Ti_5Si_4, TiSi and $TiSi_2$. Finally, Meschel and Kleppa used direct synthesis calorimetry to obtain the enthalpies of formation of all five Ti silicides. The experimentally obtained values of these studies are listed in Table 4.9.

For the phase Ti_5Si_3, the data from different authors are in fairly good agreement. For Ti_3Si

Table 4.9.: Experimentally determined values for the enthalpies of formation of the silicides in the Ti-Si system. All values in kJ/mol of atoms.

Literature, Year	Ti_3Si	Ti_5Si_3	Ti_5Si_4	TiSi	$TiSi_2$
Meschel and Kleppa, 1998 [45]	-49.00	-73.80	-78.50	-72.60	-55.00
Kematick and Myers, 1996 [102]	-	-78.10	-75.90	-71.50	-53.50
Topor and Kleppa, 1986 [91]	-	-	-	-	-59.97
Maslov et al., 1978 [52]	-	-72.42	-	-	-
Savin, 1973 [96]	-	-76.50	-	-78.60	-60.20
Polyachenok et al., 1972 [97]	-	-72.70	-	-	-
Golutvin, 1956 [101]	-	-76.92	-	-82.05	-59.83
Robins and Jenkins, 1955 [59]	-	-72.52	-	-64.88	-44.90

and Ti_5Si_4 there are only one and two publications, respectively, concerning the values for the enthalpy of formation of the phases, due to the aforementioned difficulty in synthesising the phase in earlier publications. For Ti_5Si_4 the two experimental values are in good agreement. The values for TiSi and $TiSi_2$ scatter significantly. For the experiments by Golutvin and Savin this is most likely due to oxygen contamination of the samples analyzed. Robins and Jenkins also pointed out that the TiSi and $TiSi_2$ analysed in their study were not pure, so these data are not very reliable either. The results of the two most recent studies by Kermatick and Myers and Meschel and Kleppa are in good agreement.

4.2.2.2. Enthalpy of mixing

Several studies have been conducted on the enthalpy of mixing of the liquid phase in the Ti-Si system, all using mixing calorimetry to determine this property. In 1960, Gel'd and Gertman [99] reported the partial enthalpy of mixing for samples containing more than 99.9 at.% Si, from 1773 to 1823 K. Yuck and Block [98] published the enthalpy of mixing at 1848 K for samples ranging from 80 to 100 at.% Si. Yusin et al. [93] reported these values for a temperature of 2000 K and a compositional range of 54-100 at.% Si. Sudavtsova et al. [92] measured the property in a temperature range of 1795-1900 K, with a Si composition ranging from 74-100 at.%. No reports of specimens with higher Ti concentrations exist in this system. All measurements are in good agreement with each other.

4.2.2.3. Heat capacity

The heat capacities of the intermetallic compounds in the system Ti-Si are remarkably poorly determined. In 1959 Golutvin [100] used drop calorimetry to measure the heat contents of Ti_5Si_3 from 382 - 1170 K, of TiSi from 378 - 1352 K and of $TiSi_2$ from 407 - 1072 K as well as at 1181 K. Bondarenko et al. [95] used the same technique to determine the heat content of Ti_5Si_3 from 1250 - 1726 K and at 1749 K. Sychev et al. [94] used differential scanning calorimetry to measure the heat capacity of Ti_5Si_3 at very low temperatures in the range of 13 - 300 K. Finally, Sylla et al. [90] used the same technique to measure the heat capacity of $TiSi_2$ from 100 - 500 K. There are no experimental measurements for Ti_3Si or Ti_5Si_4.
Both Golutvin and Bondarenko et al. report that the composition of the samples deviated from the ideal $TiSi_2$. In addition, Bondarenko et al. observed reactions between the samples and the crucible, rendering most of the limited heat capacity data available in this system rather unreliable.

4.2.3. Thermodynamic assessments

There are several thermodynamic assessments of the binary system Ti-Si in the literature. The first one was published in 1979 by Kaufman [68] and is based on the results of Hansen et al. [84]. As such, it does not contain Ti_3Si. In addition, the phase Ti_5Si_3 was simplified as a line compound with stoichiometric composition. In 1987, Murray [103] assessed the system based on the experimental results of Svechnikov et al. [85] and published a phase diagram that is in good agreement with them. In 1989, Vahlas et al. [76] published a paper containing thermodynamic assessments of four Si-metal binary systems, including Ti-Si. They accepted the data of Svechnikov et al. and consequently included the phase Ti_3Si. However, the phase Ti_5Si_3 is simplified as a line compound of stoichiometric composition. In 1996, Seifert et al. [104] published an assessment of the system that considered both data from Hansen et al. and Svechnikov et al. but accepted the invariant reactions postulated by Svechnikov et al. over those of Hansen et al. Similarly, multiple sources for the thermodynamic data (where applicable) were accepted on a case-by-case basis, depending on whether the data were considered reliable for each compound individually. For the phases Ti_3Si and Ti_5Si_4, where no experimental data for the enthalpies of formation were available at the time, calculations by de Boer et al. [105] were used to optimize the values. Two different models were used for the liquid phase. Once it was modeled as a regular solution using the Redlich-Kister formalism, and once it was treated as an ionic liquid. Likewise, the phase Ti_5Si_3 was treated once as a stoichiometric line compound and once in a sublattice model, taking into account the experimentally determined homogeneity range. In 2017, Fiore et al. [106] argued that the stability of the phase Ti_3Si is controversial,

and therefore the peritectoid and eutectoid reactions involving this phase are questionable. Thus, they presented two different phase diagrams. In one, the phase Ti_3Si is assumed to be stable and the invariant reactions of Svechnikov et al. are accepted. In the other, this phase is treated as metastable and the invariant reactions of Hansen et al. are accepted. While several publications are cited that did not find the phase Ti_3Si , the evidence for the absence of impurities is almost always provided by hardness measurements. Since no defined standard is given in any of these publications, the reliability of the method is questionable. This is especially important in light of the fact that Wakelkamp et al. [86] state that even small amounts of impurities such as O and C rapidly decompose the phase Ti_3Si. Thus, without a thorough analysis of the impurities, the publications claiming that Ti_3Si is not part of the stable phase diagram are not treated as highly reliable. Another problem with the assessment of Fiore et al. is the homogeneity range of Ti_5Si_3. Although it is not modeled as a line compound, the lowest solubility of Si for this phase is 37.5 at.% according to their calculations. This is in contrast to the experimental results which show a solubility as low as 36.2 at.% Si.
Considering all the facts regarding the different evaluations of the Ti-Si system, the decision was made to accept the dataset of Seifert et al. [104]. All available experimental information is in good agreement with the calculations, and the accepted invariant responses appear to be the most reliable. Newer experimental values published after this dataset, such as the enthalpies of formation measured by Kematick and Myers [102], still agree quite well with the values of Seifert et al. Thus, there is no need to re-assess this binary system. The phase diagram calculated with the version of the dataset that treats Ti_5Si_3 as a stoichiometric compound and the liquid phase as a regular solution is shown in Figure 4.2. A comparison between the invariant equlibria data from Svechnikov et al. and Seifert et al. for the same model is shown in Table 4.10. The calculated values for the enthalpies of formation of the intermetallic phases is as follows: -50.00 $kJmol^{-1}$ for Ti_3Si, -72.67 $kJmol^{-1}$ for Ti_5Si_3, -79.00 $kJmol^{-1}$ for Ti_5Si_4, -77.76 $kJmol^{-1}$ for TiSi and -57.04 $kJmol^{-1}$ for $TiSi_2$. In all cases, these values are in good agreement to the most reliable experimental values.

4.3. The Mo-Ti system

Two stable solid phases are known for the system Mo-Ti : the hexagonal α phase and the body-centered cubic β phase. Upon quenching, sufficiently Ti-rich β phase can martensitically transform into the ω phase. The formation of this metastable phase was studied in detail by Sabeena et al. [107] in 2015. The crystallographic data of the phases are given in Table 4.11.
The binary system Mo-Ti is of limited technological importance. However, as one of the strongest β-stabilizers in Ti, Mo is added when titanium alloys with excellent weldability and formability are required, such as for implants and dental braces. These applications are typically limited

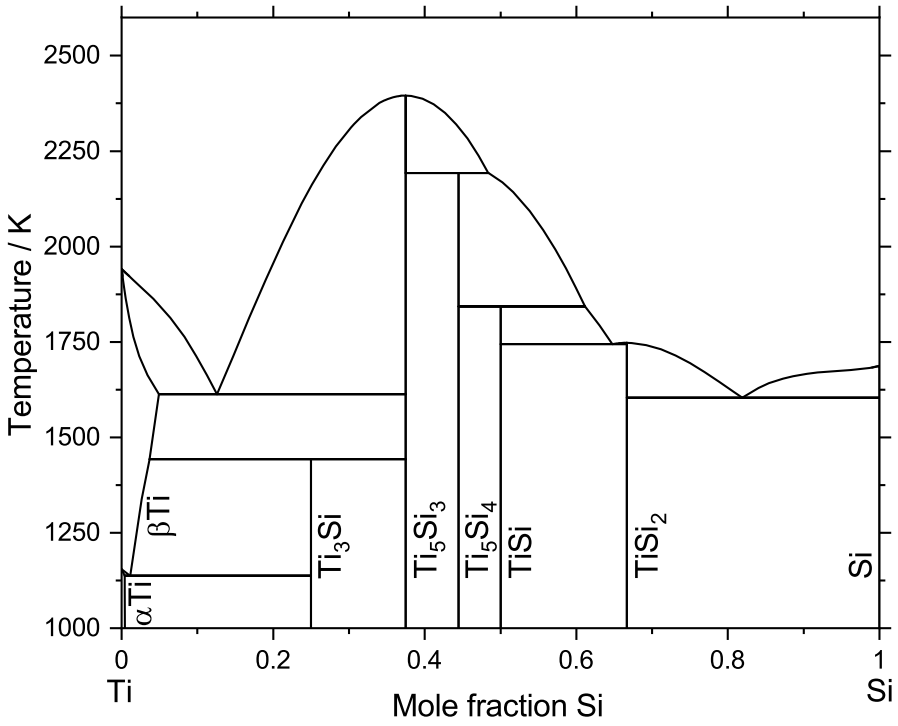

Figure 4.2.: The Ti-Si phase diagram as calculated from the dataset of Seifert et al. [104].

Table 4.10.: Comparison between the experimentally determined values of the temperatures and Si concentrations of the liquid phase for the invariant reactions in the Ti-Si system according to Svechnikov et al. [85] with the assessed values of Seifert et al. [104].

Reaction	Temperature / K		at. % Si	
	Calculated [104]	Experimental [85]	Calculated [104]	Experimental [85]
$\beta Ti \rightleftarrows \alpha Ti + Ti_3Si$	1138	1133	1.13	1.10
$\beta Ti + Ti_5Si_3 \rightleftarrows Ti_3Si$	1443	1443	3.68	4.00
$L \rightleftarrows \beta Ti + Ti_5Si_3$	1613	1613	12.59	13.70
$L \rightleftarrows Ti_5Si_3$	2396	2403	37.50	37.50
$L + Ti_5Si_3 \rightleftarrows Ti_5Si_4$	2193	2193	48.39	48.00
$L + Ti_5Si_4 \rightleftarrows TiSi$	1843	1843	61.15	60.00
$L \rightleftarrows TiSi + TiSi_2$	1744	1743	64.74	64.10
$L \rightleftarrows TiSi_2$	1748	1773	66.67	66.67
$L \rightleftarrows TiSi_2 + Si$	1604	1603	81.88	86.00

Table 4.11.: Crystallographic information about the solid phases in the Mo-Ti system.

Phase	Pearson symbol	Space group	Prototype
αTi	hP2	$P6_3/mmc$, #194	Mg
βTi	cI2	$Im\bar{3}m$, #229	W
(ωTi)	hP3	P6/mmm	ωTi

to multi-component alloys and relatively low concentrations of Mo (with a maximum of about 15 at.% Mo).

4.3.1. Phase diagram data

There are very few experimental data on the phase diagram of the system Mo-Ti. Since 1950 only four investigations have been published, which are listed in Table 4.12. In 1951, Hansen et al. [108] investigated the solidus line of the Ti-rich part of the Mo-Ti system and the phase boundaries between the solid phases by metallographic and X-ray techniques. In 1969, Rudy [109] investigated the solidus line of nearly the entire compositional range of the system by incipient melting studies. Flower et al. [110] determined the phase boundary between αTi and βTi. In 1977, Terauchi et al. [111] studied the solid phase boundaries of the system over a wide range of compositions. Contrary to previous publications, they reported a monotectoid β phase separation ($\beta \rightleftarrows \beta' + \alpha$ at 948 K) with a critical composition of the miscibility gap of 20 at.% Mo and a temperature of 1068 K. However, the phase diagram proposed by these authors is thermodynamically very unlikely, since the narrowness and asymmetry of the miscibility gap does not agree with the boundaries of the α and β regions. Brewer [79] tried to solve this by lowering the critical temperature and postulating a more reasonable diagram, but there is no new experimental evidence to support this version. As a result, it is still unclear whether the miscibility gap exists at all, and if so, where exactly it occurs.

4.3.2. Thermodynamic and thermophysical data

Due to the apparent lack of technological interest in the system, as well as the absence of intermetallic phases, there are almost no investigations of thermodynamic or thermophysical properties for the system Mo-Ti. Kuz'min and Palatnik [112] used vapor pressure measurements to determine the activity of Ti in Mo-Ti alloys from 1600 to 1800 K. Hoch and Viswanathan [113] determined the activity of Ti in β phase alloys from 30 to 100 at.% Ti using Knudsen cells. From their data they concluded that the β Ti-Mo interaction parameter is 12.1 $\pm$ 2.9 kJmol^{-1}. This implies the existence of a metastable miscibility gap with a critical temperature of 732 K.

Table 4.12.: Experimental phase diagram data of the Mo-Ti system.

Literature	Method	Equilibria	Temperature / K	at. % Mo
Terauchi et al., 1977 [111]	Metallography, X-ray, TEM, resistivity	Solid state phase boundaries	873 - 1173	2.6 - 74
Flower et al., 1974 [110]	Metallography	Solid state phase boundaries	723 - 1373	0.3 - 0.5
Rudy, 1969 [109]	Metallography	Solidus line	1923 - 2813	10 - 90
Hansen et al., 1951 [108]	Metallography, X-ray	Solid state phase boundaries and solidus line	873 - 1128	0.4 - 16

In 2017, Barzilai et al. [114] used ab-initio methods to calculate the phase diagram of Mo-Ti. They conclude that the system should have four stable intermetallic phases: MoTi, Mo_2Ti, Mo_4Ti, and Mo_5Ti. In 2020, Jiang et al.[115] used a similar technique to model the ternary system Mo-Ti-Zr. In addition to the intermetallic phases postulated by Barzilai et al. they also predict the stability of the phases Mo_9Ti, Mo_7Ti, Mo_3Ti_2 and $MoTi_2$. However, none of the experimental studies to date have found any intermetallic phases in this system.

4.3.3. Thermodynamic assessments

There are two competing thermodynamic assessments of the system Mo-Ti in the literature. In a very thorough literature review and evaluation in 1981, Murray [116] concludes that no reliable decision can be made with the given data as to whether or not the miscibility gap of the β phase should be included in the phase diagram. As a result, two versions of the phase diagram were published: one without the monotectic reaction and one with the monotectic reaction, but considering only a small part of the data of Terauchi et al. [111]. In a 1998 assessment of the system, Ansara [117] decided to disregard the data of Terauchi et al. and consequently modeled the phase diagram without a miscibility gap. This phase diagram agrees well with Murray's version without the miscibility gap.
For the purpose of this work, it was decided to accept the assessment of Ansara. Too little data is available to model the proposed miscibility gap with any confidence. In addition, the low temperature behavior of the materials is of minor importance in the context of this work. Since Ti transforms into the β phase at 1155 K, and the temperatures at which the material is studied are well above this threshold, one can even pragmatically decide that including the miscibility gap would only add a multitude of parameters that do not add to the quality of the dataset and whose

value would be mere speculation. Thus, accepting the simpler diagram is the more reasonable decision in all respects. The phase diagram calculated with Ansara et al.'s dataset is shown in Figure 4.3.

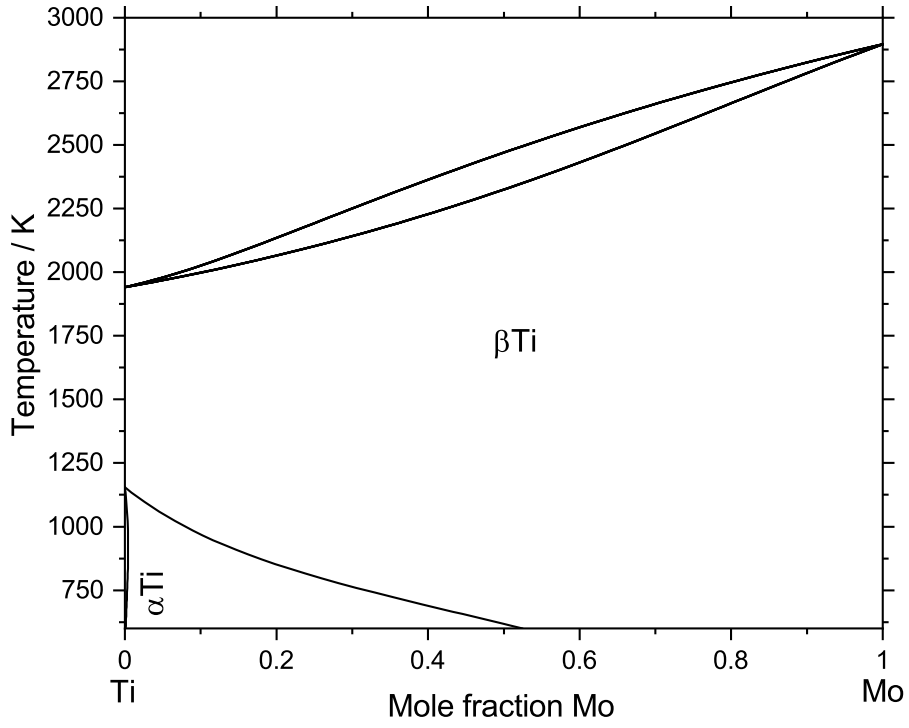

Figure 4.3.: The Mo-Ti phase diagram as calculated from the dataset of Ansara et al. [117].

4.4. The Mo-Si-Ti system

The Mo-Si-Ti system has been of interest to researchers for several decades as a promising material for high temperature structural applications. Most of the work has been derived from the Mo-Si system, where $MoSi_2$ exhibits excellent properties but a distinct lack of ductility. Alloying the material with Ti was thought to be a viable way to improve the mechanical properties of the alloy while maintaining the oxidation and corrosion resistance of the material. Thus, the vast majority of the literature is concerned with the region of the system at a silicon concentration of 66.7 at.% and its vicinity. In recent years, the focus has shifted to alloys consisting of the (Mo,Si,Ti) solid solution and one or two silicides in equilibrium with it [118, 12, 13, 14]. Since

Table 4.13.: Crystallographic information about the ternary phases in the Mo-Si-Ti system.

Phase	Pearson symbol	Space group	Prototype
(Ti,Mo)Si_2	hP9	$P6_222$, #180	$CrSi_2$
(Ti,Mo)$_6Si_5$	oI44	Ibam, #72	V_6Si_5

Mo and Ti have unlimited solubility in the solid solution, and three different intermetallic phases exist at high temperatures, a wide range of possible properties can be obtained in this way. The three intermetallic solid solutions of interest are (Mo,Ti)$_3$Si, (Mo,Ti)$_5Si_3$ and (Ti,Mo)$_5Si_3$. For the sake of legibility, even though all phases are solid solutions, the shorter names of the binary compounds they are based on will be used, so (Mo_3Si, Mo_5Si_3 and Ti_5Si_3), respectively.
In the Mo-Si-Ti system, two ternary phases exist: (Ti,Mo)Si_2 and (Ti,Mo)$_6Si_5$. The crystallographic information of these phases are listed in Table 4.13. A good overview of the system is given in the MSIT report [119], originally written by Lukas and Bondar and updated during the course of this work by the author of this work, A. K. Czerny in collaboration with V. Romaka. This report contains a great deal of information on thermodynamics and crystallography of the system. The following section uses some of these data, but discusses and explains it in more detail than the MSIT report attempts.

4.4.1. Phase diagram data

Relevant phase diagram data for the Mo-Si-Ti system can be traced back to the early 1950s. An overview of all data is given in Table 4.14.

Table 4.14.: Experimental phase diagram data of the Mo-Si-Ti system.

Literature, Year	Method	Equilibria	Temperature / K	at. % Si
Colinet et al., 2016 [120]	X-ray	Structure determination of T phase	1873	45.4
Ström et al., 2005 [121]	X-ray, SEM, EDX	Site occupation of alloyed Mo_5Si_3	1873	37.5
Yang et al., 2003 [16]	SEM, EPMA, X-ray	Isothermal sections at 1698 and 1873 K, liquidus projection	1698, 1873	10 - 63

Ström et al., 2002 [122]	SEM, EDX, X-ray	Composition of Mo_5Si_3	1873	37.5
Wei et al., 2001 [123]	DTA, SEM, EDX, X-ray	$TiSi_2$-$MoSi_2$ section	1673, RT - 1923	66.7
Boettinger et al., 1992 [124]	SEM, EPMA, DTA	$TiSi_2$-$MoSi_2$ section	1573 - 2150	66.7
Frankwicz and Perepezko, 1991 [125]	X-ray, Metallography, SEM, EDX	$TiSi_2$-$MoSi_2$ section	> 1573	66.7
Vasil'eva and Terent'eva, 1974 [126]	Metallography, EPMA, X-ray	(Ti,Mo)Si_2-$TiSi_2$-Si	as-cast state	66.7 - 100
Svechnikov et al., 1972 [17]	X-ray, EPMA, DTA	Isothermal section at 1698 K, $TiSi_2$-$MoSi_2$-Si section at 1523 K, liquidus and solidus projections, isopleths	1523 K - 2273 K	37.5 - 100
Svechnikov et al., 1972 [127]	DTA	$TiSi_2$-$MoSi_2$ section	1573 - 2273	66.7
Kocherzhinsky, 1971 [128]	DTA	$TiSi_2$-$MoSi_2$ section	1573 - 2273	66.7
Garfinkle and Davis, 1965 [129]	X-ray, EPMA, Metallography, Hardness	Reaction of liquid Ti with $MoSi_2$	1603, 1698	0 - 66.7
Kudielka and Nowotny, 1956 [130]	X-ray	$TiSi_2$-$MoSi_2$ section	1573	66.6

Schachner et al., 1954 [131]	X-ray	Structure of Mo_5Si_3	as-cast state	40
Nowotny et al., 1952 [132]	X-ray	$TiSi_2$-$MoSi_2$ section	1573	66.7

In 1952 Nowotny et al. [132] demonstrated the existence of the quasi-binary section $TiSi_2$-$MoSi_2$. They showed that $MoSi_2$ has practically no solubility for $TiSi_2$ and proved the existence of a ternary phase (Ti,Mo)Si_2 from about 40 mol% to nearly 100 mol% $TiSi_2$. Schachner et al. [131] produced two (nominal) Mo_5Si_3 samples with about 40 at.% Si each and studied their crystal structure. They concluded that the samples had the $D8_8$ structure. However, because the samples were cast in graphite crucibles, both of these samples have significant amounts of C contamination (2.5 and 1.8 at.%, respectively), which stabilizes this structure. An uncontaminated sample produced in a tungsten tube short-circuit furnace yielded the (then unknown) structure later identified as $D8_m$. Kudielka and Nowotny [130] studied ternary systems of disilicides, including $TiSi_2$-$CrSi_2$-$MoSi_2$, $TiSi_2$-$ZrSi_2$-$MoSi_2$, and $TiSi_2$-$TaSi_2$-$MoSi_2$, respectively. The proposed liquidus projections suggest that a peritectic reaction $L + MoSi_2 \rightleftarrows (Ti, Mo)Si_2$ occurs at about 2023 K. They also postulate a eutectic reaction $L \rightleftarrows TiSi_2 + (Ti, Mo)Si_2$. A problem with this paper, however, is that they found the phase $MoSi_2$ in the C40 structure, which was later shown by Frankwicz et al. [40] to be metastable, see section 4.1.1. Garfinkle and Davis [129] investigated the interaction of molten Ti with several ceramic plaques, including $MoSi_2$. They found the lowest melting point of the pair to be 1698 K. They also equilibrated such a pair at 1603 K and examined the interface. In the reaction zone they found three phases: the β(Mo,Si,Ti) solid solution, Ti_5Si_3 and a silicide which they could not identify with certainty. Since the experimental setup is effectively a diffusion couple, one can infer today that the unknown silicide must have been Mo_5Si_3, as it has since been shown that only this phase shows a three-phase equilibrium with the other two identified phases. Kocherzhinsky [128] reported the development of a new DTA for temperatures exceeding 2000 K, which was previously thought not possible. They demonstrated the device by studying the systems Mo-Si, Ti-Si, and $MoSi_2$-$TiSi_2$. A rudimentary quasi-binary section of $MoSi_2$-$TiSi_2$ was reported. The same device was used by Svechnikov et al. [127], who investigated the $MoSi_2$-$TiSi_2$ section in more detail and reported the results in 1972. In disagreement to the results from Kudielka and Nowotny, the reaction between liquid, (Ti,Mo)Si_2 and $TiSi_2$ was found to be a peritectic as opposed to a eutectic: $L + (Ti, Mo)Si_2 \rightleftarrows TiSi_2$. The quasi-binary section $MoSi_2$-$TiSi_2$ from this publication is shown in Figure 4.4.

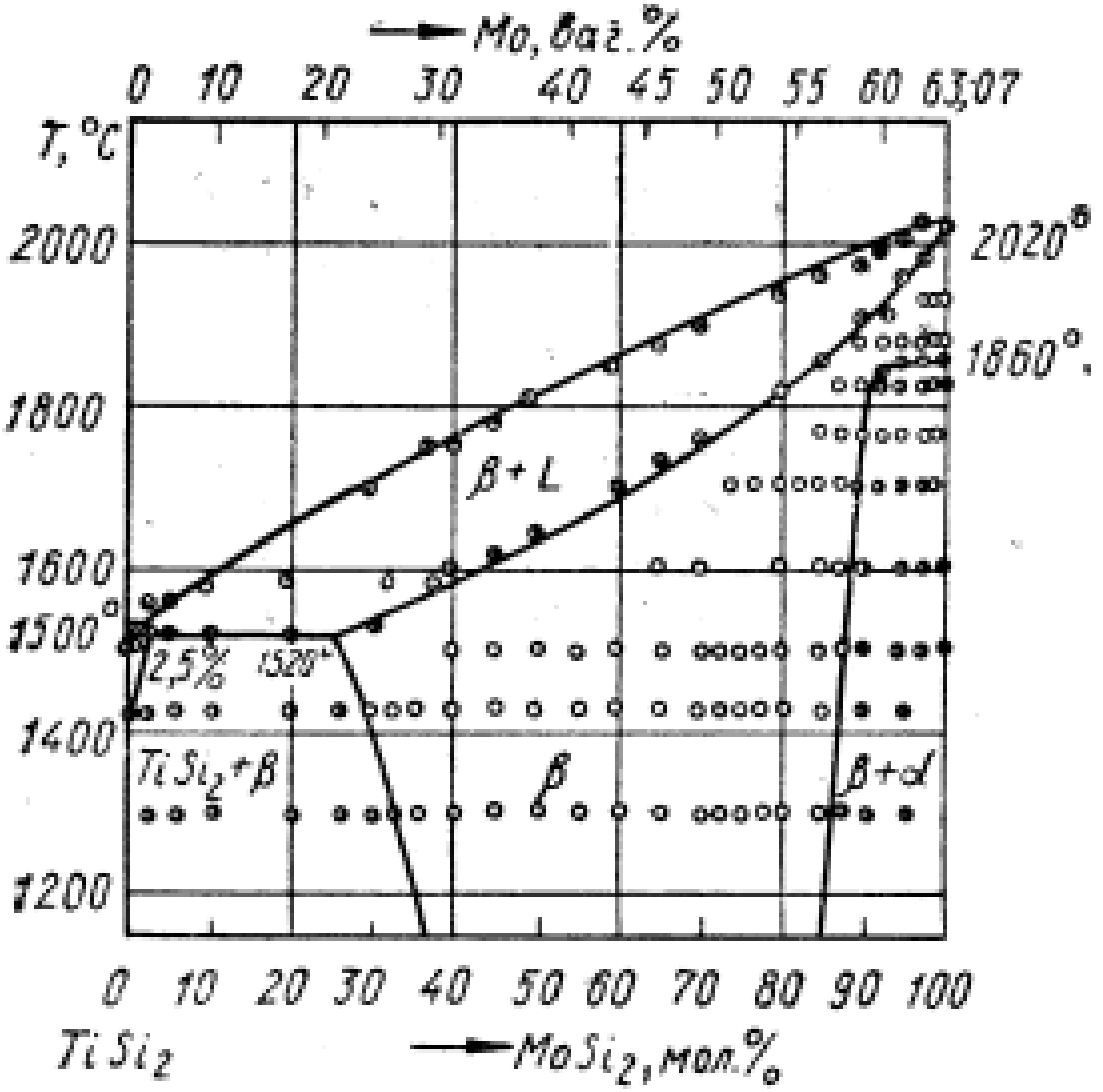

Figure 4.4.: The quasi-binary section $MoSi_2$-$TiSi_2$ from Svechnikov et al. [127].

In another paper from the same year, Svechnikov et al. [17] extensively investigated the phase equilibria in the Mo-Si-Ti system. They studied the range between 37.5 and 66.7 at.% Si at 1698 K, which is shown in Figure 4.5, and the range between 66.7 and 100 at.% Si at 1523 K, which is shown in Figure 4.6. They were the first group to report the existence of another ternary phase, located at about 45 at.% Si. This phase was later labelled T phase. In addition to the isothermal sections, they reported the liquidus and solidus projections of the section $MoSi_2$-$TiSi_2$-Si, which are shown in Figure 4.7. Finally, they published 8 isopleths, ranging from 45 - 80 wt.% Si, which are shown in Figure 4.8. It must be noted however, that the isopleths 4.8 E-H cannot be correct in the way they are drawn. Specifically, the region labelled L+$\alpha$$MoSi_2$+$\beta$ is drawn in such a way that it terminates at 0 at.% Ti and the same temperature, which, given the orientation of the section in the phase diagram, is not possible. Instead, this phase region would have to end at higher Ti content and at the liquidus line to be consistent with the rest of the data of Svechnikov et al.

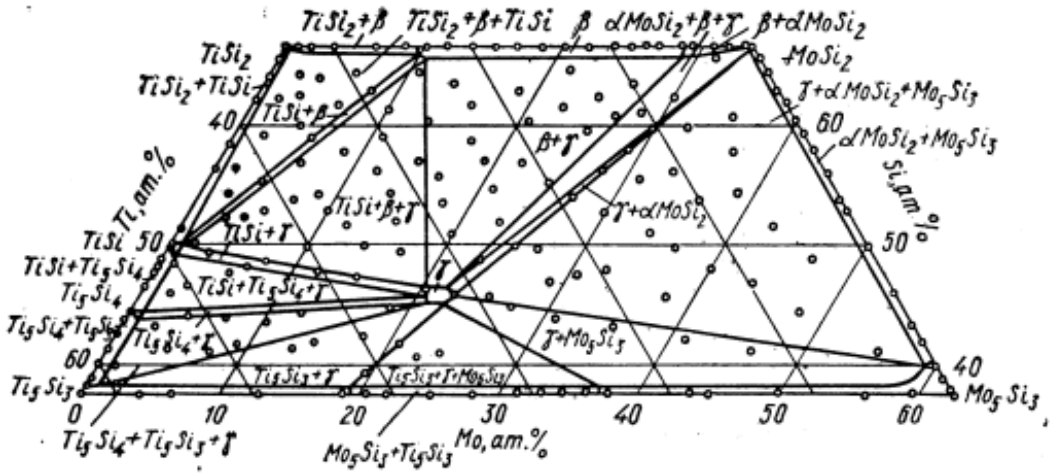

Figure 4.5.: The isothermal section of the Mo-Si-Ti system between the 5-3- and the 1-2-silicides at 1698 K, from Svechnikov et al. [17].

Vasil'eva and Terent'eva [126] investigated the phase composition of several alloys in the region Si-$MoSi_2$-$TiSi_2$. Using a combination of metallographic methods, EPMA and XRD, they concluded that all samples in the range studied were composed of the phases Si+(Ti,Mo)Si_2+$TiSi_2$. However, it should be noted that the samples in this study were produced under rapid solidification conditions in an arc melter and were not homogenized. Frankwicz and Perepezko [125] investigated the quasi-binary section $MoSi_2$-$TiSi_2$ in more detail in 1991. While confirming the existence of the phase (Ti,Mo)Si_2, the peritectic reaction $L + (Ti, Mo)Si_2 \rightleftarrows TiSi_2$ and the practically non-existent solubility of $MoSi_2$ for Ti, they reported several important differences to the section from Svechnikov et al.'s publication. Most critically, they found a peritectic reaction $L + MoSi_2 \rightleftarrows (Ti, Mo)Si_2$, resulting in significant differences on the $MoSi_2$-rich

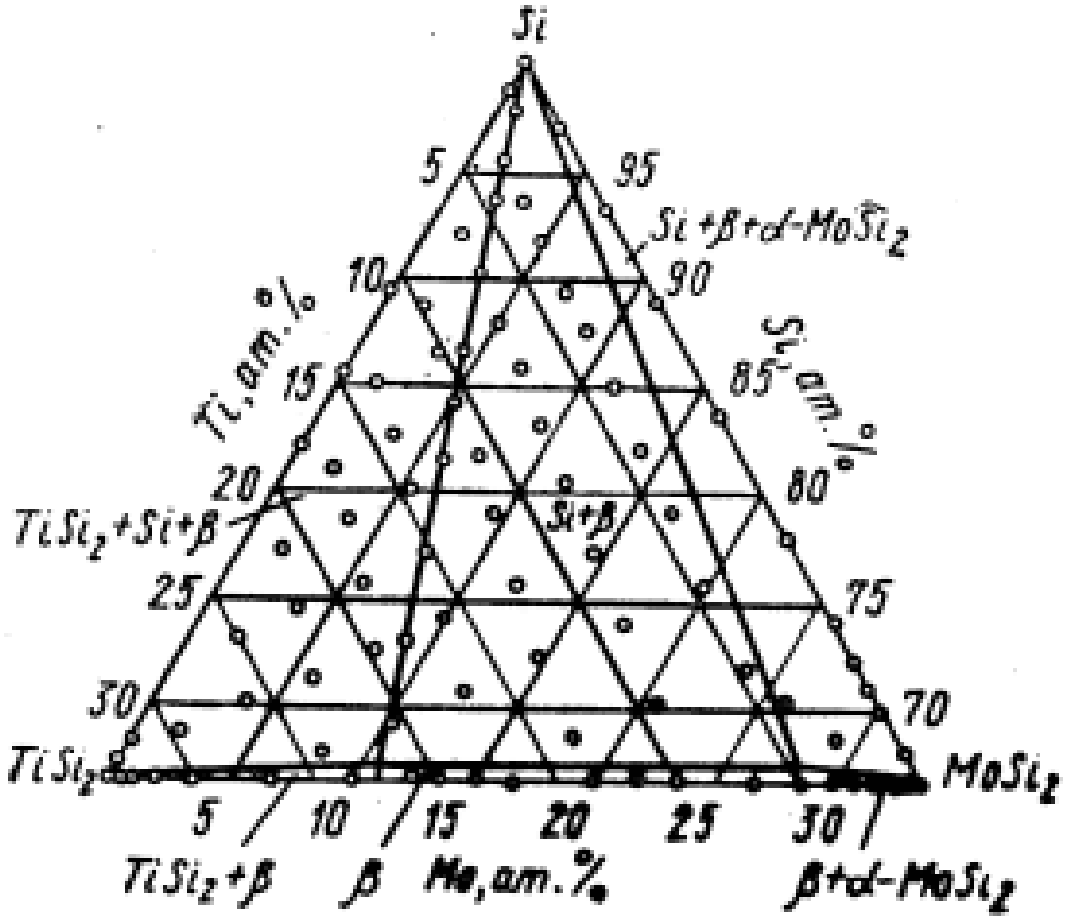

Figure 4.6.: The isothermal section of the Mo-Si-Ti system between the 1-2-silicides and Si at 1523 K, from Svechnikov et al. [17].

side. They reported a peritectic temperature above 1873 K and a peritectic composition of approximately (25Ti-75Mo)Si_2 in (Ti,Mo)Si_2. Thermodynamically, this quasi-binary section is more likely than the one of Svechnikov et al., which shows a rather unlikely curvature at the $(Ti,Mo)_2$/(Ti,Mo)Si_2+$MoSi_2$ boundary. It is also noteworthy that this is the first publication to report the absence of β- $MoSi_2$. A year later, Boettinger et al. [124] investigated several disilicide systems in more detail, including $MoSi_2$-$TiSi_2$. Qualitatively, the quasi-binary section is identical to that published a year earlier, but the invariant reaction temperatures were refined. In 2001, Wei et al. [123] investigated the section $TiSi_2$-$MoSi_2$ with DTA and samples equilibrated at 1673 K. They confirmed the reactions postulated by Boettinger, Frankwicz and Perepezko, but found a much wider homogeneity range for the phase (Ti,Mo)Si_2 than suggested by the quasi-binary sections of the previous investigators. This version of the quasi-binary section is shown in Figure 4.9.

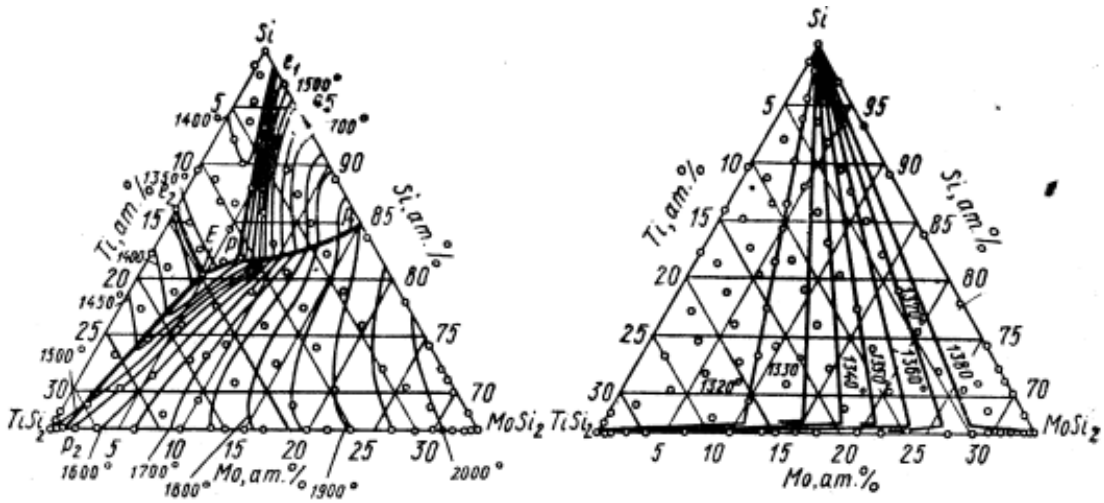

Figure 4.7.: The liquidus (left) and solidus (right) projections of the Mo-Si-Ti system between the 1-2-silicides and Si, from Svechnikov et al. [17].

Ström et al. [122] investigated the influence of alloying elements on the phase constitution of Mo_5Si_3. The sample in the Mo-Si-Ti system studied had the composition 38.1Mo-39.1Si-22.8Ti (all concentrations in at.%) and was annealed at 1873 K for 120 h. After heat treatment, the microstructure showed two phases, which were identified as Mo_5Si_3 and Ti_5Si_3. According to the phase diagrams both of Svechnikov et al. and of Yang et al., the sample would be expected to be in the two-phase region Mo_5Si_3+T. The experimental compositions of Mo_5Si_3 and Ti_5Si_3 are 38.8Mo-34.3Si-26.9Ti and 28.9Mo-34.1Si-37.0Ti, respectively. Since both phases are much lower in Si content than the sample before heat treatment, and the Mo content in both phases is also much lower than would be expected from a sample of this composition, it is very likely that the sample studied in this investigation suffered from evaporation of Mo and Si and was most likely not in equilibrium.

In 2003, Yang et al. [16] investigated the Mo-Si-Ti system between 10 and 63 at.% Si. From these data they derived the first published CALPHAD dataset of the system. For the sake of brevity, and to keep the discussion of the publication complete and concise, the following section will discuss not only the experimental results, but also the dataset and derived results where appropriate. Purely numerical and modeling information will be discussed in section 4.3.3.
The group reported isothermal sections at 1698 and 1873 K, which are shown in Figures 4.10 and 4.11, respectively. The existence of the ternary T phase first found by Svechnikov et al. is confirmed and, based on experimental observations, a stoichiometry of $(Mo,Ti)_{11}Si_9$ is assumed. Notably, this phase is treated as a line compound, in contrast to Svechnikov et al. who assumed a variable Si content. The homogeneity ranges of the phases Mo_5Si_3 and Ti_5Si_3 with respect to the other metal atom are quite different from the publication by Svechnikov et al. As a consequence, Yang et al. reported the equilibria Ti_5Si_4+Mo_5Si_3, Ti_5Si_4+$TiSi_2$ and Ti_5Si_4+$(Ti,Mo)Si_2$, while

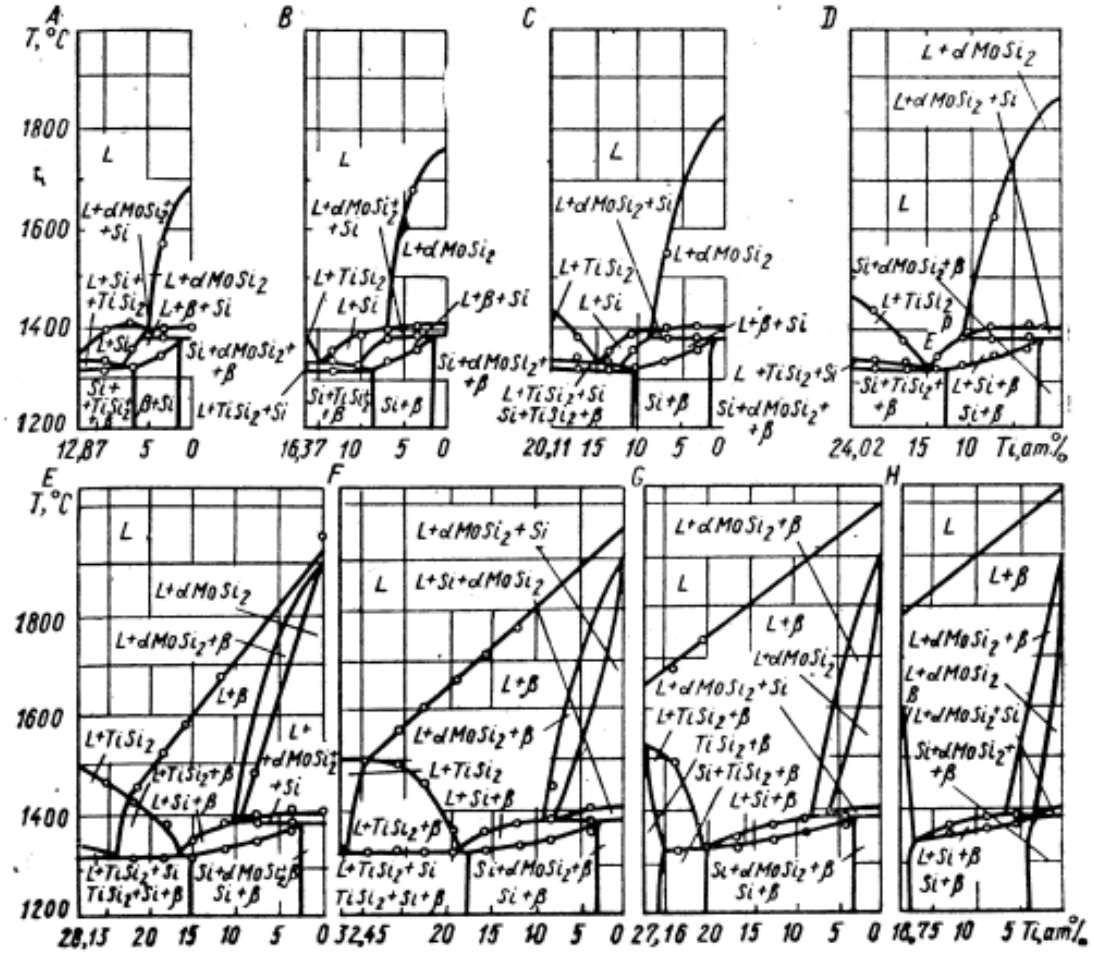

Figure 4.8.: The isopleths from Svechnikov et al. [17]. A: 80 mass% Si, B: 75 mass% Si, C: 70 mass% Si, D: 65 mass% Si, E: 60 mass% Si, F: 55 mass% Si, G: 50 mass% Si, H: 45 mass% Si.

Svechnikov et al. reported equilibria between Ti_5Si_3+T phase and TiSi+T phase. In the metal-rich region, two tie-triangles consisting only of solid phases were reported; one equilibrium between β+Mo_3Si+Mo_5Si_3 and the other equilibrium β+Mo_5Si_3+Ti_5Si_3. Both triangles did not change much in composition as a function of temperature, especially in the case of the latter tie triangle.

From the binary systems, as well as the quasi-binary section $MoSi_2$-$TiSi_2$, Yang et al. also derived the liquidus projection of the system. It is shown in Figure 4.12 as it was printed in the MSIT system report [119], but modified to highlight the two transition reactions in the metal-rich area. The system has several saddle points and transition reactions that can lead to quite complex and unique solidification behavior. At several locations, two transition reactions are very close to each other, adding to the complexity of the liquidus projection. Both saddle points p_1 and e_2 are highly relevant to this work because of the edges of double saturation connected to them.

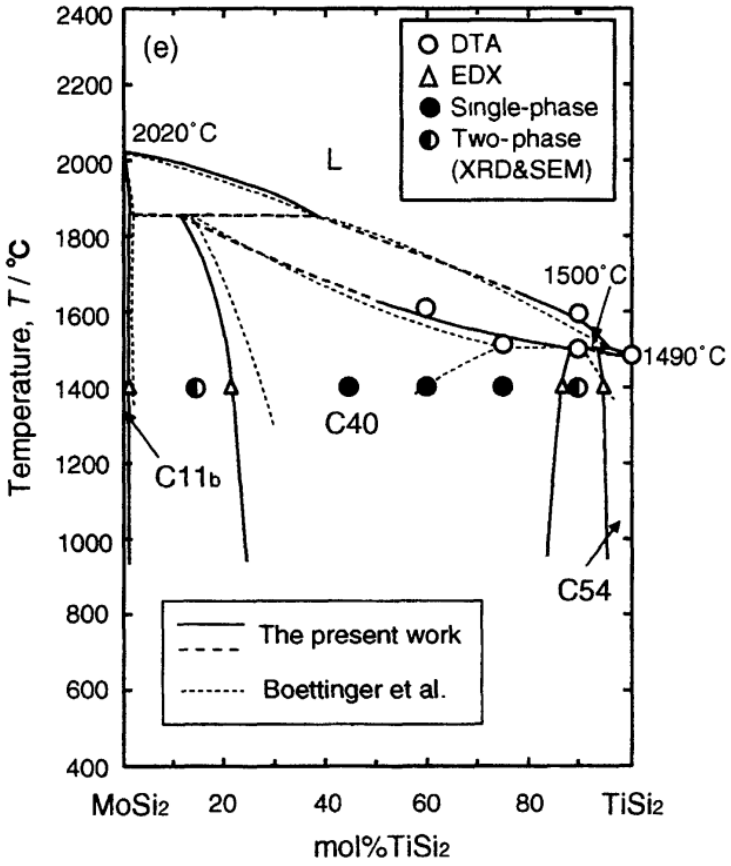

Figure 4.9.: The quasi-binary section $MoSi_2$-$TiSi_2$ from Wei et al. [123]. The labels $C11_b$, C40 and C54 refer to $MoSi_2$, $(Ti,Mo)Si_2$ and $TiSi_2$, respectively.

From p_1 towards higher Mo concentrations, a eutectic trough is found, while a peritectic reaction connects this saddle point and transition reaction U2. Similarly, e_2 leads to a peritectic reaction for higher Mo concentrations, while a eutectic trough connects the saddle point with transition reaction U3. It should be noted, however, that there is no experimental evidence for the ternary reactions, nor for the exact location of the saddle points or even the edges of double saturation. Since the reaction temperatures exceed the reliable measurement ranges of DSC and DTA, the liquidus projection was modeled solely from data derived from binary and quasi-binary sections and later compared with cast microstructures. As such, the only thing that can be stated with certainty is that this liquidus projection does not contradict any of the experimental data from Yang et al. However, other equally valid liquidus projections are theoretically possible that meet this requirement. Nonetheless, a list of invariant ternary reactions according to the data from Yang et al. is presented in Table 4.15. The Scheil reaction scheme, as it was printed in the MSIT system report, is shown in Figure 4.13, with the invariant reactions in the metal-rich area of the

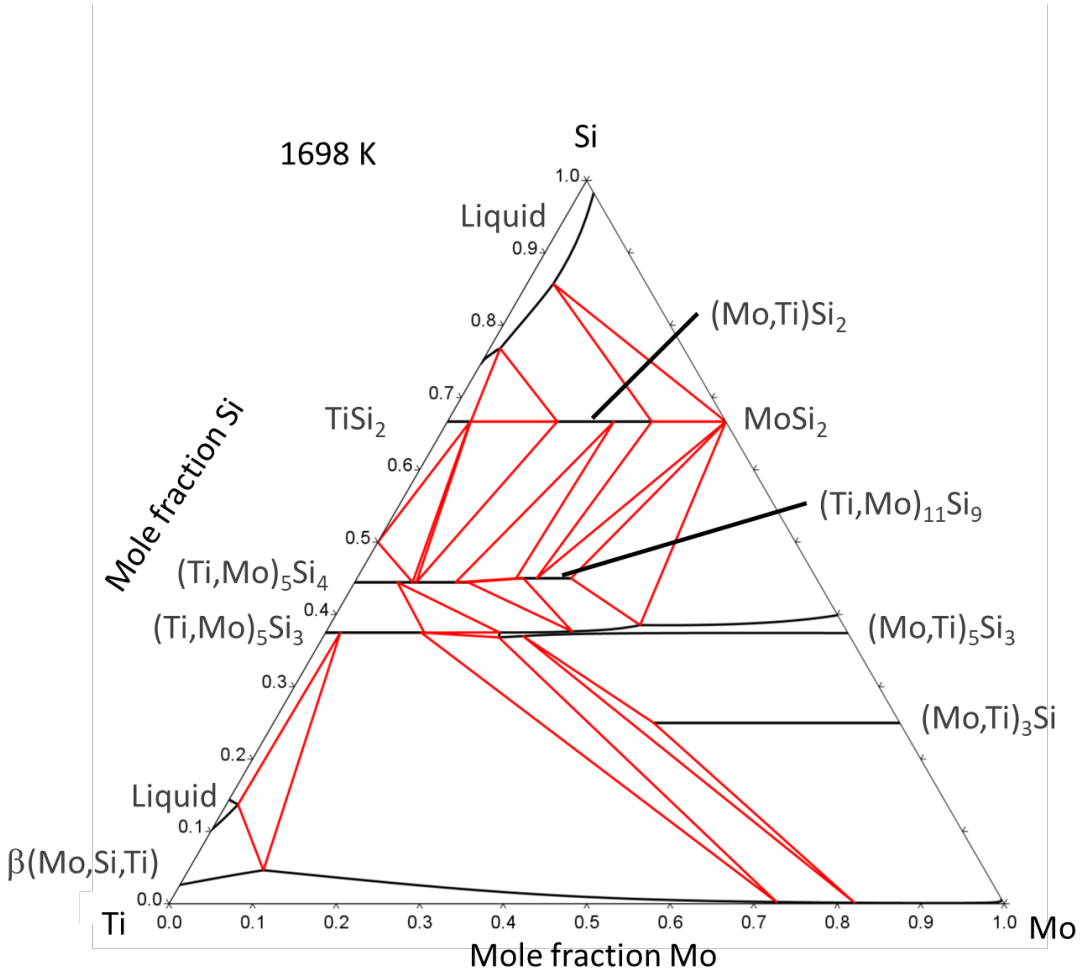

Figure 4.10.: The isothermal section of the system Mo-Si-Ti at 1698 K, calculated with the dataset from Yang et al. [16].

system highlighted for this thesis in red. Note that the temperatures of the invariant reactions are slightly different in Figure 4.13 and Table 4.15 (maximum deviation of around 5 K). A calculation of the values with the dataset of Yang et al. by the author of this dissertation confirmed the values of the MSIT report, so these data were preferred whenever they conflicted.

The evolution of the equilibria in the metal-rich region of the system as the ternary invariant reactions take place will be discussed next, based on the dataset of Yang et al., but calculated by the author of this work. Below the temperature of U_6, Ti_5Si_3 + $Mo_3Si \rightleftarrows \beta$ + Mo_5Si_3 at 2143,4 K, the three-phase equilibria β+Mo_5Si_3+Ti_5Si_3 and β+Mo_3Si+Mo_5Si_3 are stable down to room temperature, as can be seen in Figures 4.10 and 4.11. The next relevant temperature range of interest is between 2200 and 2210 K. Figure 4.14 shows the isothermal section at 2200 K. This is just below the temperature of U_3, β + $Ti_5Si_3 \rightleftarrows Mo_3Si$ + L at 2203 K. The liquid phase has

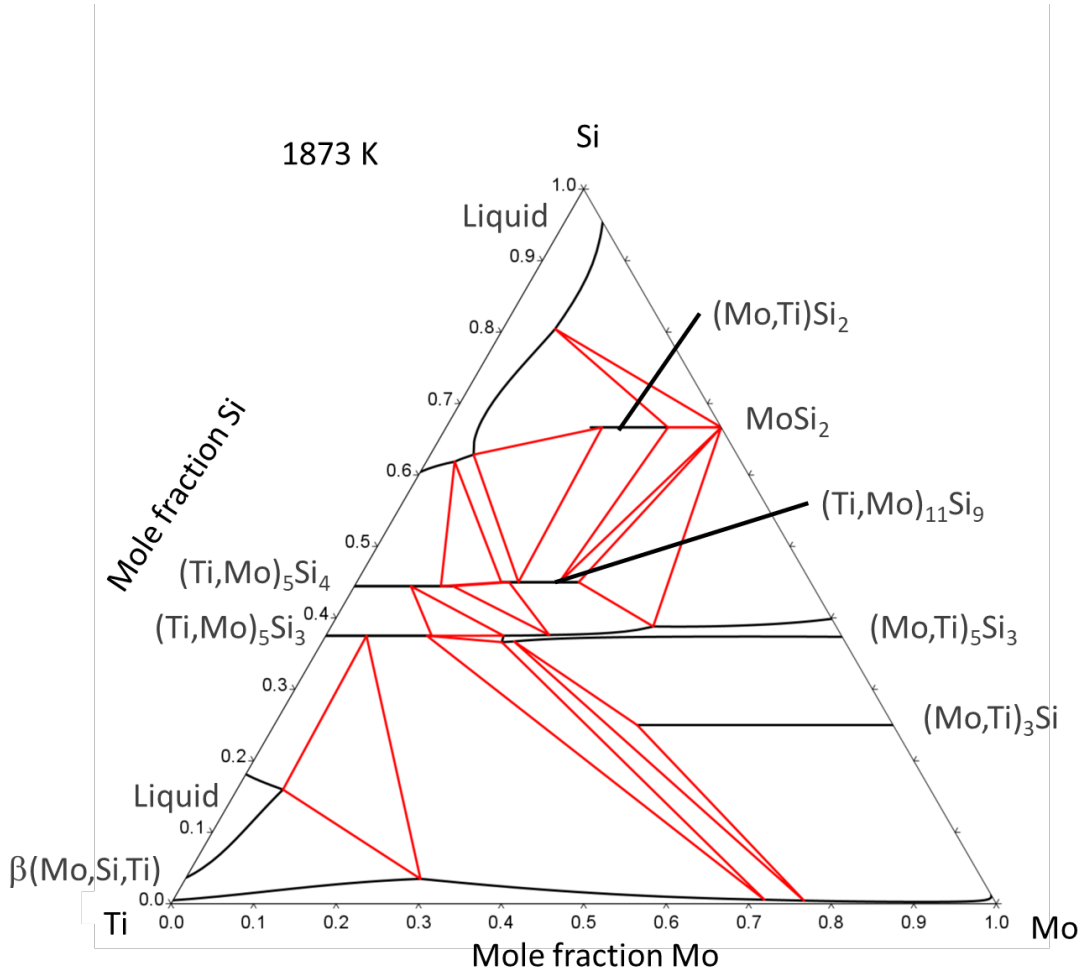

Figure 4.11.: The isothermal section of the system Mo-Si-Ti at 1873 K, calculated with the dataset from Yang et al. [16].

advanced well into the Ti-rich corner of the system, and the following three three-phase equilibria are stable: β+L+Ti_5Si_3, β+Mo_3Si+Ti_5Si_3, and Mo_3Si+Mo_5Si_3+Ti_5Si_3.

At higher temperature than the U_3 temperature level of 2203 K, this reaction U_3 has already taken place. This is shown as an example for 2205 K in Figure 4.15. Consequently the two equilibria β+L+Ti_5Si_3 and β+Mo_3Si+Ti_5Si_3 have now changed to the equilibria β+L+Mo_3Si and L+Mo_3Si+Ti_5Si_3. Since the reaction U_2, L + $Mo_5Si_3 \rightleftarrows Mo_3Si + Ti_5Si_3$ at 2208 K has not yet taken place, the equilibrium Mo_3Si+Mo_5Si_3+Ti_5Si_3 remains stable.

This changes for the temperature 2210 K, which is shown in Figure 4.16. Here, U_2 has just occurred, and as a result, the two Si-richer equilibria have now changed to L+Mo_3Si+Mo_5Si_3

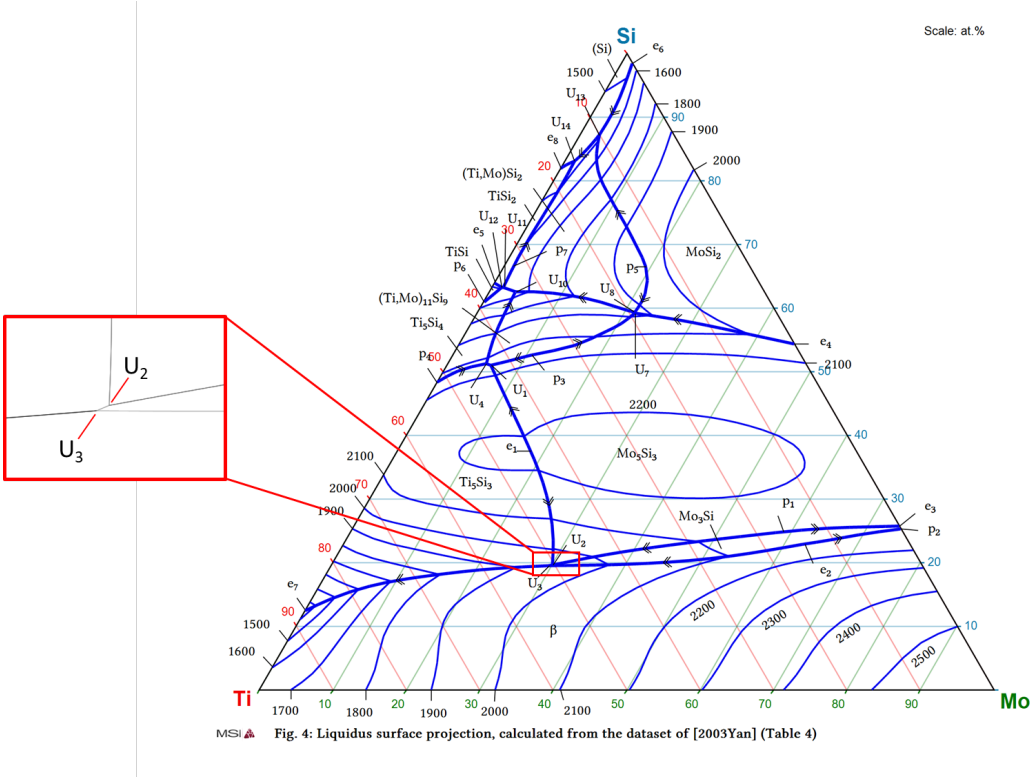

Figure 4.12.: The calculated liquidus projection of the system Mo-Si-Ti. Figure modified from the MSIT system report [119].

and L+Mo_5Si_3+Ti_5Si_3. The third equilibrium remains stable because it is not affected by this reaction.

The second temperature range of interest is between 2390 and 2400 K, where the saddle points of two lines of double saturation are located. Figure 4.17 shows the isothermal section of the system at 2390 K, which is slightly below the reaction temperature of e_2, L $\rightleftarrows$ β + Mo_3Si at 2396.2 K. At this temperature, a significant portion of the system consists of or is in equilibrium with the liquid phase. However, all solid phases still have some range of stability, so the three-phase equilibria β+L+Mo_3Si and L+Mo_3Si+Mo_5Si_3 exist on the Mo rich side. According to the calculation, $(Mo,Ti)_3Si$ is stable for intermediate Mo concentrations, but not for pure Mo_3Si or solid solutions containing very high amounts of Mo, which is why two separate domains of liquid and three-phase equilibrium exist. In addition to these equilibria, the region L+Mo_5Si_3+Ti_5Si_3 is stable.

At 2398 K, shown in Figure 4.18, the reaction e_2 has just taken place. As a result, the two three-phase regions in the Si-lean region of the phase diagram have disappeared.

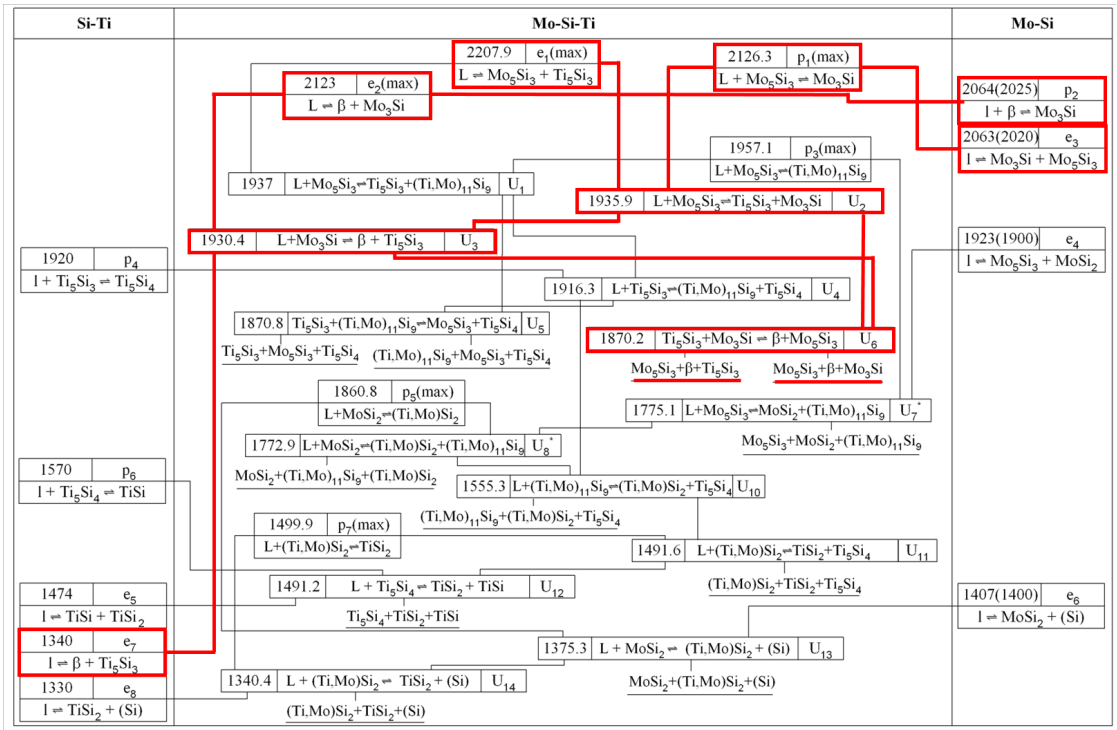

Fig. 3: Mo-Si-Ti: Reaction scheme, calculated from the dataset of [2003Yan] (Table 5); U_7* and U_8*, taken from Table 5 of [2003Yan] replace U7 + U8 + U9 of Table 4 of this report

Figure 4.13.: The Scheil reaction scheme of the system Mo-Si-Ti. Figure modified from the MSIT system report [119].

At 2400 K, which is just above the reaction temperature of p_1, L + $Mo_5Si_3 \rightleftarrows Mo_3Si$ at 2399.5 K, the last remaining Mo_3Si has just disappeared. This is shown in Figure 4.19. Consequently, there are no three-phase regions left in the Mo rich region. However, the tie triangle L+Mo_5Si_3+Ti_5Si_3 is still stable at this temperature. Note that both in the single phase region of β as well as in the two phase region β+Liquid Thermo-Calc draws incomplete lines that end somewhere in the respective phase region. These are both artifacts and have no meaning or actual consequence for any calculations.

This changes at 2481.1 K with the reaction e_1, L $\rightleftarrows$ Mo_5Si_3 + Ti_5Si_3. Figure 4.20 shows the isothermal section at 2480 K, slightly below the reaction temperature. Here, the equilibrium L+Mo_5Si_3+Ti_5Si_3 is small, but still stable.

At 2490 K, as shown in the Figure 4.21, this reaction has taken place and the remaining Ti_5Si_3 has melted. The last stable silicide is Mo_5Si_3, which is only in equilibrium with the liquid phase. At even higher temperatures, this phase will eventually disappear, followed by the melting of the remaining β phase.

Table 4.15.: Ternary invariant reactions calculated with the dataset from Yang et al. [16]. The designations of the reactions were directly from Thermo-Calc and may be different from the ones chosen in the MSIT report [119].

Designation	Temperature / K	Reaction
U1	2209.9	$L + Mo_5Si_3 \rightleftarrows (Mo,Ti)_{11}Si_9 + Ti_5Si_3$
U2	2208.0	$L + Mo_5Si_3 \rightleftarrows Mo_3Si + Ti_5Si_3$
U3	2203.1	$\beta + Ti_5Si_3 \rightleftarrows L + Mo_3Si$
U4	2189.6	$L + Ti_5Si_3 \rightleftarrows (Mo,Ti)_{11}Si_9 + Ti_5Si_4$
U5	2048.3	$L + MoSi_2 \rightleftarrows Mo_5Si_3 + (Mo,Ti)Si_2$
U6	2046.0	$L + Mo_5Si_3 \rightleftarrows (Mo,Ti)_{11}Si_9 + (Mo,Ti)Si_2$
U7	1828.4	$L + (Mo,Ti)_{11}Si_9 \rightleftarrows (Mo,Ti)Si_2 + Ti_5Si_4$
U8	1764.7	$L + (Mo,Ti)Si_2 \rightleftarrows TiSi_2 + Ti_5Si_4$
U9	1764.4	$L + Ti_5Si_4 \rightleftarrows TiSi_2 + TiSi$
U10	1648.5	$Si + (Mo,Ti)Si_2 \rightleftarrows L + MoSi_2$
U11	1613.6	$Si + TiSi_2 \rightleftarrows L + (Mo,Ti)Si_2$
e1	2481.1	$L \rightleftarrows Mo_5Si_3 + Ti_5Si_3$
e2	2396.2	$L \rightleftarrows \beta + Mo_3Si$
p1	2399.5	$L + Mo_5Si_3 \rightleftarrows Mo_3Si$
p2	2230.3	$L + Mo_5Si_3 \rightleftarrows (Mo,Ti)_{11}Si_9$
p3	2134.0	$L + MoSi_2 \rightleftarrows (Mo,Ti)Si_2$
p4	1773.1	$L + (TI,Mo)Si_2 \rightleftarrows TiSi_2$

In 2005, Ström et al. [121] investigated the site occupancy of ternary alloyed Mo_5Si_3, again with Ti as one of the alloying elements. They prepared two samples in the single-phase region of Mo_5Si_3, with the compositions $Mo_3Ti_2Si_3$ and $Mo_4Ti_1Si_3$. They compared the crystallographic data measured by XRD with that of a pure Mo_5Si_3 sample in the as-cast state. It was reported that the unit cell volume increases monotonically with increasing Ti content, but for unknown reasons the c-parameter of the unit cell is smaller for $Mo_3Ti_2Si_3$ than for $Mo_4Ti_1Si_3$. In addition, they found that Ti occupies both the 16k and 4b sites of the lattice, with a preference for the 16k site. In 2019, Colinet et al. [120] investigated the structure of the T phase by both ab initio calculations and XRD. After calculating the most likely crystal structure for the compound, they synthesized a sample with the composition 22.6Mo-45.4Si-32Ti and annealed it at 1873 K for 8 h. The diffractogram as well as the DFT calculation confirm the structure of the V_6Si_5 prototype, which agrees fairly well with the publication of Yang et al. [16].

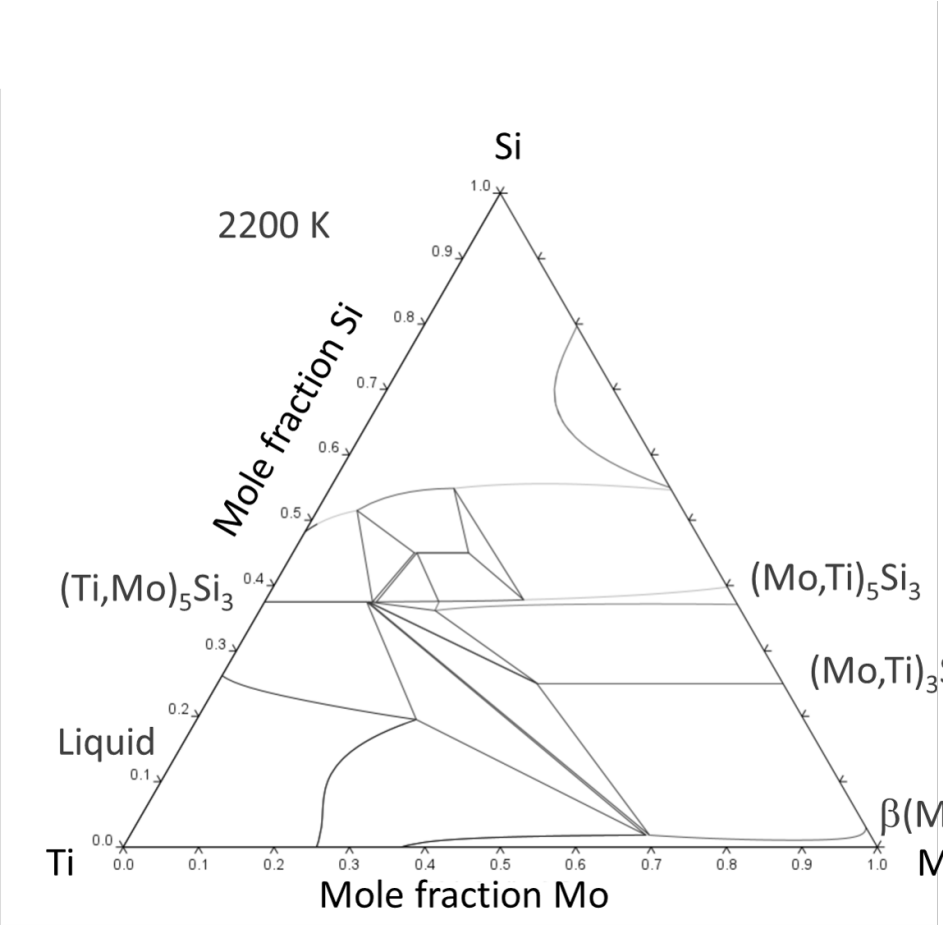

Figure 4.14.: The isothermal section of the Mo-Si-Ti system at 2200 K, according to the dataset of Yang et al. [16].

4.4.2. Thermodynamic and thermophysical data

There are no experimental measurements of thermodynamic or thermophysical data for ternary compounds in the Mo-Si-Ti system. However, in the supplementary material of the aforementioned publication by Colinet et al. [63], enthalpies of formation for both stable and unstable end members of each intermetallic phase in the system are calculated by DFT. This type of information is invaluable for CALPHAD assessments, as experimental investigations of the unstable compounds are not possible, but necessary for modeling. Without such data, key parameters of a dataset would need to be estimated or even guessed. The results are listed in Table 4.16.

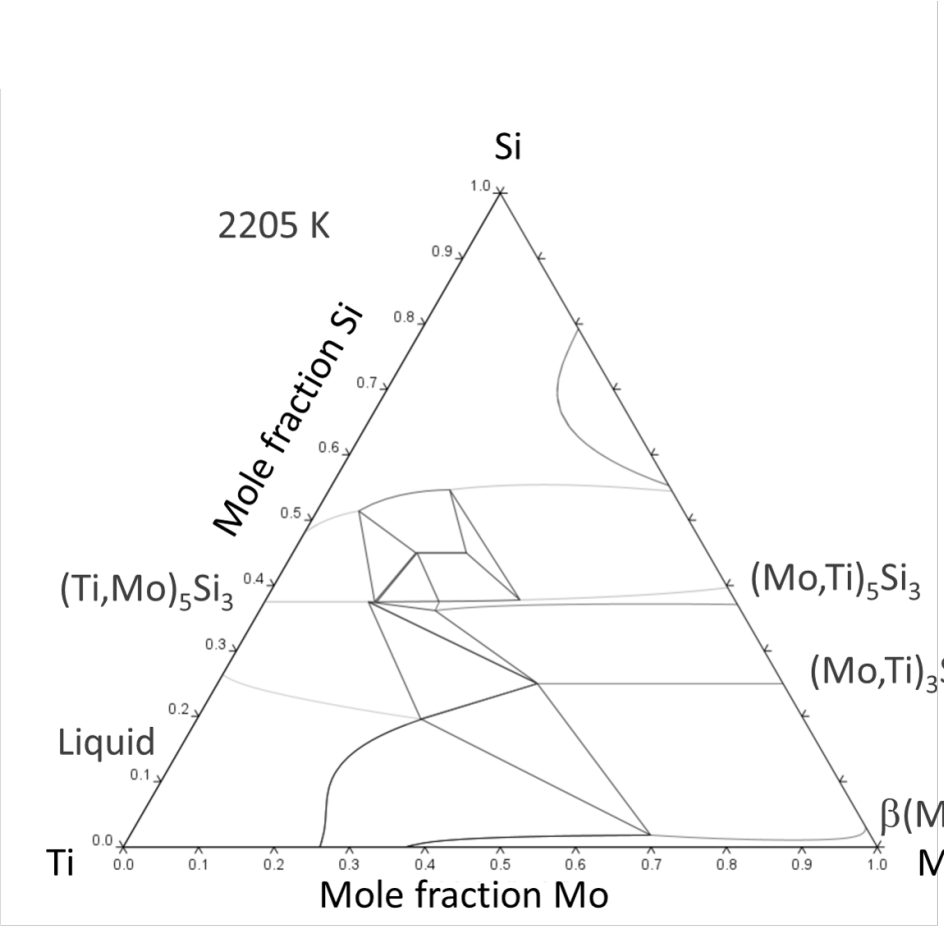

Figure 4.15.: The isothermal section of the Mo-Si-Ti system at 2205 K, according to the dataset of Yang et al. [16].

4.4.3. Thermodynamic assessments

As mentioned in section 4.4.1, Yang et al. [16] published the first CALPHAD assessment of the Mo-Si-Ti system in 2003. While many aspects of this publication have been discussed in the previous section, several aspects that are purely computational will be discussed below.
Yang et al. chose to accept the binary evaluations of Seifert et al. [104], Ansara et al. [117], and Liu et al. [80] for the Ti-Si, Mo-Ti, and Mo-Si systems, respectively. From the publication of Seifert et al. the version of the dataset was chosen which simplifies the phase Ti_5Si_3 as a line compound. Consequently, the only phase in the system modeled with a homogeneity range with respect to Si is Mo_5Si_3. The experimental data of Svechnikov et al. [17] were not used for the optimization. The experimental data of Boettinger et al. [124] were used to model the quasi-binary section $MoSi_2$-$TiSi_2$, where Yang et al. themselves did not place any sample compositions.

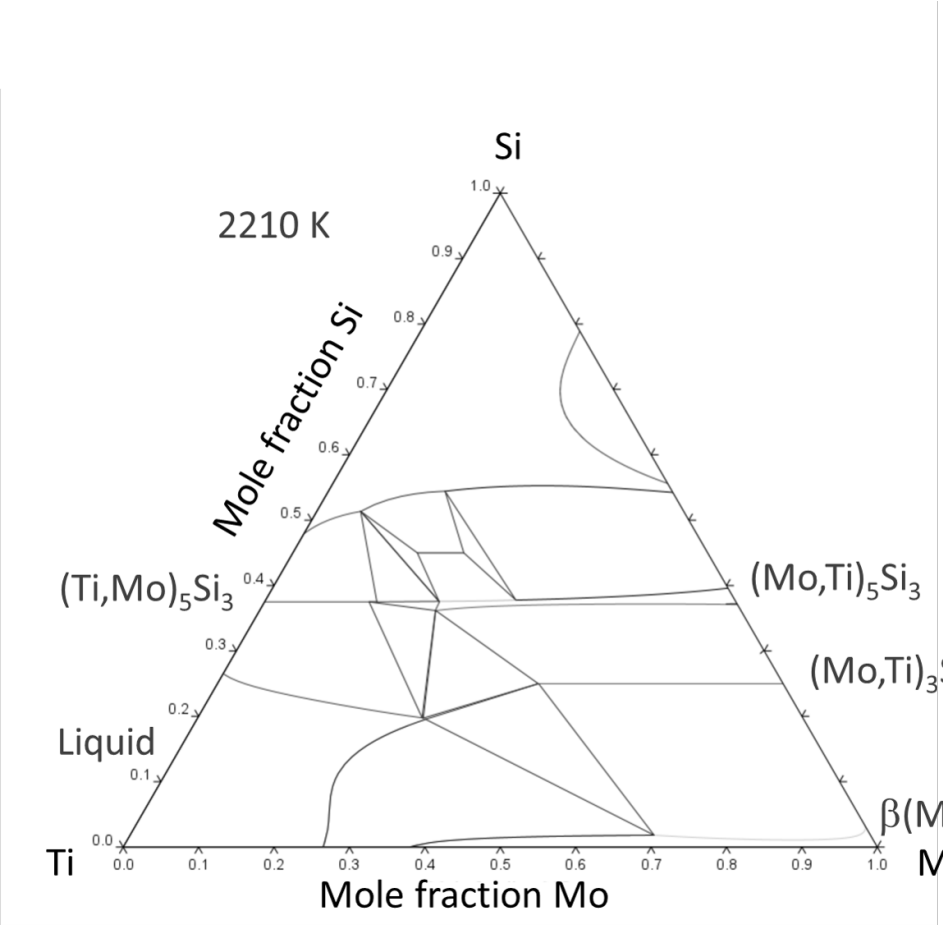

Figure 4.16.: The isothermal section of the Mo-Si-Ti system at 2210 K, according to the dataset of Yang et al. [16].

In general, the agreement between calculated and experimental results is quite high, if the experimental data of Yang et al. are accepted over the conflicting data of Svechnikov et al. The experimentally observed equilibria are correctly modeled and at the temperatures given no major problems can be detected. However, there are some concerns regarding the dataset. First, the phase Mo_3Si was modeled with a composition of 25 at% Si, which is no longer supported by experimental evidence. While the experimental results of Yang et al. themselves show a Si deficiency, this effect was not known at the time this dataset was created and therefore could not be taken into account. Second, the solubility of the β-phase for Si is underestimated by the calculations, especially at higher Mo concentrations. Again, the experimental results of Yang et al. suggest a higher solubility, which is in good agreement with the binary data of the Mo-Si system, but the dataset does not accurately reflect this. Third, the phase $(Mo,Ti)Si_2$ extends beyond the corner of a tie triangle involving this phase, as can be seen in Figure 4.11 which is likely a numerical error. Finally, some Scheil solidification calculations by Yang et al., and the

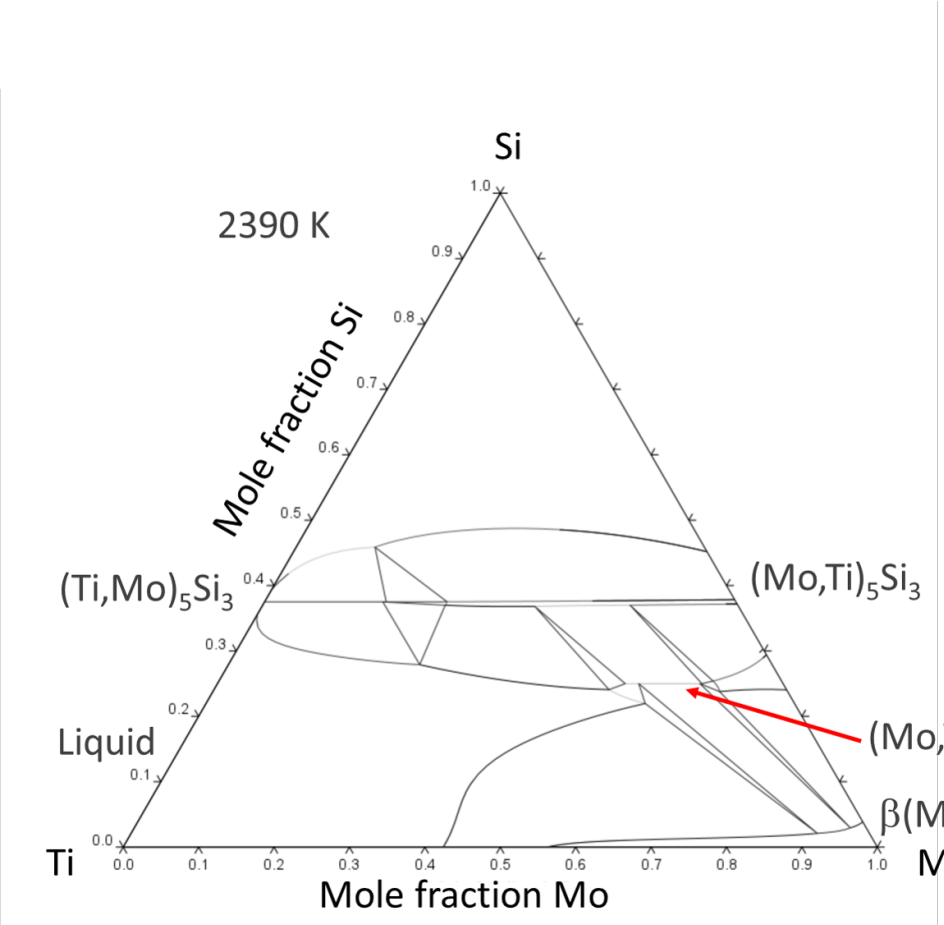

Figure 4.17.: The isothermal section of the Mo-Si-Ti system at 2390 K, according to the dataset of Yang et al. [16].

associated interpretations of the microstructural evolution of cast alloys, were done with older software that was not yet able to calculate all solidification paths correctly. Due to the complexity of this topic, it will be discussed in detail in section 5.

The dataset of Yang et al. implies the existence of a quasi-binary section Mo_5Si_3-Ti_5Si_3 due to the maximum of an edge of double saturation at 37.5 at% Si (labelled e_1 in Figure 4.12), the fact that no other edges of double saturation are cut by the section and no additional phases partially fall into the section. However, with the published dataset, it is not possible to calculate this section, probably due to a modeling or numerical error. While the phase Ti_5Si_3 is simplified as a line compound, the phase Mo_5Si_3 has been modeled to allow a homogeneity range with respect to Si. However, at high temperatures, the stoichiometric composition of the phase is not stable according to the model, while slightly Si-deficient compositions are. Therefore, at 37.5 at.% Si, there is no horizontal tie line, which is a prerequisite for the existence of the quasi-binary region. However, this behavior would be quite atypical and does not correspond to the information

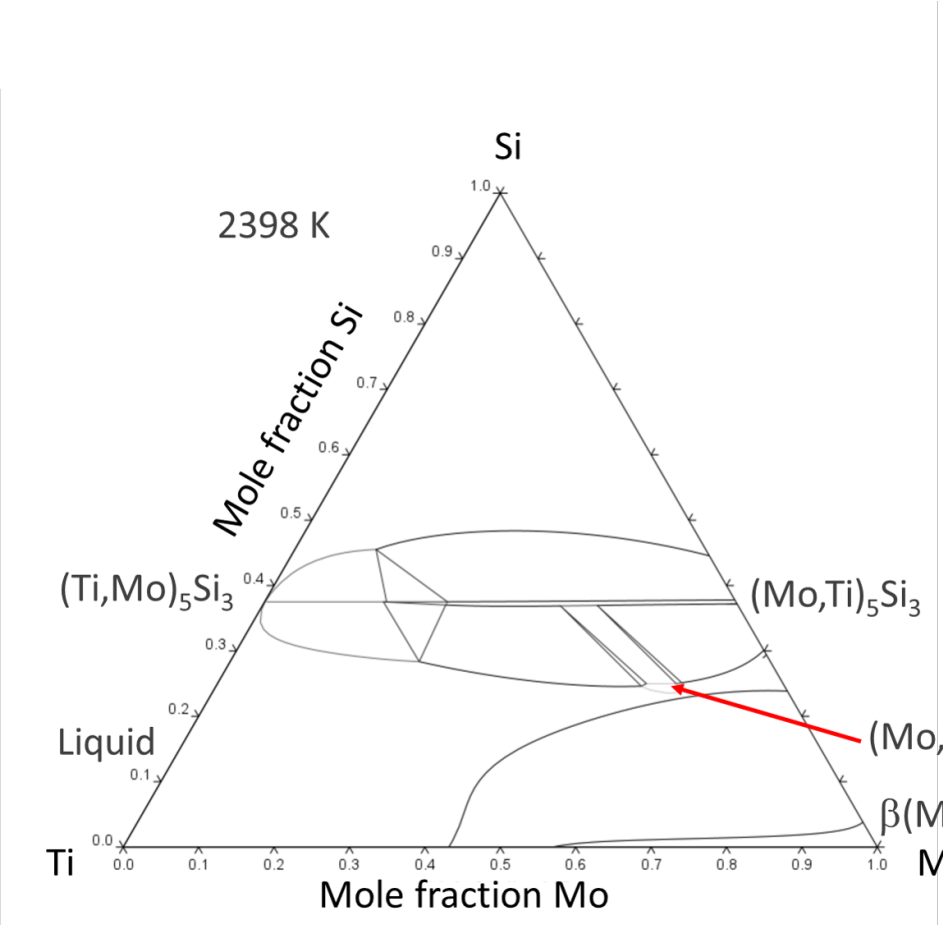

Figure 4.18.: The isothermal section of the Mo-Si-Ti system at 2398 K, according to the dataset of Yang et al. [16].

that can be derived from the Mo-Si binary, in which the phase Mo_5Si_3 melts congruently at stoichiometric composition. Thus, it seems likely that the absence of a horizontal tie line is an artifact of the model. If this phase is simplified as a line compound, as well, or the stoichiometric composition is stabilized, but all other parameters from the dataset are retained, then all criteria for a quasi-binary section are met for Mo_5Si_3-Ti_5Si_3. This hypothetical section is shown in Figure 4.22. It should be noted that none of this data, except for the melting temperatures of the pure silicides, has ever been studied experimentally, and all the lines are results of calculations only. Thus, without conflicting with the experimental data, it is quite possible to construct quasi-binary sections which look significantly different regarding the melting temperatures, or even to obtain datasets that do not include this quasi-binary section at all.

The computational result of the $MoSi_2$-$TiSi_2$ quasi-binary section, alongside experimental data by Boettinger et al., is shown in Figure 4.23. The dots that are labelled as "Tie Lines" in the graph are the respective experimental phase compositions of the investigated samples. While

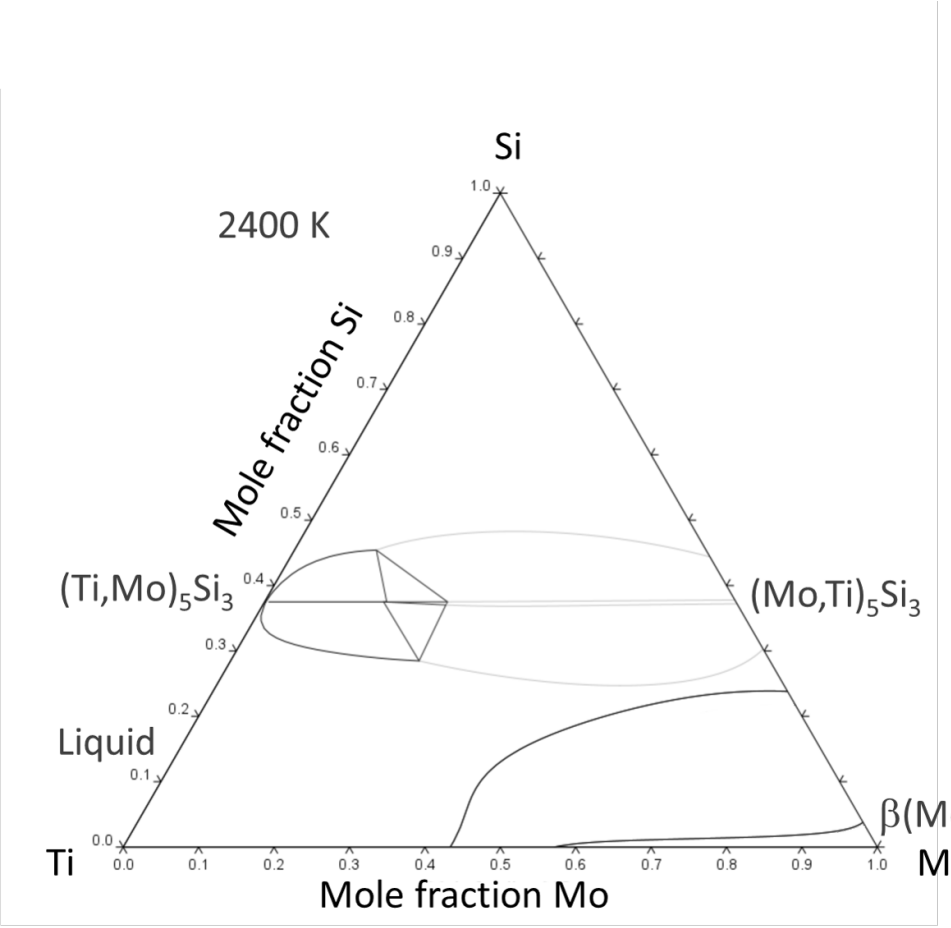

Figure 4.19.: The isothermal section of the Mo-Si-Ti system at 2400 K, according to the dataset of Yang et al. [16].

agreement between calculation and experiments is generally very high, a very unlikely phase region is present at very high Ti concentrations (visible in Figure 4.23 at x(Ti) > 0.325, for temperatures between 1480 and 1500 °C). It is likely that this is the result of a numerical error due to the model parameters of the phases.

In 2023, Daufresne et al. [133] presented the results of a reassessment of the Mo-Si-Ti system at the CALPHAD 50 conference. However, their motivation was strictly to make the descriptions of the constituent systems of the quaternary system they were working on, Mo-Si-Ti-C, compatible. As such, no new experimental data were generated, and the stated goal was to obtain a dataset that reproduced the calculations of Yang et al. while being compatible with the Ti-Si-C dataset that they accepted in their assessment. Thus, no new or significantly different results were reported for the Mo-Si-Ti system.

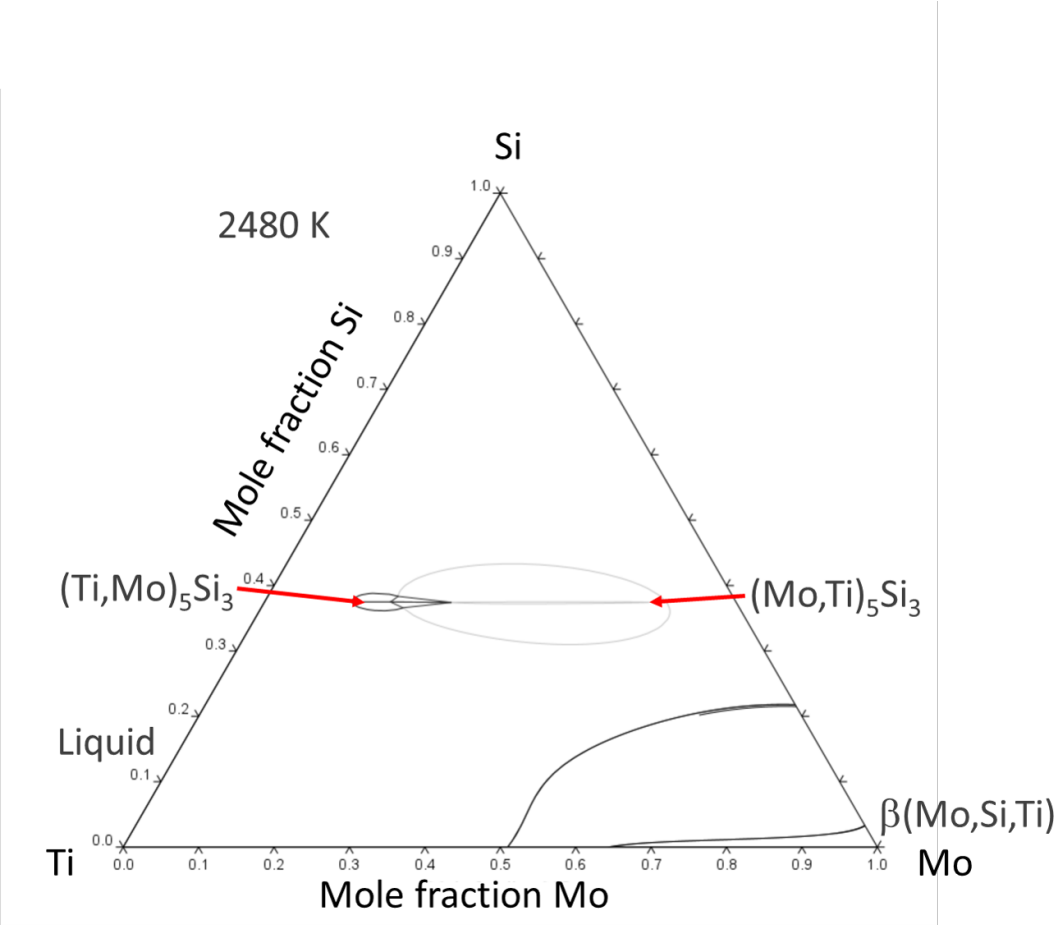

Figure 4.20.: The isothermal section of the Mo-Si-Ti system at 2480 K, according to the dataset of Yang et al. [16]. The interrupted line in the β+Liquid two-phase region is an artifact and has no impact on the results.

4.4.4. Summary and consequences

In conclusion, despite the fact that much work has been done on the Mo-Si-Ti system, there is considerable room for improvement and further experimentation. The Mo-Si binary system adopted by Yang et al. is no longer the best possible representation of the experiments and should therefore be re-evaluated. Consequently, the ternary system will also need to be updated to reflect and implement the changes in the binary system. The analysis of at least one additional isothermal section, namely at 1573 K, seems to be in order, since the experiments of Schliephake et al. have shown that certain phase equilibria may not be calculated correctly in this region of high practical relevance, as explained in chapter 1. In the range of intermediate Si contents (37.5 < x(Si) < 66.7), two significantly different sets of equilibria have been found experimentally by Yang et al. and Svechnikov et al. [17]. More work is needed to determine which of these publications, if any, is more reliable. Both seem to have been very thorough, but both also have shortcomings.

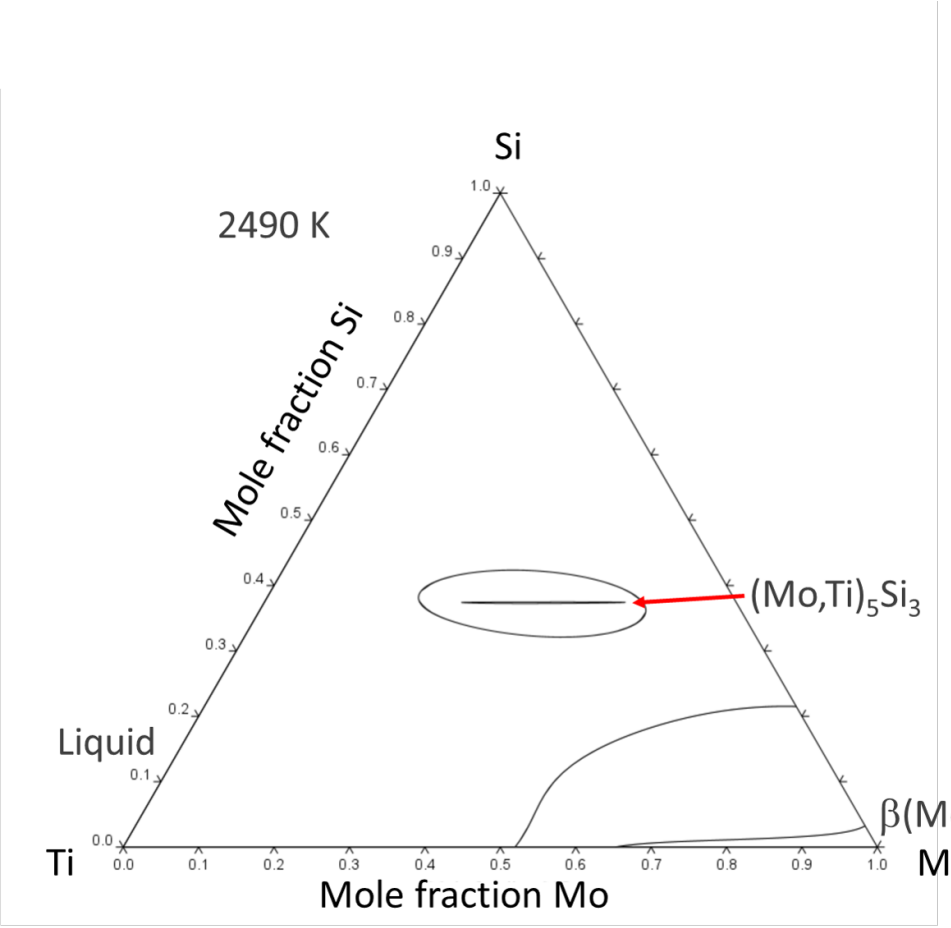

Figure 4.21.: The isothermal section of the Mo-Si-Ti system at 2490 K, according to the dataset of Yang et al. [16].

Svechnikov et al. published isopleths which are thermodynamically impossible and a quasi-binary section of $MoSi_2$-$TiSi_2$ which was later partially refuted. On the other hand, Yang et al. do not publish much evidence for their results, such as micrographs or X-ray diffractograms. It is therefore impossible to judge which data to trust until further experiments are performed. A similar lack of data applies to the liquidus projection of the system. The Yang et al. version has the distinct advantage of including the metal-rich region of the system, but it was derived only from binary data, isothermal sections, and a single isopleth. More experiments would be useful to improve the liquidus projection, especially since some of Yang et al.'s interpretations of the solidification paths of their alloys cannot be correct, as will be shown in chapter 5. One aspect that has been entirely missing is the kinetics of the system. Experiments with different annealing times and different cooling rates would be a simple way to obtain some qualitative data on the kinetics of the system.

Due to the scope of this work, not all of the suggested tasks will be attempted. It was decided

Table 4.16.: Enthalpies of formation of all relevant end members of the silicides in the Mo-Si-Ti system, according to Colinet et al. [120].

Compound	Type	Pearson symbol	Space group	ΔfE / kJmol^{-1}
A15-Mo_3Si	Cr_3Si	cP8	$Pm\bar{3}n$	-29.50
tP32-Mo_3Si	PTi_3	tP32	$P4_2/n$	-21.12
$D8_m$-Mo_5Si_3	W_5Si_3	tI32	I4/mcm	-38.44
$D8_8$-Mo_5Si_3	Mn_5Si_3	hP16	$P6_3$/mcm	-29.71
tP36-Mo_5Si_4	Zr_5Si_4	tP36	$P4_12_12$	-22.91
oI44-Mo_6Si_5	V_6Si_5	oI44	Ibam	-31.60
B27-MoSi	FeB	oP8	Pnma	-34.21
$C11_b$-$MoSi_2$	$MoSi_2$	tI6	I4/mmm	-47.89
C40-$MoSi_2$	$CrSi_2$	hP9	P6222	-45.25
C54-$MoSi_2$	$TiSi_2$	oF24	Fddd	-40.33
tP32-Ti_3Si	Ti_3P	tP32	$P4_2/n$	-48.24
A15-Ti_3Si	Cr_3Si	cP8	$Pm\bar{3}n$	-42.71
$D8_8$-Ti_5Si_3	Mn_5Si_3	hP16	$P6_3$/mcm	-74.28
$D8_m$-Ti_5Si_3	W_5Si_3	tI32	I4/mcm	-71.93
tP36-Ti_5Si_4	Zr_5Si_4	tP36	$P4_12_12$	-76.45
oI44-Ti_6Si_5	V_6Si_5 ,Ti_6Ge_5	oI44	Ibam	-72.02
B27-SiTi	FeB-b	oP8	Pnma	-74.44
C54-$TiSi_2$	$TiSi_2$	oF24	Fddd	-53.54
C40-$TiSi_2$	$CrSi_2$	hP9	P6222	-52.17
$C11_b$-$TiSi_2$	$MoSi_2$	tI6	I4/mmm	-34.96

to reassess the Mo-Si system as previously mentioned. In addition, the isothermal section of the system at 1573 K will be investigated in detail. Furthermore, the kinetics of the system will be studied by a two-step heat treatment in which the same specimens are first furnace cooled, then briefly annealed again, and then quenched. In addition, the microstructures of cast samples will be analyzed to test the suitability of the liquidus projection and to highlight its applicability and shortcomings. Finally, these data, as well as the most reliable literature data, will be used to update the ternary data set, including the reassessed Mo-Si system. All of this work will, however, be restricted to the metal-rich area of the system which is relevant for gas turbine applications.

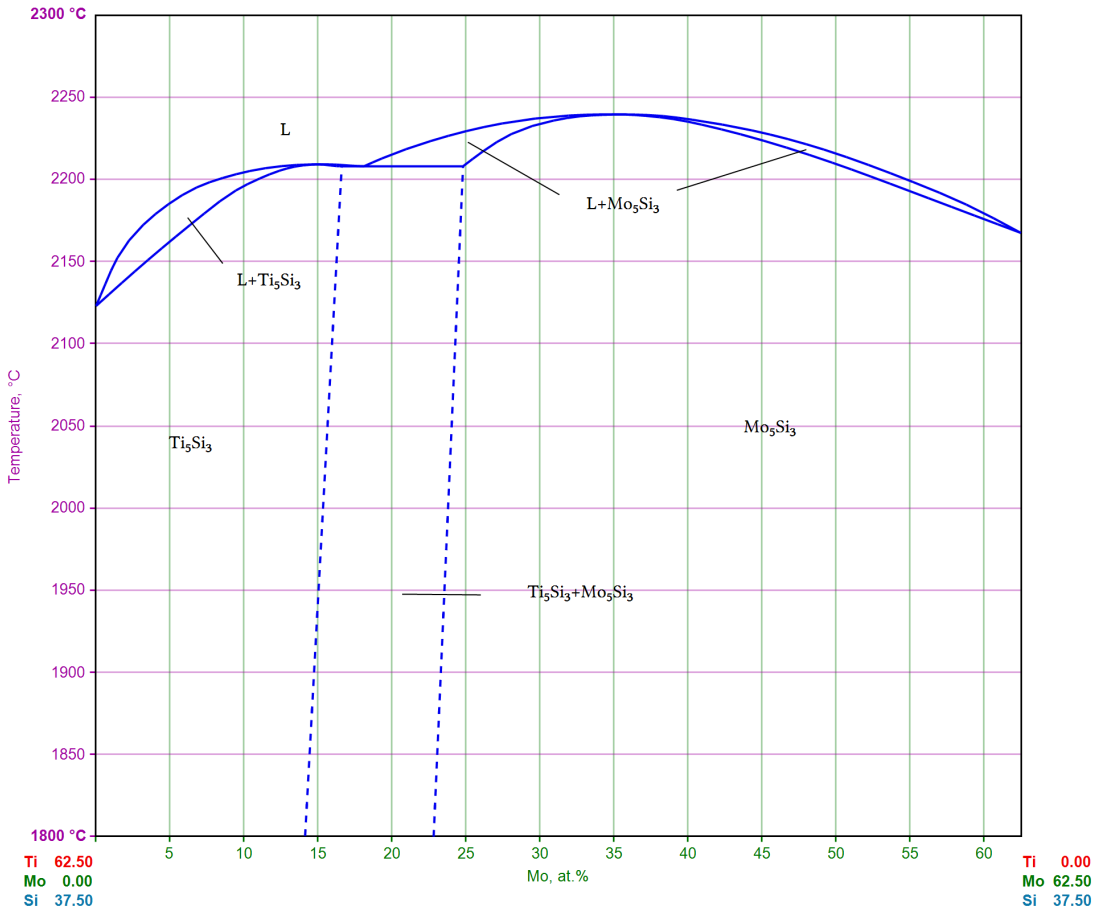

Figure 4.22.: The quasi-binary section Mo_5Si_3-Ti_5Si_3 calculated from the dataset of Yang et al. if the phase Mo_5Si_3 is simplified as a line compound. Figure from [119].

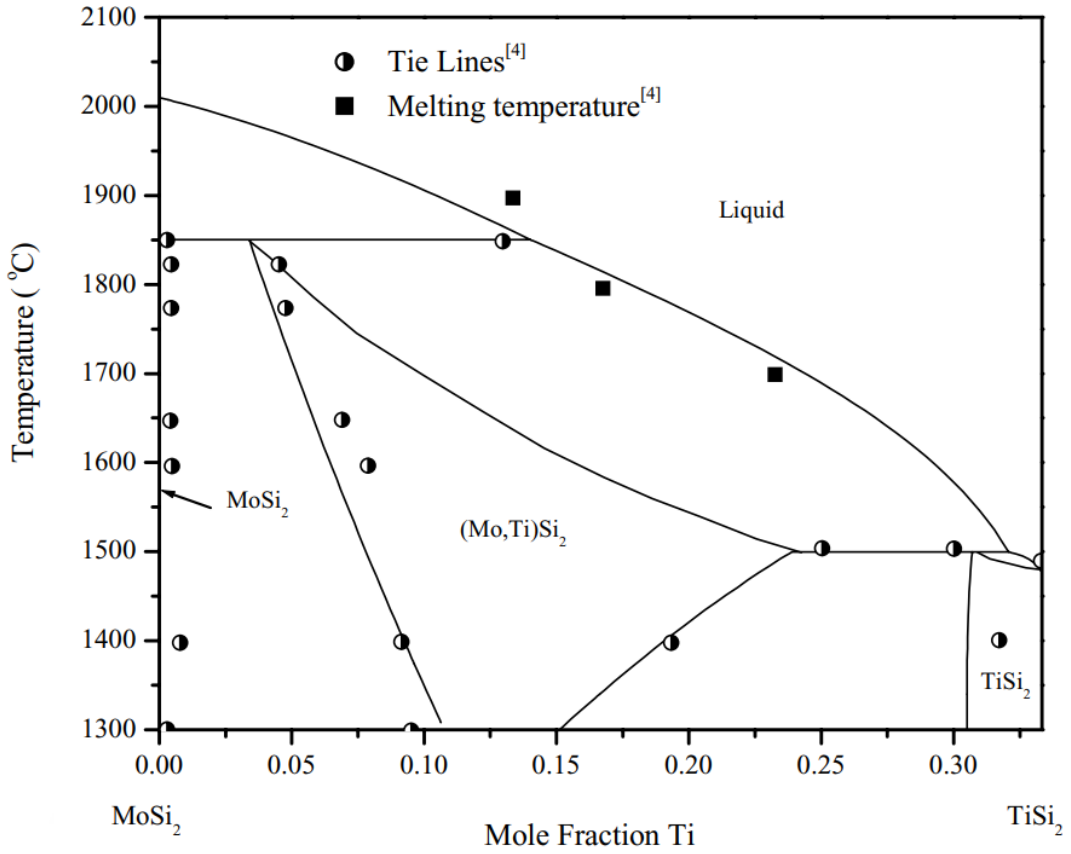

Figure 4.23.: The quasi-binary section $MoSi_2$-$TiSi_2$ from Yang et al. [16], alongside the experimental results from Boettinger et al. [124]. Image taken from [16].

5. Scheil solidification

Scheil solidification is a mathematical model to describe non-equilibrium solidification under the assumption that no diffusion takes place in the solid phases formed. Also called Scheil-Gulliver solidification, it goes back to G. H. Gulliver, who described phenomenologically general assumptions on non-equilibrium solidification of alloys [134]. In 1942, based on Gulliver's work, E. Scheil formulated a mathematical model to describe the distribution of elements in an alloy during non-equilibrium solidification [135]. In the years since, the theory has been further developed and is now a powerful tool for calculating solidification and predicting microstructure. Detailed explanations can be found, for example, in the books by Porter, Easterling and Sherif [136] and by Cantor [137].
The following chapter is divided into two sections. First, the general assumptions and equations of Scheil solidification are explained. The general cases and limits of its applicability are discussed. In the second section, the application of the Scheil model to the Mo-Si-Ti system will be discussed using the publication by Yang et al. [16] as an example. It will be shown that not all Scheil solidification calculations have been interpreted completely correctly and that a re-evaluation of the results is in order.

5.1. General assumptions, equations and consequences

5.1.1. General assumptions

Scheil solidification requires three conditions:

1. No diffusion in the solid phase
2. Infinitely fast diffusion in the liquid phase
3. Thermodynamic equilibrium at the solid-liquid interface

In earlier models, the fourth condition was that the solidus and liquidus lines were linear, but with the development of modern numerical methods such as CALPHAD, this simplification is no longer necessary and is usually discarded. The first three conditions each lead to significant consequences. The first one means that once a solid phase has formed, it will retain its

composition and undergo no transition of any kind, including the dissolution of concentration gradients. The second condition leads to a homogeneous distribution of all elements in the liquid phase, so no local concentration profiles are ever formed at any point of the solidification. The third condition means that at the interface, the current equilibrium phase diagram at the reaction temperature and composition of the remaining liquid and formed solid remain valid.
With these assumptions, it is possible to calculate and predict highly inhomogeneous microstructures, such as those often formed during casting or rapid prototyping. When the first solid is formed, the liquid is depleted of the elements that entered the solid. Subsequently, the next solid that forms will have a different composition according to the lever rule. At each point, the equilibrium phase diagram is valid, but since diffusion cannot occur in the solid phase, each solid formed retains its individual composition. The result is a layered crystal with a composition gradient from the nucleus to the grain boundary. Note that the material may still be polycrystalline due to the formation of multiple nucleation sites.

5.1.2. Scheil-Gulliver Equations

If the assumption that the liquidus and the solidus lines are linear, analytical equations for the composition of the liquid C_L and solid phases C_S can be derived. As mentioned, numerical solvers can calculate non-equilibrium solidification without this simplification, but it is useful to derive the equations for a deeper understanding of the process. This derivation is well explained in the book by Porter, Easterling and Sherif [136], but because of its importance, it is summarized below. First, the partition coefficient k is defined:

$$k = \frac{C_S}{C_L} \tag{5.1}$$

In an alloy with the mean total concentration C_0 of a given element, the first solid to form has the concentration kC_0 and the volume fraction f_S. The volume fraction of the liquid fraction is f_L, and by definition

$$f_S + f_L = 1 \tag{5.2}$$

Since the total amount of the respective element must be constant, the following equation applies:

$$(C_L - C_S)df_S = f_L dC_L \tag{5.3}$$

This equation, combined with equations 5.1 and 5.2 yield:

$$C_L(1-k)df_S = (1-f_S)dC_L \tag{5.4}$$

The boundary conditions that no solid phase is present at the start ($f_S(0) = 0$) and, consequently, the concentration of the respective element in the liquid phase is equal to the overall composition in the alloy ($C_L(0) = C_0$), can be used to integrate equation 5.4:

$$\int_0^{f_S} \frac{df_S}{1-f_S} = \frac{1}{1-k} \int_{C_0}^{C_L} \frac{dC_L}{C_L} \tag{5.5}$$

This yields the **Scheil-Gulliver equations** for the compositions of the liquid and solid phases during non-equilibrium solidification:

$$C_S = kC_0(1-f_S)^{k-1} \tag{5.6}$$

$$C_L = C_0 f_L^{k-1} \tag{5.7}$$

5.1.3. Consequences

The most important application of the Scheil-Gulliver equations and their modern numerical successors is the prediction of microstructures under conditions of very rapid cooling. These conditions are typically encountered in quenching from the liquid phase, as in arc melting or in rapid prototyping ("3D printing") of metallic alloys. In these cases, the phases formed can often be predicted with fairly high accuracy. An important consequence of Scheil solidification is that not all invariant reactions, and thus solidification paths, can take place due to the practical absence of diffusion in the solid. For example, in a peritectic reaction, the solid phase is an educt of the reaction. If a peritectic reaction $\alpha + L \rightleftarrows \beta$ is encountered during solidification, this reaction could in principle occur (due to the condition that the solid-liquid interface is in local equilibrium). However, the solid phase α at the interface is subsequently transformed into the product solid phase β, which then acts as a diffusion barrier and shields the remaining α phase from contact with the liquid phase. Therefore, at most one monomolecular layer of β can be formed before the peritectic reaction terminates. For this reason, no invariant reaction that has a solid phase on the educt side can take place in any significant way. Instead, the composition of the liquid phase continues to change, until a reaction with only liquid on the educt side (such as a eutectic reaction) is reached.
The assumptions of Scheil solidification are not always fully met in reality. For example, even in

slowly diffusing systems, the condition that no diffusion at all can take place is often too strict, and therefore concentration gradients in the formed solid are rarely as pronounced in reality as the model predicts. In addition, according to the calculation, solidification almost always ends with a eutectic structure, because the non-equilibrium solidus line sooner or later coincides with a eutectic reaction, if one is present in the system. Again, this is often not the case in reality. Finally, classical Scheil solidification calculations fail when elements with very small atomic radius are involved, which can often diffuse freely. In particular, the solidification of steels cannot be accurately described due to the presence of small interstitial carbon atoms and the importance of peritectic reactions. In reality, diffusion of such elements is hardly hindered even during quenching, which is not reflected by classical Scheil solvers, which changes the solidification behavior significantly. However, in recent years, new models have been developed to solve this problem, for example allowing partial redistribution of fast diffusers [138]. New versions of most CALPHAD software take these models into account and allow to define certain elements as fast diffusers, which allow infinitely fast diffusion of these elements in the solid phase.

5.2. Scheil solidification calculations in the Mo-Si-Ti system

In their "2003 publication", Yang et al. [16] used their dataset to show that the microstructures of selected as-cast samples can be accurately explained by Scheil solidification calculations. However, two of the three examples given are not entirely accurate because they assume reactions that cannot take place. These examples are discussed below, and a corrected version of the solidification path obtained in a newer version of Thermo-Calc (ver. 2021b) is presented.

5.2.1. Example 1: 40Mo-20Si-40Ti

The microstructure of the sample 40Mo-20Si-40Ti (all values in at.%) as published by Yang et al. is shown in Figure 5.1a. There are primary grains of the β phase as well as of Mo_3Si surrounded by a lamellar structure of β+Ti_5Si_3 and possibly β+Mo_3Si, although the latter is not specifically indicated and the resolution of the image is not high enough to decide for certain if this structure is present. According to the corresponding Scheil solidification calculation from the same publication, shown in Figure 5.1b, the sample is in the region of primary solidification of β. This is supposed to be followed by the peritectic reaction L+β $\rightleftarrows$ Mo_3Si. This is then succeeded by the transition reaction L+Mo_3Si $\rightleftarrows$ β+Ti_5Si_3, which cannot take place because it only occurs at a single point. The rest of the alloy solidifies according to the eutectic reaction L $\rightleftarrows$ β+Ti_5Si_3.

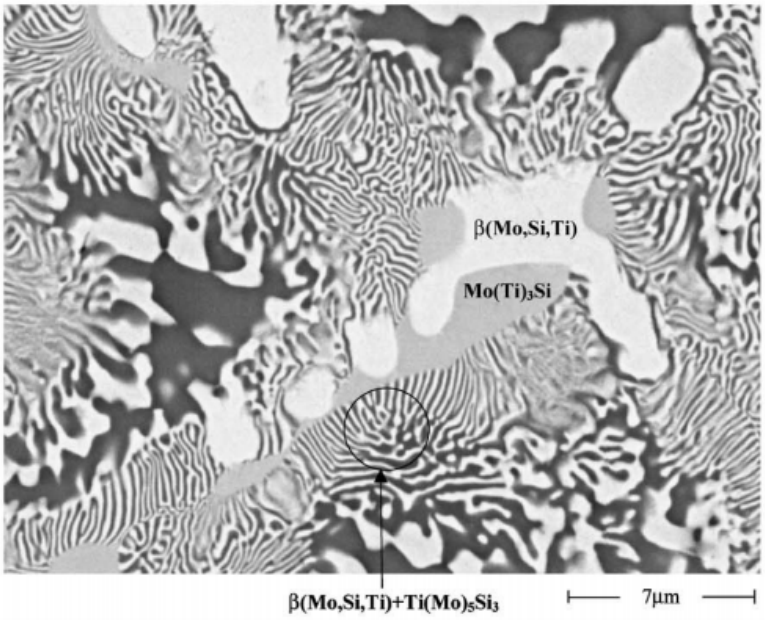

(a) As-cast microstructure

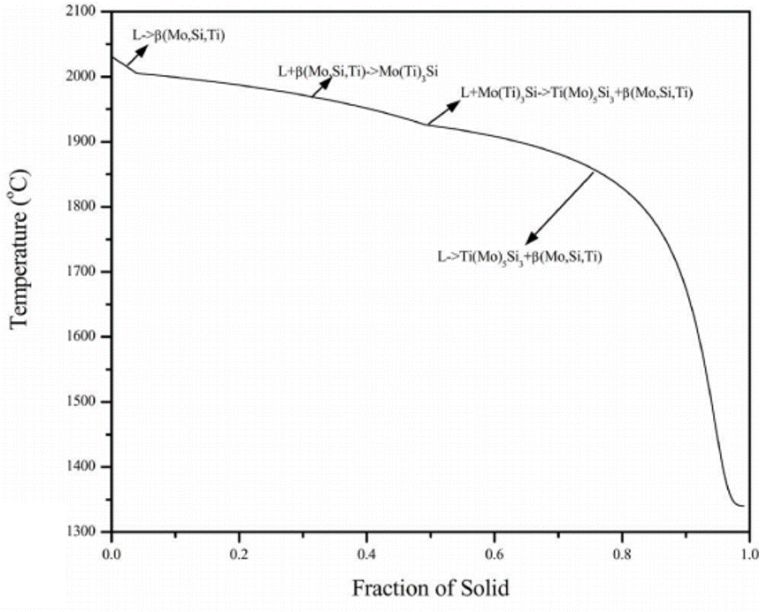

(b) Scheil solidification calculation

Figure 5.1.: The microstructure of the sample 40Mo-20Si-40Ti in the as-cast state and the Scheil solidification calculation of this composition, according to the publication of Yang et al. [16].

Following the explanation from the previous section, this calculation seems doubtful because of the proposed peritectic reaction, which would involve a rather large fraction of the solid phase. The result of the same calculation with a more recent solver (Thermo-Calc 2021b) is shown in Figure 5.2. Here, the first solid to form is Mo_3Si, which is inconsistent with Yang et al.'s claim of primary solidification of β. This is unlikely to be related to solver issues, since the composition 40Mo-20Si-40Mo is clearly in the region of primary solidification of Mo_3Si according to Yang et al.'s own liquidus projection. Why Yang et al. come to a different result is not clear. Primary solidification is followed by the eutectic reaction L $\rightleftarrows$ β+Mo_3Si, not by a peritectic reaction involving these phases. While this reaction is present in the system, the line of double saturation has a eutectic character in this region. This is supported by the partial phase fraction diagram shown in Figure 5.3. Here the mole fraction of the β phase is plotted against the total mole fraction of solid formed during Scheil solidification. It can be clearly seen that the amount of β is steadily increasing, which means that a formation reaction is taking place; if it were the educt of the peritectic reaction proposed by Yang et al, this phase would be consumed. This reaction is followed by the transition reaction L + Mo_3Si $\rightleftarrows$ β+Ti_5Si_3, but since it only happens at one specific temperature and composition, it is not displayed by the software. This is followed by the eutectic reaction L $\rightleftarrows$ β+Ti_5Si_3, which is indeed correctly predicted by Yang et al. It should be noted that the course of the graph plotted by Yang et al. is almost identical to that calculated by the author of this work, with the exception of the region of primary solidification. This strongly suggests that the Pandat version used by Yang et al. was able to calculate the solidification reactions correctly in principle, but the labeling was not always correct.

5.2.2. Example 2: 40Mo-25Si-35Ti

Another alloy produced and discussed by Yang et al. is 40Mo-25Si-35Ti. The microstructure, as published by Yang et al. in Figure 5.4a, shows large, continuous grains of both Mo_5Si_3 and Mo_3Si. In addition, lamellar structures of β+Mo_3Si and of β+Ti_5Si_3 are visible. The Scheil solidification calculation of this composition from the same publication is shown in Figure 5.4b and raises questions. According to it, Mo_5Si_3 is the first primary solidified phase, which agrees with the liquidus projection proposed by Yang et al. After primary solidification, another peritectic reaction, L+$Mo_5Si_3$$\rightleftarrows$$Mo_3Si$, is supposed to take place for much of the solidification process. For the same reasons as above, it is unlikely that a peritectic reaction would have such a strong influence during Scheil solidification. This is followed by secondary solidification of another single phase, Mo_3Si, but the mechanism how and why the liquid composition would fall in this region is not elaborated. Finally, the rest of the alloy solidifies along the transition reaction L+$Mo_3Si$$\rightleftarrows$ β+Ti_5Si_3. As noted above, transition reactions occur only at one point at a fixed

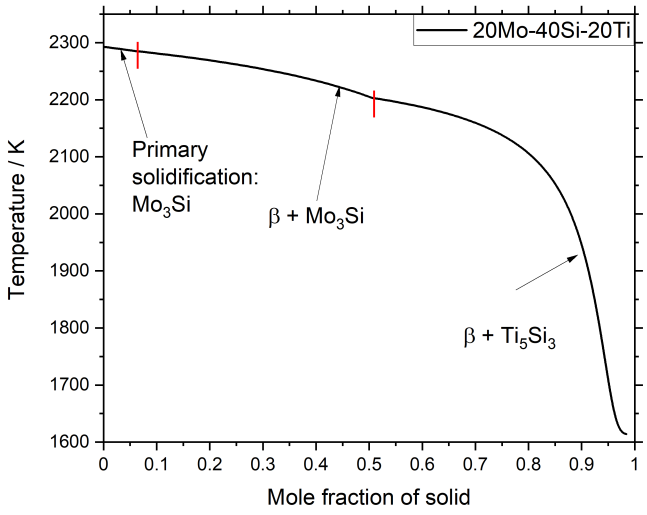

Figure 5.2.: The Scheil solidification of the alloy 40Mo-20Si-40Ti made with a newer solver.

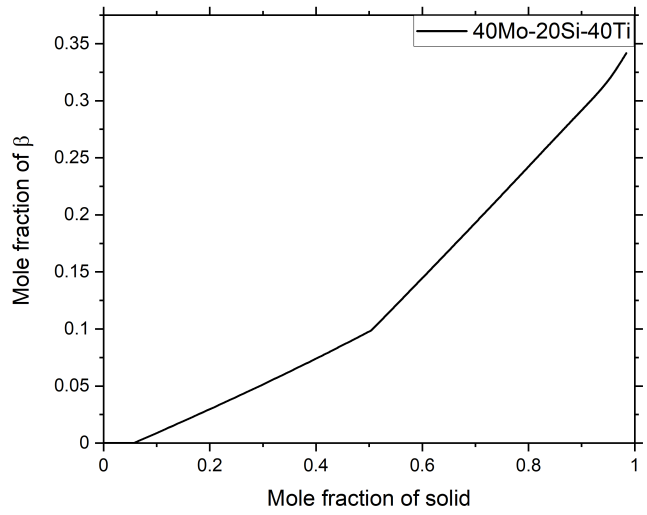

Figure 5.3.: The mole fraction of the β phase over the mole fraction of solid formed during Scheil solidification of the alloy 40Mo-20Si-40Ti.

temperature and composition, so this is impossible. The accompanying text in the paper claims that the *"rest of the solidification path is the same as that of the $Mo_{40}Si_{20}Ti_{40}$ alloy"* would indeed be the correct interpretation, but this is not what Yang et al.'s own calculation shows. Again, it is likely that the calculation was correct, but the labeling was not.

The recalculation of the Scheil solidification of this composition using Thermo-Calc 2021b is shown in Figure 5.5. Again, the first solid to form is primary solidified Mo_5Si_3. The peritectic reaction L+Mo_5Si_3⇄Mo_3Si is indeed met and indicated, but it occurs only for such a short time that it appears as little more than a dot on the indicated red vertical bar. Immediately after this reaction, the sample composition falls into the region of primary solidification of Mo_3Si, because the peritectic reaction cannot be "followed" under Scheil conditions. This phase is formed until the liquid composition reaches the eutectic trough of L⇄ β+Mo_3Si. This reaction continues until the transition reaction L+Mo_3Si⇄ β+Ti_5Si_3 is reached, which is not displayed again by Thermo-Calc because it does not affect the microstructure or solidification. This reaction is followed by the eutectic reaction L⇄ β+Ti_5Si_3, which is actually identical to the rest of the solidification path of 40Mo-20Si-40Ti.

The rather complex solidification path of the alloy can be better understood by plotting the liquid composition on the liquidus projection of the system, as shown in Figure 5.6. The composition of the sample, indicated by the black square, is in the region of primary solidification of Mo_5Si_3. As solid is formed, the remaining liquid composition, indicated by the red line, changes until a line of double saturation is reached. Here this line has a peritectic character, that is, L+Mo_5Si_3⇄Mo_3Si. As a result, this reaction occurs, but only very briefly. The reaction stops quickly due to the lack of solid educt under Scheil conditions, and the remaining liquid composition falls into the region of primary solidification of Mo_3Si. This, rather than the occurrence of a peritectic reaction as proposed by Yang et al., is the reason why both Mo_5Si_3 and Mo_3Si take the form of large, continuous grains in the microstructure - the alloy composition actually falls into two separate regions of primary solidification. Again, the liquid composition changes until another line of double saturation is reached. This time it has a eutectic character, L⇄ β+Mo_3Si. This reaction is "allowed" under Scheil conditions, so the line is followed until the transition reaction takes place. As explained above, this transition reaction itself has no effect on solidification, but it does lead to another line of double saturation, L⇄ β+Ti_5Si_3. Since this is also a eutectic reaction and there are no solid phases on the educt side, this line can be followed. It ends at a binary eutectic point in the Ti-Si system, which terminates solidification.

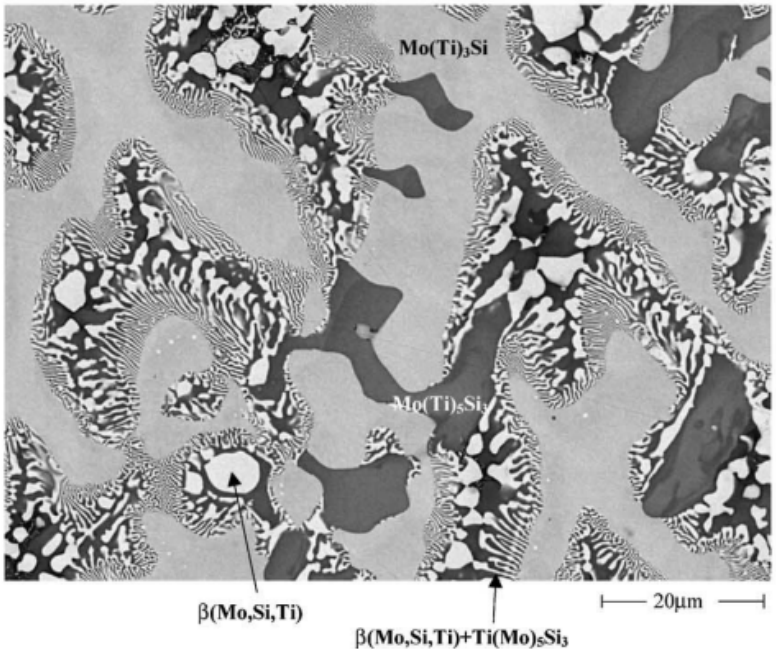

(a) As-cast microstructure

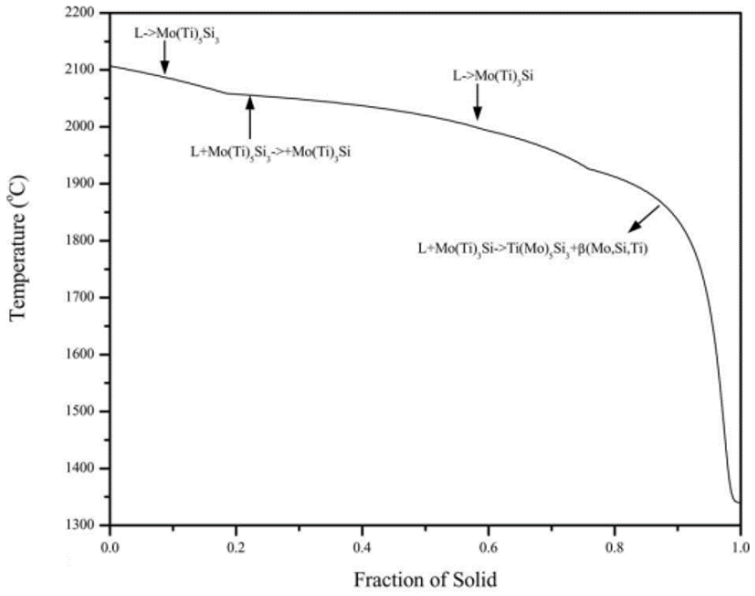

(b) Scheil solidification calculation

Figure 5.4.: The microstructure of the sample 40Mo-25Si-35Ti in the as-cast state and the Scheil solidification calculation of this composition, according to the publication of Yang et al. [16].

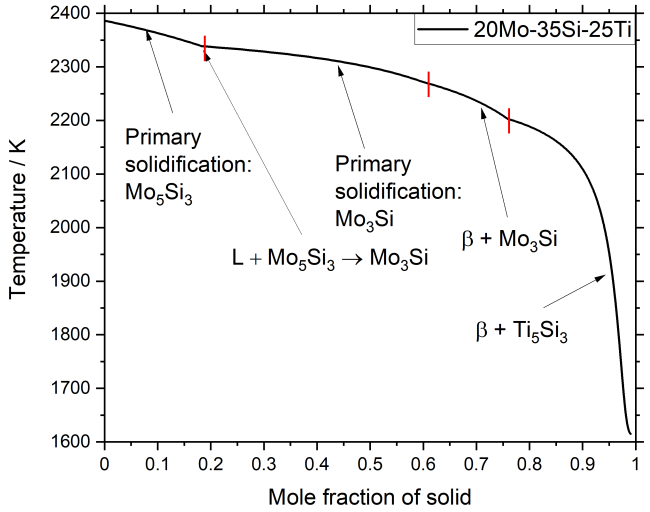

Figure 5.5.: The Scheil solidification of the alloy 40Mo-25Si-35Ti made with a newer solver.

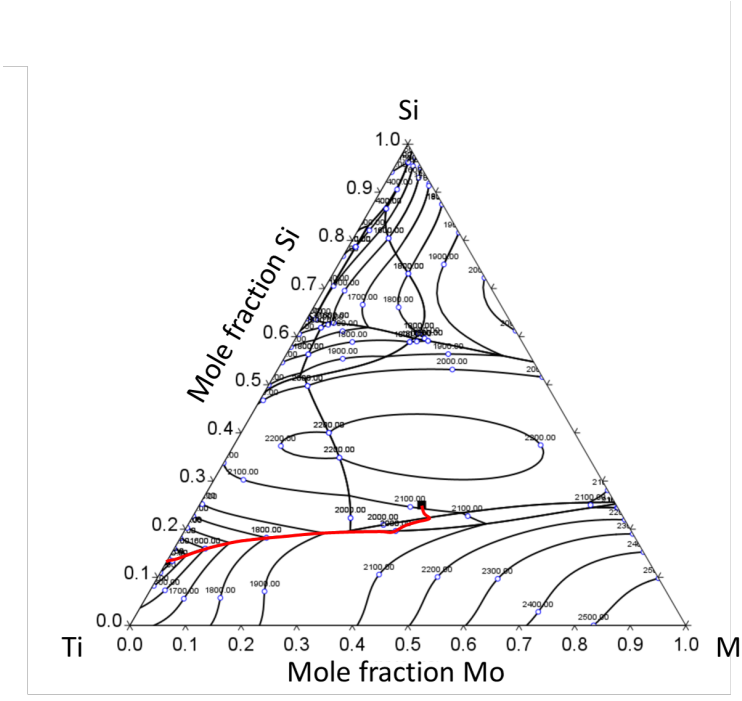

Figure 5.6.: The Scheil solidification path of the alloy 40Mo-25Si-35Ti shown on the liquidus projection.

5.2.3. Conclusion and Consequences

The discussion in this chapter has shown that the interpretation of as-cast samples by Yang et al. [16] according to the Scheil solidification model is not always correct. Often, due to errors in the solvers that cannot be reproduced with modern software, reactions have been postulated that cannot have a significant influence on solidification, as explained in subsection 5.1. With Thermo-Calc 2021b, the solver can distinguish between invariant reactions that have no effect on the microstructure, such as transition reactions, which are completely ignored, those that terminate after a very short time, such as peritectic reactions, and those that can freely occur, such as eutectic reactions. As a result, predictions with this software are much more realistic and accurate. However, not all inaccuracies of Yang et al. can be explained by the software alone. For example, it is unclear why the result that the alloy 40Mo-20Si-40Si showing primary solidification of the β phase was trusted, although the composition is clearly in the region of primary solidification of Mo_3Si according to Yang et al.'s own liquidus projection. Similarly, Pandat's result showing that the final solidification path of 40Mo-25Si-35Ti occurs via a transition reaction was not rejected, but rather misinterpreted in a way that ended up being correct. For these reasons, the liquidus projection of the Mo-Si-Ti system warrants dedicated examination. Two of the three examples given by Yang et al. are raising questions, so it is unclear which information is reliable. Ideally, a complete study would include the measurement of liquidus temperatures of several samples, which could be used to optimize the dataset. However, this alone is a considerable task, well beyond the scope of this dissertation. Instead, it was decided to analyze a number of selected samples in the as-cast state and compare the microstructure with Scheil solidification calculations. In this way, a qualitative statement can be made regarding the viability of the liquidus projection and the reactions proposed by Yang et al. While this does not provide data that can be directly used in a reassessment, it does indicate which parts of the liquidus projection need to be further investigated in future studies.

6. Experimental results and discussion

The experimental investigations of this thesis can be divided into three sections. In the first section of this chapter, general methods that were developed during this work are presented and discussed. This included the development and characterization of a novel quenching furnace and the determination of the purity of the raw materials used in this work. The second section of this chapter deals with the experiments in the binary system Mo-Si. Here, the focus was on investigating the composition of the Mo_3Si phase to verify the Si deficiency reported in the literature and found in preliminary experiments. The third section concerns the ternary Mo-Si-Ti system and represents the main effort of this work. Throughout this section, compositions are generally given in at.% unless otherwise specified. This is true both when phase compositions are given in tables, etc., and when sample compositions are given in the form aMo-bSi-cTi, where a, b, and c represent the amount of the respective element. Any SEM images shown in this chapter were taken in the BSE mode, unless specified otherwise. Regarding the annotation of the ternary phase diagrams, only the phases present in the metal-rich region ($x(Si) \leq 37.5$ at.%) are labeled in the figures, since this was the focus of this work and no samples richer in silicon were prepared.

6.1. Development and characterization of a novel type of quenching furnace

Early in the project, it was decided to quench each prepared sample to ensure that the analyzed frozen-in state was as close to high temperature equilibrium as possible. Although the Mo-Si-Ti system is highly refractory and slow diffusion is expected, it was possible that changes in phase composition could occur during the time required for typical furnace cooling. In fact, this was thought to be one of the main reasons why initial samples showed improbable phase combinations or even an excessive number of different phases, clearly indicating that the samples could not be in equilibrium. However, typical quenching furnaces allow only a small number of samples at a time (usually only one or two samples per treatment), have very limited time constraints (maximum annealing times of about 48 h), and tend to expose the samples to ambient air during quenching. The reason for this is that in typical quenching furnaces, the samples are placed in crucibles suspended on platinum-rhodium wires. These wires are melted in a controlled manner

when the samples are dropped into the quench medium. If these wires are exposed for too long to the annealing temperatures required for the purpose of this thesis, they tend to break prematurely. The maximum weight that can be supported in this way is also quite limited, so only one or two samples can be annealed at a time. Finally, the wires are very expensive and a consumable. All of these factors lead to the conclusion that while quenching the samples is necessary, typical commercial quenching furnaces are not suitable for the amount of samples expected to be analyzed over the course of the project. For these reasons, it was decided to issue a tender to furnace manufacturers to develop a new type of quenching furnace that would meet the specific requirements of this project. The key requirements were as follows:

- The furnace must allow annealing temperatures of up to around 2000 K.
- The atmosphere within the furnace must be inert, i.e. high purity argon or nitrogen.
- Samples must not be exposed to ambient air at any point.
- Heat treatment of at least four spherical specimens of 1 cm diameter at once must be possible.
- The quenching medium should be water.

The company HTM Reetz GmbH [139] developed the most convincing concept. Instead of a vertical furnace with a wire-suspended crucible, they designed a furnace that was essentially a typical horizontal tube furnace, but added a compartment for quenching samples within the apparatus. This was achieved by adding a water reservoir and a quenching compartment to the furnace, as shown in the schematic in Figure 6.1. During annealing, the samples are placed in the tube as usual. Immediately before quenching, the water reservoir is filled with water. Finally, by tilting the entire apparatus 90°, the samples and the water from the reservoir are dropped into the quenching chamber. A metal "bridge" extending from the tube to the quench compartment ensures that the samples cannot fall anywhere other than where they are intended to fall. Because this is a closed system, except for the brief period when water is added to the reservoir, environmental contamination is kept to an absolute minimum. Due to the high mechanical stress caused by tilting the furnace for quenching, the typical materials for high temperature heating elements, such as $MoSi_2$, cannot be used because of their brittleness. Instead, continuous coils of pure Mo were used as the heating element. To prevent evaporation of the material, the heating element is embedded in oxygen getter material, the composition of which is unknown due to manufacturer compliance issues.

Due to the novelty of the design, rigorous testing was conducted to verify that the furnace met specifications and rework was initiated where necessary. These tests included, for example, ensuring that the amount of water vapor generated during quenching was not sufficient to affect

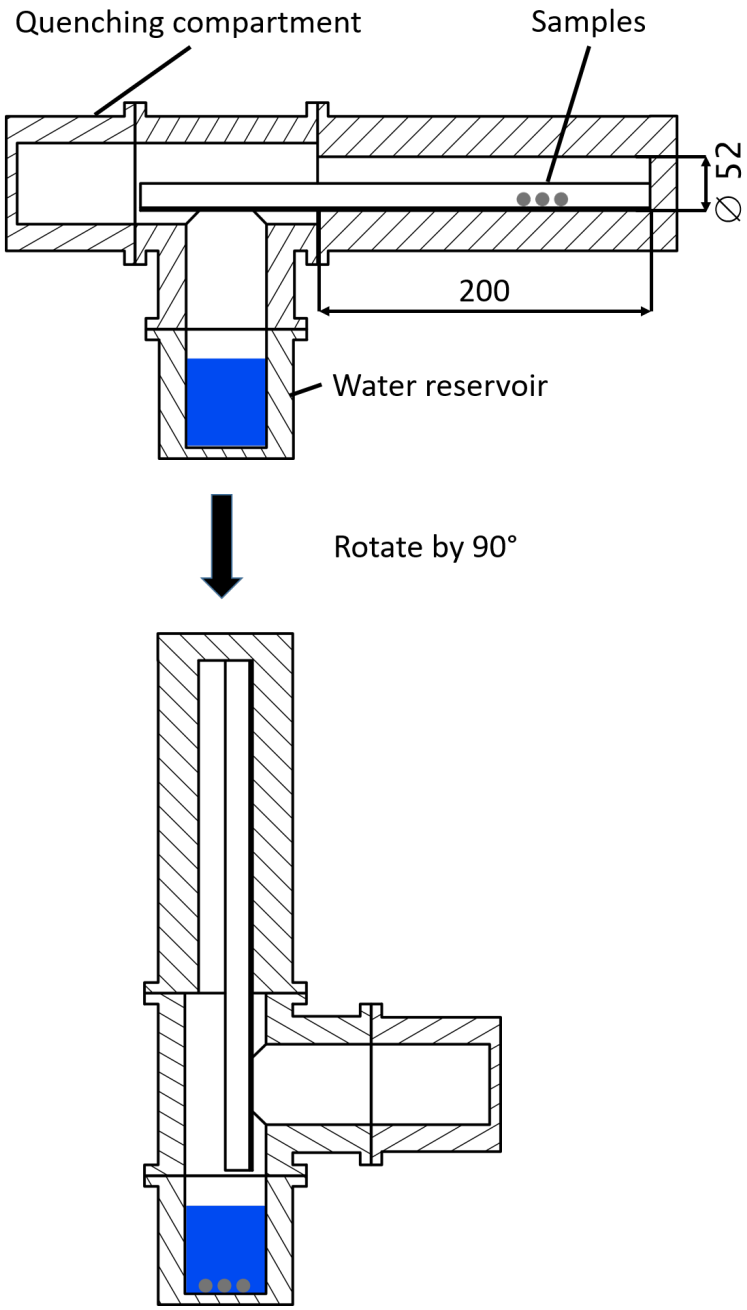

Figure 6.1.: A schematic drawing of the furnace when quenching. The top image shows the furnace shortly before quenching, when the samples are still in the tube and the water reservoir has already been filled. The bottom image shows the furnace after quenching, when the whole device has been tilted by 90° and both the water and the samples were dropped into the quenching compartment.

the hot alumina tube in a way that could damage it. Another important specification was air-tightness. The design of the alumina tube had to be significantly modified from that of conventional furnaces to ensure that the ceramic could withstand the stress of rapidly tilting the hot apparatus for quenching. For this reason, the alumina tube is interrupted rather than continuous, otherwise the temperature gradient between the heated zone and the relatively cool zone at the exit of the furnace would fracture the brittle material. While this design was found to be necessary when testing the furnace, it created the problem that gas tightness could only be ensured in a flowing gas atmosphere. The interrupted tube also meant that the volume of the furnace that had to be purged with inert gas each time the apparatus was opened was much larger than for conventional tube furnaces. Therefore, a series of measurements were made to determine the purging time required to purge the system of residual oxygen so that heat treatment could begin. To do this, the furnace was opened and exposed to the environment as it would be for a normal sample change. After closing, it was evacuated to a residual pressure of 20 mbar and filled with high purity argon (99.9999% purity) to atmospheric pressure. This process was repeated three times to remove the oxygen as efficiently as possible. Finally, a gas flow of 0.2 standard liters per minute (slm) was selected to operate the apparatus. The oxygen concentration was measured continuously with an oxygen probe (E2010 from Zirox GmbH) and the time was measured until the oxygen concentration in the effluent was equal to the oxygen concentration in the process gas. As shown in Figure 6.2, a purging time of about 20 h was found to be necessary to ensure a complete purging of the furnace atmosphere.

The next step was to measure the temperature profile of the furnace. As mentioned above, it was required that at least four samples could be annealed at a time, which means that a (nearly) constant temperature had to be maintained over a minimum length of about 60 mm. To measure the temperature in the tube, the T-connector that connects the furnace to the water tank and quench chamber was removed and replaced with a flange with a hole for a type S thermocouple. Since this thermocouple could be inserted into the tube at any depth, the actual temperature could be measured as a function of the probe position in the tube. The furnace was purged as previously described and the temperature was set to 1273 and 1673 K, respectively. Once the control thermocouple used to regulate the operating temperature showed the nominal temperature, the actual temperature in the tube was measured. The result of these measurements is shown in Figure 6.3. The nominal temperatures are drawn as a dashed line, the points are the measured temperatures. The red and black data correspond to the nominal temperatures of 1673 and 1273 K respectively. It can be seen that the temperature drops quite rapidly towards the outlet of the tube (corresponding to the low probe positions). However, after about 75 mm, the actual temperature is very close to the nominal value in both cases and does not vary much with the probe position. Thus, it can be concluded that only the 7-8 cm closest to the exit of the tube is unsuitable for heat treatment, while the zone of constant temperature exceeds the minimum requirements. In

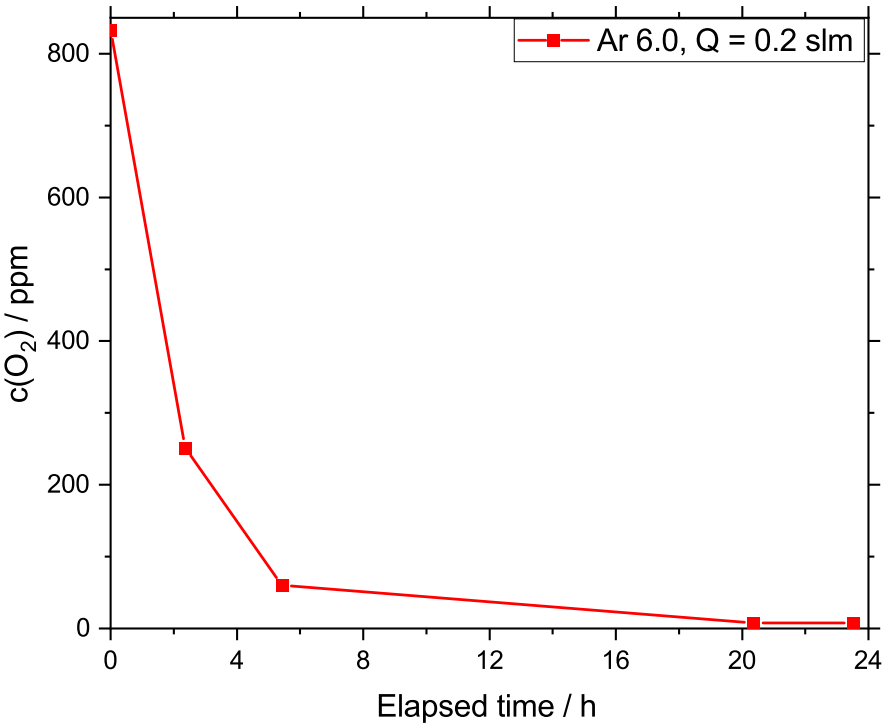

Figure 6.2.: A measurement of the oxygen concentration within the furnace over time. The measurement was started immediately after the operating gas flow of 0.2 slm was turned on. The process gas was argon 6.0 (99.9999% purity).

addition, because the nominal and actual temperatures are in quite good agreement, the furnace user can be confident that the temperature displayed by the control thermocouple is an accurate sample temperature.

As a further test, the cooling conditions of the novel furnace were investigated in the case of uncontrolled furnace cooling. This is practically relevant when samples have no specific cooling requirements, e.g. quenching or cooling at a specific cooling rate. For this purpose, the furnace was purged as described and heated to a temperature of 1573 K. Once this temperature was reached and maintained, the power to the heating elements was turned off and the furnace was cooled "naturally". The temperature of the control thermocouple was measured as a function of time. The result of this experiment is shown in Figure 6.4. The temperature drops very quickly at the beginning and then at a decreasing rate. This is an exponential behavior which fits the equation

$$T = 299.08 + 1223.16e^{-0.0156t} \tag{6.1}$$

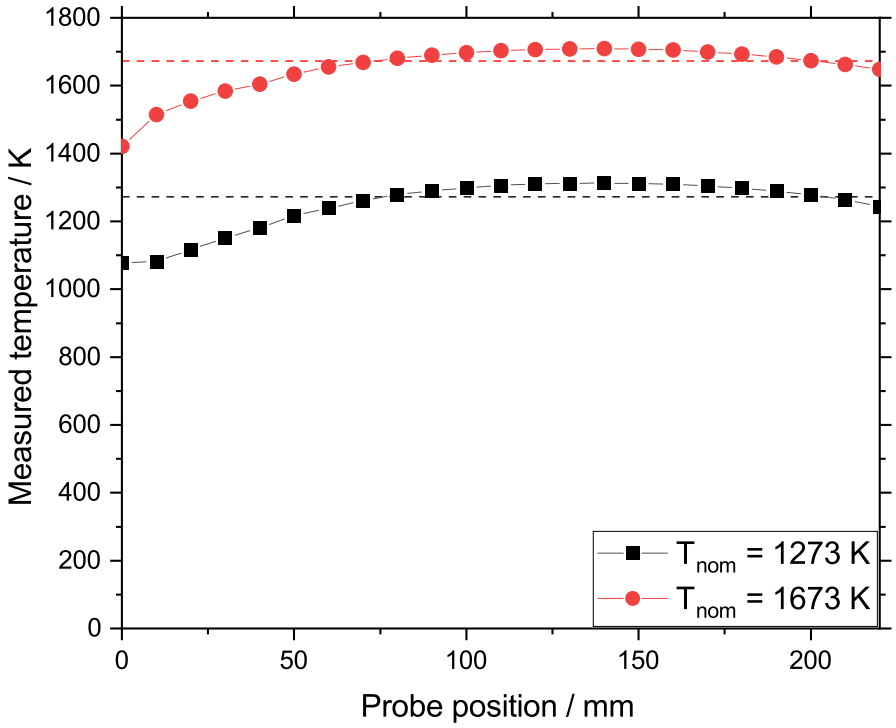

Figure 6.3.: The temperature profile of the furnace, measured by inserting a thermocouple into the tube and measuring the true temperature. The two nominal temperatures tested were 1273 and 1673 K.

During the operation of the furnace, it became apparent that the design of the apparatus was not without flaws. A major problem was the interrupted tube and the associated need for a flowing gas atmosphere. Despite the high purity of the process gas, it was found that even the small amount of residual oxygen in the gas was sufficient to oxidize the highly susceptible materials at the long annealing times required to equilibrate Mo-Si-Ti alloys. After the first heat treatments of real samples, it was found that they were all catastrophically oxidized. Figure 6.5 shows the example of the alloy 22.5Mo-30Si-47.5Ti after annealing at 1573 K for 330 h, which is the typical heat treatment regime chosen for this work. In order to be able to anneal oxidation-prone alloys, a purifier (OxiClear - DGP-R1-3000B Purifier from LabClear Inc.) was used to filter out as much of the remaining impurities as possible. This resulted in an oxygen concentration in the effluent that was below the limit of quantification the lambda probe, and in fact made it possible to successfully anneal Mo-Si-Ti samples even in regions that offer virtually no oxidation resistance.

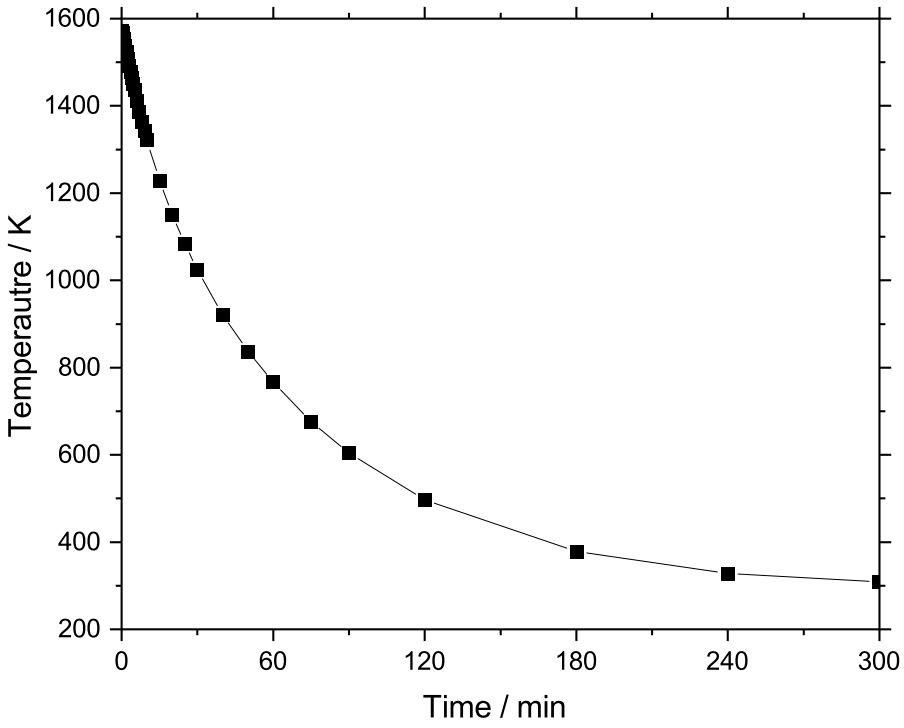

Figure 6.4.: The cooling curve of the quenching furnace when cooling down uncontrolled from 1573 K.

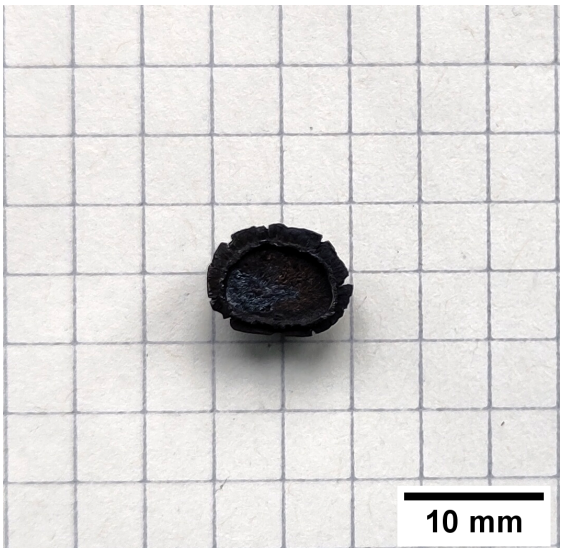

Figure 6.5.: The sample 22.5Mo-30Si-47.5Si after annealing for 330 h at 1573 K. The sample shows catastrophic oxidation, making it unusable for analysis.

Another problem was the electric valves used to automatically control the gas flow. In theory, the furnace control unit would open and close the appropriate valves as the tube was evacuated or flooded with process gas. However, it quickly became apparent that the electronic valves could not withstand the temperatures of the exhaust gas and soon became inoperable. A major rewrite of the control software by the manufacturer would be required to allow the furnace to operate without the electronic valves, as the software relies on them to function. For example, the furnace cannot be heated until it has been purged, and since the pressure in the tube is measured automatically, this process depends on the valves working. In practice, however, it was discovered that even inoperable valves still send the correct signals (i.e. whether they are open or not) to the control unit, allowing the process to start even though the valve is not switching. This was exploited by the operator by replacing the electronic devices with manual valves. In this way, the software receives the signal that the valve is in the correct position and allows all processes to continue, while flushing and operation can be performed by switching the manual valves accordingly. While this mode of operation is inherently susceptible to human error, the process is relatively easy to learn, relatively stable in the face of operator error, and far preferable to reworking the entire system by the manufacturer.
Another shortcoming of the furnace as it was delivered was the built-in mass flow controller. It allowed a maximum gas flow of 5 slm, which is quite high considering the relatively small volume of the tube. While this is advantageous for rapid purging of the system, during operation it was found that a flow of 0.2 to 0.3 slm was sufficient to maintain a stable, low oxygen content (see Figure 6.2). For this reason, the tube supplying the furnace with process gas was split into two before the gas inlet; one tube used the existing mass flow controller and could be used for purging. During operation, this valve is closed and the second tube is opened. This tube leads to a mass flow controller with a maximum flow rate of 2 slm. This allowed for much more precise adjustment of the gas flow, ensuring that 0.3 slm could be reliably used as the setpoint. While the other mass flow controller is in principle capable of setting 0.3 slm, it is prone to fluctuations at such small rates, resulting in either too little flow and thus increased oxygen concentration, or too much flow and thus waste of process gas and, in the worst case, premature emptying of the gas cylinder.

6.2. Purity of the raw materials

Prior to sample preparation, the purity of the raw materials was measured. The oxygen content was determined by CGHE, while the carbon concentration was measured by ICP-OES. All four raw materials described in section 3.1 were analyzed. The results of the measurements are shown in Table 6.1.

Table 6.1.: Impurity measurement of the raw materials used in this work. All values in mass%. MV, SD and IOM stand for mean value, standard deviation and inaccuracy of measurement, respectively. The limit of quantification for C and O were 0.0035 and 0.0200, respectively.

	Mo				**Si**		
	MV	SD	IOM		MV	SD	IOM
C	0.0244	0.002	0.0024	C	< 0.0035	-	-
O	0.0278	0.0003	0.0070	O	0.0315	0.0020	0.0079
$\sum$	0.0522			$\sum$	0.0315		
	Ti lumps				**Ti foil**		
	MV	SD	IOM		MV	SD	IOM
C	< 0.0035	-	-	C	0.0279	0.0007	0.0028
O	0.0894	0.0008	0.0224	O	0.0798	0.0020	0.0200
$\sum$	0.0894			$\sum$	0.1077		

The concentration of impurities is very low for all raw materials. In the case of C in Si and the Ti lumps (which is the more common form of Ti used in this work), the value is even below the limit of quantification. The standard deviations between the measurements are also extremely small, which is important because it shows that the raw material is not only pure but also homogeneous. In conclusion, the values obtained from the chemical analysis of the raw materials show that they are suitable for use.

6.3. Experimental investigation of the Mo-Si binary system

While most aspects of the binary Mo-Si system are well studied, as explained in section 4.1, it was decided to investigate a number of samples containing the phase Mo_3Si. The goal was to determine the stoichiometry under the given conditions and to increase the number of sample compositions that could be included in the thermodynamic optimization of the system. While it was clear from the literature that this phase is typically Si deficient, relatively little data were available in a format that could be used in the CALPHAD method. The results of this investigation are published [33] and are briefly summarized in the following section.

Four samples were prepared by VAM. Their nominal compositions, together with the expected phases, are listed in Table 6.2. The objective was to examine two samples in each two-phase region adjacent to Mo_3Si and thus gain information not only about the phase composition but also about a possible homogeneity range. All samples were annealed at 1573 K for 330 h and quenched in purified water. The samples were then bisected, ground and polished to a roughness of 0.05 µm. Images were taken by SEM in BSE mode and are shown in Figure 6.6. The phase compositions were analyzed by EPMA. In all alloys studied, the areas of each phase are large enough to ensure a sound analysis, i.e. to avoid measuring surrounding phases by mistake. In addition, powder XRD was used to investigate the phases present in each sample.

The experimentally determined compositions of the phases of each alloy are listed in Table 6.3. While the Si content of the phase Mo_5Si_3 is slightly lower than 37.5 at.% for both alloys, this is well within the expected homogeneity range of the phase. The composition of the β phase is in agreement with the literature: 1.8 at.% and 1.5 at.%, respectively (standard deviations: 0.2 at.% and 0.1 at.%, respectively). For the phase Mo_3Si, the experiments confirm the Si deficiency, with an average Si content of about 23 at.%. This is true for alloys in the two-phase region β+Mo_3Si as well as in the two-phase region Mo_3Si+Mo_5Si_3. The standard deviations of the measurements were 0.2-0.7 at.%, depending on the individual sample. Thus, it can be concluded that this phase has no significant homogeneity range.

The X-ray diffractograms of the four samples are shown in Figure 6.7. For the two samples in the two phase region β+Mo_3Si (Figures 6.7 a) and b)) only the expected phases are present. For the samples in the two phase region Mo_3Si+Mo_5Si_3 (Figures 6.7 c) and d)) traces of the β phase were detected in addition to the two expected intermetallic phases. The origin of this phase is not known. It is possible that some amount of this phase remained due to insufficient heat treatment. Another possibility is that the phase is a remnant from the outer layer of the sample affected by oxygen in the furnace, although the entire sample was generously ground around the perimeter prior to pulverization. Regardless of its origin, however, the intensity of its associated peaks is very low and no traces of it could be detected by SEM or EPMA. Thus, the effect of this phase on the composition of the sample as a whole is negligible.

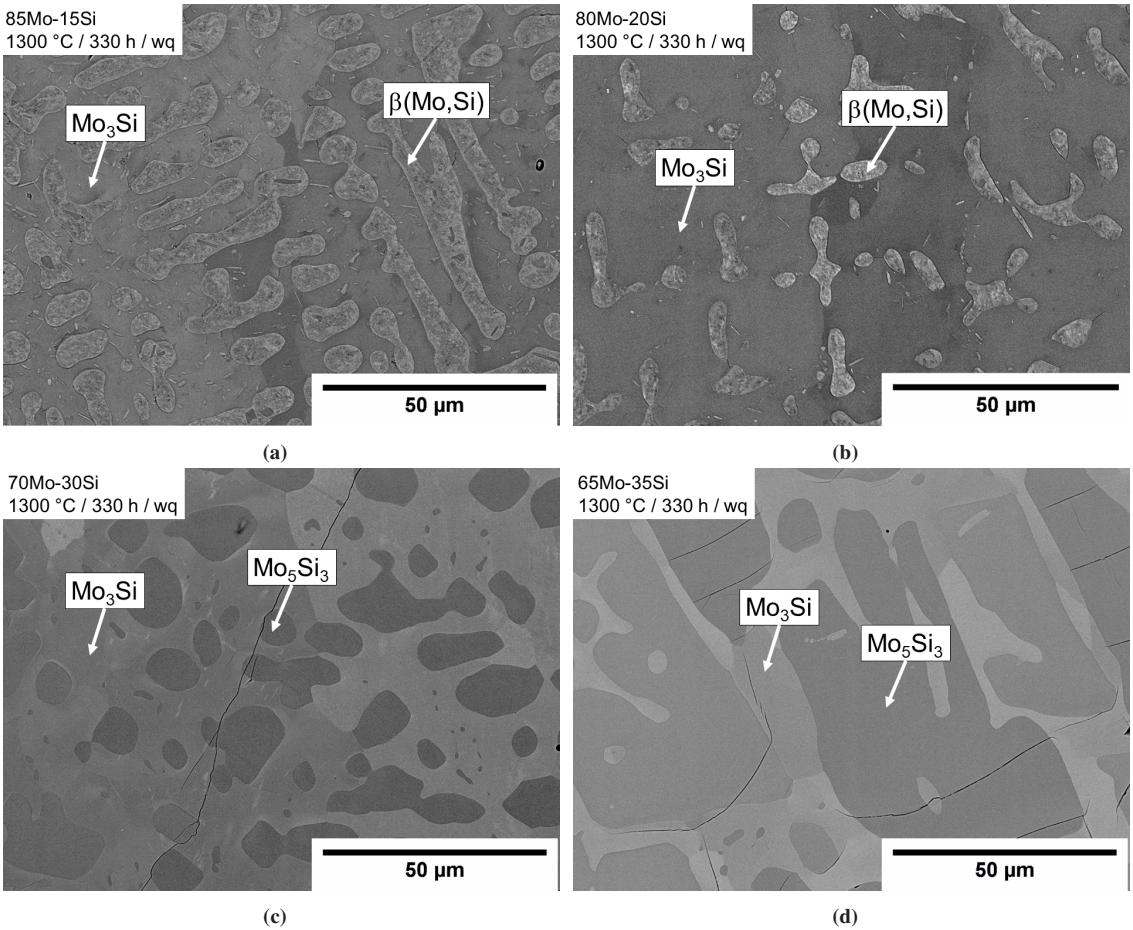

Figure 6.6.: BSE images of the microstructures of the samples after annealing at 1573 K for 330 h and quenching. a) Sample 1: 85Mo-15Si, b) Sample 2: 80Mo-20Si, c) Sample 3: 70Mo-30Si, d) Sample 4: 65Mo-35Si.

Table 6.2.: The nominal compositions and the expected phases of the alloys investigated in this work.

Alloy number	Mo / at.%	Si / at.%	Expected phases
1	85	15	bcc + Mo_3Si
2	80	20	bcc + Mo_3Si
3	70	30	Mo_3Si + Mo_5Si_3
4	65	35	Mo_3Si + Mo_5Si_3

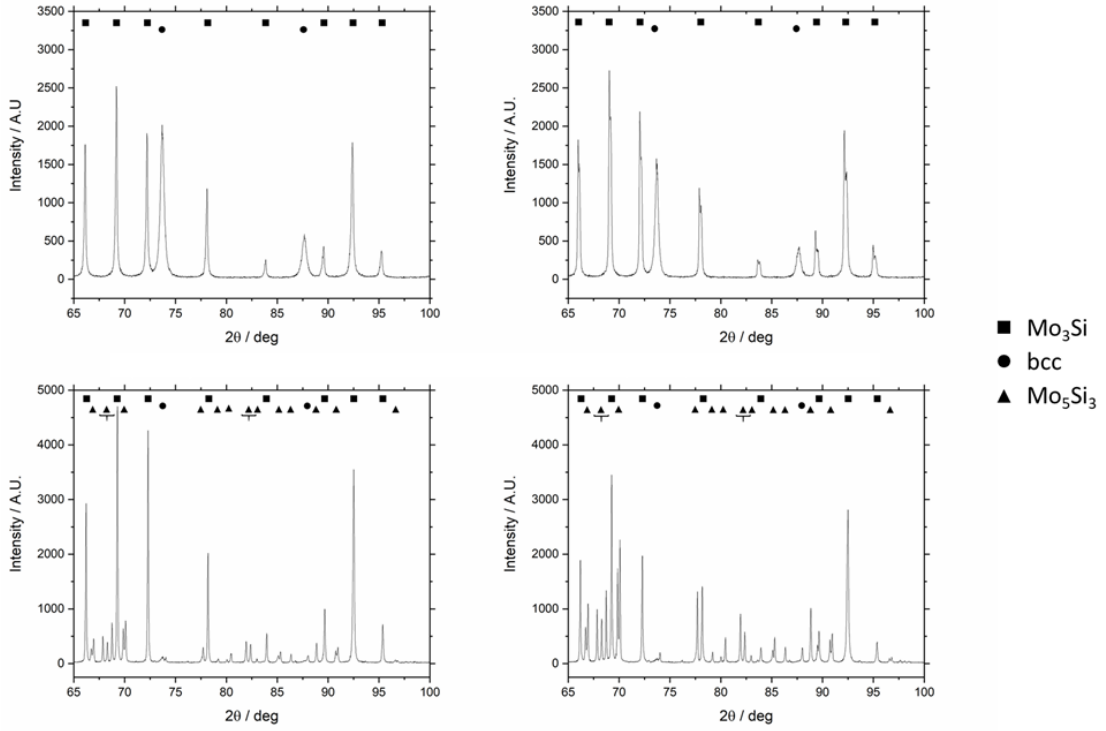

Figure 6.7.: X-ray diffraction patterns of the samples after annealing at 1573 K for 330 h and quenching. a) Sample 1: 85Mo-15Si, b) Sample 2: 80Mo-20Si, c) Sample 3: 70Mo-30Si, d) Sample 4: 65Mo-35Si.

Table 6.3.: The phase compositions for each sample, as determined by EPMA.

Alloy number	Detected phases	Mo / at.%	Si / at.%
1	bcc	98.2 ±0.1	1.8 ±0.1
	Mo_3Si	75.9 ±0.5	24.1 ±0.5
2	bcc	98.5 ±0.2	1.5 ±0.2
	Mo_3Si	77.3 ±0.5	22.7 ±0.5
3	Mo_3Si	76.9 ±0.7	23.1 ±0.7
	Mo_5Si_3	62.9 ±0.7	37.1 ±0.7
4	Mo_3Si	77.2 ±0.2	22.8 ±0.2
	Mo_5Si_3	63.0 ±0.2	37.0 ±0.2

6.4. Experimental investigation of the Mo-Si-Ti ternary system

The first part of this section deals with the testing of a casting mold that was promising to obtain samples with an advantageous geometry for calorimetry. The second subsection discusses the thermal analysis of a sample as a way to investigate an invariant reaction proposed in a student's master thesis prior to this work. The third subsection reports the results of a series of experiments to investigate the influence of quenching on microstructure and phase composition compared to furnace cooling. The penultimate subsection deals with a powder metallurgical route of sample processing that was attempted to promote mixing of the components. The last subsection reports on the investigation of the samples used to study the isothermal section of Mo-Si-Ti at 1573 K. Finally, conclusions are drawn on how the results affect the interpretation of the literature, and the reassessment of the Mo-Si-Ti system.

6.4.1. Testing of a casting mold for cylindrical samples

Relatively early in the project, it was decided to test a casting device for the arc melter to obtain cylindrical samples. This would allow easier and faster sample preparation for methods such as calorimetry and thermal analysis, where the sample geometry can affect the measurement and disk-shaped specimens with flat surfaces and precisely known diameter are preferable. The casting device is a cylindrical copper crucible that is set into the crucible of the arc melter. It is schematically shown in Figure 6.8. The cylinder has a length of 30 mm and a diameter of 5 mm. The device is connected to a vacuum pump that is independent of the one used to control the atmosphere of the arc melter. The material is melted in the rounded part. When completely molten, the vacuum pump is activated, pulling the material into the mold, and a cylindrical sample is obtained.

While this method seemed promising, experiments showed that it was not viable for refractory alloys. The problems were the high melting point of the alloys and the extreme energies required to superheat the materials enough to be drawn consistently into the crucible. Typically, very little material would enter the crucible before solidifying, clogging the narrow inlet. Increasing the beam energy to a level that would heat the material to a high enough temperature to remain liquid long enough to fill the crucible completely tended to result in non-negligible mass loss of the sample due to evaporation. An additional problem was the amount of material required for the apparatus. To completely fill the cylinder with a Mo-Si-Ti alloy typically required about 500-600 mg of material, which exceeded the required smaller sample size by a factor of 2 to 3. Using less material is not possible, as this will result in the surfaces of the cylinder being

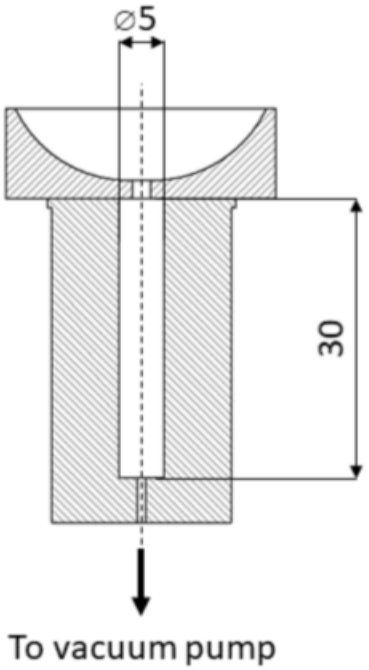

Figure 6.8.: A schematic drawing of the casting device tested as part of this work. All parts are rotationally symmetric with respect to the center axis. The length of the cavity is 30 mm with a diameter of 5 mm.

coated with the alloy, but the core of the cylinder remaining hollow. Modifying the casting device with a smaller crucible cylinder and a correspondingly longer evacuation channel only led to more complications during casting, as the underpressure was not applied quickly enough for the material to be drawn in reliably. Finally, to prove that the device itself was principally functional but not suitable for refractory alloys, attempts were made to cast simpler materials, such as pure iron. These experiments worked without problems, demonstrating that the problems were with the material itself and not with the device. Figure 6.9 shows typical attempts at casting a Mo-Si-Ti alloys (here: 88Mo-1Si-11Ti) and pure iron. Since the benefits of the cylindrical sample geometry were minimal compared to the effort required to develop a viable casting routine with the device, it was decided to reject the equipment and cast button ingots instead.

6.4.2. Differential scanning calorimetry

Prior to this dissertation, a master thesis on heterogeneous equilibria in the systems Mo-Si-Ti and Mo-Si-Ti-B was completed by Clemens Hausner at the IAM-AWP of the KIT. One of the crucial results of this work was the fact that several samples heat treated at 1698 K showed equilibria not previously reported in the literature. These were the three-phase regions Mo_3Si-Ti_5Si_3-β

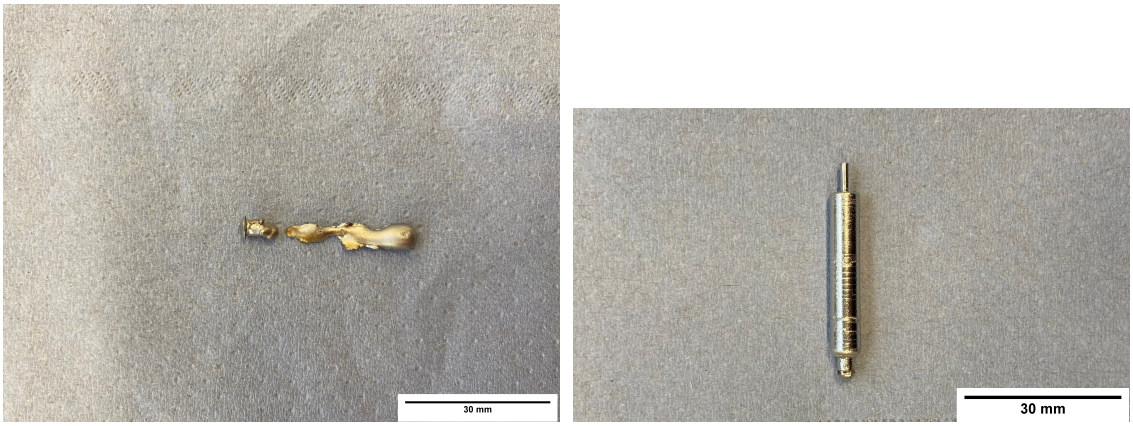

(a) (b)

Figure 6.9.: Examples of a Mo-Si-Ti alloy and pure iron, cast in the casting device for cylindrical samples. a) 88Mo-1Si-11Ti, b) Fe.

and Mo_3Si-Ti_5Si_3-Mo_5Si_3. However, other samples annealed in the same way agreed quite well with the equilibria postulated by Yang et al. [16]. Thus, it was unclear what was causing the problem, and two hypotheses were put forward: either the alloys from Hausner's work were not in equilibrium (due to insufficient heat treatment or impurities), or a transition reaction was taking place very close to the chosen annealing temperature. The transition reaction in question is proposed to be Mo_3Si + $Ti_5Si_3 \rightleftarrows$ β+Mo_5Si_3. In this case, the equilibria reported by Yang et al. would exist above the invariant reaction temperature, while the one proposed by Hausner would exist below it. Extrapolating from Hausner's data, the reaction temperature should be approximately 1200-1500 K. The diagonals of the tetragon opened by the phases β, Mo_3Si, Ti_5Si_3 and Mo_5Si_3 intersect at the composition of 50.5Mo-24.5Si-25.0Ti. At this composition, the invariant reaction should be most easily observed experimentally at the correct temperature, if it exists. This is illustrated in Figure 6.10, which is directly taken from Hausner's thesis. The labels A15, T1 and D88 stand for Mo_3Si, Mo_5Si_3 and Ti_5Si_3, respectively. Shown in this figure are the two tie triangles, β+Mo_3Si+Ti_5Si_3 and Mo_3Si+Mo_5Si_3+Ti_5Si_3, that Hausner found experimentally. In addition, the intersection of the diagonals of the two tie triangles is indicated by a red dot labelled KP. While no composition labels are offered, the accompanying text states that KP is at the composition of 50.5Mo-24.5Si-25.0Ti.

Testing Hausner's hypothesis was not within the scope of his master thesis, which is why it became an objective of this dissertation. For this purpose, a differential scanning analysis (DSC) measurement of a sample with the composition 50.5Mo-24.5Si-25.0Ti was planned. Since the invariant reaction was postulated to take place below 1500 K, the sample was annealed at 1073 K. This way, any reaction above the annealing temperature would be fairly easily visible in the DSC signal. To compensate for the relatively low annealing temperature and the correspondingly slow diffusion, an annealing time of 660 h was chosen. Since Mo alloys are prone to catastrophic

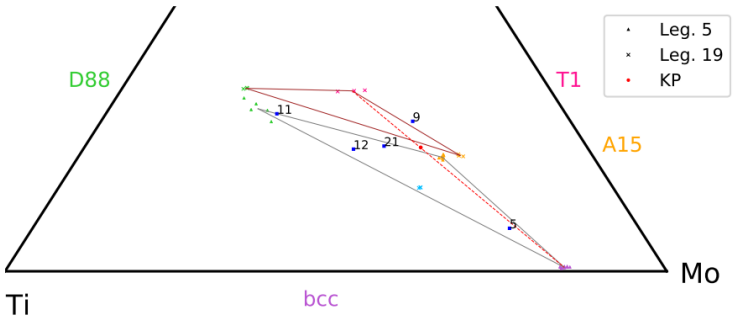

Figure 6.10.: The image taken from Hausner's master thesis, showing the tie triangles found in his work. A15, T1 and D88 stand for the phases Mo_3Si, Mo_5Si_3 and Ti_5Si_3, respectively. The red dot indicates the intersection of the diagonals of the triangles, and thus the sample composition where the proposed transition reaction should be best observed. While no composition labels are provided in this image, the composition of KP is 50.5Mo-24.5Si-25.0Ti, according to the accompanying text in the thesis.

oxidation at this temperature due to pesting [13], the sample was encapsulated in quartz glass filled with Ar. This method is viable only at such low temperatures, because quartz glass has a maximum temperature limit of appoximately 1300 K. After heat treatment, a roughly disk-shaped specimen of about 3 mm diameter and about 1 mm thickness was prepared and both surfaces were polished. A DSC 404 C (NETZSCH-Gerätebau GmbH) was used for the measurement. A baseline of empty alumina crucibles was measured prior to the sample. The masses of the empty sample and reference crucibles were 241.66 mg and 246.20 mg, respectively. The mass of the sample was 145.23 mg. A heating and cooling rate of 10 K/min was chosen, which is sufficiently slow to detect invariant reactions. The sample was measured three times, with the temperature cycling between 1073 and 1473 K. The result of the experiment is shown in Figure 6.11.

There are no peaks in either the heating or cooling curves. The cooling curves are completely featureless and show the expected behavior of a sample not undergoing transformation. In the heating curves, a step is visible at about 1225 K. While this is reproducible in each of the three curves, the shape of this feature does not indicate a transformation reaction, which would be a distinct peak rather than an increase followed by a plateau. In addition, any transformation reaction would also be visible in the cooling curve, which shows no evidence of a reaction at this temperature. Thus, it can be concluded that these steps are most likely due to a change of the heat capacity of the sample as a result of changing phase fractions rather than a peak due to sample transformation and that no invariant reaction takes place at the postulated temperature. Since it is entirely possible that the reaction takes place at a slightly higher temperature, or even the chosen annealing temperature itself, another scan of the same sample was done from 1473 to 1773 K. All other parameters were kept the same. The result is shown in Figure 6.12. Again, the curves show no discernible peaks. Therefore, the most likely explanation for the unexpected phase regions in Hausner's master thesis is that the samples were not in equilibrium. Without

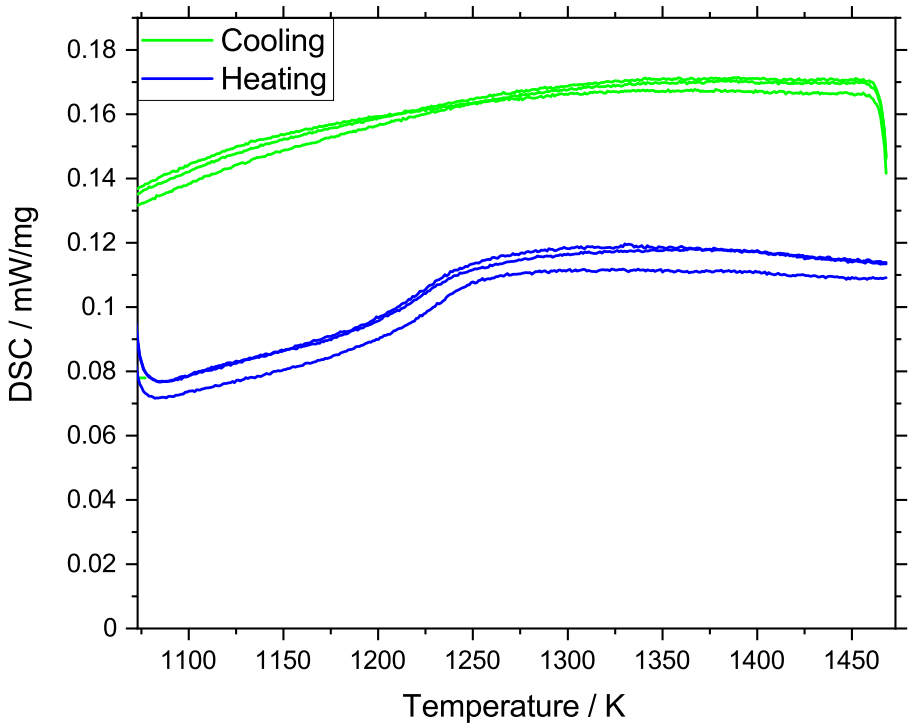

Figure 6.11.: The resulting curve of the DSC measurement of the sample 50.5Mo-24.5Si-25.0Ti (annealed at 1073 K for 660 h) between 1073 and 1473 K. The heating and cooling rates were 10 K/min, the crucible material was alumina.

further experiments, it is not clear whether this is due to insufficient annealing times or to impurities. Ti_5Si_3 is known to have a significant affinity to dissolve carbon, nitrogen and oxygen as interstitials [140]. It is very likely that once a sufficient concentration of these impurities is present, the phase is stabilized and will not readily dissolve even after prolonged heat treatment. In fact, all the new equilibria reported by Hausner show an unexpected presence of only the phase Ti_5Si_3. If this phase is formed during sample preparation and stabilized by impurities, the heat treatment chosen was possibly insufficient to dissolve it completely. As a conclusion of the DSC experiment and the explanation derived from it, additional care was taken to ensure that all samples in this work were as free of impurities as possible. Such measures included the use of an arc melter in an argon-filled glove box and the furnace with the special gas purification system described in section 6.1.

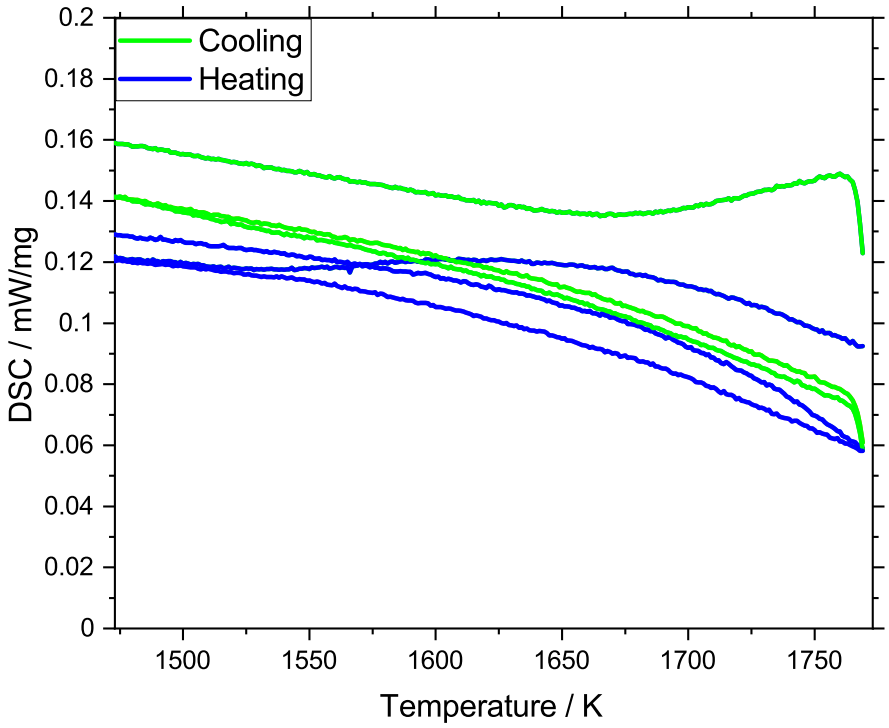

Figure 6.12.: The resulting curve of the DSC measurement of the sample 50.5Mo-24.5Si-25.0Ti (annealed at 1073 K for 660 h) between 1473 and 1773 K. The heating and cooling rates were 10 K/min, the crucible material was alumina.

6.4.3. Investigation of samples in the as-cast state

Based on the conclusions of chapter 5, 14 samples were prepared to investigate the as-cast microstructures of Mo-Si-Ti samples after vacuum arc melting. The selected sample compositions are listed in Table 6.4 and shown in Figure 6.13 superimposed on the liquidus projection of the system. These samples were not selected specifically for this task, but parts of these samples were to be annealed and studied. This was done at a relatively early, exploratory stage of the project, so the sample compositions may appear to change rather erratically from one sample to the next. However, these same samples were suitable to study the as-cast microstructure and discuss the soldification pathways, as well.

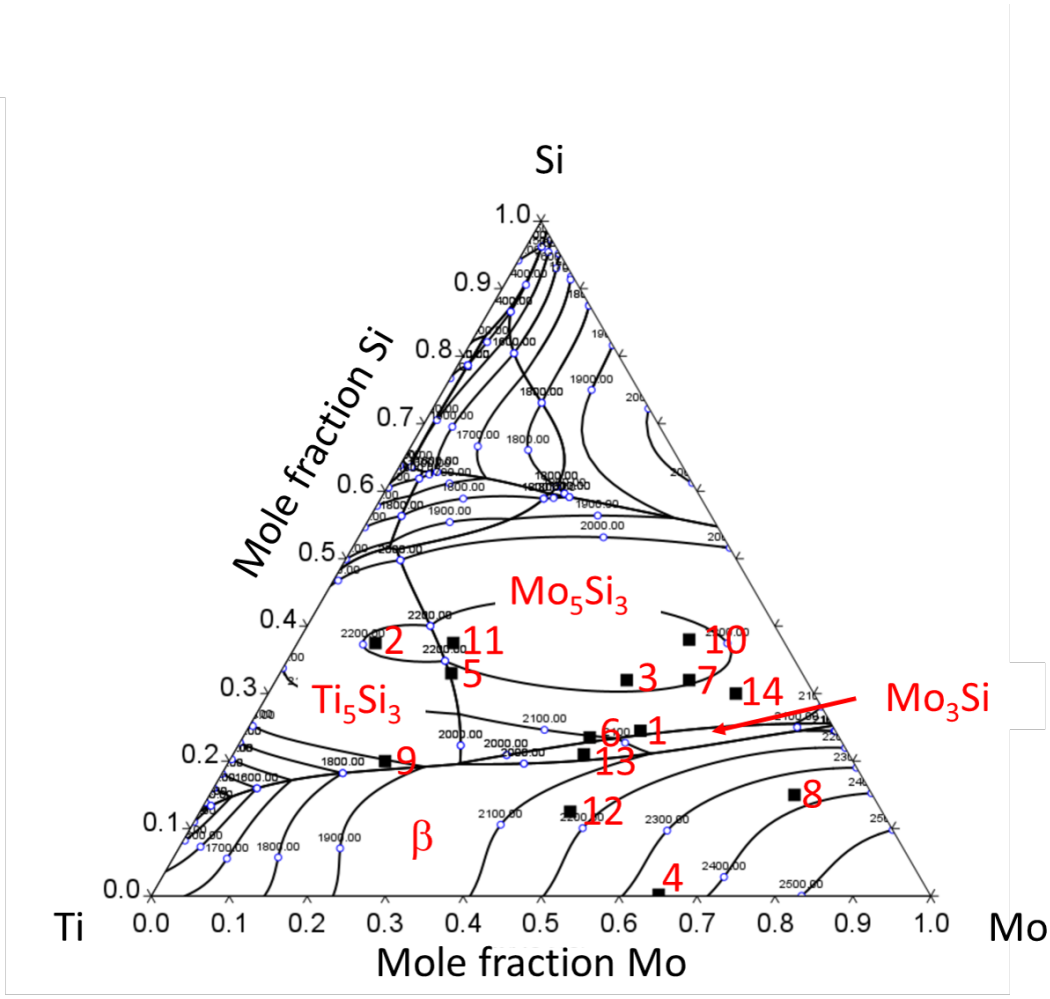

Figure 6.13.: The compositions of the samples used to investigate the solidification behavior in the Mo-Si-Ti system, shown on the liquidus projection calculated with the dataset from Yang et al. [16]. Areas of primary solidification are indicated with the respective phases.

Table 6.4.: The composition of the samples used to investigate the solidification behavior.

Sample designation	Nominal composition
SSC1	50.5Mo-24.5Si-25Ti
SSC2	10Mo-37.5Si-52.5Ti
SSC3	45Mo-32Si-23Ti
SSC4	65Mo-0.2Si-34.8Ti
SSC5	22Mo-33Si-45Ti
SSC6	44.5Mo-23.5Si-32Ti
SSC7	53Mo-32Si-15Ti
SSC8	75Mo-15Si-10Ti
SSC9	20Mo-20Si-60Ti
SSC10	50Mo-38Si-12Ti
SSC11	20Mo-37.5Si-42.5Ti
SSC12	47.5Mo-12.5Si-40Ti
SSC13	45Mo-21Si-34Ti
SSC14	60Mo-30Si-10Ti

6.4.3.1. SSC1: 50.5Mo.24.5Si.25Ti

Figure 6.14a shows the microstructure of the sample 50.5Mo-24.5Si.25Ti. There are large, continuous grains of Mo_3Si as well as numerous smaller grains of Mo_5Si_3. There are very few areas in the sample where lamellar structures are visible, indicating eutectic solidification of some parts of the sample, but the grain sizes are too small to determine the phases. The composition of the phases are listed in Table 6.5. The Scheil solidification calculation shown in Figure 6.14b only partially fits the experimental observation. As the sample is in the region of primary solidification of Mo_5Si_3, this is the first phase to form. The composition of the remaining liquid then falls onto the peritectic line L+$\beta \rightleftarrows$ Mo_3Si. Since this would require a solid phase to participate in the reaction, the liquid composition does not follow this line, but instead continues into the region of primary solidification of Mo_3Si. This phase is formed until about 80% of the sample has solidified. At this point, the remaining liquid composition has reached the eutectic trough L $\rightleftarrows$ β+Mo_3Si is formed. Since eutectic reactions can occur under Scheil conditions, this eutectic trough is followed until the transition reaction U_3 occurs. Because the transition reaction itself has no effect on the microstructure, it is not specifically indicated in the graph. However, the remaining liquid composition then follows another eutectic trough (L $\rightleftarrows$ β+Ti_5Si_3) until the entire sample is solidified. The phase fraction diagram of this sample is shown in Figure 6.15.

Table 6.5.: Phase compositions of the sample SSC1, 50.5Mo-24.5Si-25Ti.

50.5Mo-24.5Si-25Ti			
	x(Mo) / at.%	x(Si) / at.%	x(Ti) / at.%
Mo_3Si	56.5 ± 2.6	22.4 ± 0.5	21.0 ± 3.1
Mo_5Si_3	37.5 ± 3.0	36.1 ± 0.3	26.3 ± 2.8

Table 6.6.: Phase compositions of the sample SSC2, 10Mo-37.5Si-52.5Ti.

10Mo-37.5Si-52.5Ti			
	x(Mo) / at.%	x(Si) / at.%	x(Ti) / at.%
β	36.4 ± 5.2	4.1 ± 0.4	59.4 ± 5.3
Ti_5Si_3	9.0 ± 1.1	37.6 ± 0.3	53.4 ± 1.2

It shows that the vast majority of the sample consists of Mo_3Si, while the other phases make up only a small fraction of the microstructure. In particular, Ti_5Si_3 makes up only a few percent of the total solid formed. While the micrograph agrees fairly well with the amount of Mo_3Si, the other phases do not appear to be correct. Mo_5Si_3 clearly makes up a fairly large portion of the microstructure, but according to the calculation, its phase fraction is roughly the same as the β phase. Even under the assumption that the lamellar structures are β+Ti_5Si_3, the amount of the latter two phases seems to be significantly overestimated by the calculation.

6.4.3.2. SSC2: 10Mo-37.5Si.52.5Ti

The microstructure of the sample 10Mo-37.5Si.52.5Ti is shown in Figure 6.16a. The majority of the sample consists of Ti_5Si_3. In addition, β phase is present in the form of elongated precipitates, apparently at the grain boundaries of the Ti_5Si_3 grains, and as lamellar structures. The phase compositions of this sample are listed in Table 6.6. The corresponding Scheil solidification calculation is shown in Figure 6.16b. While the formation of continuous Ti_5Si_3 agrees well, the presence of the β phase is completely missing from the calculation. Only in the very last increment of the calculation does the eutectic reaction L $\rightleftarrows$ β + Ti_5Si_3 take place and the temperature suddenly drops to 1613 K, at which this reaction occurs. However, this is likely a numerical issue because the solver forces the final liquid composition to end at the binary eutectic point. Since the phase fraction of β in the micrograph is quite large, the discrepancy between experiment and calculation for this sample is significant.

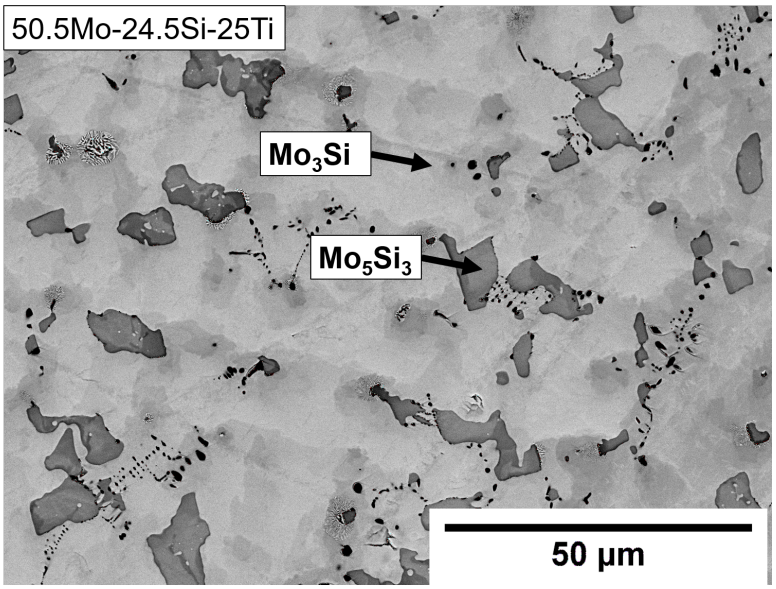

(a)

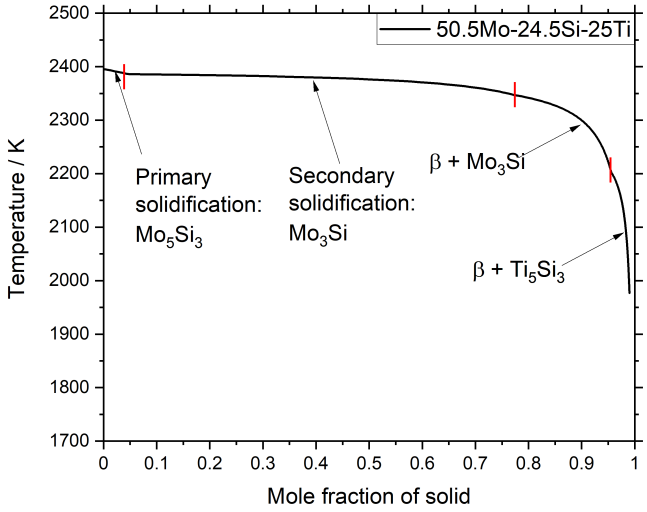

(b)

Figure 6.14.: Results for SSC1, 50.5Mo-24.5Si-25Ti. a) The microstructure of the sample SSC1 in the as-cast state. b) The Scheil solidification calculation of this composition.

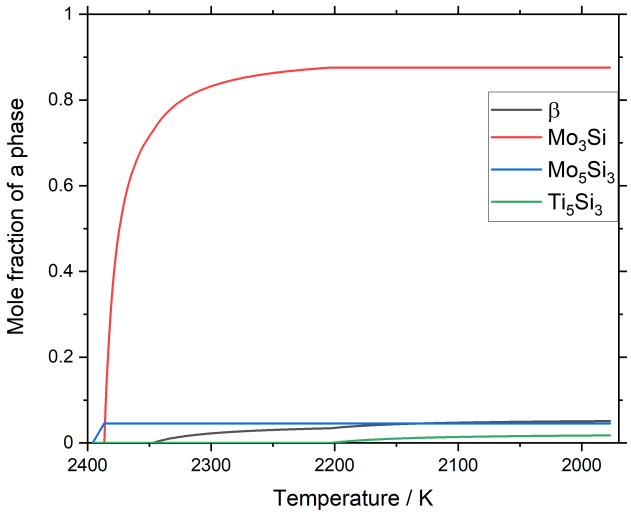

Figure 6.15.: The calculated phase fraction diagram of sample SSC1, 50.5Mo-24.5Si-25Ti.

6.4.3.3. SSC3: 45Mo-32Si-23Ti

The microstructure of the sample 45Mo-32Si-23Ti is shown in Figure 6.17a. It consists of the two phases Mo_5Si_3 and Mo_3Si. Both phases take the form of large, continuous grains with no detectable lamellar structures. On the edges of the Mo_5Si_3 samples, the changing composition of the phase due to the rapid solidification is well visible, as it leads to different hues in the BSE image. Since the sample is extremely brittle, a relatively high amount of porosity and scratches are visible. The phase compositions are shown in Table 6.7. The corresponding Scheil solidification calculation result is shown in Figure 6.17b. Again, the sample is in the Mo_5Si_3 primary solidification region and first reaches a peritectic reaction. Because the peritectic reaction is not significant, see above, this leads to the subsequent Mo_3Si secondary solidification. Finally, the remaining liquid composition falls into the eutectic trough of β+Mo_3Si, which is followed until the sample is completely solidified. The phase fraction diagram is shown in Figure 6.18. It shows that about 60% of the solid fraction formed is Mo_5Si_3, while almost 40% is Mo_3Si. A small amount of β is predicted and no Ti_5Si_3. For this sample the experiment and the calculation are in good agreement. Both Mo_5Si_3 and Mo_3Si take the form of primary solidified grains and both are formed in significant amounts, with slightly more Mo_5Si_3 than Mo_3Si. No β phase is visible in the micrograph, which agrees well with the nearly negligible amount formed according to the calculation.

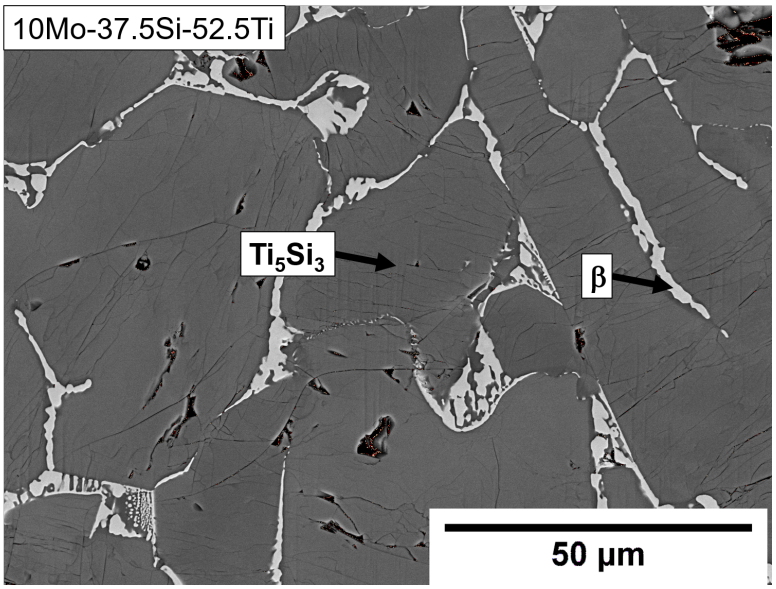

(a)

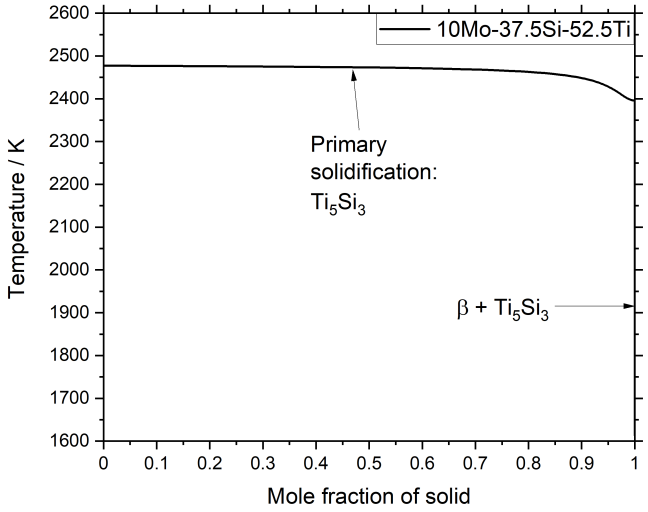

(b)

Figure 6.16.: Results for SSC2, 10Mo-37.5Si-52.5Ti. a) The microstructure of the sample SSC2 in the as-cast state. b) The Scheil solidification calculation of this composition.

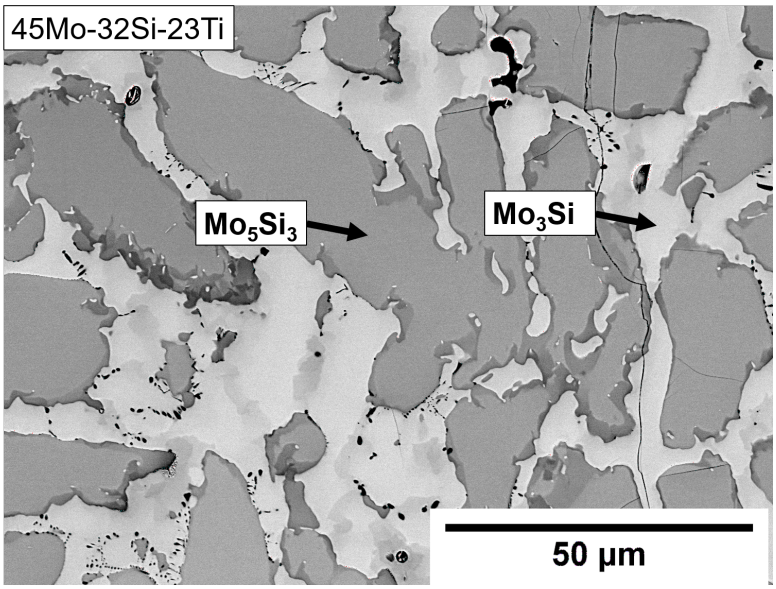

(a)

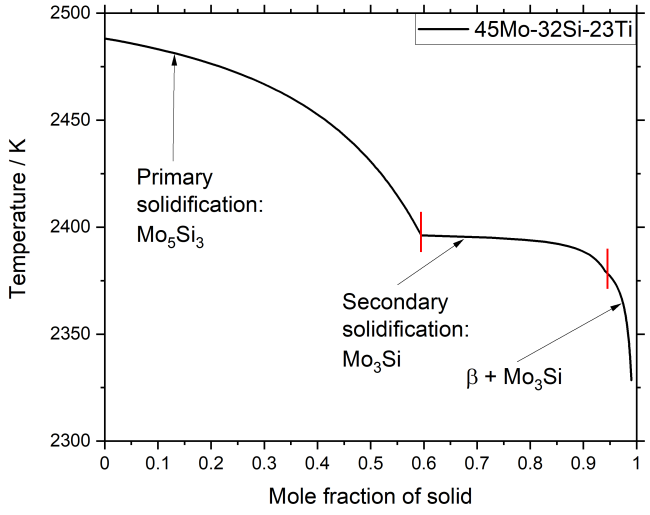

(b)

Figure 6.17.: Results for SSC3, 45Mo-32Si-23Ti. a) The microstructure of the sample SSC3 in the as-cast state. b) The Scheil solidification calculation of this composition.

Table 6.7.: Phase compositions of the sample SSC3, 45Mo-32Si-23Ti.

45Mo-32Si-23Ti			
	x(Mo) / at.%	x(Si) / at.%	x(Ti) / at.%
Mo_3Si	57.8 ± 3.0	22.6 ± 0.5	19.5 ± 3.2
Mo_5Si_3	39.4 ± 3.7	35.8 ± 0,4	24.8 ± 3.8

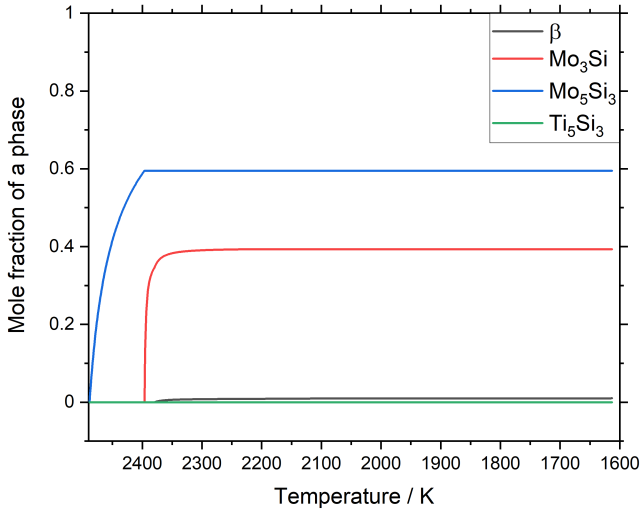

Figure 6.18.: The calculated phase fraction diagram of sample SSC3, 45Mo-32Si-23Ti.

6.4.3.4. SSC4: 65Mo-0.2Si-34.8Ti

The microstructure of the sample 65Mo-0.2Si.34.8Ti is shown in Figure 6.19a. Even in the as-cast state, it is single phase β with no precipitates of another phase detectable throughout the sample. The small black areas are pores as well as precipitation of pure Ti. The composition of the phases are listed in Table 6.8. The result of the Scheil solidification calculation shown in Figure 6.19b is in good agreement. Because the sample composition is so far away from any lines of double saturation, the entire sample solidifies in the primary solidification region of β. For the same reason that was discussed for sample SSC2, no silicide formation is calculated. In the case of this sample, however, this corresponds well with the microstructure.

6.4.3.5. SSC5: 22Mo-33Si-45Ti

The microstructure of the sample 22Mo-33Si-45Ti is shown in Figure 6.20a. It consists of the three phases Mo_5Si_3, Ti_5Si_3 and β. Mo_5Si_3 exists only in the form of continuous grains, while

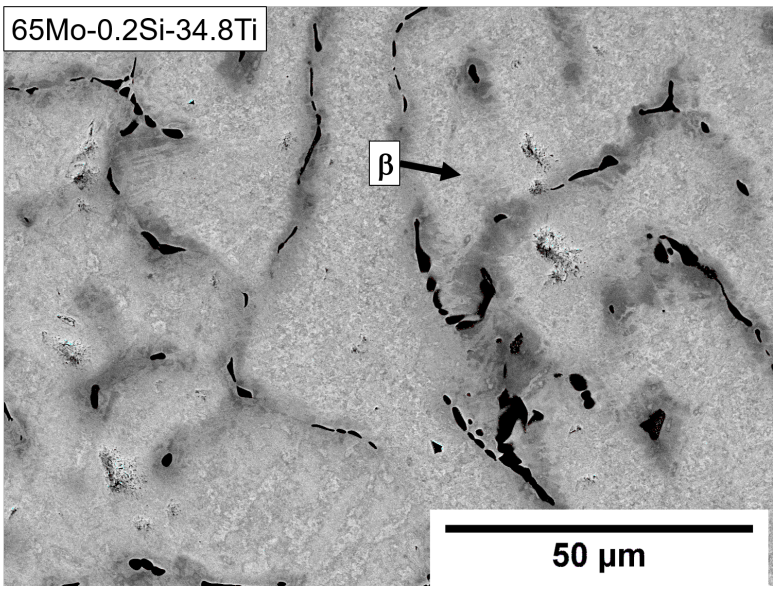

(a)

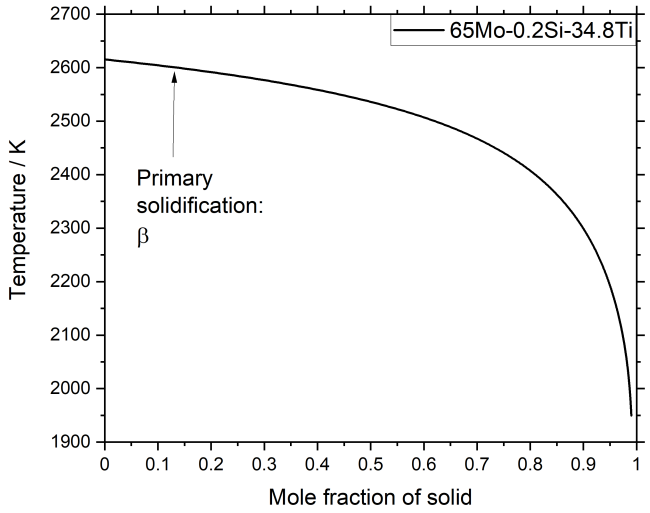

(b)

Figure 6.19.: Results for SSC4, 65Mo-0.2Si-34.8Ti. a) The microstructure of the sample SSC4 in the as-cast state. b) The Scheil solidification calculation of this composition.

Table 6.8.: Phase compositions of the sample SSC4, 65Mo-0.2Si-34.8Ti.

65Mo-0.2Si-34.8Ti			
	x(Mo) / at.%	x(Si) / at.%	x(Ti) / at.%
β	70.2 ± 3.7	1.1 ± 0.3	28.6 ± 3.6

Table 6.9.: Phase compositions of the sample SSC5, 22Mo-33Si-45Ti.

22Mo-33Si-45Ti			
	x(Mo) / at.%	x(Si) / at.%	x(Ti) / at.%
β	57.6 ± 2.9	5.1 ± 0.7	37.3 ± 3.0
Mo_5Si_3	22.9 ± 0.4	36.7 ± 0.3	40.3 ± 0.4
Ti_5Si_3	15.5 ± 1.7	37.0 ± 0.5	47.5 ± 1.7

Ti_5Si_3 exists in the form of both large continuous grains and lamellae. The β phase is present only as small, mostly lamellar precipitates intertwined with Ti_5Si_3. The phase compositions are listed in Table 6.9. The Scheil solidification calculation shown in Figure 6.20b is in good agreement with the experiment. The primary solidification of Mo_5Si_3 is calculated correctly. In the next step, the simultaneous solidification of both 5-3 silicides is calculated. This can be explained by the microstructure as well, as Mo_5Si_3 grains continue to grow, while Ti_5Si_3 start to form. The final step of the calculation agrees with the experimental microstructure, too, as the simultaneous formation of β+Ti_5Si_3 is clearly visible in the form of the fine, eutectic precipitations. The phase fraction diagram of this sample is shown in Figure 6.21. Over 50% of the sample is calculated to be Ti_5Si, another 30% is Mo_5Si_3 and about 10% should be β phase. All these phase fractions agree well with the micrograph.

6.4.3.6. SSC6: 44.5Mo-23.5Si-32Ti

The microstructure of the sample 44.5Mo-23.5Si-32Ti is shown in Figure 6.22a. It is quite complex, with the phases β, Mo_3Si, Mo_5Si_3 and Ti_5Si_3 all present. Mo_5Si_3 forms relatively small but continuous grains and makes up a relatively small fraction of the structure. Mo_3Si, on the other hand, is present as both continuous grains and lamellae. The continuous grains are quite large and make up the majority of the structure. The lamellae are intertwined with the β phase. In addition, β lamellae are also present in the form of another two-phase structure, intertwined with Ti_5Si_3. Apart from these two lamellar regions, no β is present elsewhere, and Ti_5Si_3 exists only in the lamellar structure together with β. The phase compositions are listed in Table 6.10. The Scheil solidification calculation shown in Figure 6.22b is in very good agreement with this experiment. According to it, a rather small amount of Mo_5Si_3 solidifies first, followed by secondary solidification of Mo_3Si after the irrelevant peritectic reaction L + $\beta \rightleftarrows Mo_3Si$. This fits well with the presence of continuous grains of these phases in the micrographs. Subsequently, the remaining liquid compositions fall first on the eutectic trough L $\rightleftarrows$ β + Mo_3Si, meets the transition reaction U_3, which is again insignificant. Finally, the liquid composition falls on the eutectic trough L $\rightleftarrows$ β + Ti_5Si_3. Consequently, two different eutectic structures are expected, one of β and Mo_3Si and one of β and Ti_5Si_3. This corresponds very well to the experimental

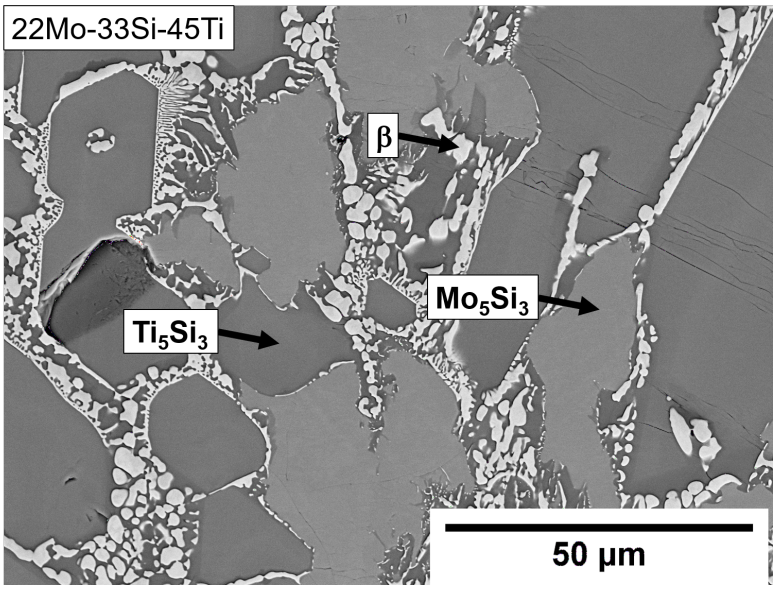

(a)

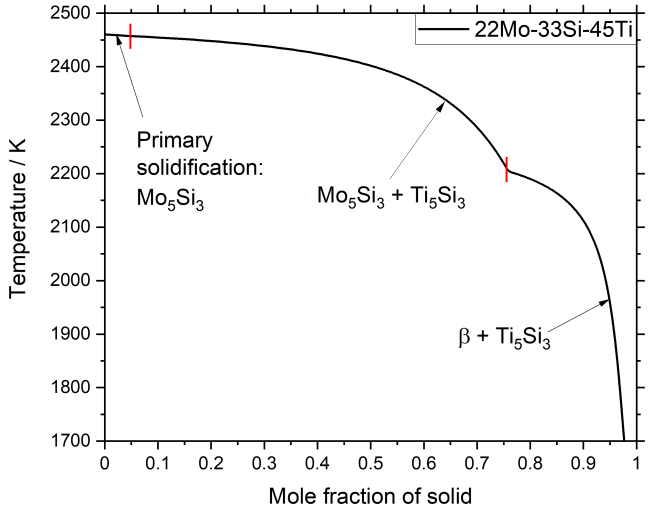

(b)

Figure 6.20.: Results for SSC5, 22Mo-33Si-45Ti. a) The microstructure of the sample SSC5 in the as-cast state. b) The Scheil solidification calculation of this composition.

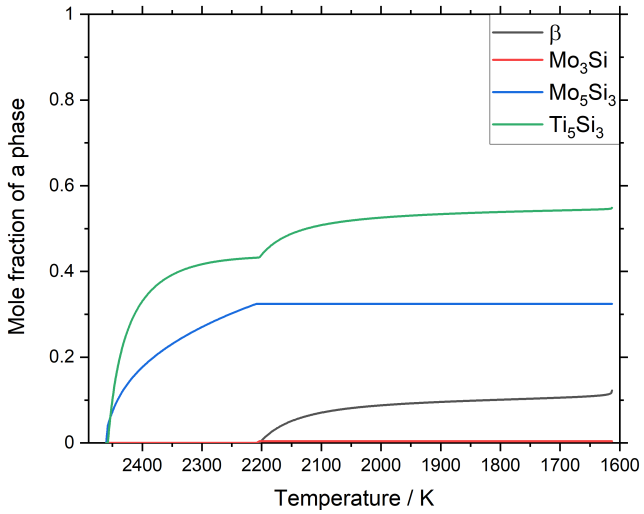

Figure 6.21.: The calculated phase fraction diagram of sample SSC5, 22Mo-33Si-45Ti.

Table 6.10.: Phase compositions of the sample SSC6, 44.5Mo-23.5Si-32Ti.

44.5Mo-23.5Si-32Ti			
	x(Mo) / at.%	x(Si) / at.%	x(Ti) / at.%
β	65.6 ± 1.3	5.9 ± 0.8	28.5 ± 1.0
Mo_3Si	53.5 ± 1.3	22.0 ± 0.5	24.5 ± 1.5
Mo_5Si_3	33.9 ± 1.8	35.9 ± 0.3	30.2 ± 1.7
Ti_5Si_3	18.0 ± 0.7	36.7 ± 0.4	45.2 ± 0.6

microstructure where exactly this behavior is observed. The phase fraction diagram shown in Figure 6.23 also agrees well with the microstructure. According to the calculation, the majority of the sample consists of Mo_3Si. A relatively small amount of Mo_5Si_3 is expected, formed only during its primary solidification step. The β phase and Ti_5Si_3 are expected to be present in relatively small but easily detectable amounts of about 10% each. This agrees well with the microstructure, including the fact that more β is formed than Ti_5Si_3.

6.4.3.7. SSC7: 53Mo-32Si-15Ti

The microstructure of the sample 53Mo-32Si-15Ti is shown in Figure 6.24a. It consists of Mo_3Si and Mo_5Si_3. Both phases form continuous large grains and the fractions of both phases are nearly identical, with slightly more Mo_5Si_3. No other features are visible anywhere in the sample. The compostion of the phases are shown in Figure 6.11. The corresponding result of

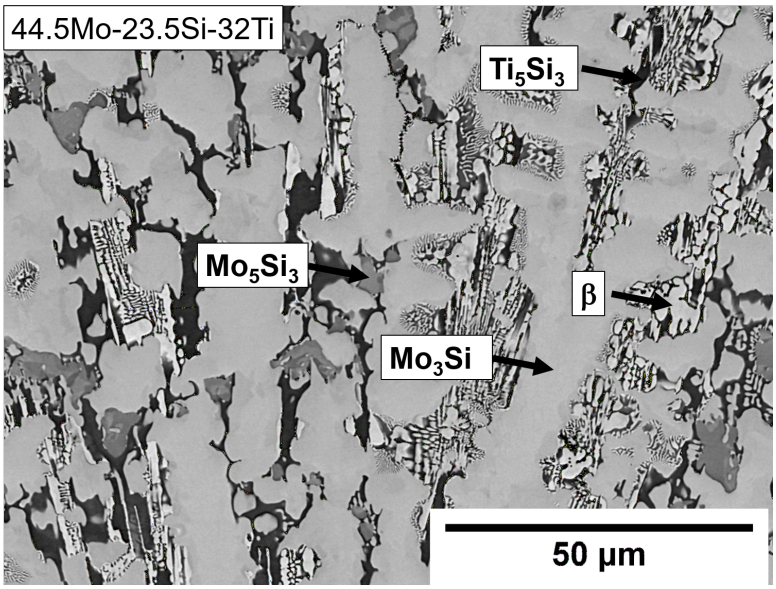

(a)

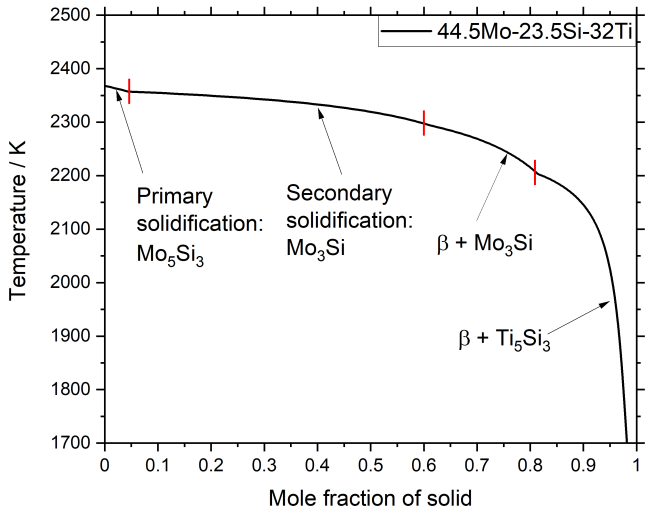

(b)

Figure 6.22.: Results for SSC6, 44.5Mo-23.5Si-32Ti. a) The microstructure of the sample SSC6 in the as-cast state. b) The Scheil solidification calculation of this composition.

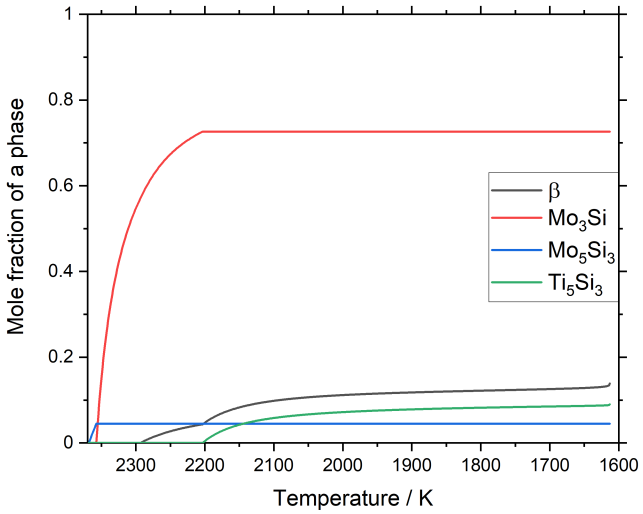

Figure 6.23.: The calculated phase fraction diagram of sample SSC6, 44.5Mo-23.5Si-32Ti.

Table 6.11.: Phase compositions of the sample SSC7, 53Mo-32Si-15Ti.

53Mo-32Si-15Ti			
	x(Mo) / at.%	x(Si) / at.%	x(Ti) / at.%
Mo_3Si	65.5 ± 0.7	23.1 ± 0.3	11.4 ± 0.6
Mo_5Si_3	50.2 ± 0.7	35.7 ± 0.4	14.0 ± 0.7

the Scheil solidification calculation is shown in Figure 6.24b. The phases formed are correctly predicted. Mo_5Si_3 is formed during primary solidification, followed by eutectic solidification of Mo_5Si_3 and Mo_3Si. The phase fraction diagram is shown in Figure 6.25. It agrees well with the micrograph and sheds additional light on the microstructural evolution. About 60% of Mo_5Si_3 is formed during primary solidification, which agrees well with Figure 6.24a. In the next step, the eutectic reaction, only a small amount of additional Mo_5Si_3 is formed, while the remaining liquid solidifies almost exclusively as Mo_3Si. This is in good agreement with the grain morphology and shows that even eutectic reactions can sometimes produce an unusual microstructure.

6.4.3.8. SSC8: 75Mo-15Si-10Ti

The microstructure of the sample 75Mo-15Si-10Ti is shown in Figure 6.26a. Two phases are present: β and Mo_3Si. Both take the form of rather large, continuous grains. No other features such as lamellae are visible anywhere in the sample. The phase compositions are listed in Table 6.12. The Scheil solidification calculation shown in Figure 6.26b is in fairly good agreement

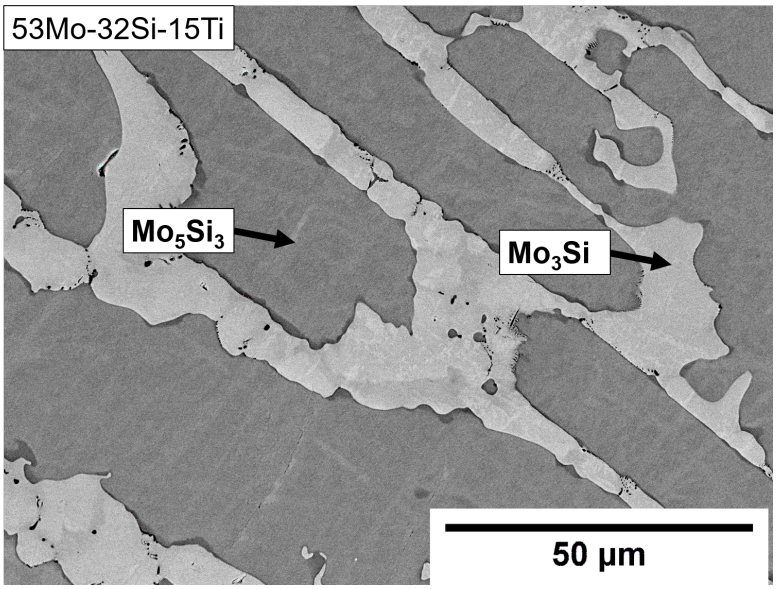

(a)

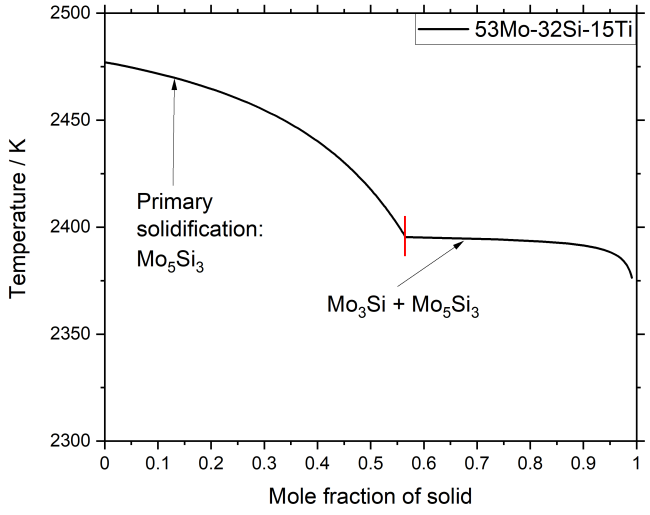

(b)

Figure 6.24.: Results for SSC7, 53Mo-32Si-15Ti. a) The microstructure of the sample SSC7 in the as-cast state. b) The Scheil solidification calculation of this composition.

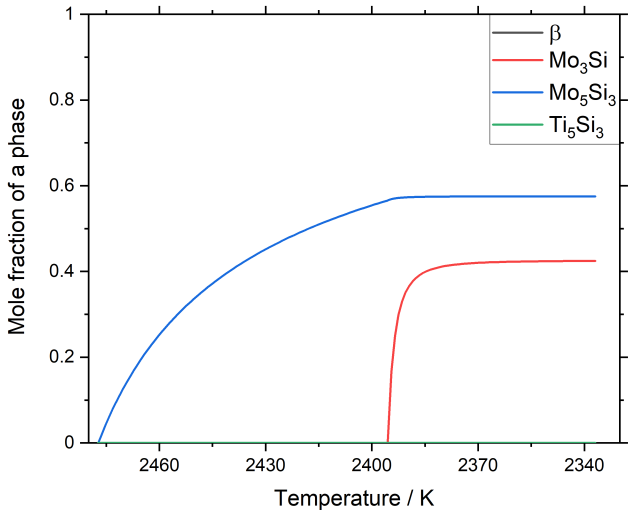

Figure 6.25.: The calculated phase fraction diagram of sample SSC7, 53Mo-32Si-15Ti.

Table 6.12.: Phase compositions of the sample SSC8, 75Mo-15Si-10Ti.

75Mo-15Si-10Ti			
	x(Mo) / at.%	x(Si) / at.%	x(Ti) / at.%
β	88.0 ± 1.0	5.9 ± 0.7	6.2 ± 0.4
Mo_3Si	68.6 ± 0.4	21.6 ± 0.3	9.7 ± 0.3

with the experiment. The predicted primary solidification of β is correct, as is the subsequent formation of β and Mo_3Si. The phase fraction diagram is shown in Figure 6.27. The agreement with the micrograph is only moderate. According to the calculation, primary solidification of leads to about 10% of β. In the following eutection reaction, this amount increased to about 15%. Mo_3Si is formed only in this step and makes up nearly 60% of the total solid formed. The first observation is that the amount of β phase seems to be significantly underestimated. More importantly, the total amount of solid in the phase fraction diagram does not add up to 100%, even though this was the boundary condition chosen for the calculation. No other phases, indicated in the legend or not, are calculated to form, so it is unclear why this problem occurs for this sample. It seems likely that the solver has encountered an unknown termination condition and the calculation stops before it reaches a proper end. However, none of the modifiable conditions had any effect on this behavior. Therefore, no method can be presented at this time to fix this obviously erroneous calculation.

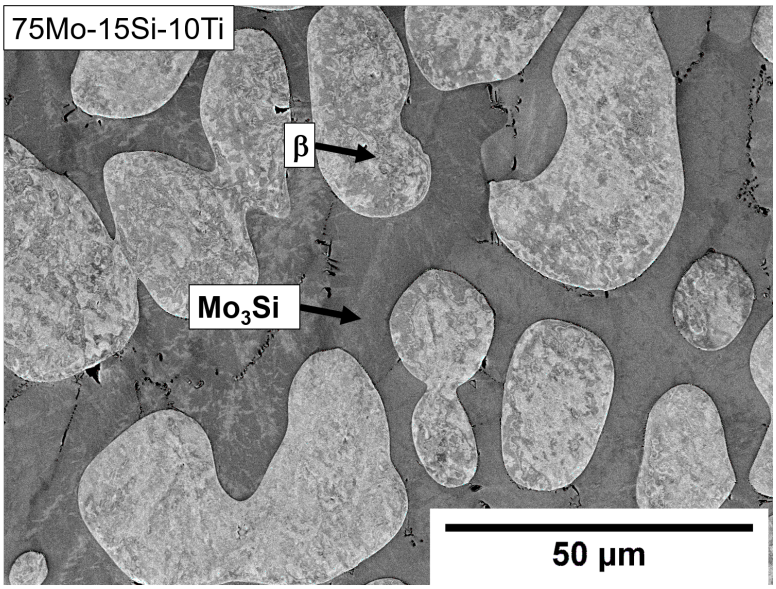

(a)

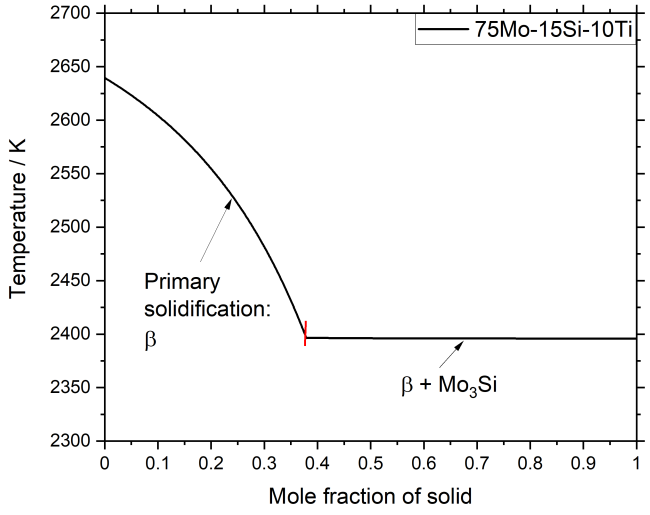

(b)

Figure 6.26.: Results for SSC8, 75Mo-15Si-10Ti. a) The microstructure of the sample SSC8 in the as-cast state. b) The Scheil solidification calculation of this composition.

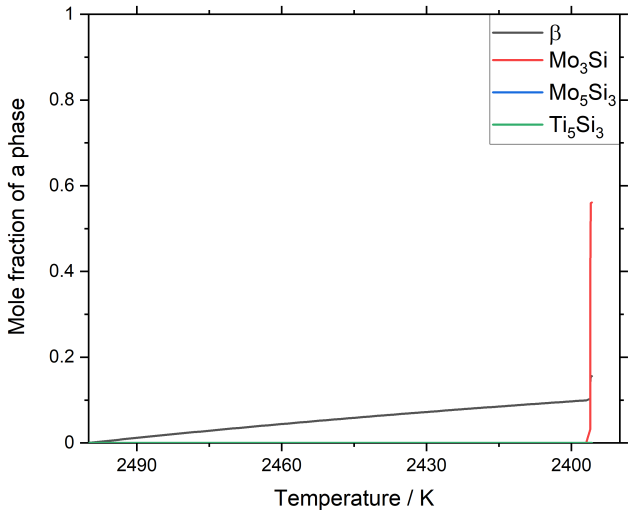

Figure 6.27.: The calculated phase fraction diagram of sample SSC8, 75Mo-15Si-10Ti.

Table 6.13.: Phase compositions of the sample SSC9, 20Mo-20Si-60Ti.

20Mo-20Si-60Ti			
	x(Mo) / at.%	x(Si) / at.%	x(Ti) / at.%
β	34.8 $\pm$ 5.3	4.1 $\pm$ 0.4	61.1 $\pm$ 5.3
Ti_5Si_3	7.8 $\pm$ 1.5	37.4 $\pm$ 0.3	54.7 $\pm$ 1.6

6.4.3.9. SSC9: 20Mo-20Si-60Ti

The microstructure of the sample 20Mo-20Si-60Ti is shown in Figure 6.28a. It consists almost entirely of a lamellar structure of β and Ti_5Si_3. There are some larger, continuous grains of Ti_5Si_3 that may have formed by primary solidification. No other features or phases are present in the sample. The compositions of the phases are listed in Table 6.13. The Scheil solidification calculation shown in Figure 6.28b agrees well with this result. A very small amount of primary solidification of Ti_5Si_3 is predicted, which explains the few larger grains of this phase. Most of the solidification takes place via the eutectic trough L $\rightleftarrows$ β + Ti_5Si_3, which accounts for the lamellae of these phases that make up the bulk of the microstructure. The phase fraction diagram is shown in Figure 6.29. It also agrees well with the experiment. The amount of primary solidified Ti_5Si_3 is rather small, while the final phase fraction of both samples is almost identical.

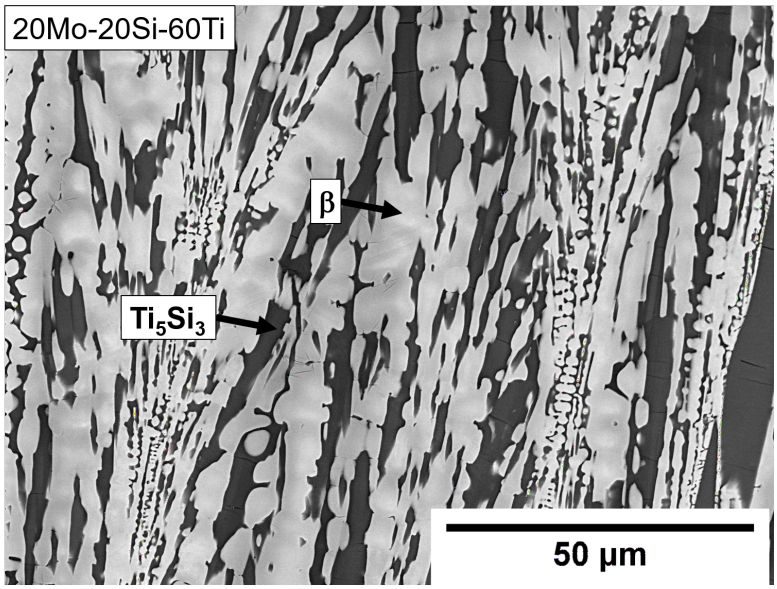

(a)

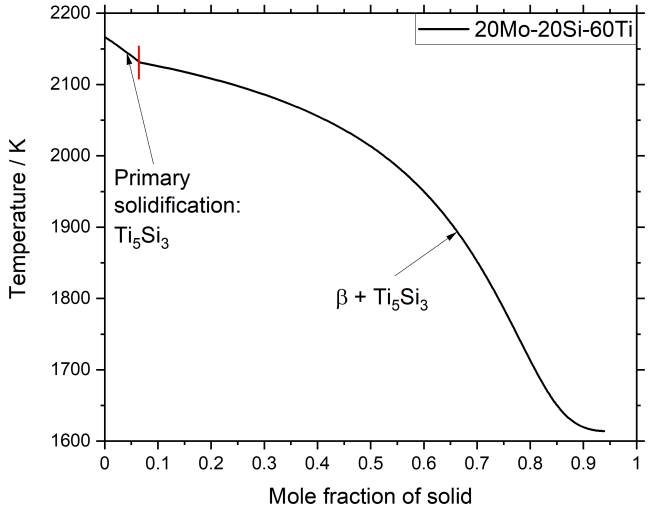

(b)

Figure 6.28.: Results for SSC9, 20Mo-20Si-60Ti. a) The microstructure of the sample SSC9 in the as-cast state. b) The Scheil solidification calculation of this composition.

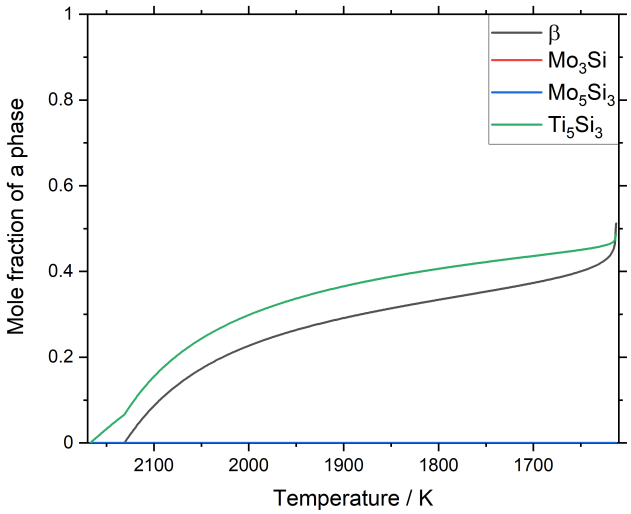

Figure 6.29.: The calculated phase fraction diagram of sample SSC9, 20Mo-20Si-60Ti.

6.4.3.10. SSC10: 50Mo-38Si-12Ti

The microstructure of the sample 50Mo-38Si-12Ti is shown in Figure 6.30a. The majority of the sample consists of Mo_5Si_3, with some continuous grains of Mo_3Si present in a much smaller fraction. Due to the rather brittle nature of the sample, which is composed entirely of intermetallic phases, a fairly large amount of porosity and cracking is visible. The phase compositions are listed in Table 6.14. The Scheil solidification calculation is shown in Figure 6.30b. It is in only partial agreement with the experiment. The fact that the vast majority of the sample consists of primary solidified Mo_5Si_3 is accurately predicted. However, the calculations subsequently hit the eutectic trough L $\rightleftarrows$ Mo_5Si_3 + $MoSi_2$. In the experiment, the presence of the disilicide was not detected anywhere in the sample. Conversely, the phase Mo_3Si found experimentally was not predicted by the calculation. Although the line of double saturation is hit only for the last 2-3 mole percent of solid formed, this is not an insignificant deviation, as it indicates that this sample composition has a rather different solidification path in reality than suggested by the calculation. Similarly, the phase fraction diagram shown in Figure 6.31 is only in partial agreement with the experiment. Nearly 100% of the solid phases formed are expected to be Mo_5Si_3, which overestimates the actual phase fraction. Of course, since there is no formation reaction for Mo_3Si according to the calculation, this phase does not appear in the phase fraction diagram. Instead, a small single digit percentage of $MoSi_2$ is expected. This result indicates that the position of the temperature maximum of the liquidus projection in the region of primary solidification of Mo_5Si_3 requires some refinement. According to the calculation, the slope results in the liquid concentration to fall in the direction of Si-rich compositions. The experiment however shows that for this alloy,

Table 6.14.: Phase compositions of the sample SSC10, 50Mo-38Si-12Ti.

50Mo-38Si-12Ti			
	x(Mo) / at.%	x(Si) / at.%	x(Ti) / at.%
Mo_3Si	67.5 ± 0.6	23.2 ± 0.3	9.4 ± 0.8
Mo_5Si_3	52.9 ± 0.4	36.1 ± 0.4	10.9 ± 0.3

Table 6.15.: Phase compositions of the sample SSC11, 20Mo-37.5Si-42.5Ti.

20Mo-37.5Si-42.5Ti			
	x(Mo) / at.%	x(Si) / at.%	x(Ti) / at.%
β	57.5 ± 1.6	5.6 ± 0.7	36.9 ± 1.2
Mo_5Si_3	23.6 ± 0.7	37.1 ± 0.4	39.3 ± 0.8
Ti_5Si_3	16.8 ± 1.5	37.1 ± 0.8	46.0 ± 1.6

the liquid moves towards metal-rich compositions and follows a similar solidification path as the alloy SSC7.

6.4.3.11. SSC11: 20Mo-37.5Si-42.5Ti

The microstructure of the sample 20Mo-37.5Si-42.5Ti is shown in Figure 6.32a. Three phases are visible: Ti_5Si_3, Mo_5Si_3 and β. Both silicides are present as large, continuous grains, while β is present as small precipitates intertwined with Ti_5Si_3. The fraction of β is rather small, while those of the silicides appear to be fairly equal. The phase compositions are listed in Table 6.15. The result of the Scheil solidification calculation shown in Figure 6.32b is in good agreement with the experiment. In the first step, the primary solidification of Mo_5Si_3 is correctly predicted. In the next step, the eutectic reaction L$\rightleftarrows$$Mo_5Si_3$+$Ti_5Si_3$ is reached. Since no other structures have formed to inhibit further growth of the primary solidified grains, it is quite possible that these will continue to grow while Ti_5Si_3 grains are formed. In this case, despite the eutectic reaction, no lamellar structure would be expected, but the structure observed experimentally is entirely possible. However, the β phase, which is most likely formed by a eutectic trough L $\rightleftarrows$ β + Ti_5Si_3 according to the micrograph, is completely missing from the calculation result. This is most likely again a result of the termination condition of Thermo-Calc, since the solidification path should eventually hit this eutectic trough. The phase fraction diagram for this composition, shown in Figure 6.33, is also in fairly good agreement with the experiment, except for the absence of the β phase in the calculation.

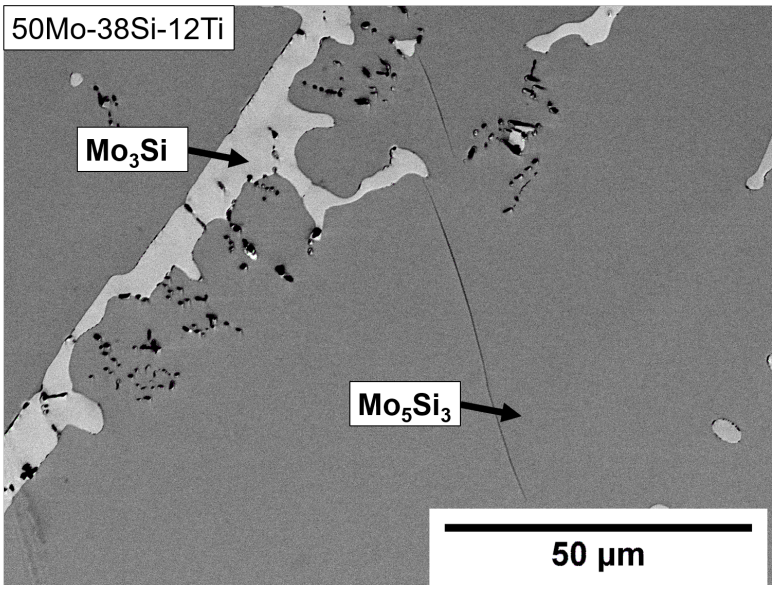

(a)

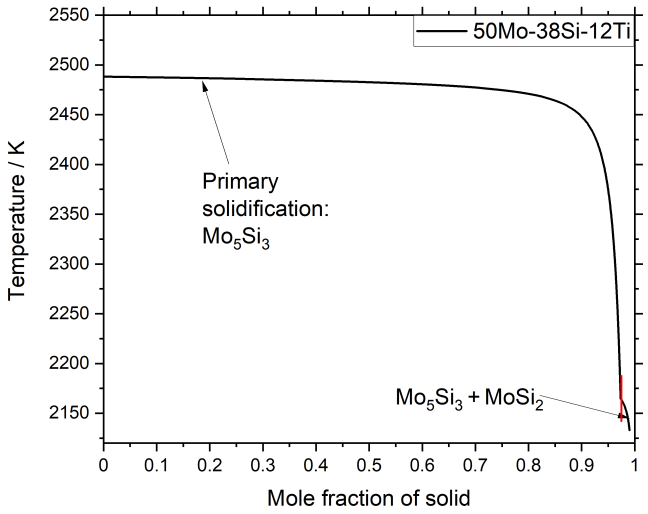

(b)

Figure 6.30.: Results for SSC10, 50Mo-38Si-12Ti. a) The microstructure of the sample SSC10 in the as-cast state. b) The Scheil solidification calculation of this composition.

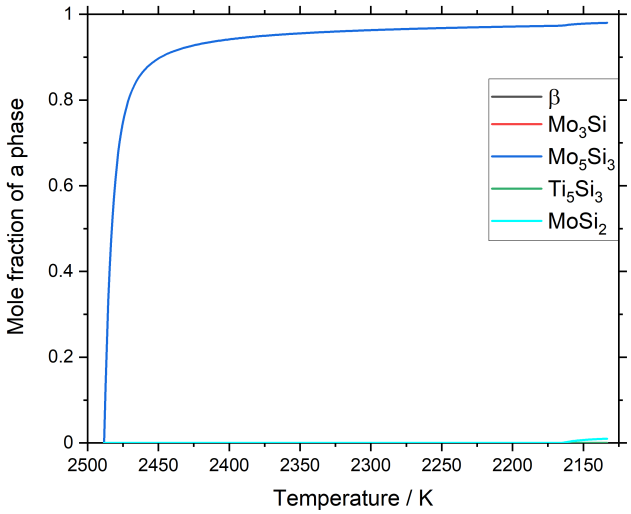

Figure 6.31.: The calculated phase fraction diagram of sample SSC10, 50Mo-38Si-12Ti.

6.4.3.12. SSC12: 47.5Mo-12.5Si-40Ti

The microstructure of the sample 47.5Mo-12.5Si-40Ti is shown in Figure 6.34a. The β phase is present both as larger, continuous grains and as small, lamellar precipitates intertwined with Ti_5Si_3. The silicide is not present in other forms and no other silicides or structures are present. In addition, numerous small circular precipitates of pure or nearly pure Ti are visible. The compositions of the phases are listed in Table 6.16. The result of the Scheil solidification calculation, shown in Figure 6.34b, is in good agreement with the experiment. The primary solidification of β is accurately predicted. The calculation then predicts the eutectic formation of β and Mo_3Si. No evidence for the phase Mo_3Si was found in the sample. The remaining liquid then solidifies according to the eutectic reaction L$\rightleftarrows$ β+Ti_5Si_3, which is in good agreement with the micrograph. A notable difference between calculation and experiment is the presence of nearly pure Ti in the sample, which is not predicted. However, such a phase is not known to exist in the literature, so it is unclear why or how these precipitates are formed, and it is therefore difficult to draw conclusions. For this reason, the absence of Ti in the calculation is logical, as no suitable phase is present in the dataset. The phase fraction diagram shown in Figure 6.35 also agrees well. The β phase is expected to make up the majority of the solid fractions formed, with a significantly smaller amount of Ti_5Si_3. Both are in good agreement with the micrograph. The phase fraction of Mo_3Si is calculated to be about 5%, which should be high enough to be detectable in the SEM. Why this phase does not appear to have formed is unclear at this point.

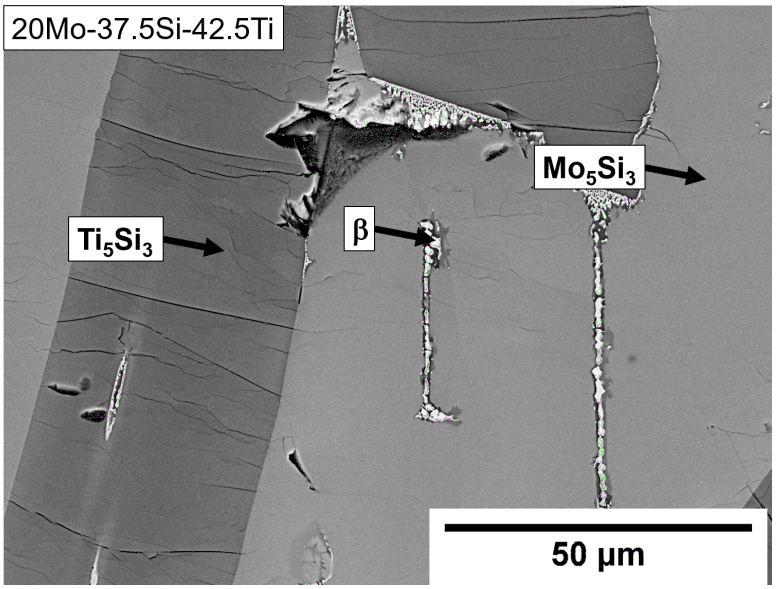

(a)

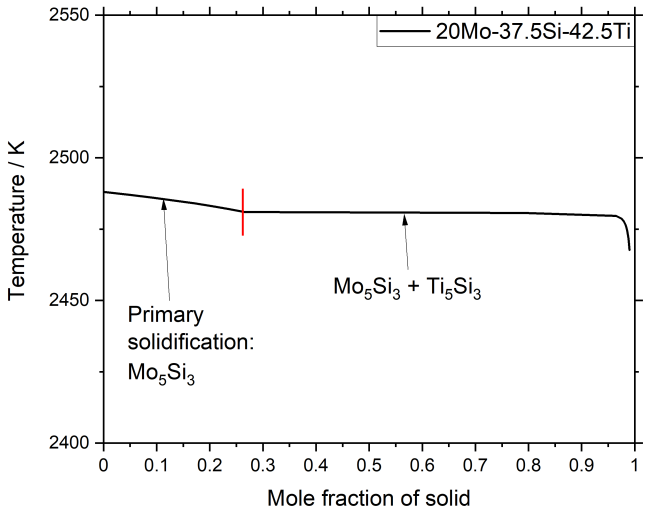

(b)

Figure 6.32.: Results for SSC11, 20Mo-37.5Si-42.5Ti. a) The microstructure of the sample SSC11 in the as-cast state. b) The Scheil solidification calculation of this composition.

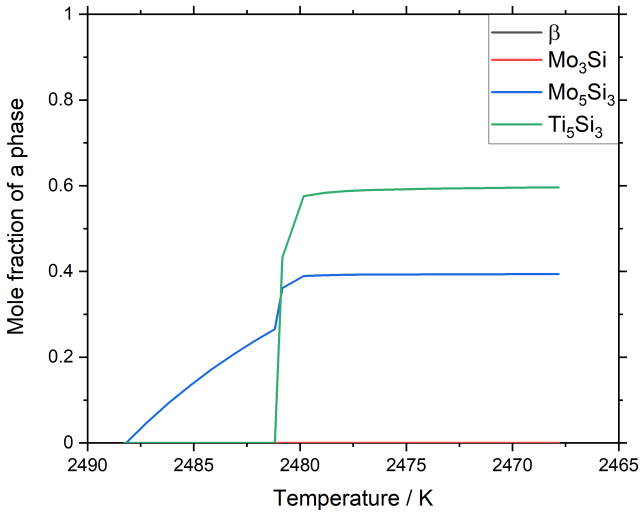

Figure 6.33.: The calculated phase fraction diagram of sample SSC11, 20Mo-37.5Si-42.5Ti.

Table 6.16.: Phase compositions of the sample SSC12, 47.5Mo-12.5Si-40Ti.

47.5Mo-12.5Si-40Ti			
	x(Mo) / at.%	x(Si) / at.%	x(Ti) / at.%
β	70.4 ± 5.1	3.8 ± 0.5	25.8 ± 4.9
Ti_5Si_3	13.6 ± 2.7	35.9 ± 1.8	50.5 ± 1.6
Ti	1.5 ± 0.3	0.7 ± 0.7	97.8 ± 1.0

6.4.3.13. SSC13: 45Mo-21Si-34Ti

The microstructure of the sample 45Mo-21Si-34Ti is shown in Figure 6.36a. It consists of a rather large fraction of continuous grains of Mo_3Si as well as two different lamellar structures. First, there is a lamellar structure of β and Mo_3Si, second there is another lamellar structure of β and Ti_5Si_3. There are also numerous small precipitations of Ti. In this sample, these precipitates typically form dendritic structures, suggesting that they are not due to insufficient mixing of the materials, but are an effect of the solidification of the sample. The phase compositions are listed in Table 6.17. Except for the inexplicable unknown Ti phase, the Scheil solidification calculation is in very good agreement with the experiment. First, Mo_3Si is formed by primary solidification, followed by eutectic formation of β and Mo_3Si. Finally, the remaining liquid composition follows another eutectic trough, $L \rightleftarrows \beta + Ti_5Si_3$. These predictions agree exactly with the microstructure of the sample. With respect to the Ti precipitates, it should be noted that this sample was also examined in the as-cast state by Schliephake et al. [12], and the microstructure they reported

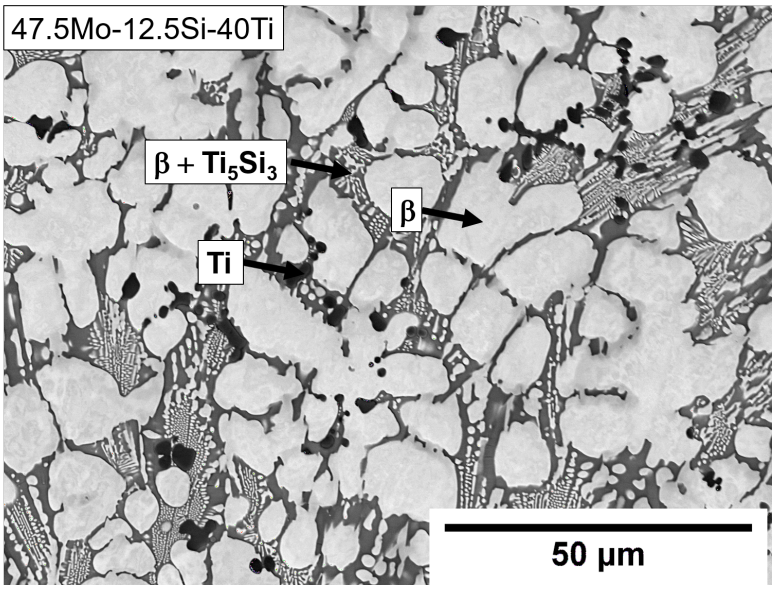

(a)

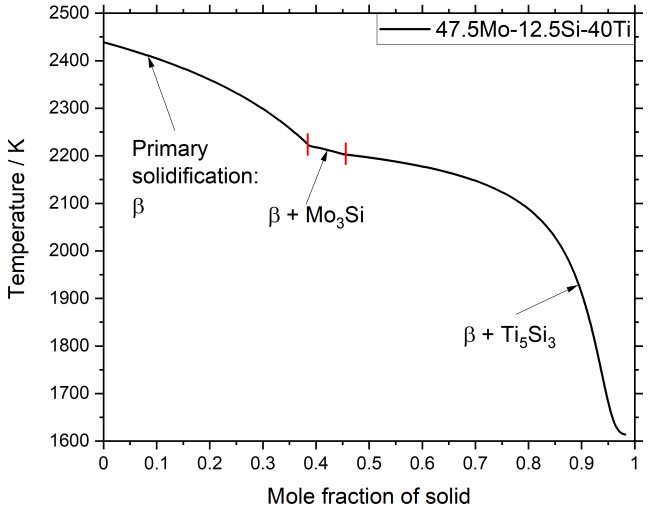

(b)

Figure 6.34.: Results for SSC12, 47.5Mo-12.5Si-40Ti. a) The microstructure of the sample SSC12 in the as-cast state. b) The Scheil solidification calculation of this composition.

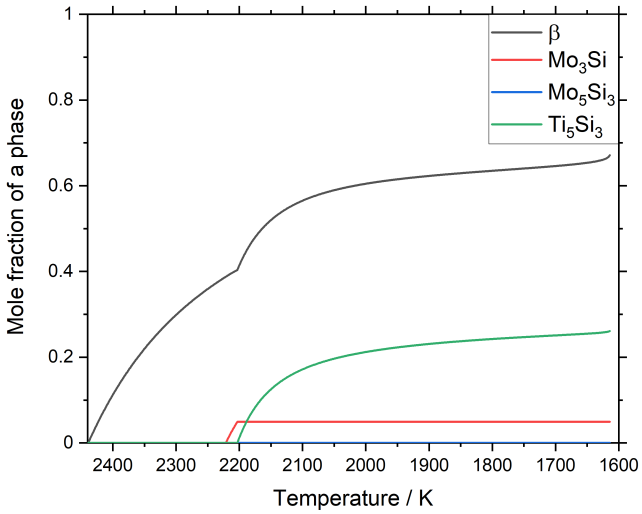

Figure 6.35.: The calculated phase fraction diagram of sample SSC12, 47.5Mo-12.5Si-40Ti.

was virtually identical to that found in this work, but with far fewer pure Ti precipitates. The micrograph of this sample as reported in their paper is shown in Figure 6.37. Since the samples used by Schliephake et al. were much larger than those used in this work (approximately 150 g and 1.5 g, respectively), it is reasonable to assume that the cooling rate is a critical factor in the formation of the Ti precipitates. However, it should be noted that the conclusion drawn by Schliephake et al. regarding the formation of this structure is not supported by the dataset. They claim that the lamellar structures, even in the as-cast state, are at least partially formed by eutectoid decomposition. However, as explained in chapter 5, eutectoid reactions cannot take place under rapid solidification conditions due to the inhibited diffusion of the solid phases. Furthermore, no eutectoid reactions are reported in this region of the Mo-Si-Ti system or calculated with the dataset of Yang et al. (which are the data accepted in the PanMo database used by Schliephake et al.). Instead, the microstructure of the sample results from two successive eutectic troughs as explained above. Even the equilibration at 1573 K reported by Schliephake et al. where the Mo_3Si fraction decreases and eventually becomes zero, while β and Mo_5Si_3 are formed, is not a true eutectoid reaction since it would require the formation of three solid phases in a ternary system. The phase fraction diagram for this composition is shown in Figure 6.38. It also agrees rather well with the experiment, with the majority of the sample consisting of Mo_3Si, the β phase as the second most formed phase and Ti_5Si_3 making up the rest of the microstructure.

In the context of this sample, it is also useful to plot the composition of the β phase over the temperature during solidification. The result of this calculation is shown in Figure 6.39. It can

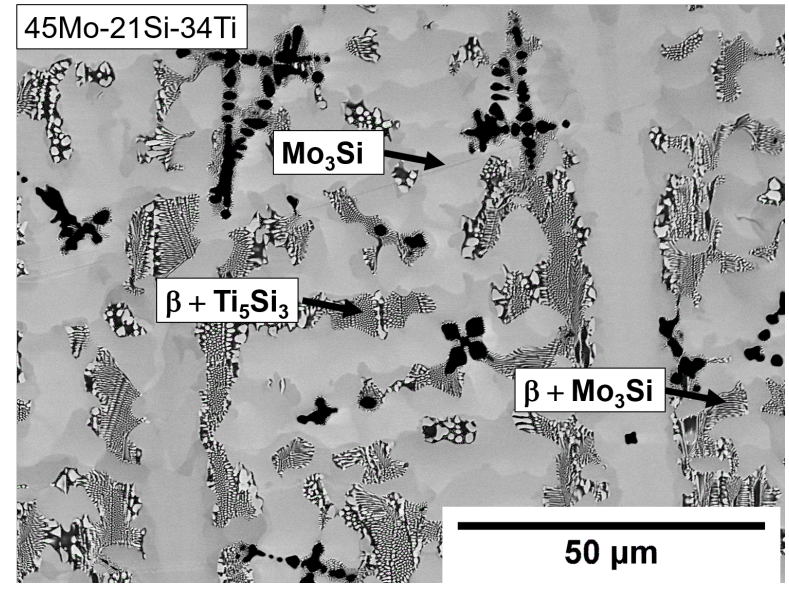

(a)

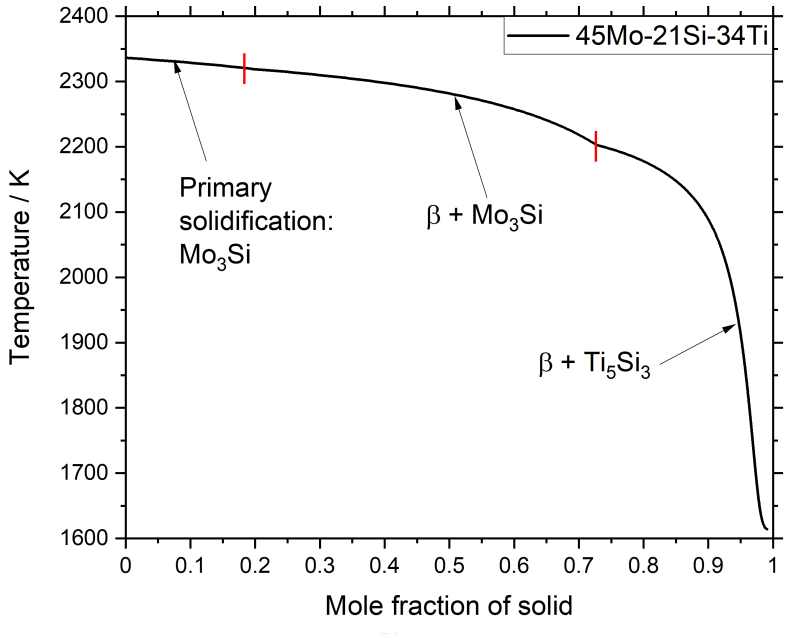

(b)

Figure 6.36.: Results for SSC13, 45Mo-21Si-34Ti. a) The microstructure of the sample SSC13 in the as-cast state. b) The Scheil solidification calculation of this composition.

Table 6.17.: Phase compositions of the sample SSC13, 45Mo-21Si-34Ti.

45Mo-21Si-34Ti			
	x(Mo) / at.%	x(Si) / at.%	x(Ti) / at.%
β	70.2 ± 5.9	6.1 ± 0.9	23.8 ± 5.4
Mo_3Si	52.8 ± 2.3	21.5 ± 0.4	26.7 ± 2.3
Ti_5Si_3	19.2 ± 1.9	35.5 ± 1.0	45.3 ± 1.1

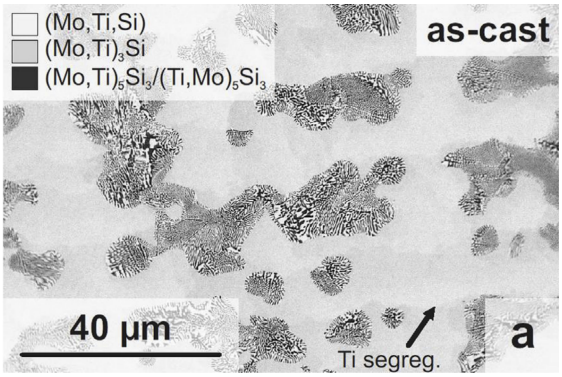

Figure 6.37.: The microstructure of the sample 45Mo-21Si-34Ti in the as-cast state as reported by Schliephake et al. [12]. Image taken directly from the corresponding paper.

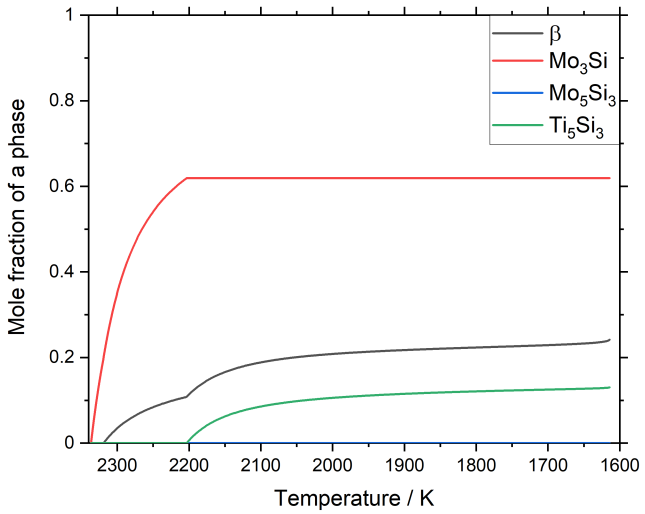

Figure 6.38.: The calculated phase fraction diagram of sample SSC13, 45Mo-21Si-34Ti.

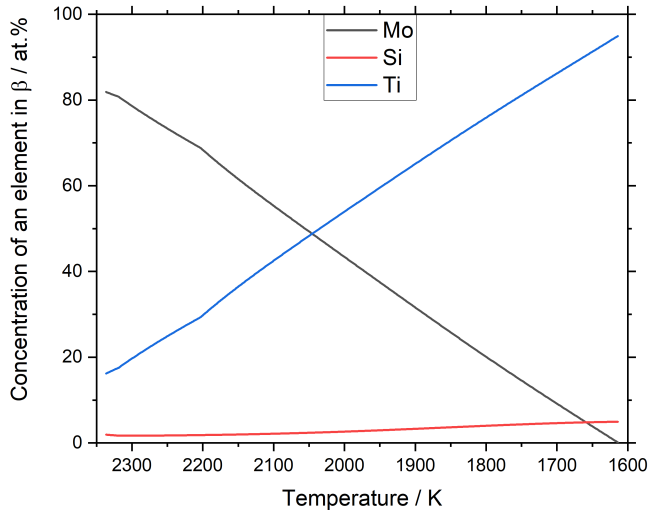

Figure 6.39.: The composition of the β phase of the sample SSC13, 45Mo-21Si-34Ti over the temperature during solidification.

be seen that the Ti concentration in the β phase increases to around 95 at.% over the course of the solidification, which may account for the grains of nearly pure Ti observed experimentally.

6.4.3.14SSC14: 60Mo-30Si-10Ti

The microstructure of the sample 60Mo-30Si-10Ti is shown in Figure 6.40a. It consists of large, continuous grains of Mo_5Si_3 and Mo_3Si. Due to the brittle nature of the sample, which consists entirely of intermetallic phases, a large amount of cracking and porosity is visible. Other than that, no additional phases or features can be detected. Overall, the microstructure is quite similar to that of sample SSC7. The phase compositions of this sample are listed in Table 6.18. The result of the Scheil solidification calculation is shown in Figure 6.40b. As in the case of SSC7, the agreement is very high. The solidification path between SSC14 and SSC7 is nearly identical, so it will not be explained again here. The phase fraction diagram shown in Figure 6.41 is also in good agreement with the experiment. The majority of Mo_5Si_3 is formed during primary solidification. The subsequent eutectic reaction leads almost exclusively to the formation of Mo_3Si, which explains the large, continuous grains of both phases.

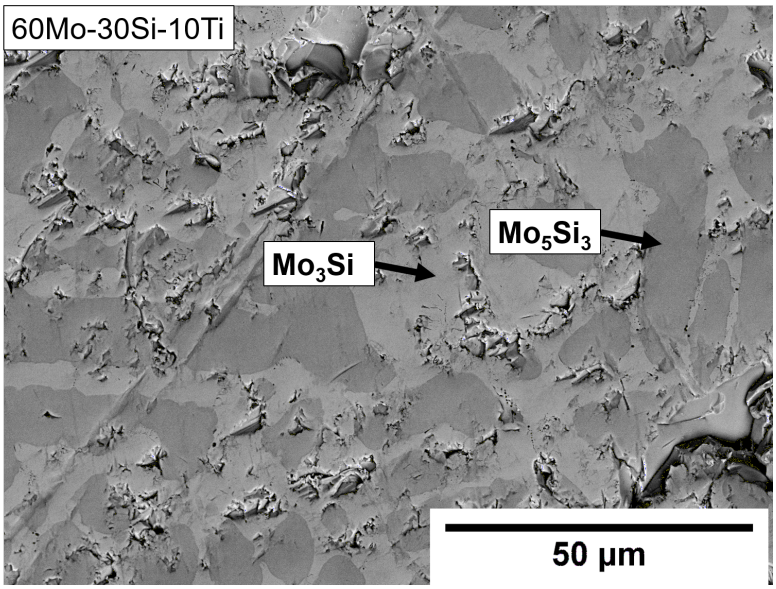

(a)

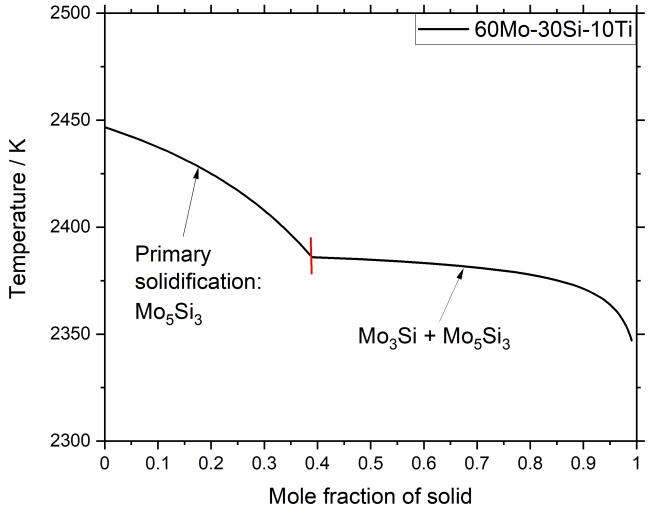

(b)

Figure 6.40.: Results for SSC14, 60Mo-30Si-10Ti. a) The microstructure of the sample SSC14 in the as-cast state. b) The Scheil solidification calculation of this composition.

Table 6.18.: Phase compositions of the sample SSC14, 60Mo-30Si-10Ti.

60Mo-30Si-10Ti			
	x(Mo) / at.%	x(Si) / at.%	x(Ti) / at.%
Mo_3Si	69.6 ± 0.7	23.8 ± 0.6	6.7 ± 0.5
Mo_5Si_3	55.4 ± 0.8	36.1 ± 0.7	8.4 ± 0.7

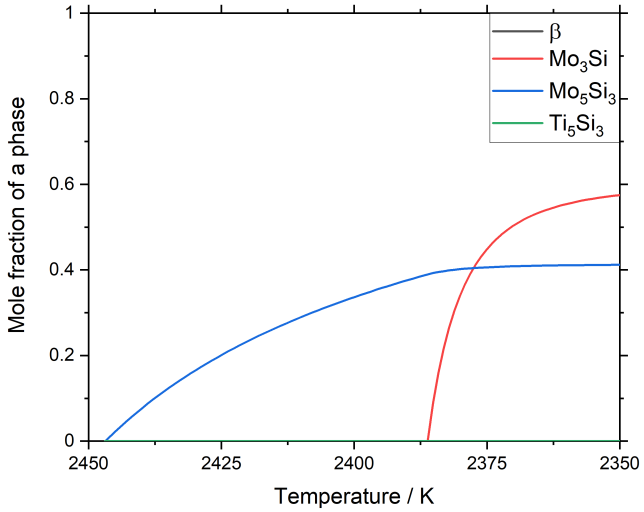

Figure 6.41.: The calculated phase fraction diagram of sample SSC14, 60Mo-30Si-10Ti.

6.4.3.15. Conclusions

In conclusion, the dataset by Yang et al. [16] is fairly well suited for predicting the microstructures formed by rapid solidification when using a contemporary solver. The regions of primary solidification are fairly accurate, and all eutectic troughs are supported by experiments. Many peritectic lines leading to secondary solidification of a single phase under Scheil solidification conditions are also implicitly confirmed. However, several small discrepancies were found, such as inaccurate phase fractions. Most of the differences between calculations and experiments can be explained by the extension of the eutectic and peritectic lines into the compositional space. As explained in section 4.4.1, there are two saddle points in the region of interest, each with a eutectic trough on one side and a peritectic reaction on the other. By slightly changing the location of each saddle point and moving the eutectic and peritectic lines accordingly, many of the observed microstructures could likely be accurately calculated. Overall, however, the liquidus projection of Yang et al. has been shown to be largely suitable for predicting microstructures

formed by casting samples in an arc melter and should be retained to a large extent in future reassessments of the Mo-Si-Ti system.

6.4.4. The effect of quenching on the microstructure

To investigate the effect of quenching on microstructure and phase composition compared to furnace cooling, ten specimens were prepared. Each of the samples was subjected to a two-phase annealing regime. After arc melting, they were heat treated at 1573 K for 330 h and furnace cooled. In this state, they were analyzed by SEM with EDX. Subsequently, the same samples were annealed at the identical temperature for another 48 h to re-equilibrate them and then quenched in water. The samples were analyzed in this condition in the same manner. This method is schematically shown in Figure 6.42. Selected samples were additionally analyzed by EPMA to investigate if there are differences between the two electron optical methods for Mo-Si-Ti samples or if the simpler and less time demanding EDX is sufficient. The compositions of the samples as well as the expected phases according to the dataset of Yang et al. [16] are listed in Table 6.19. Figure 6.43 shows the sample compositions in the phase diagram at 1573 K, also calculated with the dataset of Yang et al. The compositions of samples QE1-QE7 were chosen to investigate one sample per phase region. QE8-QE10 were then subsequently prepared to obtain additional informations about the equilibria β+Mo_5Si_3, β+Mo_5Si_3+Ti_5Si_3 and Mo_3Si+Mo_5Si_3, respectively. It should be noted that of the ten samples heat treated in this manner, nine were also analyzed in the as-cast condition and previously discussed in section 6.4.3. Their respective designations have been changed for this section, but the following discussion will clarify which SSC designation corresponds to which QE designation.

6.4.4.1. QE1: 22Mo-33Si-45Ti

The microstructure of the sample 22Mo-33Si-45Ti is shown in Figure 6.44. The three expected phases β, Mo_5Si_3 and Ti_5Si_3 are present in both states. Due to the Mo content, the β phase appears in the lightest shade, Mo_5Si_3 is seen as a medium gray and Ti_5Si_3 is the darkest gray. While both silicides have fairly large grains, β is present as fine precipitates. There is no difference between the microstructures of the furnace cooled and the water quenched samples, neither in the shape nor in the distribution of the grains. The compositions of the phases, listed in Table 6.20, are also virtually identical for both conditions. This is a clear indication that for this sample the slow cooling had little or no effect on the sample. To investigate possible differences between EDX and EPMA, the sample was additionally analyzed in the quenched state by EPMA. The result is shown in Table 6.21. It can be seen that the difference between EPMA and EDX is generally fairly minor. The only significant difference lies in the standard deviation of the values, which is

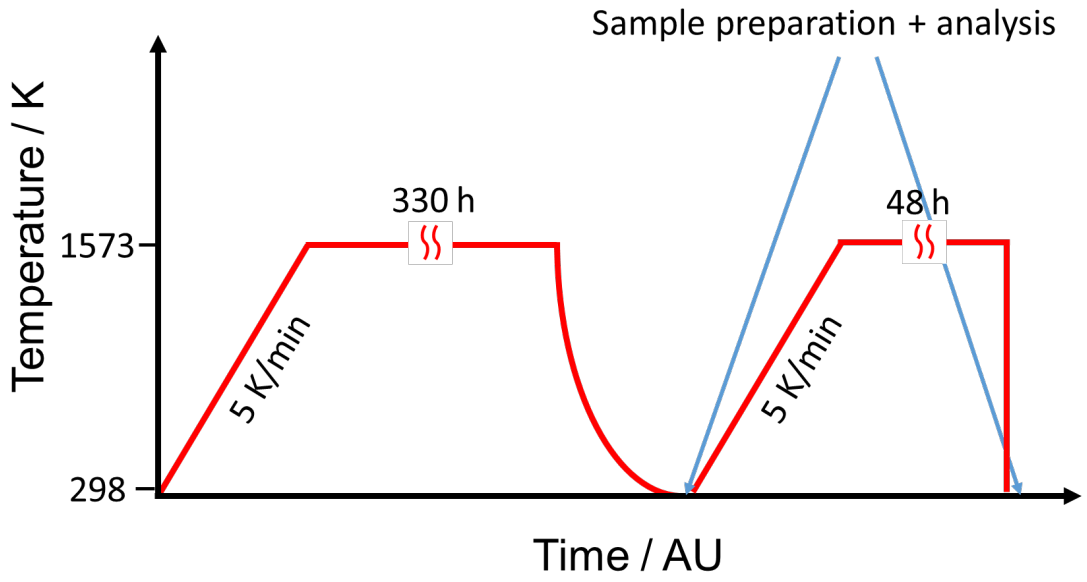

Figure 6.42.: A schematic drawing of the two-staged heat treatment used to investigate the effect of quenching compared to furnace cooling.

Table 6.19.: The nominal compositions and expected phases according to the dataset of Yang et al. [16] of the samples used to study the effect of quenching on the microstructure and phase composition.

Sample designation	Nominal composition	Expected phases
QE1	22Mo-33Si-45Ti	β+Mo_5Si_3+Ti_5Si_3
QE2	44.5Mo-23.5Si-32Ti	β+Mo_5Si_3
QE3	53Mo-32Si-15Ti	Mo_3Si+Mo_5Si_3
QE4	75Mo-15Si-10Ti	β+Mo_3Si
QE5	50Mo-38Si-12Ti	Mo_5Si_3
QE6	20Mo-37.5Si-42.5Ti	Mo_5Si_3+Ti_5Si_3
QE7	47.5Mo-12.5Si-40Ti	β+Ti_5Si_3
QE8	45Mo-21Si-34Ti	β+Mo_5Si_3
QE9	25Mo-33Si-42Ti	β+Mo_5Si_3+Ti_5Si_3
QE10	60Mo-30Si-10Ti	Mo_3Si+Mo_5Si_3

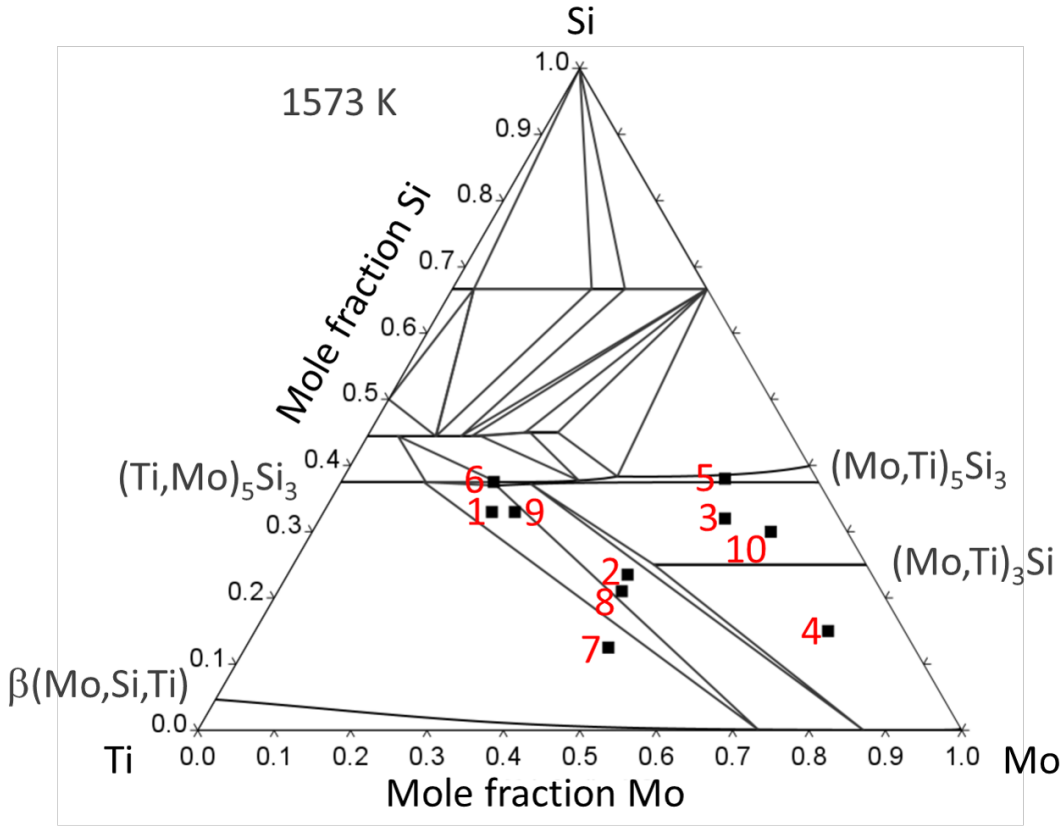

Figure 6.43.: The nominal compositions used in the quenching experiments in the isothermal section at 1573 K of the Mo-Si-Ti system according to the dataset of Yang et al. [16].

typically higher for EDX than for EPMA. However, this is not due to a methodological difference, but to a deliberate choice by the respective operators. While the EDX operator measured a large number of different points per phase and included concentrations with a relatively high scatter, the EPMA operator chose to exclude points with compositions that deviated greatly from the mean before summarizing the result. While this method eliminates unreliable data and measurements where the different phases were inadvertently excited at the same time, it can introduce bias into the experiment and skew the results toward the "desired" concentrations. However, from the similar mean values of the EDX and EPMA measurements, it can be concluded that no such shift was introduced in this case and that both techniques are equally reliable.

Compared to the microstructure and phase composition in the as-cast condition (SSC5, Figure 6.14 on page 112 and Table 6.5 on page 111, respectively), annealing slightly altered the sample. The microstructure appears largely identical, but the composition of the β phase

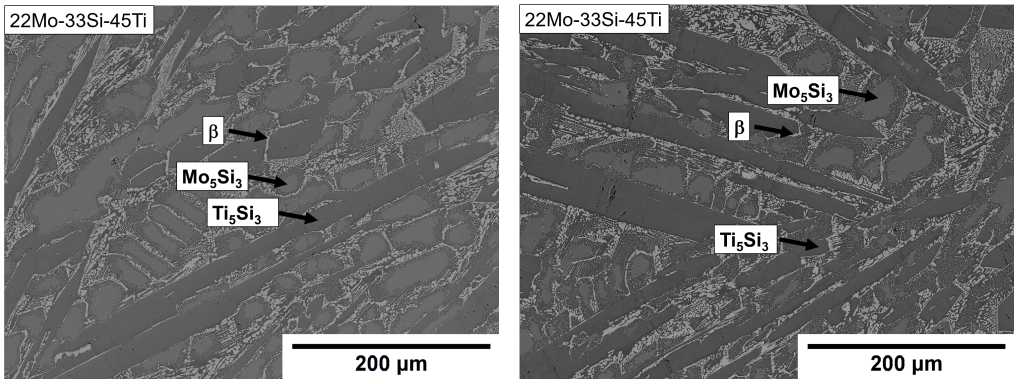

(a) **(b)**

Figure 6.44.: The microstructure of the sample QE1, 22Mo-33Si-45Ti. a) After furnace cooling, b) after quenching.

Table 6.20.: The composition of the phases of the sample QE1, 22Mo-33Si-45Ti, after furnace cooling and after quenching.

22Mo-33Si-45Ti						
	Furnace cooled			water quenched		
	x(Mo) / at.%	x(Si) / at.%	x(Ti) / at.%	x(Mo) / at.%	x(Si) / at.%	x(Ti) / at.%
β	61.7 ± 2.4	6.5 ± 1.5	31.8 ± 1.6	65.5 ± 3.2	6.3 ± 2.4	28.2 ± 1.4
Mo_5Si_3	22.7 ± 0.5	36.9 ± 1.0	40.4 ± 0.8	22.2 ± 0.5	37.1 ± 0.3	40.7 ± 0.4
Ti_5Si_3	15.1 ± 2.4	37.2 ± 0.5	47.6 ± 2.3	15.7 ± 1.9	37.3 ± 0.5	47.0 ± 2.0

changed significantly. For both silicides, however, the compositions in the cast state and after annealing are nearly identical. This most likely indicates that equilibration occurred mainly in the β phase, where diffusion is expected to be fastest, while the silicides were either already close to equilibrium or no significant diffusion could take place under the experimental conditions.

Table 6.21.: The composition of the phases of the sample QE1, 22Mo-33Si-45Ti, after quenching, measured by EMPA

22Mo-33Si-45Ti			
	Water quenched EPMA		
	x(Mo) / at.%	x(Si) / at.%	x(Ti) / at.%
β	61.4 ± 1.8	4.5 ± 0.8	34.1 ± 1.6
Mo_5Si_3	20.9 ± 0.2	37.0 ± 0.1	42.1 ± 0.2
Ti_5Si_3	15.2 ± 0.2	37.0 ± 0.2	47.7 ± 0.3

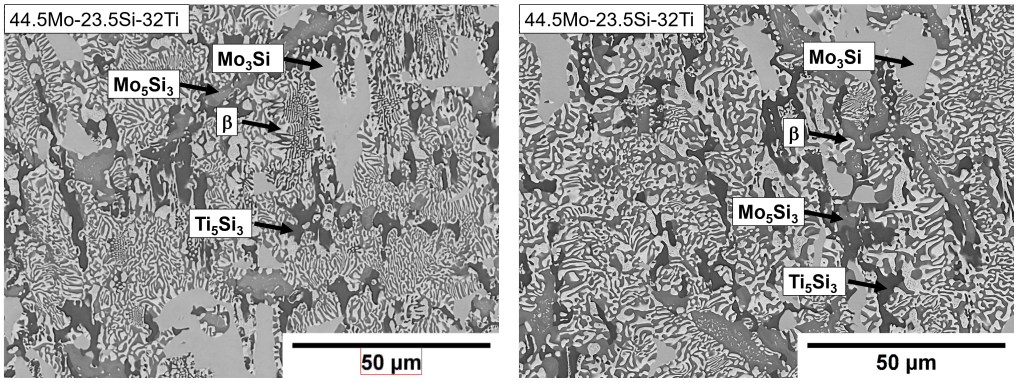

Figure 6.45.: The microstructure of the sample QE2, 44.5Mo-23.5Si-32Ti. a) After furnace cooling, b) after quenching.

Table 6.22.: The composition of the phases of the sample QE2, 44.5Mo-23.5Si-32Ti, after furnace cooling and after quenching.

44.5Mo-23.5Si-32Ti						
	Furnace cooled			Water quenched		
	x(Mo) / at.%	x(Si) / at.%	x(Ti) / at.%	x(Mo) / at.%	x(Si) / at.%	x(Ti) / at.%
β	73.4 ± 4.3	6.4 ± 1.7	20.1 ± 2.9	79.4 ± 2.1	3.3 ± 1.1	17.3 ± 1.1
Mo_3Si	54.1 ± 0.6	22.2 ± 0.3	23.8 ± 0.7	54.7 ± 2.5	22.4 ± 0.8	22.9 ± 3.1
Mo_5Si_3	30.7 ± 2.1	36.5 ± 0.5	32.7 ± 2.0	31.9 ± 5.6	36.6 ± 0.4	31.5 ± 5.4
Ti_5Si_3	19.0 ± 1.9	36.5 ± 1.1	44.5 ± 1.0	18.2 ± 3.8	36.8 ± 1.4	45.0 ± 2.5

6.4.4.2. QE2: 44.5Mo-23.5Si-32Ti

The microstructure of the sample 44.5Mo-23.5Si-32Ti is shown in Figure 6.45. Instead of the two expected phases, β and Mo_5Si_3, all four possible stable phases in the metal-rich region of the phase diagram are present. Again, β is the brightest, followed by Mo_3Si, then Mo_5Si_3, and the darkest is Ti_5Si_3. The microstructure is generally extremely fine, with only Mo_3Si and Mo_5Si_3 appearing as somewhat larger grains. The microstructure appears to be slightly different between the two heat treatments. In the quenched sample, the β and Mo_5Si_3 precipitates appear to be coarser than after furnace cooling, while slightly less Mo_3Si appears to be present. Similarly, the phase compositions listed in Table 6.22 are slightly different, although not by much. These results indicate that for a sample with such a complex microstructure, equilibration may not be possible within the given time frame. It is possible that the effect is not a result of the cooling rate, but rather that the additional 48 h at 1573 K changed the microstructure for this sample.

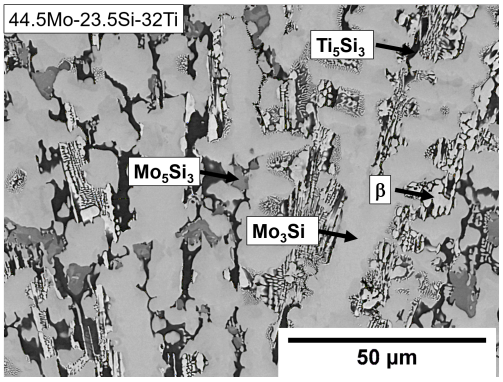

Figure 6.46.: The microstructure of the sample QE2, 44.5Mo-23.5Si-32Ti, in the as-cast state.

To provide further evidence to support or reject this theory, the heat treated microstructure was compared with the as-cast state, designated SSC6 in the previous section. The microstructure is shown again in Figure 6.46 for convencience. It is in fact a rather complex microstructure even in the as-cast state, with both Mo_5Si_3 and Mo_3Si as primary solidified phases and two distinct eutectic structures. One eutectic is between β and Mo_3Si, while the other is between β and Ti_5Si_3. These two eutectic structures, recognizable by the fine lamellar morphologies of the two respective phases, have nearly the same volume fraction, whereas primary solidified Mo_3Si accounting for the majority of the total volume fraction. Primary solidified Mo_3Si, on the other hand, is present in comparatively small amounts. Not only is this microstructure quite complex, with four phases present, but it is also far from equilibrium at 1573 K. The majority of the cast structure consists of Mo_3Si, both in large grains and in a fine eutectic structure, while this phase is not stable at all in equilibrium. Therefore, it is reasonable to expect that such a sample would require more than 330 h to reach equilibrium, considering the slow diffusion in Mo alloys. For this reason, the sample that was previously annealed for a total of 378 h (330 h/fc + 48 h/wq) was annealed for another 330 h at 1573 K. The microstructure after this step is shown in Figure 6.47. While the microstructure has changed compared to the shorter annealing time, there is still a significant amount of Ti_5Si_3 present, indicating a very high barrier for this sample to reach equilibrium. Therefore, it was decided that if a sample did not reach equilibrium after 330 h, it could not be expected to reach equilibrium in any reasonable or viable amount of time.

6.4.4.3. QE3: 53Mo-32Si-15Ti

The microstructure of the sample 53Mo-32Si-15Ti is shown in Figure 6.48. It consists of the two expected phases, Mo_3Si and Mo_5Si_3, the former being the lighter shade and the latter the darker gray. The Mo_5Si_3 grains contain Mo_3Si precipitates inside, while Mo_3Si is virtually free of other phases. Different grains of Mo_3Si can be distinguished by slightly different hues; however, there is no detectable difference in composition as a function of hue. This means that the difference

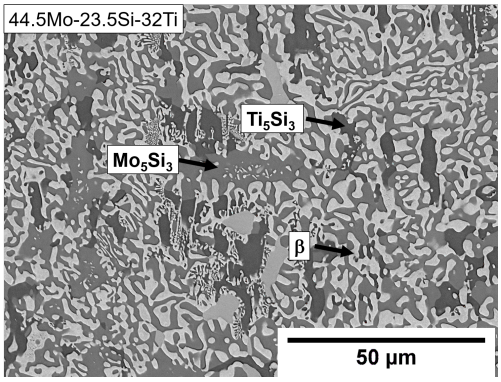

Figure 6.47.: The microstructure of the sample QE2, 44.5Mo-23.5Si-32Ti, after a total of 708 h at 1573 K, water quenched after the final step.

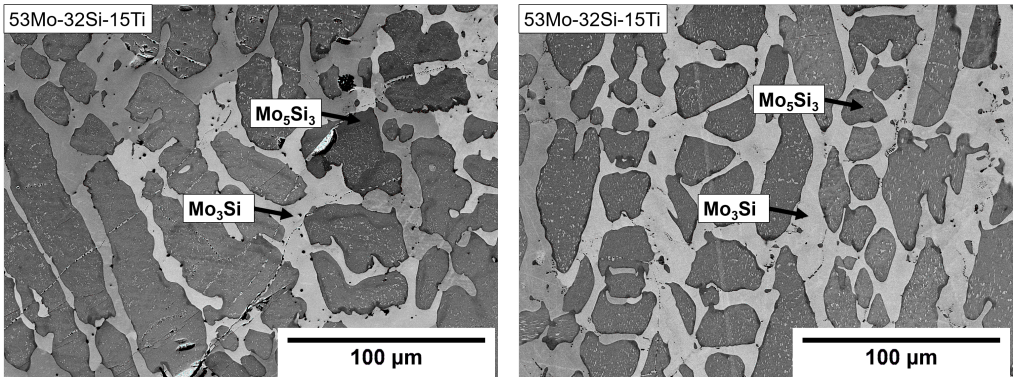

(a) **(b)**

Figure 6.48.: The microstructure of the sample QE3, 53Mo-32Si-15Ti. a) After furnace cooling, b) after quenching.

in hue is most likely an effect of grain orientation. The microstructure between the two states is virtually identical, as are the compositions of the phases, as shown in Table 6.23. This indicates that for this sample composition there is little or no difference between furnace cooling and water quenching.

As with sample QE1, this sample was also measured by EPMA to see possible differences between EPMA and EDX. The result of the EPMA measurement is shown in Table 6.24. As

Table 6.23.: The composition of the phases of the sample QE3, 53Mo-32Si-15Ti, after furnace cooling and after quenching.

53Mo-32Si-15Ti						
	Furnace cooled			Water quenched		
	x(Mo) / at.%	x(Si) / at.%	x(Ti) / at.%	x(Mo) / at.%	x(Si) / at.%	x(Ti) / at.%
Mo_3Si	62.1 ± 5.4	23.6 ± 1.9	13.3 ± 4.6	64.3 ± 5.3	23.2 ± 0.4	12.5 ± 5.2
Mo_5Si_3	49.0 ± 3.1	35.3 ± 1.4	14.9 ± 2.2	49.3 ± 2.5	35.9 ± 0.9	14.8 ± 2.6

Table 6.24.: The composition of the phases of the sample QE3, 53Mo-32SI-15Ti, after quenching, measured by EMPA

53Mo-32Si-15Ti			
	Water quenched EPMA		
	x(Mo) / at.%	x(Si) / at.%	x(Ti) / at.%
Mo_3Si	63.3 ± 0.3	23.7 ± 0.2	13.0 ± 0.1
Mo_5Si_3	47.7 ± 0.3	37.0 ± 0.4	15.2 ± 0.1

Table 6.25.: The composition of the phases of the sample QE4, 75Mo-15Si-10Ti, after furnace cooling and after quenching.

75Mo-15Si-10Ti						
	Furnace cooled			Water quenched		
	x(Mo) / at.%	x(Si) / at.%	x(Ti) / at.%	x(Mo) / at.%	x(Si) / at.%	x(Ti) / at.%
β	90.1 ± 2.9	2.8 ± 0.6	5.7 ± 0.8	90.8 ± 1.6	3.3 ± 1.2	5.9 ± 0.7
Mo_3Si	67.8 ± 2.1	22.1 ± 1.3	9.6 ± 1.1	67.8 ± 3.9	22.2 ± 1.2	10.0 ± 4.5

before, the difference between the methods is negligible, showing that both are equally suitable for Mo-Si-Ti samples.

A comparison of the annealed sample with the as-cast state (SSC7, Figure 6.24 on page 123 and Table 6.11 on page 122 for microstructure and phase composition, respectively) shows a clear effect of annealing on the microstructure. While the phase compositions appear to have changed relatively little, numerous small precipitates of Mo_3Si have formed within the Mo_5Si_3 grains. This proves that, at least in the case of the Mo silicides, diffusion is fast enough under the experimental conditions that significant changes can occur in the sample during annealing.

6.4.4.4. QE4: 75Mo-15Si-10Ti

The microstructure of the sample 75Mo-15Si-10Ti is shown in Figure 6.49. It consists of the two expected phases, β and Mo_3Si. Here β is the lighter shade and the silicide is the darker. Both the microstructures and the phase compositions, listed in Table 6.25, are identical in both states, indicating that equilibrium has been reached for this sample and that diffusion is too slow for furnace cooling to significantly change the sample. Once more, this sample was additionally measured by EPMA, the result of which is listed in Table 6.26. Again, the difference between EPMA and EDX is negligible. The comparison of all four phases across different samples leads to the conclusion that both analytical techniques are equally viable for Mo-Si-Ti samples.

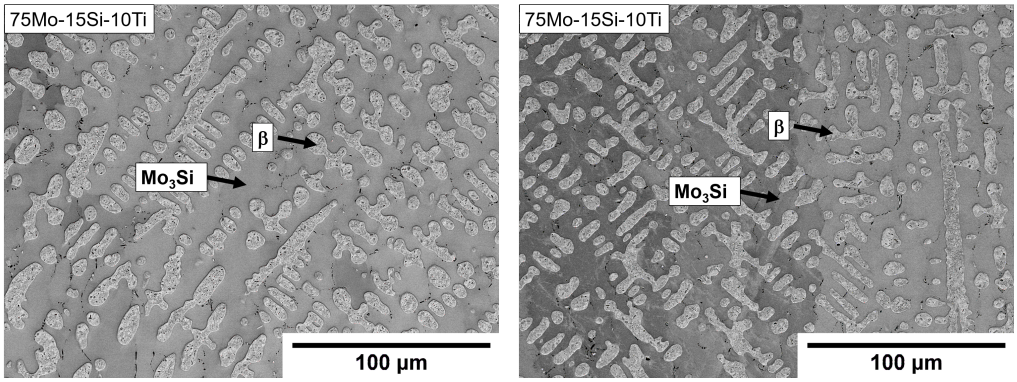

(a) (b)

Figure 6.49.: The microstructure of the sample QE4, 75Mo-15Si-10Ti. a) After furnace cooling, b) after quenching.

Table 6.26.: The composition of the phases of the sample QE4, 75Mo-15Si-10Ti, after quenching, measured by EMPA

75Mo-15Si-10Ti			
	Water quenched EPMA		
	x(Mo) / at.%	x(Si) / at.%	x(Ti) / at.%
β	90.3 ± 0.5	2.3 ± 0.6	7.4 ± 0.3
Mo_3Si	66.2 ± 0.3	22.3 ± 0.1	11.4 ± 0.3

A comparison of the annealed sample with the cast state (SSC8, Figure 6.26 on page 125 and Table 6.12 on page 124 for microstructure and phase composition, respectively) shows remarkably little influence of the heat treatment on the sample. Both the morphology of the phases and their respective compositions are virtually identical in the cast state and after annealing. This may indicate that this sample was already close to thermodynamic equilibrium conditions after casting and no significant equilibration could occur.

6.4.4.5. QE5: 50Mo-38Si-12Ti

The microstructure of the sample 50Mo-38Si-12Ti is depicted in Figure 6.50. In addition to the expected phase Mo_5Si_3, small precipitates of the phase Mo_3Si were found in the form of narrow, elongated grains. This is not particularly surprising, as the phase Mo_5Si_3 has a rather narrow homogeneity range, making the preparation of a single-phase sample by arc melting almost impossible. Both phases are present after furnace cooling and after quenching, although slightly more of the second phase appears to be present in the quenched sample. However, it is unclear whether this is an effect of the additional heat treatment time or the quenching itself. The

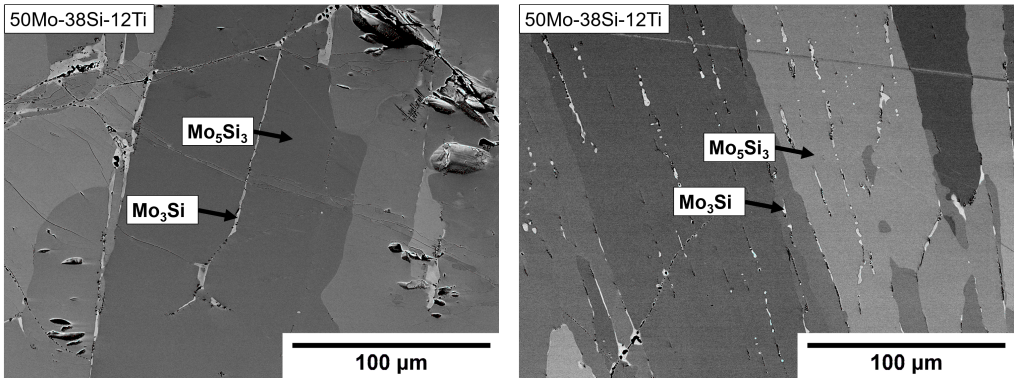

(a) (b)

Figure 6.50.: The microstructure of the sample QE5, 50Mo-38Si-12Ti. a) After furnace cooling, b) after quenching.

Table 6.27.: The composition of the phases of the sample QE5, 50Mo-38Si-12Ti, after furnace cooling and after quenching.

50Mo-38Si-12Ti						
	Furnace cooled			Water quenched		
	x(Mo) / at.%	x(Si) / at.%	x(Ti) / at.%	x(Mo) / at.%	x(Si) / at.%	x(Ti) / at.%
Mo_3Si	65.7 ± 1.2	22.5 ± 0.3	9.2 ± 0.4	58.4 ± 1.6	22.1 ± 1.6	6.3 ± 1.0
Mo_5Si_3	51.5 ± 1.2	35.1 ± 0.8	10.7 ± 0.3	51.0 ± 1.1	34.9 ± 0.6	10.6 ± 0.3

phase compositions listed in Table 6.27 are virtually identical for both states, indicating a rather negligible influence of the quenching. For the water quenched sample, the SEM operator included light elements such as oxygen in the EDX analysis, which alters the values somewhat. However, these elements cannot reliably be quantified, so they are omitted from this table. The intention was rather to investigate if significant intake of contaminants occur during heat treatment, which does not appear to be the case.

A comparison of the annealed sample with its cast state (SSC10, Figure 6.30 on page 130 and Table 6.14 on page 129 for microstructure and phase composition, respectively) shows the effect of the heat treatment on the sample. Both the microstructure and the phase composition did not change significantly during the heat treatment. This may indicate that the sample was already close to thermodynamic equilibrium at the selected conditions after casting.

6.4.4.6. QE6: 20Mo-37.5Si-42.5Ti

The microstructure of the sample 20Mo-37.5Si-42.5Ti is shown in Figure 6.51. In addition to the two expected phases, Ti_5Si_3 and Mo_5Si_3, the β phase is present in both the furnace cooled and water quenched states. While both silicides take the form of large, homogeneous grains,

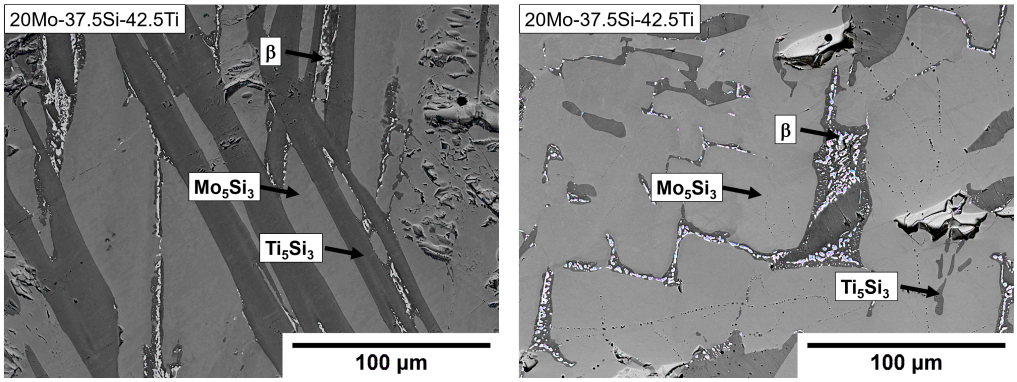

(a) (b)

Figure 6.51.: The microstructure of the sample QE6, 20Mo-37.5Si-42.5Ti. a) After furnace cooling, b) after quenching.

Table 6.28.: The composition of the phases of the sample QE6, 20Mo-37.5Si-42.5Ti, after furnace cooling and after quenching.

20Mo-37.5Si-42.5Ti						
	Furnace cooled			Water quenched		
	x(Mo) / at.%	x(Si) / at.%	x(Ti) / at.%	x(Mo) / at.%	x(Si) / at.%	x(Ti) / at.%
β	73.3 ± 3.8	4.7 ± 1.9	20.3 ± 1.6	71.1 ± 5.0	5.0 ± 2.4	19.9 ± 1.9
Mo_5Si_3	24.3 ± 1.1	36.3 ± 0.5	37.0 ± 1.3	24.0 ± 2.3	36.2 ± 0.4	38.1 ± 0.6
Ti_5Si_3	17.4 ± 1.0	36.5 ± 0.5	44.0 ± 1.2	17.1 ± 0.7	36.6 ± 0.5	44.8 ± 0.9

β precipitates as very fine particles. The general morphology of the phases is not strongly influenced by the cooling rate, although it appears that the quenched sample contains slightly less Ti_5Si_3. The compositions of the phases listed in Table 6.28 are completely independent of the cooling rate. This leads to the conclusion that equilibrium has been reached for this sample and that quenching has a rather small overall effect on the sample.

Comparison with the as-cast state (SSC1, Figure 6.32 on page 132 and Table 6.15 on page 129 for microstructure and phase composition, respectively) shows that the β phase composition has changed significantly during heat treatment. The Mo content increased during annealing (from 57.5 ± 1.6 to 71.1 ± 5.0 at.%), while the Ti content decreased from 36.9 ± 1.2 to 19.9 ± 1.9 at.%. At the same time, the amount of β precipitates increased. As a result, there are a large number of small precipitates in the annealed state, which accounts for the higher standard deviation of the phase composition value. However, both silicides remained virtually unchanged by the heat treatment. This is another indication that the diffusion in the β phase is quite fast compared to the silicides.

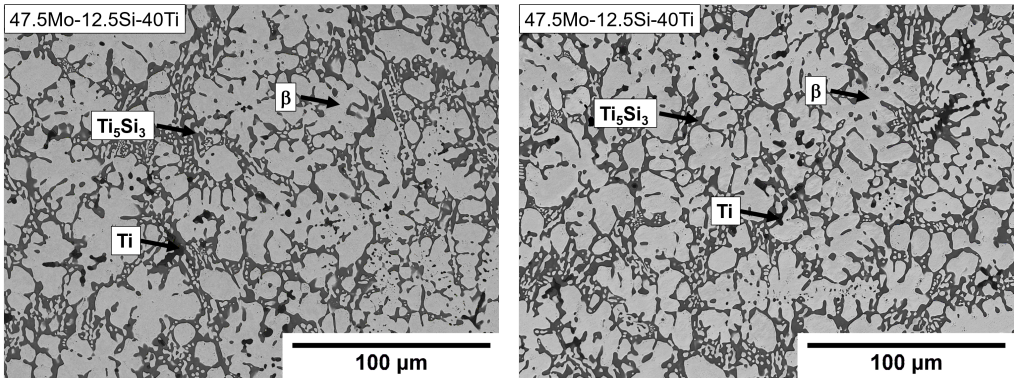

(a) (b)

Figure 6.52.: The microstructure of the sample QE7, 47.5Mo-12.5Si-40Ti. a) After furnace cooling, b) after quenching.

6.4.4.7. QE7: 47.5Mo-12.5Si-40Ti

The microstructure of the sample 47.5Mo-12.5Si-40Ti is shown in Figure 6.52. In addition to the two expected phases, β and Ti_5Si_3, the sample shows small precipitates of nearly pure Ti after both furnace cooling and water quenching. The β phase is present in the form of a flower-like morphology typical of dendritic structures as well as smaller interdendritic particles. In contrast, Ti_5Si_3 exists only in the interdendritic regions, while the Ti-rich third phase shows no discernible regularity. There is no difference between the microstructures in the furnace cooled and water quenched states. The same is true for the phase compositions listed in Table 6.29. It is unclear what the Ti-rich phase is. There is no literature data on stable phases of (almost) pure Ti in this region. As mentioned previously, it may be formed due to rapid solidification. While this would suggest that the phase should not be present after furnace cooling, its presence can also be interpreted to show that due to the slow diffusion in the Mo-Si-Ti system, even furnace cooling can be considered fairly rapid. This conclusion agrees with the fact that for all samples discussed so far, there is little to no discernible difference between furnace cooled and water quenched samples. However, a more detailed analysis of this phase in a separate, dedicated project is recommended.

When compared to the as-cast state (SSC12, Figure 6.34 on page 134 and Table 6.16 on page 133 for microstructure and phase composition, respectively), it is immediately apparent that the heat treatment resulted in a significant coarsening of the β particles in the eutectic regions. At the same time, their Ti content increased from 25.8 ± 4.9 to 37.0 ± 0.6 at.%, at the expense of both Mo (70.4 ± 5.1 to 66.5 ± 1.4 at.%) and Si (3.8 ± 0.5 to 1.6 ± 0.3 at.%). This coarsening is also responsible for the marked decrease in the standard deviation of the composition value for this phase. The composition of Ti_5Si_3 did not change significantly during annealing.

Table 6.29.: The composition of the phases of the sample QE7, 47.5Mo-12.5Si-40Ti, after furnace cooling and after quenching.

47.5Mo-12.5Si-40Ti						
	Furnace cooled			Water quenched		
	x(Mo) / at.%	x(Si) / at.%	x(Ti) / at.%	x(Mo) / at.%	x(Si) / at.%	x(Ti) / at.%
β	66.1 ± 1.4	2.0 ± 0.5	27.2 ± 0.9	66.5 ± 1.4	1.6 ± 0.3	37.0 ± 0.6
Ti_5Si_3	10.8 ± 1.8	36.1 ± 1.1	51.9 ± 1.0	10.4 ± 0.7	36.9 ± 0.4	51.7 ± 0.8
Ti	2.0 ± 1.1	1.0 ± 1.8	93.5 ± 3.3	1.2 ± 0.3	0.4 ± 0.3	95.9 ± 1.7

6.4.4.8. QE8: 45Mo-21Si-34Ti

The microstructure of the sample 45Mo-21Si-34Ti is shown in Figure 6.53. In addition to the two expected phases β and Mo_5Si_3, the two silicides Ti_5Si_3 and Mo_3Si are present. While all phases form mainly small precipitates with no particular regularity, some larger grains of Mo_3Si as well as dendritic structures of Ti_5Si_3 are visible. There is a clear difference between the furnace cooled and water quenched samples. In the water quenched sample, the dendrites have much clearer contours, whereas in the furnace cooled sample they look much more diffuse. This is a strong indication that quenching is able to "freeze" the microstructure while some diffusion takes place during the slow cooling in the furnace. However, the presence of four phases is also a clear indication that the sample is not in equilibrium after the chosen time (330 h + 48 h). A comparison with the as-cast state (SSC13, Figure 6.36 on page 136 and Table 6.17 on page 137 for the microstructure and phase compositions, respectively) shows that annealing has a distinct influence on this sample. Much of the Mo_3Si has disappeared, while Mo_5Si_3 was formed. The latter phase was not detectable at all in the cast state. The compositions of the β phase and Ti_5Si_3 are distinctly different in the annealed state compared to the cast state as well, whereas Mo_3Si, although it transforms, has approximately the same composition in both states. Interestingly, the sample exhibits dendritic structures both before and after heat treatment. However, the dendrites after casting are consistently almost pure Ti, similar to the precipitates found in the sample QE7, whereas after annealing, they consist of Ti_5Si_3. In fact, no pure Ti precipiates are found after annealing. This fact is an indication that the pure Ti is not stable after all, but equilibrates under certain conditions. Why these conditions are met for the comparatively simpler microstructure of QE7 is unclear. Regarding the overall equilibrium state of sample QE8, it can be concluded that, analogous to QE2, that the time chosen may not be sufficient to equilibrate samples that have very complex microstructures after casting.

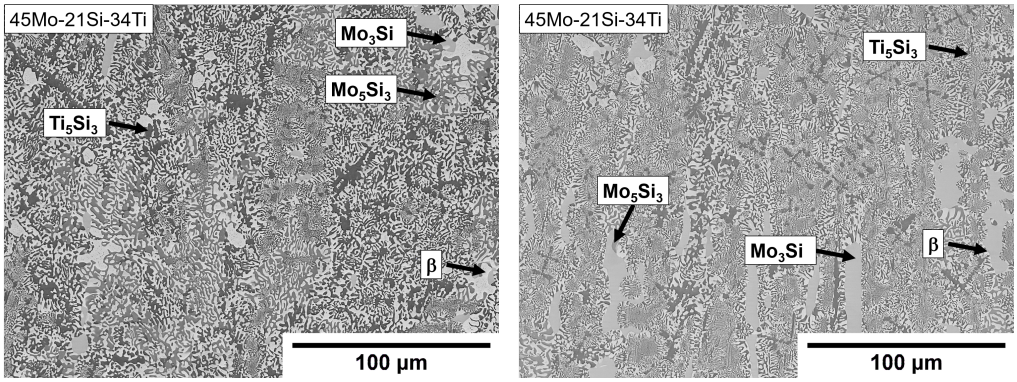

Figure 6.53.: The microstructure of the sample QE8, 45Mo-21Si-34Ti. a) After furnace cooling, b) after quenching.

Table 6.30.: The composition of the phases of the sample QE8, 45Mo-21Si-34Ti, after furnace cooling and after quenching.

45Mo-21Si-34Ti						
	Furnace cooled			Water quenched		
	x(Mo) / at.%	x(Si) / at.%	x(Ti) / at.%	x(Mo) / at.%	x(Si) / at.%	x(Ti) / at.%
β	77.6 ± 3.1	3.1 ± 1.7	15.9 ± 1.5	77.2 ± 3.3	2.5 ± 1.2	16.4 ± 0.8
Mo_3Si	52.6 ± 2.2	22.5 ± 0.8	20.9 ± 2.3	51.9 ± 1.0	22.1 ± 0.5	22.2 ± 0.6
Mo_5Si_3	25.5 ± 0.4	35.8 ± 0.3	36.2 ± 0.7	26.4 ± 1.8	34.7 ± 1.4	36.7 ± 2.6
Ti_5Si_3	16.9 ± 1.3	36.1 ± 0.8	44.9 ± 0.8	17.6 ± 1.4	36.0 ± 0.9	45.4 ± 0.9

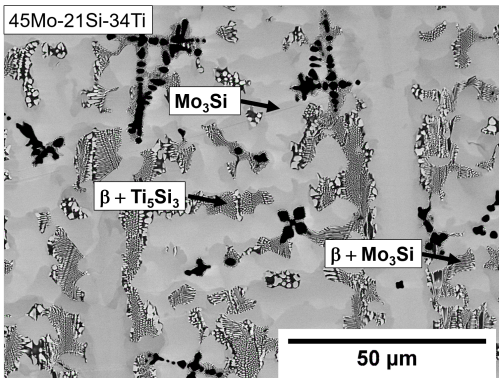

Figure 6.54.: The microstructure of the sample QE8, 45Mo-21Si-34Ti, in the as-cast state (designated SSC13 above, shown again here for convenience).

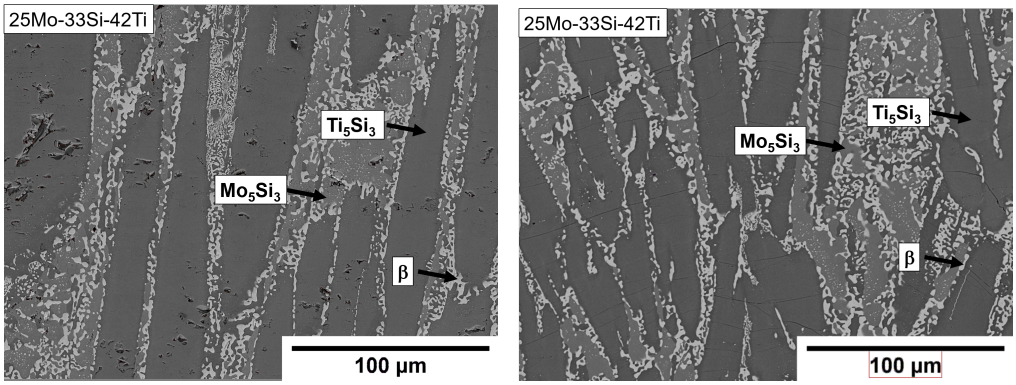

Figure 6.55.: The microstructure of the sample QE9, 25Mo-33Si-42Ti. a) After furnace cooling, b) after quenching.

Table 6.31.: The composition of the phases of the sample QE9, 25Mo-33Si-42Ti, after furnace cooling and after quenching.

25Mo-33Si-42Ti						
	Furnace cooled			Water quenched		
	x(Mo) / at.%	x(Si) / at.%	x(Ti) / at.%	x(Mo) / at.%	x(Si) / at.%	x(Ti) / at.%
β	78.4 ± 3.7	4.1 ± 1.8	17.5 ± 2.1	80.4 ± 1.5	2.6 ± 1.0	17.0 ± 1.0
Mo_5Si_3	25.4 ± 1.1	37.6 ± 0.7	37.0 ± 1.0	25.4 ± 1.9	37.2 ± 0.6	37.4 ± 1.1
Ti_5Si_3	18.1 ± 1.1	37.9 ± 1.0	44.0 ± 1.2	18.6 ± 0.4	37.9 ± 0.6	43.5 ± 0.6

6.4.4.9. QE9: 25Mo-33Si-42Ti

The microstructure of the sample 25Mo-33Si-42Ti is shown in Figure 6.55. Only the three expected phases β, Mo_5Si_3 and Ti_5Si_3 are present. Ti_5Si_3 takes the form of large, nearly hexagonal grains, while β and Mo_5Si_3 are small precipitates. There is no difference between the furnace cooled sample and the water quenched sample. Similarly, the phase compositions listed in Table 6.31 are nearly identical in both states. This indicates that the sample is in equilibrium and slow cooling has little or no effect on the sample. Note that this sample was not analyzed in the as-cast state, so no SSC designation exists for this composition.

6.4.4.10. QE10: 60Mo-30Si-10Ti

The microstructure of the sample 60Mo-30Si-10Ti is shown in Figure 6.56. Only the two expected phases, Mo_5Si_3 and Mo_3Si, are present. Mo_5Si_3 takes the form of oval grains while the majority of the sample consists of Mo_3Si. This does not change after water quenching. Like the microstructure, the phase compositions of this sample, listed in Table 6.32, are identical for

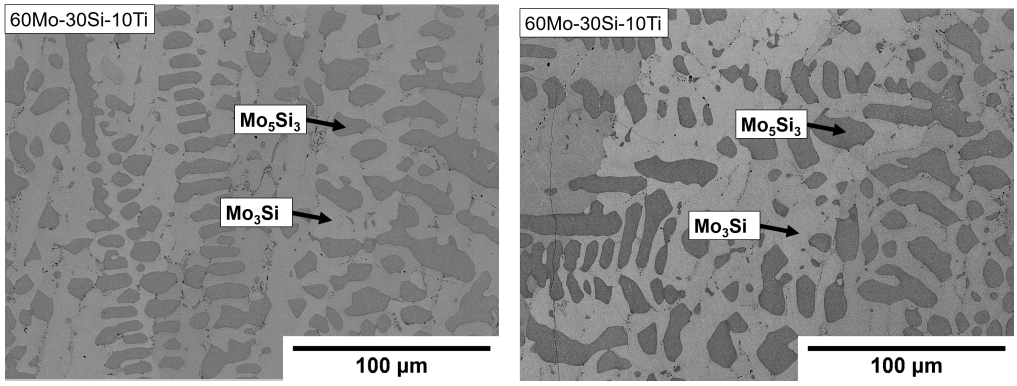

(a) (b)

Figure 6.56.: The microstructure of the sample QE10, 60Mo-30Si-10Ti. a) After furnace cooling, b) after quenching.

Table 6.32.: The composition of the phases of the sample QE10, 60Mo-30Si-10Ti, after furnace cooling and after quenching.

60Mo-30Si-10Ti						
	Furnace cooled			Water quenched		
	x(Mo) / at.%	x(Si) / at.%	x(Ti) / at.%	x(Mo) / at.%	x(Si) / at.%	x(Ti) / at.%
Mo_3Si	68.5 ± 2.3	24.0 ± 0.9	7.6 ± 2.3	69.0 ± 0.7	24.1 ± 0.6	6.9 ± 0.5
Mo_5Si_3	54.6 ± 1.1	36.7 ± 0.9	8.7 ± 0.9	54.2 ± 1.5	36.9 ± 0.7	8.9 ± 1.1

both states. This indicates that this sample is in equilibrium and slow cooling has no discernible effect on it.

Comparison with the as-cast state (SSC14, Figure 6.40 on page 139 and Table 6.18 on page 140 for microstructure and phase composition, respectively) shows that no significant changes appear to occur during annealing. This is true for both the morphology and the composition of the two phases. This result is in good agreement with sample QE5, where the same phases were present as in this sample. Thus, the conclusion that the samples in this region of the system are close to thermodynamic equilibrium under the selected conditions after casting can be maintained.

6.4.4.11. Conclusions

To conclude the results of this section, the effect of water quenching compared to relatively slow furnace cooling was studied on several samples. While the majority of the samples show no difference between the two cooling rates, as expected for slowly diffusing refractory alloys, some samples show minor or even pronounced differences, such as sample QE8. In addition, it was found that some samples do not reach equilibrium even after 708 h. This is the case when the microstructure in the cast state is very complex, either with many different phases that are not

stable in equilibrium, or with very fine grain morphologies. In fact, a comparison of the annealed state with the as-cast state revealed that the effect of heat treatment is often quite small in general. Although some differences could be detected in most of the samples, such as a change in the phase composition of the β phase or the growth or precipitation of one or more phases, the effects were usually relatively limited. In particular, it can be concluded from the experiments that the presence of Ti_5Si_3 appears to have a detrimental effect on the kinetics of the system. In samples where this phase was present, it tended to be too stable to disappear completely, resulting in a non-equilibrium state, or resulted in very small overall changes in the microstructure and composition of the sample. At this point, however, it is unclear in many cases whether this is because the respective sample is not in thermodynamic equilibrium after 330 h at 1573 K, or whether the phase composition after casting happened to be so close to the high temperature equilibrium state that little transformation could occur. To investigate this, considerably longer annealing times would be required, with analysis after several time intervals and comparison with the previous state. Since annealing times in excess of 4 weeks are not practical, it was decided to retain 330 h as the standard annealing time and to focus on sample compositions that could reasonably be expected to reach equilibrium in that time.

6.4.5. Evaluation of a powder metallurgical processing route

During the experiments, a relatively common problem was that samples were occasionally not fully mixed during arc melting. Even though each sample was melted five times and turned between each remelt, the high melting point of Mo (2896 K) meant that some alloys were very difficult to fully melt and mix. While it is visible in the arc melter when the sample has liquefied on the outside, one cannot be certain that the entire ingot has been completely remelted. In cases where complete remelting was not achieved, macroscopic areas of β phase would be visible in the microstructure, see Figure 6.57 for an example of the alloy 47Mo-24.5Si-28.5Ti after the two-step heat treatment used in section 6.4.4. Such inclusions would not dissolve by annealing in a reasonable time. Furthermore, they only become visible during the polishing step of a sample, meaning that a significant amount of time has already been expended on a sample that is not viable. Since this sample was discarded due to insufficient mixing during melting, it was not assigned a designation for this dissertation and was not subjected to any further analysis.

To attempt a different way to promote mixing of the components of the alloys, a powder metallurgical route was tested. Four samples were prepared via arc melting in the usual way described in section 3.1. Since the experimental series described in section 6.4.4 had not yielded useful results concerning the three-phase region β+Mo_3Si+Mo_5Si_3 due to insufficient mixing of the analyzed sample, all four samples were placed in this area. The sample compositions are

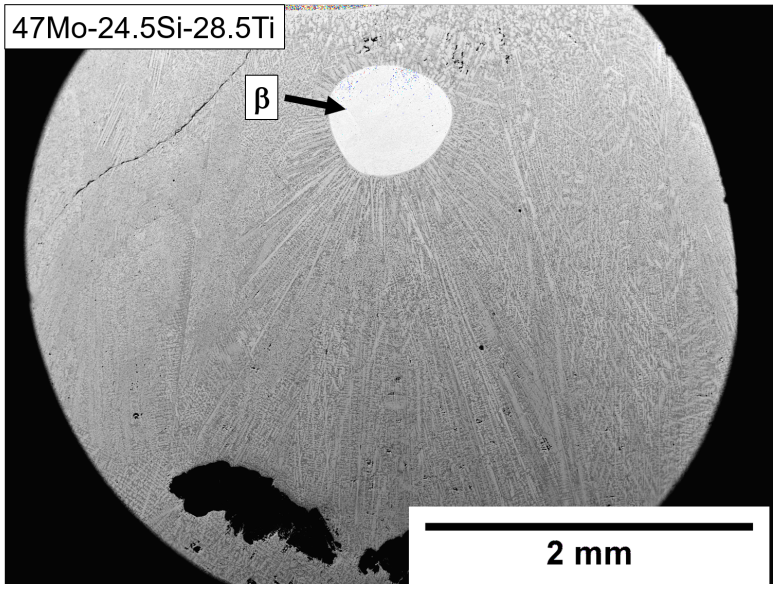

Figure 6.57.: An SEM image of the sample 47Mo-24.5Si-28.5Ti after a total of 378 h at 1573 K, quenched in water after the final step. Clearly visible at the top center of the image is a large spot of unmixed Mo, with a diameter of about 0.7 mm.

Table 6.33.: The composition of the samples used to investigate the suitability of a powder metallurgical processing route for Mo-Si-Ti alloys.

Sample designation	Nominal composition	Expected phases
PM1	43Mo-27Si-30Ti	β+Mo_3Si+Mo_5Si_3
PM2	46Mo-25Si-29Ti	
PM3	50Mo-23Si-27Ti	
PM4	55Mo-20Si-25TI	

listed in Table 6.33 and shown in the isothermal section at 1573 K, calculated with the dataset of Yang et al. [16], in Figure 6.58.

After arc melting, the samples were first homogenized at 1573 K for 330 h and water quenched. They were then pulverized using an agate mortar. No attempt was made to characterize the particle size. The powder was then pressed into pellets of 5 mm diameter and about 2 mm height using a cold isostatic press (KIP 300 E, Paul-Otto Weber GmbH) at approximately 500 MPa pressure. Finally, these samples were annealed for another 330 h at 1573 K and quenched with water. In this state, they were analyzed by SEM.
It was observed that powder metallurgy is not an appropriate process for Mo-Si-Ti alloys. The reason for this is that pulverization significantly increases the surface area of the sample, giving oxygen a larger target area. As a result, all four samples were heavily oxidized, despite the use

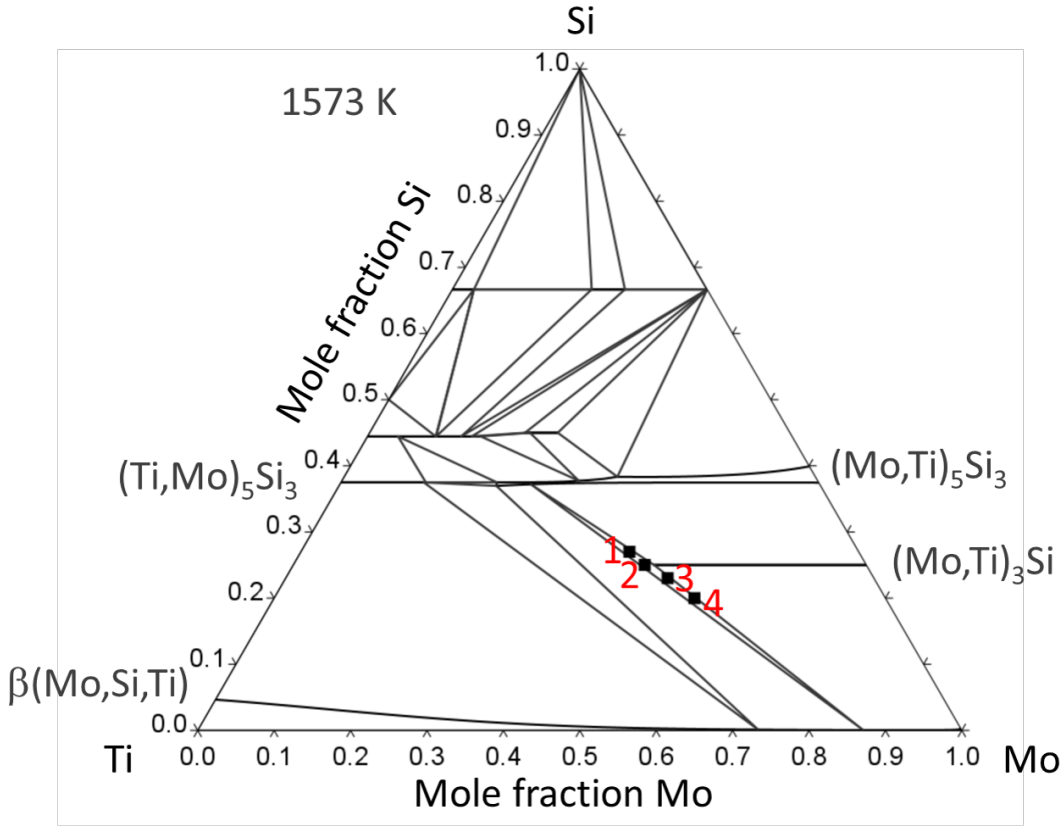

Figure 6.58.: The composition of the samples used to investigate the suitability of a powder metallurgical processing route for Mo-Si-Ti alloys shown in the isothermal section at 1573 K calculated with the dataset of Yang et al. [16].

of the oxygen purifier and Ti getters. Therefore, no attempt was made to quantify the phase compositions by EDX. Figure 6.59 shows an image of the microstructure of sample PM3 (50Mo-23Si-27Ti) as an example. This image was taken in SE mode to get a topographical contrast and highlight the porosity of the sample, which was present even within grains. This is most likely due to the evaporation of volatile MoO_3. In addition, it was found that the method does not guarantee sufficient mixing of the components, as shown in Figure 6.60. This image shows the microstructure of the sample 43Mo-27Si-30Ti. It is clearly visible that the microstructure is not homogeneous, but there are several grains with significantly different microstructures compared to the rest of the sample. This suggests that despite pulverization and isostatic pressing, some inhomogeneities may be retained within the sample. It is even reasonable to assume that due to the generally porous microstructures of pulverized samples, local equilibria can easily form if there are areas of the sample where grains have little or no contact with the rest of the material. For these reasons, it has been concluded that the powder metallurgical method is not viable for

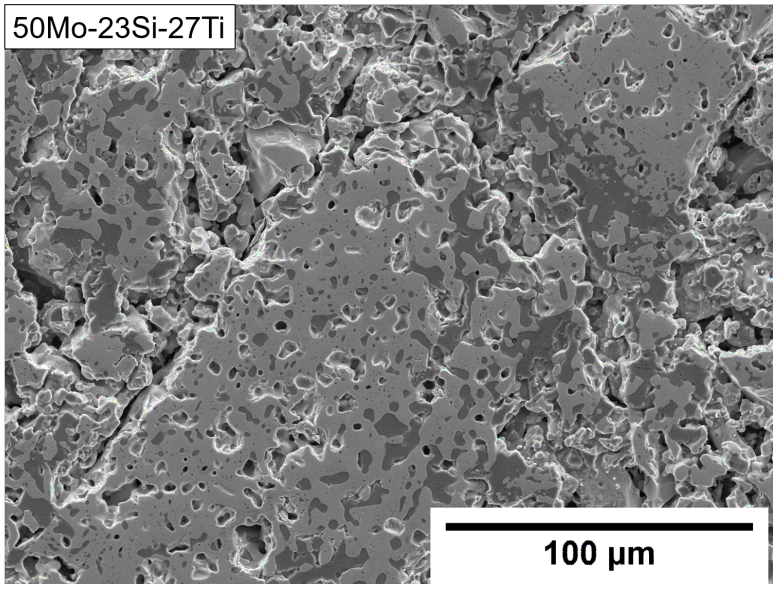

Figure 6.59.: The microstructure of the sample PM3, 50Mo-23Si-27Ti, after powderization, cold isostatic pressing and annealing for 330 h at 1573 h. The image was taken in SE mode.

Mo-Si-Ti alloys and that the only suitable way to obtain useful samples is to ensure at least good mixing of the components during arc melting.

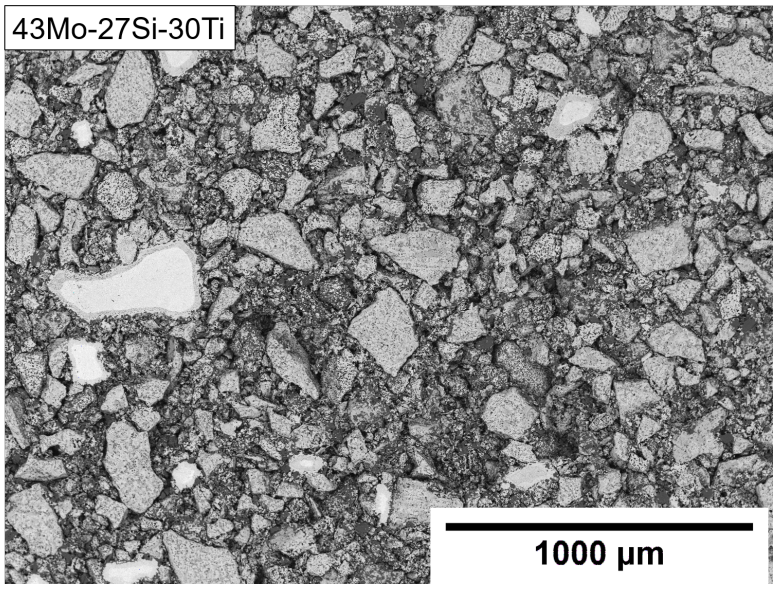

Figure 6.60.: The microstructure of the sample PM1, 43Mo-27Si-30Ti, after powderization, cold isostatic pressing and annealing for 330 h at 1573 h.

6.4.6. The isothermal section of Mo-Si-Ti at 1573 K

The primary objective of this work in the ternary system was to investigate the metal-rich area of the isothermal section at 1573 K. The samples discussed in section 6.4.4 allow a preliminary construction of parts of this section, if the samples that are obviously not in equilibrium are discarded. In Figure 6.61, the tie lines or tie triangles of the remaining samples are superimposed on the isothermal section calculated using the dataset of Yang et al. [16]. Although no data were obtained from this study for several equilibria, some conclusions can be drawn. First, three equilibria proposed by Yang et al. were confirmed. These were the two-phase regions β+Mo_3Si and Mo_3Si+Mo_5Si_3 and the three-phase region β+Mo_5Si_3+Ti_5Si_3. There was also evidence that the β phase can solve far more Si than the dataset suggests. All four samples containing this phase consistently show a solubility of approximately 2-5 at.% Si, while the dataset allows virtually no solubility for this element at Mo concentrations exceeding 60 at.%. It should be noted that the three-phase equilibrium data for the β phase are highly scattered and thus of limited reliability. This is due to the small size of the precipitates, which makes precise EDX and EPMA measurements difficult. However, the two-phase sample QE4 has quite large β grains (see Figure 6.49b), so it is reasonable to assume that no such error influenced the measurement here. For the β phase of this sample, the Si content is also quite significant (3.3 ± 1.2 at.%). In addition, the phase Mo_3Si was found to exhibit the same Si deficiency as in the binary system, with an average Si content of approximately 23 at.% (see Tables 6.26, 6.27 and 6.32 for the exact compositions of annealed samples). In fact, these were the first samples chronologically where this was found in this study and what triggered the decision to reassess the underlying binary system. Furthermore, it can be concluded that these samples are likely to be in thermodynamic equilibrium, since the sample compositions fall almost perfectly on the measured tie line in all cases. Finally, it appears from these samples that the three-phase region β+Mo_5Si_3+Ti_5Si_3 is generally shifted toward higher Mo concentrations than suggested by the dataset. While there is some scatter in these data as well, all three samples in this region consistently show that both 5-3 silicides are richer in Mo than previously thought.

While these results were a good first step for the isothermal section of interest, it was clear that samples specifically prepared for the task were needed. In this way, all the information and experience gained during the series of experiments described in the previous sections could be used to select sample compositions that would have the highest chance of providing usable data. A more detailed analysis of the sample was also desirable. This included determination of the actual sample compositions as well as impurity concentrations by ICP-OES and CGHE. In addition, it was decided to measure powder XRD diffractograms of selected samples to potentially find phases that had been missed in the SEM.

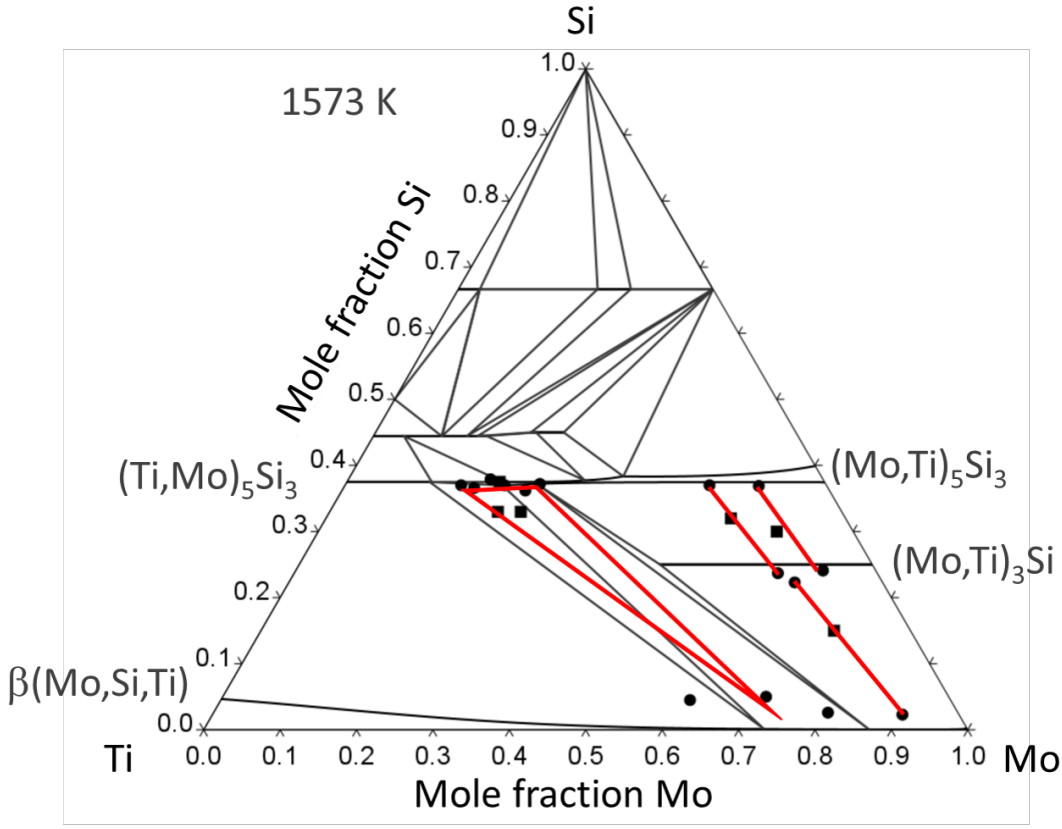

Figure 6.61.: The samples from the quenching experiments that are most likely in equilibrium, along with their respective phase compositions, superimposed on the isothermal section of the Mo-Si-Ti system at 1573 K. The isothermal section was calculated using the dataset of Yang et al. [16]. The equilibria found in this work are shown in red. Sample compositions are squares, phase compositions are circles.

Therefore, 17 samples were prepared for the task of studying the isothermal section of the Mo-Si-Ti system at 1573 K. The sample mass was increased by 500 mg compared to the previous series of experiments, which meant that all samples had a mass of 2000 mg each. This allowed for the chemical analysis of the samples, for which approximately 500-600 mg of sample material is needed. All samples were annealed for 330 h and quenched in water unless specified otherwise. Their nominal compositions and expected phases are listed in Table 6.34. They are shown in the phase diagram calculated with the dataset of Yang et al. in Figure 6.62. At least two samples were placed in each phase area. Care was taken to ensure that the respective compositions are not so close to each other that similar results could be expected even if the samples are not in equilibrium. In the two-phase region β+Ti_5Si_3, four samples were placed, two of which were furnace cooled and two of which were water quenched. The reason for this was the presence of the Ti-rich phase previously reported for sample QE8 and the hypothesis that the cooling rate might affect this phase.

Table 6.34.: The nominal compositions of the samples used to investigate the isothermal section of Mo-Si-Ti at 1573 K. All samples were water quenched, unless specified otherwise.

Sample designation	Nominal composition	Note
β+Mo_5Si_3+Ti_5Si_3		
ITS1	17Mo-35Si-48Ti	
ITS2	21Mo-35Si-44Ti	
ITS3	35Mo-25Si-40Ti	
β+Mo_3Si+Mo_5Si_3		
ITS4	54Mo-20Si-26Ti	
ITS5	50Mo-23Si-27Ti	
ITS6	55Mo-20Si-25Ti	
β+Mo_3Si		
ITS7	75Mo-15Si-10Ti	Composition identical to SSC8/QE4
ITS8	75Mo-10Si-15Ti	
Mo_3Si+Mo_5Si_3		
ITS9	60Mo-30Si-10Ti	Composition identical to SSC14/QE10
ITS10	53Mo-32Si-15Ti	Composition identical to SSC7/QE3
β+Ti_5Si_3		
ITS11	10Mo-20Si-70Ti	Furnace cooled
ITS12	20Mo-20Si-60Ti	Composition identical to SSC9. Furnace cooled
ITS13	20Mo-20Si-60Ti	Composition identical to SSC9.
ITS14	30Mo-20Si-50Ti	
β+Mo_5Si_3		
ITS15	27Mo-35Si-38Ti	
ITS16	41Mo-25Si-34Ti	
ITS17	74Mo-5Si-21Ti	

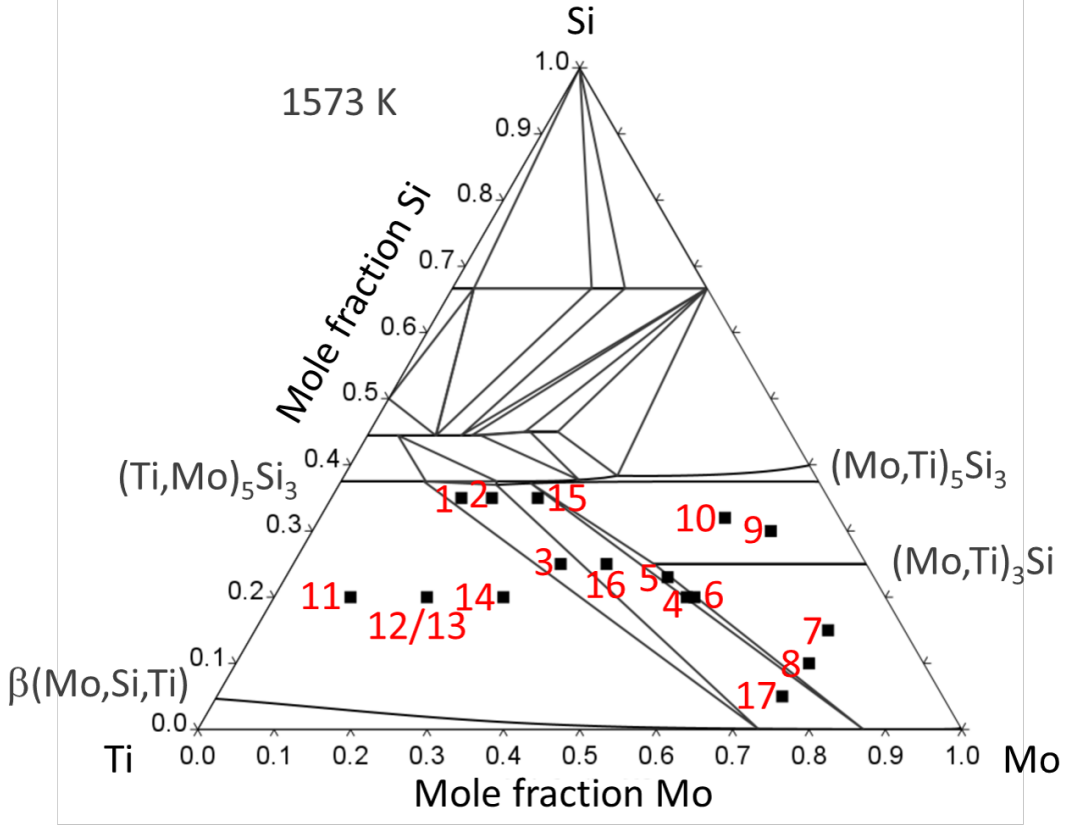

Figure 6.62.: The nominal compositions of the samples used to investigate the isothermal section of Mo-Si-Ti at 1573 K, depicted on the phase diagram calculated using the dataset by Yang et al. [16].

6.4.6.1. The equilibrium β+Mo_5Si_3+Ti_5Si_3: samples ITS1-3

The compositions of the samples ITS1-ITS3, which were used to investigate the three-phase region β+Mo_5Si_3+Ti_5Si_3, are listed in Table 6.35. The differences between nominal and actual compositions are very small, with a maximum difference of 1 at.%. The concentration of impurities is also small, especially in the case of C, so no adverse effects are to be expected.

The microstructures of the three samples are shown in Figure 6.63. In the case of ITS1 and ITS2, the three expected phases are clearly visible; β is the light gray phase, Mo_5Si_3 is medium gray, and the darkest shade belongs to Ti_5Si_3. No additional phases can be detected. The microstructures of ITS1 and ITS2 (Figures 6.63a and 6.63b, respectively) are quite similar, with small β precipitates and relatively large silicide grains. The distribution of the phases agrees

Table 6.35.: The compositions of the samples in the three-phase region β+Mo_5Si_3+Ti_5Si_3 measured by ICP-OES and CGHE.

Sample designation	Nominal composition	x(Mo) / at.%	x(Si) / at.%	x(Ti) / at.%	x(C) / at.%	x(O) / at.%
ITS1	17Mo-35Si-48Ti	17.7	34.7	47.5	0.09	0.13
ITS2	21Mo-35Si-44Ti	21.2	34.0	44.6	0.06	0.16
ITS3	35Mo-25Si-40Ti	34.7	24.1	40.9	0.05	0.18

well with the expectations based on the lever rule. Both samples ITS1 and ITS2, which contain a fairly high amount of Si (35 at.%). show a clear majority of the silicides in terms of phase fractions and comparatively little β phase. The sample ITS3 (Figure 6.63c) on the other hand appears to be a two-phase alloy, with virtually no Mo_5Si_3 present. The sample shows a large β phase fraction and relatively large precipitates thereof. The Ti_5Si_3 grains on the other hand show a clear change in hue on the inside of the grains compared to their edges. This is a very strong indication that the sample is not in thermodynamic equilibrium, as the diffusion of the elements was not yet completed when the specimen was quenched after 330 h; otherwise, the hue in BSE mode would have been uniform.

The compositions of each phase of the three samples are listed in Table 6.36. No experimental uncertainty is listed for the β phase of sample ITS1. This is because the EPMA operator measured only a small number of precipitates of this phase due to their small size, so no statistical evaluation can reasonably be made here. There is remarkably little variation between the samples. In all cases, the β phase consists of approximately 70 at.% Mo and 3 at.% Si, while both silicides have a Si content of about 37 at.%. There is a distinct difference in the Mo contents between the silicides, with Mo_5Si_3 having a Mo content of about 20 at.%, while the Ti silicide has a much lower Mo content of around 15 at.%.

The XRD diffractograms of the samples, which are shown in Figure 6.64, confirm the findings. Both samples ITS1 and ITS2 show reflections that correspond to the structures of β, Mo_5Si_3 and Ti_5Si_3. No reflections that cannot be described by these three phases were found in the diffractogram, proving that no phase was overlooked in the micrographs. The diffractogram of the sample ITS3 can be described by the structures of β and Ti_5Si_3 alone, further reinforcing that this is in fact a two-phased sample instead of a three-phased one. Some small reflections can be detected which may hint to the presence of Mo_5Si_3 additionally, but they are extremely low in intensity and not all reflections from this phase could be found in the samples diffractogram.

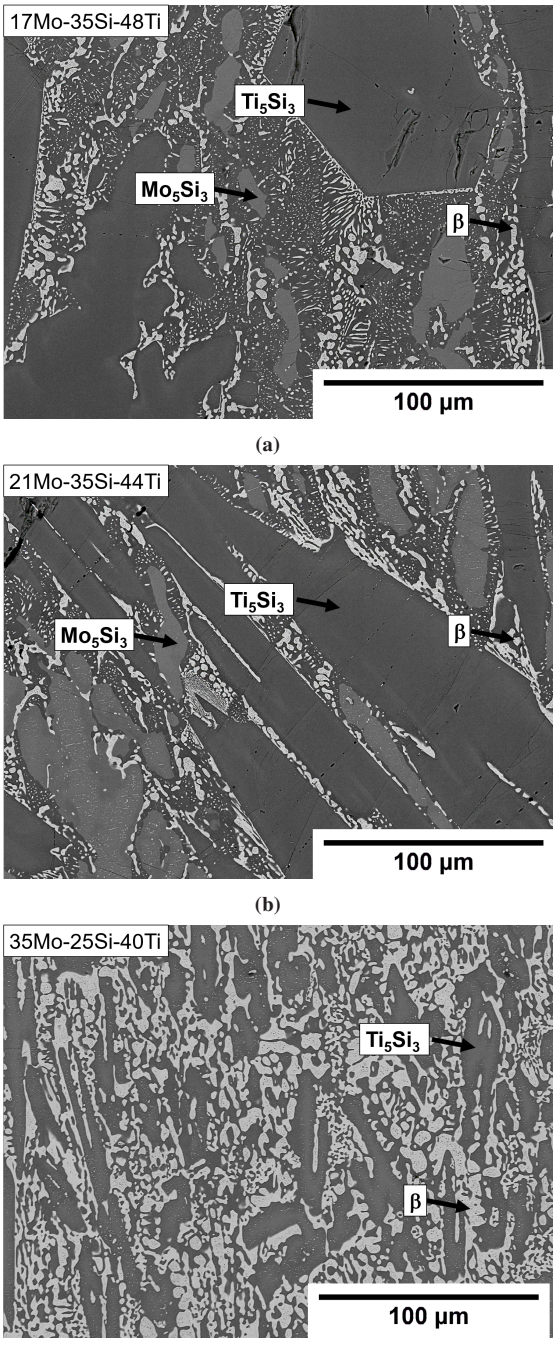

Figure 6.63.: The microstructures of the samples ITS1-3 after annealing for 330 h at 1573 K and water quenching. a) ITS1: 17Mo-35Si-48Ti, b) ITS2: 21Mo-35Si-44Ti, c) ITS3: 35Mo-25Si-40Ti.

Table 6.36.: The phase compositions of the samples in the three-phase region β+Mo_5Si_3+Ti_5Si_3, measured by EDX and EPMA.

Sample designation	Phase	x(Mo) / at.%	x(Si) / at.%	x(Ti) / at.%
ITS1	β	69.4	3.0	27.2
	Mo_5Si_3	19.9 ± 0.5	36.4 ± 0.1	43.7 ± 0.5
	Ti_5Si_3	12.6 ± 0.5	36.6 ± 0.2	50.8 ± 0.5
ITS2	β	71.4 ± 1.5	3.1 ± 1.1	25.5 ± 0.6
	Mo_5Si_3	22.4 ± 0.7	36.3 ± 0.4	41.3 ± 0.7
	Ti_5Si_3	15.4 ± 0.5	36.8 ± 0.2	47.8 ± 0.5
ITS3	β	76.2 ± 1.8	2.7 ± 1.0	21.1 ± 1.2
	Ti_5Si_3	14.6 ± 2.0	37.2 ± 1.8	48.2 ± 0.3

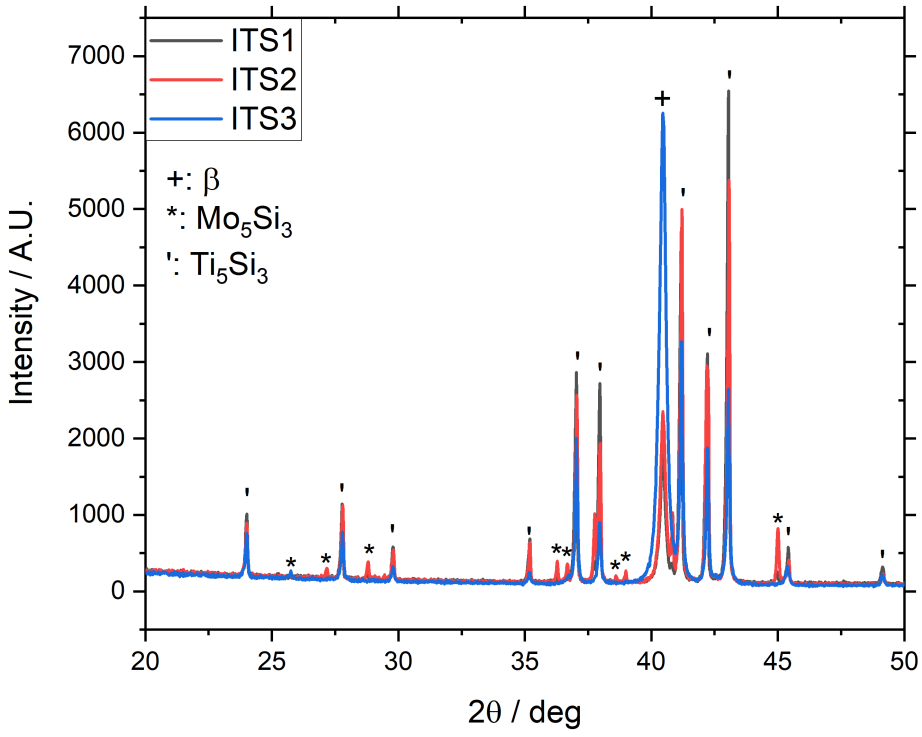

Figure 6.64.: The X-ray diffractograms of the samples ITS1-3 from 2θ=20-50°.

Table 6.37.: The compositions of the samples in the three-phase region β+Mo_3Si+Mo_5Si_3 measured by ICP-OES and CGHE.

Sample designation	Nominal composition	x(Mo) / at.%	x(Si) / at.%	x(Ti) / at.%	x(C) / at.%	x(O) / at.%
ITS5	50Mo-23Si-27Ti	53.9	21.4	24.5	b.l.d	0.30
ITS6	55Mo-20Si-25Ti	53.9	19.0	25.3	1.47	0.31

6.4.6.2. The equilibrium β+Mo_3Si+Mo_5Si_3: samples ITS4-6

The samples ITS4-ITS6 were prepared to investigate the second three-phase region of the metal-rich area of the system, β+Mo_3Si+Mo_5Si_3. The compositions of the samples ITS5 and ITS6 are listed in Table 6.37. For sample ITS4, no determination was possible as it was one of the earlier samples in this study. Thus, it was prepared, but not annealed, before the decision was made to prepare samples of 2000 mg mass for this series of experiments and not enough material remained for analysis. The measured compositions of ITS5 and ITS6 are quite close to the nominal compositions, especially in the case of ITS6. ITS5 shows a somewhat notable deviation, especially for the Mo content, but overall the composition is still quite close to the nominal composition. The impurity concentrations are rather low, with the C content in ITS5 even below the detection limit.

The microstructures of the three samples are shown in Figure 6.65. Three phases are visible, with β as the light gray phase, Mo_3Si as the medium gray phase, and a 5-3 silicide as the dark gray phase. The microstructures of ITS4 and ITS6 (Figures 6.65a and 6.65c) are very similar, as expected given the small difference in composition. In both cases the distribution between the three phases is quite even. However, the dark phase exists only as relatively fine precipitates, while Mo_3Si forms relatively large grains, and β exists as both fine precipitates and larger grains. In the case of ITS5 (6.65b), Mo_3Si forms large elongated grains, while the other two phases form smaller precipitates.

The phase compositions of samples ITS4-ITS6 measured by EDX are listed in Table 6.38. There is a remarkable agreement between the three samples. The β phase consistently shows a Mo content of approximately 83 at.% and a Si content of approximately 3 at.%. The Mo content of Mo_3Si is about 56 at.% and the phase shows the same Si deficiency as in the binary system, with an average Si content of about 23 at.%. The Si content of the 5-3 silicide is about 38 at.% and its Mo content is about 19 at.%, which was initially interpreted to mean that this phase was Mo_5Si_3, as this was the expected stable third phase in this region.

The XRD results of the samples ITS5 and ITS6, which are shown in Figure 6.66, lead to a vastly different conclusion however. The diffractograms clearly show the structures of the

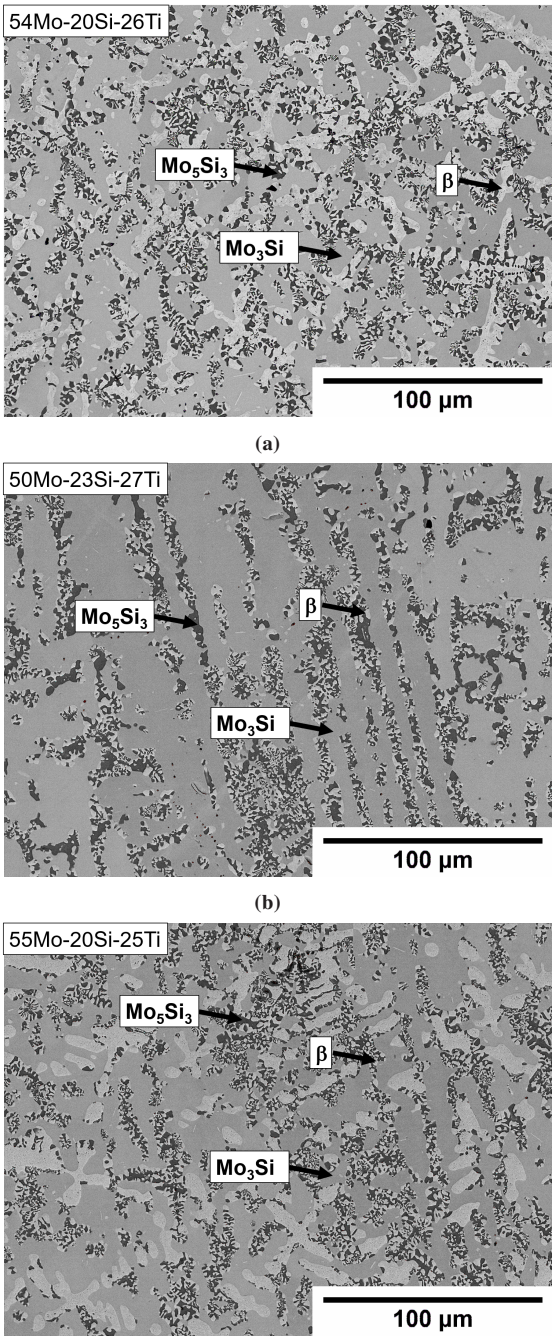

Figure 6.65.: The microstructures of the samples ITS4-6 after annealing for 330 h at 1573 K and water quenching. a) ITS4: 54Mo-20Si-26Ti, b) ITS5: 50Mo-23Si-27Ti, c) ITS6: 55Mo-20Si-25Ti.

Table 6.38.: The phase compositions of the samples in the three-phase region β+Mo_3Si+Mo_5Si_3, measured by EDX.

Sample designation	Phase	x(Mo) / at.%	x(Si) / at.%	x(Ti) / at.%
ITS4	β	82.3 ± 3.4	3.1 ± 2.0	14.6 ± 1.5
	Mo_3Si	56.5 ± 1.0	23.8 ± 0.7	19.7 ± 0.7
	Mo_5Si_3	20.0 ± 2.1	36.4 ± 1.4	43.6 ± 1.1
ITS5	β	83.4 ± 1.3	2.5 ± 0.9	14.1 ± 0.7
	Mo_3Si	56.4 ± 1.1	23.5 ± 0.8	20.1 ± 0.8
	Mo_5Si_3	18.1 ± 1.3	38.2 ± 0.8	43.8 ± 1.0
ITS6	β	83.6 ± 1.6	3.2 ± 1.1	13.2 ± 1.2
	Mo_3Si	57.5 ± 1.5	23.5 ± 0.7	19.0 ± 1.6
	Mo_5Si_3	19.0 ± 2.0	38.0 ± 0.8	43.0 ± 1.6

phases β, Mo_3Si and Ti_5Si_3. No amount of the $D8_m$ structure, which belongs to Mo_5Si_3, can be detected at all. Consequently, the conclusion must be drawn that these samples are not in thermodynamic equilibrium. The equilibria β+Mo_5Si_3+Ti_5Si_3, suggested by samples ITS1 and ITS2, and β+Mo_3Si+Ti_5Si_3, suggested by these samples, cannot exist simultaneously, as they would intersect. Scheil solidification calculations, which were shown to be generally fairly reliable to predict as-cast microstructures in section 6.4.3, are shown in Figure 6.67. They show that all phases that are observed in the samples are formed on solidification, which explains their presence. Similar to the conclusion drawn in section 6.4.4, the microstructures of the phases may have been so complex and diffusion so slow that equilibrium could not be reached under these conditions at 1573 K within 330 h. Instead, the as-cast microstructure was retained and, due to the complete lack of Mo_5Si_3 in the diffractogram, it must be concluded that the samples are extremely far from equilibrium.

6.4.6.3. The equilibrium β+Mo_3Si: samples ITS7-8

The compositions of samples ITS7 and ITS8, which were used to study the two-phase region β+Mo_3Si, are listed in Table 6.39. The difference between nominal and measured composition does not exceed 0.6 at.% for any element. The amount of impurities is also very low, with C in both cases well below 0.1 at.%. However, there was a relatively high scatter among the data, which may indicate macroscopic inhomogeneities of the samples that are not visible in the micrograph.

The microstructures of samples ITS7 and ITS8 are shown in Figure 6.68. Only the two expected phases are visible, with β being the lighter tone and Mo_3Si being the darker one. In both cases,

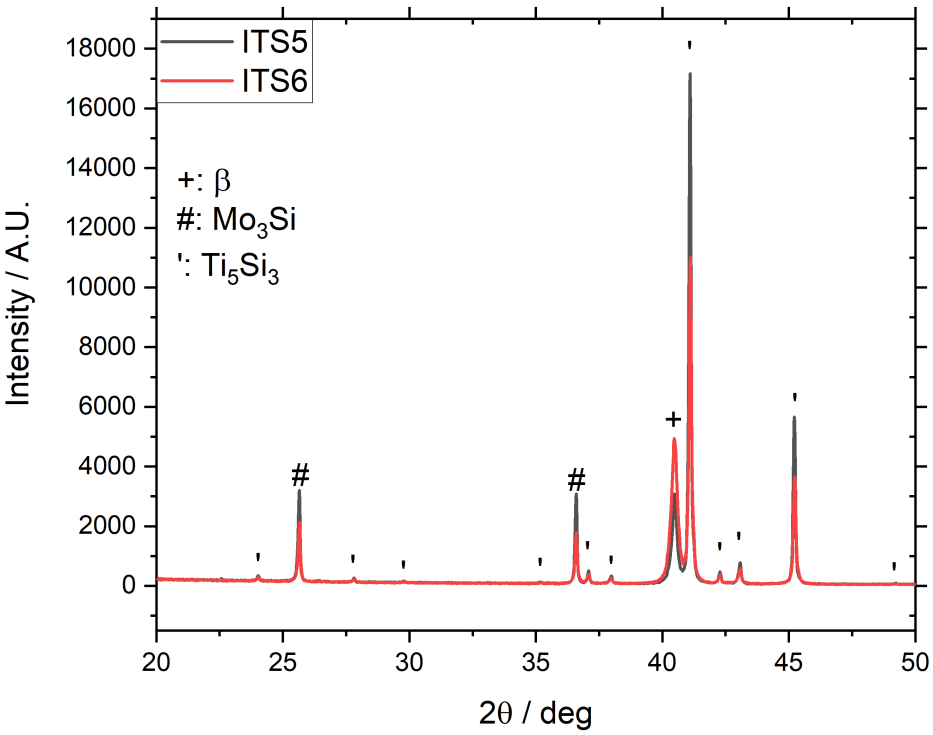

Figure 6.66.: The X-ray diffractograms of the samples ITS5-6 from 2θ=20-50°.

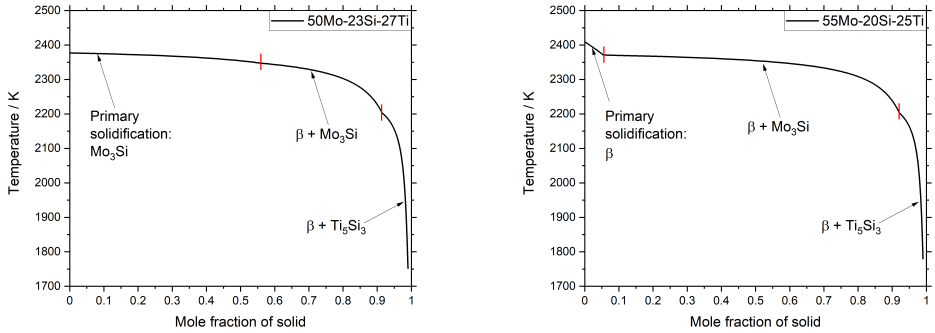

(a) **(b)**

Figure 6.67.: The Scheil solidification calculation of the samples ITS5 and ITS6 using the dataset from Yang et al. [16]. a) ITS5: 50Mo-23Si-27Ti, b) ITS6: 55Mo-20Si-25Ti.

Table 6.39.: The compositions of the samples in the two-phase region β+Mo_3Si measured by ICP-OES and CGHE.

Sample designation	Nominal composition	x(Mo) / at.%	x(Si) / at.%	x(Ti) / at.%	x(C) / at.%	x(O) / at.%
ITS7	75Mo-15Si-10Ti	74.5	14.7	9.6	0.042	1.14
ITS8	75Mo-10Si-15Ti	74.6	9.9	15.3	0.068	0.195

the precipitates of Mo_3Si have a distinct shape reminiscent of dendrites, with the structures in sample ITS7 (Figure 6.68a) being significantly smaller and having a lower total phase fraction than in sample ITS8 (Figure 6.68b).

The phase compositions of samples ITS7 and ITS8 are listed in Table 6.40. The Si deficiency is again confirmed for both samples, with an average Si concentration in the phase Mo_3Si of approximately 23 at.%. The β phase also shows a significant Si solubility of about 2.5 at.%,

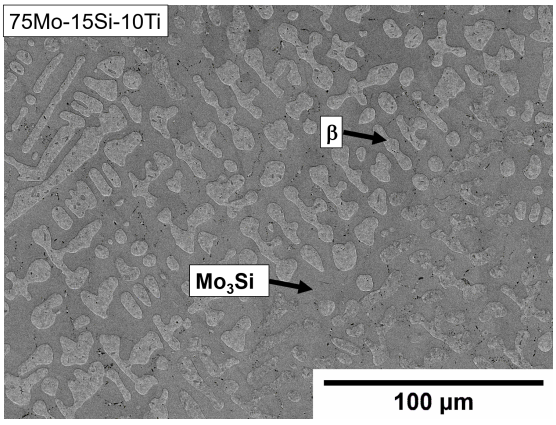

(a)

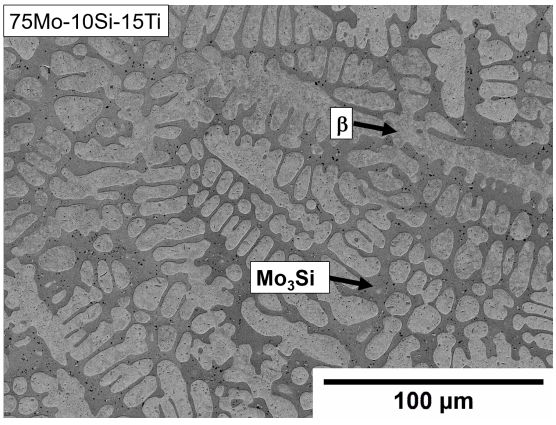

(b)

Figure 6.68.: The microstructures of the samples ITS7-8 after annealing for 330 h at 1573 K and water quenching. a) ITS7: 75Mo-15Si-10Ti, b) ITS8: 75Mo-10Si-15Ti.

Table 6.40.: The phase compositions of the samples in the two-phase region β+Mo_3Si, measured by EDX.

Sample designation	Phase	x(Mo) / at.%	x(Si) / at.%	x(Ti) / at.%
ITS7	β	92.2 ± 1.1	2.7 ± 0.7	5.1 ± 0.8
	Mo_3Si	69.9 ± 1.4	22.3 ± 1.2	7.8 ± 1.0
ITS8	β	88.9 ± 1.9	2.5 ± 1.1	8.7 ± 1.6
	Mo_3Si	61.6 ± 4.4	23.1 ± 1.1	15.3 ± 4.4

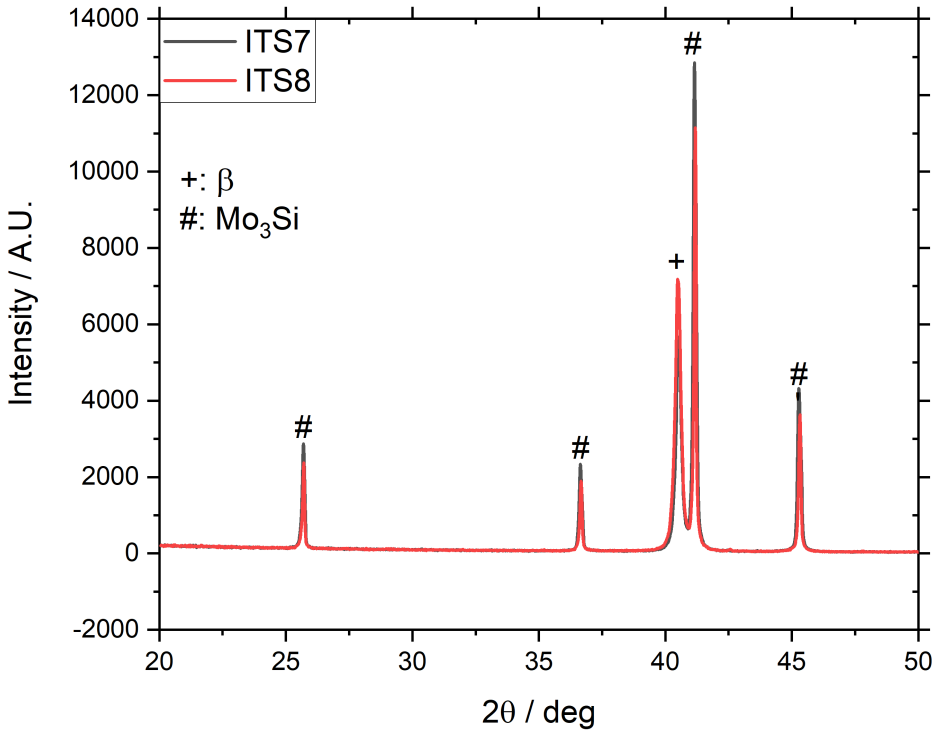

Figure 6.69.: The X-ray diffractograms of the samples ITS7-8 from 2θ=20-50°.

while the dataset of Yang et al. suggests zero Si solubility for this phase in this region of the isothermal section.

Figure 6.69 shows the XRD diffractograms of the samples ITS7 and ITS8. All peaks can be explained by the structures of the phases β and Mo_3Si, which means that the samples are, in fact, two-phased.

Table 6.41.: The compositions of the samples in the two-phase region Mo_3Si+Mo_5Si_3 measured by ICP-OES and CGHE.

Sample designation	Nominal composition	x(Mo) / at.%	x(Si) / at.%	x(Ti) / at.%	x(C) / at.%	x(O) / at.%
ITS9	60Mo-30Si-10Ti	60.9	27.9	10.1	0.031	1.13
ITS10	53Mo-32Si-15Ti	54.3	30.4	15.1	0.042	0.057

Since sample ITS7 has the same composition as sample SSC8/QE4, a comparison of the two samples in the same heat treated condition (1573 K/330 h/wq) was made. The microstructure and phase compositions of QE4 are shown in Figure 6.49b on page 149 and Table 6.25 on page 148, respectively. The microstructure of both samples looks almost identical. Also the composition of the β phase and the Mo_3Si are very similar. Therefore, it can be concluded that the reproducibility for this sample composition is very high. However, since SSC8/QE4 also showed very little change from the as-cast state after annealing, it is unclear whether the reproducibility is due to thermodynamic equilibrium being easily reached under the selected annealing conditions, or whether the annealing conditions are insufficient to induce any changes and the as-cast state is retained.

6.4.6.4. The equilibrium Mo_3Si+Mo_5Si_3: samples ITS9-10

The compositions of samples ITS9 and ITS10, which were used to investigate the two-phase region Mo_3Si+Mo_5Si_3, are given in Table 6.41. The measured compositions agree quite well with the nominal ones. Only the Mo content of sample ITS10 and the Si content of both samples exceed 1 at.% difference, but even here the deviation is not very large. The amount of impurities in both samples is very small.

The microstructures of the two samples are shown in Figure 6.70. Only the two expected phases are present, with Mo_3Si appearing in light gray and Mo_5Si_3 appearing in dark gray. In sample ITS9 (Figure 6.70a) the phase Mo_3Si has a higher phase fraction than in sample ITS10 (Figure 6.70b). Also the grains of phase Mo_5Si_3 seem to be larger in sample ITS10 than in ITS9. Furthermore, there are small precipitates of Mo_3Si in the Mo_5Si_3 grains of sample ITS10, which meant that the EDX operator had to be careful when choosing the measurement spots so that the other phase did not influence the results. It should also be noted that some of the Mo_3Si grains in ITS9 are significantly brighter in the BSE image than the surrounding microstructure. However, it was confirmed by EDX that this is not a compositional effect, as no difference between relatively brighter and darker areas could be detected. It was concluded that the difference in hue was most likely due to grain orientation effects.

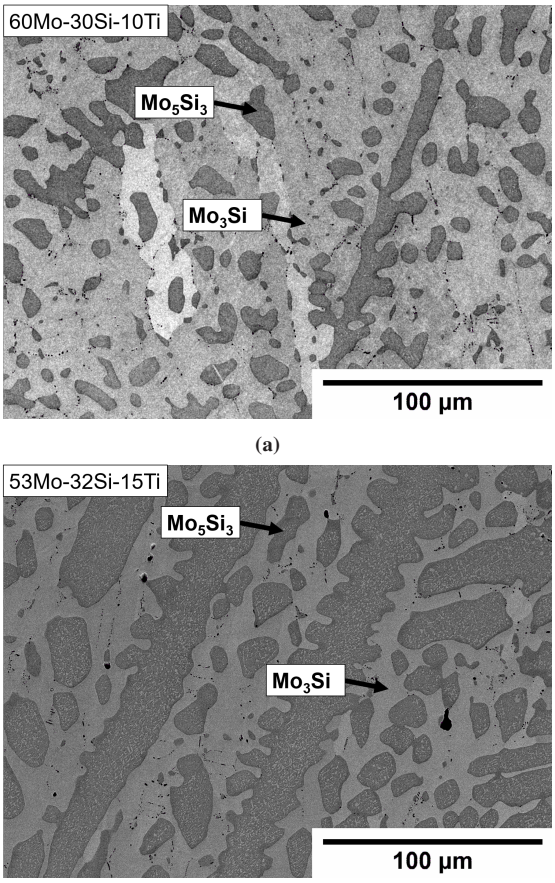

Figure 6.70.: The microstructures of the samples ITS9-10 after annealing for 330 h at 1573 K and water quenching. a) ITS9: 60Mo-30Si-10Ti, b) ITS10: 53Mo-32Si-15Ti.

The phase compositions of samples ITS9 and ITS10 are listed in Table 6.42. The only notable result here is that the Si deficiency of the phase Mo_3Si is again confirmed, with an average Si content well below the stoichiometric composition of 25 at.%.

Since samples ITS9 and ITS10 have the same composition as samples SSC14/QE10 and SSC7/QE3, respectively, these samples were compared. The microstructures of ITS9 and QE10 after identical heat treatment (1573 K/330 h/wq) are very similar. The majority of both samples consists of Mo_3Si, with grains of Mo_5Si_3 embedded within. The phase compositions are also quite similar for both phases. The mean values of both samples are well within the standard deviation of each other, except for the Ti content of Mo_3Si. The difference, however, is quite minor. Thus, it can be concluded that this sample composition is very reproducible. Since SSC14 and QE10 (the same sample but in the as-cast and annealed state, respectively) are also remarkably similar, it is not possible to conclude whether this is because equilibrium has been reached or because no changes occur at all under the chosen conditions. In the case of ITS10,

Table 6.42.: The phase compositions of the samples in the two-phase region Mo_3Si+Mo_5Si_3, measured by EDX.

Sample designation	Phase	x(Mo) / at.%	x(Si) / at.%	x(Ti) / at.%
ITS9	Mo_3Si	68.0 ± 1.0	23.7 ± 0.5	8.3 ± 0.7
	Mo_5Si_3	52.8 ± 1.4	36.1 ± 0.3	11.1 ± 1.3
ITS10	Mo_3Si	64.7 ± 0.9	24.3 ± 0.3	10.1 ± 0.8
	Mo_5Si_3	47.2 ± 2.4	36.6 ± 0.7	16.3 ± 2.3

Table 6.43.: The compositions of the samples in the two-phase regionβ+Ti_5Si_3 measured by ICP-OES and CGHE.

Sample designation	Nominal composition	x(Mo) / at.%	x(Si) / at.%	x(Ti) / at.%	x(C) / at.%	x(O) / at.%
ITS11	10Mo-20Si-70Ti	10.4	18.8	70.4	0.12	0.30
ITS12	20Mo-20Si-60Ti	20.3	19.2	60.0	0.28	0.32
ITS13	20Mo-20Si-60Ti	20.0	19.4	60.4	-	0.22
ITS14	30Mo-20Si-50Ti	29.9	18.8	51.2	-	0.142

both the microstructure and the phase compositions are very similar to QE3 after heat treatment and water quenching. Both samples show large grains of both Mo_3Si and Mo_5Si, as well as small precipitates of Mo_3Si in the Mo_5Si_3 grains. However, since the as-cast structure of ITS10 was not analyzed, no additional information is available as to whether these precipitates were formed during annealing, as in SSC7/QE3, or during solidification.

The XRD diffractograms of the samples ITS9 and ITS10 are shown in Figure 6.71. All peaks can be assigned to the phases Mo_3Si and Mo_5Si_3. This means that the phases were correctly identified and no additional phases were missed during SEM analysis.

6.4.6.5. The equilibrium β+Ti_5Si_3: samples ITS11-14

The compositions of the samples ITS11-ITS14, which were used to investigate the two-phase region β+Ti_5Si_3, are listed in Table 6.43. All measured compositions are close to the nominal ones, with only the Si content of sample ITS11 exceeding 1 at.%, but even then not by much. The impurity concentrations are also satisfactory since they are very low. For the samples ITS13 and ITS14, the concentration of C could not be measured.

The microstructures of the samples ITS11-ITS14 are shown in Figure 6.72. First, the two furnace cooled samples ITS11 and ITS12 (Figures 6.72a and 6.72b) are discussed. In both samples, in addition to the two expected phases β and Ti_5Si_3, almost pure Ti could be detected. The β phase

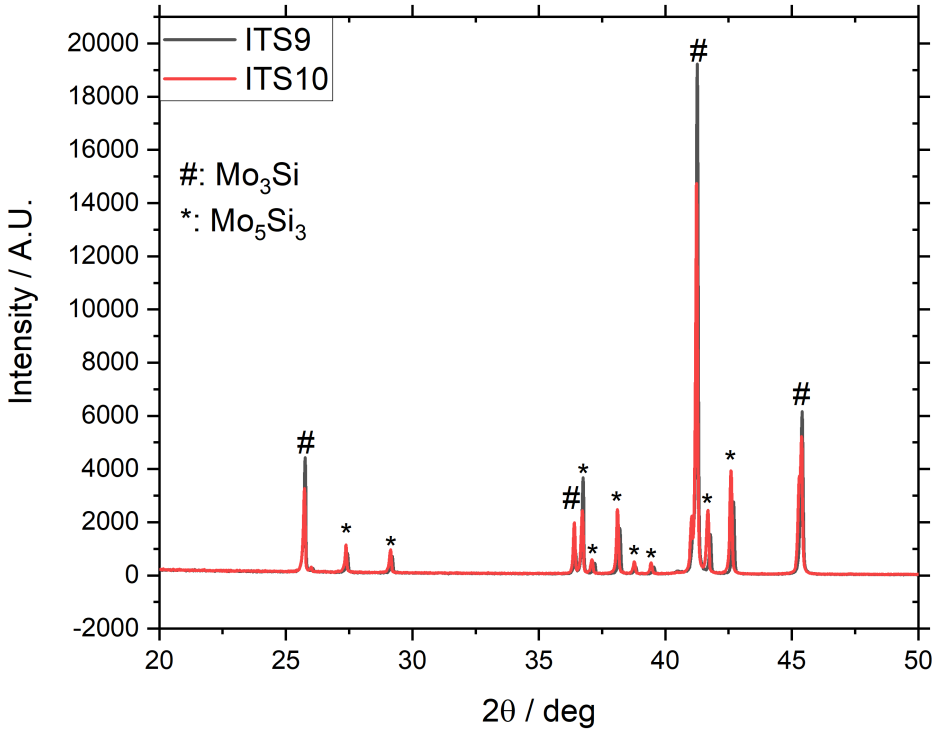

Figure 6.71.: The X-ray diffractograms of the samples ITS9-10 from 2θ=20-50°.

is the light gray shade, Ti_3Si_3 appears in dark gray and Ti in almost black. Ti_5Si_3 and β take the form of rather large, elongated precipitates in both samples ITS11 and ITS12. However, the phase fraction of β appears to be much higher in sample ITS12 than in sample ITS11. The nature of the (almost) pure Ti precipitates is still unclear. According to all literature, such a phase should not be stable and no convincing argument was found why some Ti should remain undissolved. To investigate whether the cooling rate after annealing has an influence on this phase, two additional samples, ITS13 and ITS14, were prepared. Their microstructures are shown in Figures 6.72c and 6.72d, respectively. No qualitative difference between the furnace cooled and the quenched samples is discernible. In both states, Ti precipitates are visible and have the same morphology. This supports the hypothesis that, in the context of Mo-Si-Ti alloys, furnace cooling can be considered rapid cooling due to the slow diffusion of the system.

The phase compositions of samples ITS11-ITS14 are listed in Table 6.44. The Ti precipitates have been omitted from this table. However, the presence of this phase significantly affects the equilibria of the samples. The samples in this two-phase region are the only ones examined where the sample compositions are quite far from the tie lines. This is to be expected when an

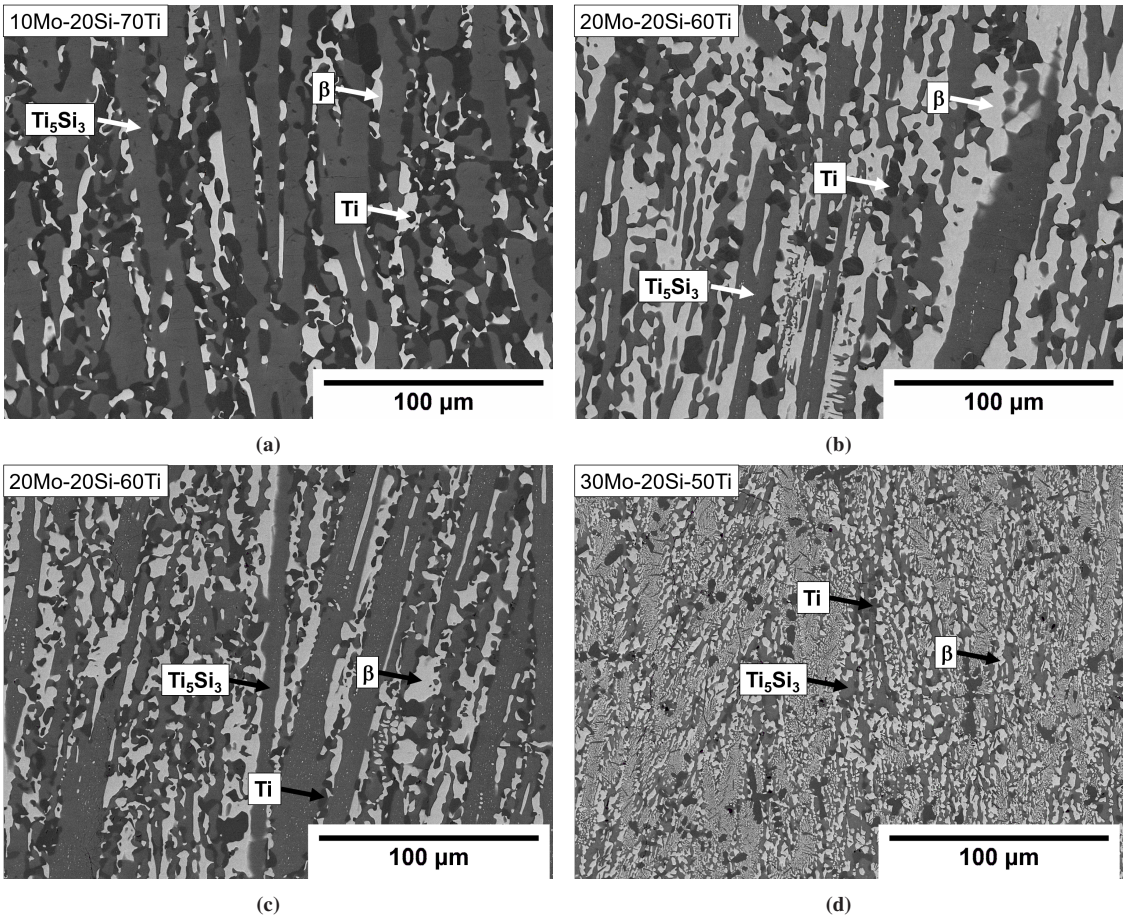

Figure 6.72.: The microstructures of the samples ITS11-14 after annealing for 330 h at 1573 K. ITS 11 and ITS12 were furnace cooled, ITS13 and ITS14 were water quenched. a) ITS11: 10Mo-20Si-70Ti, b) ITS12: 20Mo-20Si-60Ti, c) ITS13: 20Mo-20Si-60Ti, d) ITS14: 30Mo-20Si-50Ti.

entire phase is ignored, but until a way is found to dissolve the Ti precipitates, only preliminary measurements can be presented. However, the results do allow the conclusion that the sample is not in a previously unknown β+Ti_5Si_3+Ti three-phase equilibrium. In this case, the compositions of the phases β and Ti_5Si_3, respectively, between the four samples would be expected to be close to each other, as they would be the corners of the same tie triangle. Since they are significantly different, Ti is very likely metastable.

Since ITS12, ITS13 and SSC9 have identical compositions, they were compared. It should be noted that SSC9 was not heat treated, whereas ITS12 and ITS13 were not analyzed in the cast state. Therefore, direct comparison between SSC9 and the ITS samples can only be somewhat limited. The microstructure and phase compositions of SSC9 are shown in Figure 6.28 on page 127 and Table 6.13 on page 126 respectively. Several differences between the samples are immediately evident. First of all, SSC9 does not show any Ti precipiations, unlike ITS12 and

Table 6.44.: The phase compositions of the samples in the two-phase region β+Ti_5Si_3, measured by EDX.

Sample designation	Phase	x(Mo) / at.%	x(Si) / at.%	x(Ti) / at.%
ITS11	β	62.3 ± 1.4	2.1 ± 0.4	35.6 ± 1.3
	Ti_5Si_3	6.0 ± 0.7	37.9 ± 0.6	56.1 ± 1.0
ITS12	β	55.2 ± 5.2	2.7 ± 1.0	42.1 ± 4.8
	Ti_5Si_3	5.6 ± 0.5	38.1 ± 0.7	56.3 ± 0.8
ITS13	β	64.6 ± 0.9	1.8 ± 0.4	29.4 ± 5.8
	Ti_5Si_3	6.1 ± 0.7	37.8 ± 0.5	57.8 ± 2.8
ITS14	β	74.4 ± 1.0	1.9 ± 0.6	23.7 ± 0.7
	Ti_5Si_3	9.5 ± 1.0	37.5 ± 0.5	53.0 ± 0.9

Table 6.45.: The equilibrium phase compositions of the composition 20Mo-20Si-60Ti at 1573 K, according to a calculation with the dataset of Yang et al. [16].

Composition	Phase	x(Mo) / at.%	x(Si) / at.%	x(Ti) / at.%
20Mo-20Si-60Ti	β	35.8	1.4	62.8
	Ti_5Si_3	5.1	37.5	57.4

13. In fact, all ITS samples in the region β+Ti_5Si_3 show these segregations. Otherwise, the microstructures of the three samples are quite similar. All consist of β phase and TI_5Si_3 in lamellar structures, with some larger grains of Ti_5Si_3 also present. The phase compositions of Ti_5Si_3 are quite similar in all three samples, but the same is not true for the composition of β. Here the variation is extremely large; for example, the Mo content varies from 34.8 ± 5.3 at.% for SSC9 to 64.6 ± 0.9 at.% for SSC13. In addition, the standard deviation of SSC9 is much higher than that of the ITS samples, presumably due to the formation of a concentration gradient during solidification. To determine which, if any, of the compositions are close to equilibrium, a "single equilibrium" calculation of the composition 20Mo-20Si-60Ti at 1573 K was performed in Thermo-Calc. The stable phase compositions according to this calculation are listed in Table 6.45. This composition is remarkably close to that of SSC9, despite the fact that this sample was not annealed. This can be interpreted as an indication that heat treatment does not necessarily lead to pronounced differences compared to the cast state, since the cast state may already be close to high temperature equilibrium. The segregation of Ti, on the other hand, greatly interferes with the equilibration and reproducibility of the samples.

Table 6.46.: The compositions of the samples in the two-phase regionβ+Mo_5Si_3 measured by ICP-OES and CGHE.

Sample designation	Nominal composition	x(Mo) / at.%	x(Si) / at.%	x(Ti) / at.%	x(C) / at.%	x(O) / at.%
ITS15	27Mo-35Si-38Ti	27.6	35.0	37.3	b.l.d	0.067
ITS16	41Mo-25Si-34Ti	41.8	24.9	33.3	b.l.d	0.056
ITS17	74Mo-5Si-21Ti	74.0	4.6	21.3	b.l.d	0.069

6.4.6.6. The equilibrium β+Mo_5Si_3: samples ITS15-17

The compositions of the samples ITS15-ITS17 used to examine the two-phase equilibrium β+Mo_5Si_3 are listed in Table 6.46. The agreement between nominal and experimental compositions is remarkable, with the highest deviation being only 0.8 at.%. The impurity content is also extremely low, with C consistently below the limit of detection and the highest concentration of O below 0.07 at.%.

The microstructures of samples ITS15-ITS17 are shown in Figure 6.73. None of the three samples show only the two expected phases, β and Mo_5Si_3. Instead, up to 5 phases are present simultaneously. In sample ITS15 (Figure 6.73a), β appears in the lightest gray, Mo_3Si in a slightly darker tone, Mo_5Si_3 appears as a medium gray, Ti_5Si_3 appears in dark gray and undissolved, pure Ti appears in nearly black. The β precipitates are very fine, while Mo_3Si is slightly larger and has a very small phase fraction. Both Mo_5Si_3 and Ti_5Si_3 are present as large, elongated grains. Ti again takes the form of small, round precipitates. In sample ITS16 (Figure 6.73b) the same phases are present in the same shades, but the microstructure is very different. All phases are very fine and uniformly distributed. Only the two Mo silicides, Mo_3Si and Mo_5Si_3, appear as somewhat larger, continuous grains. Ti is clearly present in the form of dendrites in this sample, further indicating that these precipitates are formed during sample preparation. Sample ITS17 (Figure 6.73c) consists mainly of β phase with several other phases precipitating between the grains. The determination of these phases in the SEM proved unsuccessful as the precipitates are too small to allow a conclusive determination of their composition, but they appear to be a eutectic structure of Mo_3Si and Mo_5Si_3. In addition, some traces of pure Ti were found. The presence of Ti in these three samples is particularly interesting since it was not detected in the three-phase region β+Mo_5Si_3+Ti_5Si_3, which lies between the two two-phase regions where this phase was found. Due to the evident fact that these three samples were not in thermodynamic equilibrium, no attempt was made to use these samples for further investigation. However, for the sake of completeness, the phase compositions are listed in Table 6.47. The phase compositions of sample ITS17 are not listed, as they cannot be measured reliably. Although not identical, the compositions of ITS16 and SSC6/QE2, as well as SSC13/QE8, are quite similar, so these samples were compared. The microstructure and phase composition of QE2 are shown in Figure

Table 6.47.: The phase compositions of the samples in the two-phase region β+Mo_5Si_3, measured by EDX.

Sample designation	Phase	x(Mo) / at.%	x(Si) / at.%	x(Ti) / at.%
ITS15	Ti	1.0 ± 0.3	1.6 ± 0.7	97.4 ± 1.0
	β	75.2 ± 1.0	7.2 ± 1.7	17.5 ± 0.7
	Mo_3Si	53.4 ± 1.1	23.1 ± 0.7	23.2 ± 1.0
	Mo_5Si_3	32.5 ± 0.4	36.8 ± 0.3	30.7 ± 0.5
	Ti_5Si_3	22.0 ± 0.5	37.3 ± 0.3	40.7 ± 0.5
ITS16	Ti	1.3 ± 0.5	1.4 ± 0.9	97.4 ± 1.3
	β	80.2 ± 0.7	5.6 ± 0.5	14.2 ± 0.3
	Mo_3Si	54.6 ± 0.2	24.2 ± 0.4	21.3 ± 0.3
	Mo_5Si_3	29.2 ± 2.0	37.6 ± 0.3	33.2 ± 2.1
	Ti_5Si_3	17.8 ± 1.0	37.2 ± 0.7	45.0 ± 0.7

6.45 on page 145 and Table 6.22 on page 145, respectively, while the same is shown for QE8 in Figure 6.53 on page 154 and Table 6.53 on page 154, respectively. The microstructures of all three samples are quite similar. All consist of very finely dispersed precipitates of the phases, as well as some larger grains of Mo_3Si and Mo_5Si_3. The phase compositions are similar but distinctly different between the samples. This is further evidence that all three samples are far from equilibrium, as the variance of the phase composition is still quite high. As a conclusion, the results from these three samples confirm the findings of section 6.4.4, that specimens in this region of the phase diagram require excessive annealing times to reach equilibrium.

6.4.6.7. Post-annealing chemical analysis

After annealing and characterization of the samples ITS1-ITS17, enough material was left from some samples to perform further analysis by ICP-OES and CGHE. The chemical analysis of the annealed state provided two more important pieces of information about the series of experiments. First, it was possible to determine whether the sample composition changed significantly during heat treatment. This could be the case if elements evaporate during annealing, for example due to the formation of volatile oxides such as MoO_3. In addition, by measuring the oxygen content of the samples it was possible to investigate whether, despite all the measures described in section 6.1, the samples take up increased amounts of oxygen during heat treatment as a result of the unavoidable residual oxygen in the process gas. After annealing, the concentration of C was not examined because there is no additional source of this element in the process. This introduced a small error because the calculation of the concentrations of the atoms in at.% normalizes the

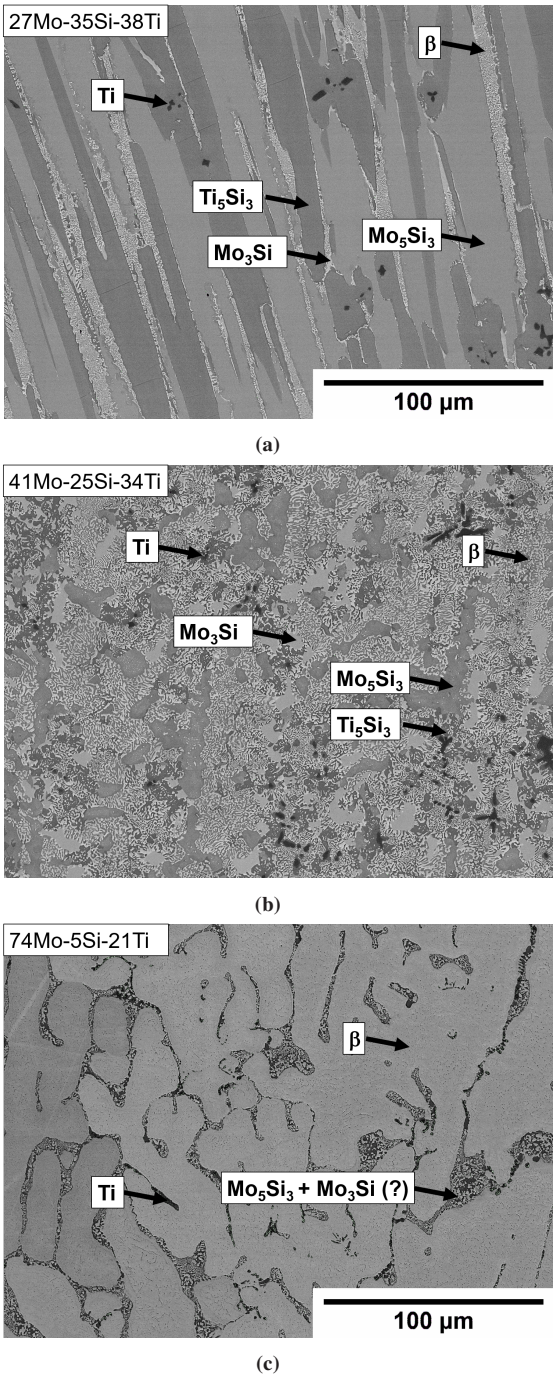

Figure 6.73.: The microstructures of the samples ITS15-17 after annealing for 330 h at 1573 K and water quenching. a) ITS15: 27Mo-35Si-38Ti, b) ITS16: 41Mo-25Si-34Ti, c) ITS17: 74Mo-5Si-21Ti

values to 100 %. This means that any element that is present, but not accounted for, will cause an offset. However, due to the small amount of C impurities in the samples, this error was considered acceptable. Prior to measurement, the surface of each sample was ground with #120 SiC paper to remove any oxide layer that may have formed on the surface. This was important because the EPMA, EDX and XRD measurements were taken close to the core of the sample, where the influence of impurities from the processing gas should be minimal, whereas metallic samples will always form an oxide layer on the surface. Thus, by measuring the annealed samples in this way, the comparability with the other measurements in these sections is higher and the error due to the inclusion of the oxide layer is avoided. The results of the measurement are listed in Table 6.48. Even after annealing, the differences between nominal and experimentally determined sample compositions are quite small. One noteworthy case is the composition of the sample ITS3. Here, the Si composition decreases to a degree that the real sample compositions falls nearly exactly onto the border between the three-phase region β+Mo_5Si_3+Ti_5Si_3, where the sample was supposed to be located, and the adjacent two-phase region β+Ti_5Si_3, according to the dataset from Yang et al. Following the conclusions drawn from this work, the three-phase region in question is actually shifted towards slightly higher Mo concentrations. This shift is fairly small, but sufficient to put the measured composition of the sample ITS3 into the region β+Ti_5Si_3, which agrees well with the microstructure of the sample. The fact that the sample was originally in a three-phase equilibrium, but shifted into a two-phase equilibrium by losing Si during annealing also explains why it is not in thermodynamic equilibrium after 330 h, unlike the other samples in this region. The exact mechanism by which Si is lost has not been investigated. It is possible that the element diffuses into the Mo foil used to separate the samples from the Al_2O_3 crucible used during heat treatment, but no analysis of this foil has yet been performed.
A comparison between the values before annealing (Tables 6.35, 6.37, 6.39, 6.41, 6.43 and 6.46) show that some Mo is typically lost in the process, likely due to the formation of volatile oxides, but only in small amounts. The concentration of oxygen increases as expected, but remains quite low. In addition, the standard deviations of some samples for O are quite high. Since standard deviations are not easily converted from wt.% to at.%, they are listed in the original data in the Appendix, where the values are given as measured in wt.% in Table A.2. A high standard deviation indicates that the sample contains considerably more oxygen in some measured spots than in others, i.e. a distinct spatial distribution of the element in question. What this most likely means is that not enough of the surface was ground away to completely remove the oxygen layer. The criterion chosen was to stop grinding when the shine of bare metal was visible. Evidently, this was not always sufficient and oxygen penetrated deeper into the sample than was optically detectable. However, even with this error, the values for oxygen content are quite low and can be expected to be even lower in the core of the sample, where the characterization of the samples with respect to phase compositions, etc. took place. Therefore, it can be concluded that the

Table 6.48.: The compositions of several samples after annealing at 1573 K for 330 h and water quenching, as well as their oxygen content, measured by ICP-OES and CGHE.

Sample designation	Nominal composition	x(Mo) / at.%	x(Si) / at.%	x(Ti) / at.%	x(O) / at.%
ITS1	17Mo-35Si-48Ti	17.7	34.1	47.5	0.7
ITS2	21Mo-35Si-44Ti	21.8	33.3	44.4	0.5
ITS3	35Mo-25Si-40Ti	35.2	23.3	40.8	0.7
ITS5	50Mo-23Si-27Ti	49.7	22.3	26.7	1.3
ITS6	55Mo-20Si-25Ti	56.8	17.7	25.1	0.4
ITS7	75Mo-15Si-10Ti	74.2	14.7	9.9	1.3
ITS8	75Mo-10Si-15Ti	76.1	9.1	14.5	0.3
ITS9	60Mo-30Si-10Ti	61.5	27.9	10.4	0.3
ITS10	53Mo-32Si-15Ti	54.2	30.5	15.0	0.2

samples investigated in this series of experiments were viable even after 330 h at 1573 K in a flowing gas atmosphere.

6.4.6.8. Discussion

The primary conclusion that can be drawn from the samples used to investigate the metal-rich area of the isothermal section of Mo-Si-Ti at 1573 K is that the system is so refractory and slowly diffusing that equilibration of the specimens is not always possible in a viable time frame. A large and important fraction of the samples were evidently not in thermodynamic equilibrium after an annealing time of 330 h. In the two-phase region β**+Ti_5Si_3**, the presence of nearly pure Ti was detected in nearly every sample. Since this region of the phase diagram has never been studied in the literature, there are no data from other authors on the nature or stability of these precipitates. However, from the binary system Ti-Si it can be deduced that there should be no pure (or nearly pure) form of Ti other than the β phase. The fact that the Ti precipitates often have a dendritic form suggests that they are formed during solidification of the melt, which is supported by micrographs of as-cast specimens, and are retained during annealing. This leads to the conclusion that even Ti-rich compositions, which would be expected to have a relatively high diffusion rate compared to alloys with a higher Mo content, are not fully equilibrated. One hypothesis regarding the formation of Ti precipitates is that the composition of the liquid increases in Ti during the precipitation of β and Ti_5Si_3 to such an extent that the last β to solidify is almost pure Ti. This agrees quite well with the composition calculation of sample SSC13 (Figure 6.39 on page 138). However, why this leads to the formation of a distinctly different phase of β, rather than a continuous gradient, is currently unknown.

The adjacent three-phase region β**+Mo_5Si_3+Ti_5Si_3** appears to be in, or at least close to, thermodynamic equilibrium, as the samples located here consistently show only the expected phases, and the phase compositions of different samples agree well with one another, even when the sample compositions are different. One sample, ITS3, showed unexpected behavior because it was a two-phase sample (β+Ti_5Si_3) when the nominal composition placed it completely within the aforementioned triangle. In addition, the phase compositions intersected the tie triangle, which is an irrefutable argument that the sample cannot be in thermodynamic equilibrium. However, further investigation of this sample showed that it had lost enough Si during processing that it eventually fell into the adjacent two-phase region. This explains why the microstructure and XRD diffractogram showed only two phases. In addition, due to this change during annealing, it is reasonable to conclude that the sample could not reach the new equilibrium within the given time, which is why the phase compositions are so far from a stable tie line.

In the two-phase region β**+Mo_5Si_3**, not a single sample reached equilibrium. Each sample showed complex microstructures with up to five phases simultaneously, which means that they are far from equilibrium. Scheil solidification calculations, as well as examination of several samples in the as-cast state, show that the complex microstructures in this region are formed during solidification. Several edges of double saturation meet in this region, some of which lead to the formation of two different eutectic reactions in succession, while others are peritectic in nature and lead to primary solidification of a second phase followed by one or more eutectic reactions. As a result, the microstructures not only consist of many phases, but are typically quite fine grained. All these factors, together with the rather slow diffusion in the system in general, contribute to the fact that the microstructure formed is very stable and does not change significantly at 1573 K even after 330 h. In section 6.4.4 it was shown for one sample (SSC6/QE2, 44.5Mo-23.5Si-32Ti) that even after a total of 708 h of annealing, the sample still showed a considerable amount of Ti_5Si_3, further emphasizing the stability of the structure once formed. Another fact to mention about samples in this two-phase region is the presence of the same precipitates of nearly pure Ti that were observed in the two-phase region β+Ti_5Si_3. This is particularly noteworthy because this phase was never found in the tie triangle between these two-phase regions. This seems to indicate that there are some conditions under which the phase is formed, which are met for the regions β+Ti_5Si_3 and β+Mo_5Si_3, but not for the three-phase region β+Mo_5Si_3+Ti_5Si_3 in between. However, this avenue was not followed in this work and should be the subject of a dedicated investigation, as it seems likely that much information about the unknown precipitates can be obtained in this way.

For similar reasons, no successful sample with the equilibrium β**+Mo_3Si+Mo_5Si_3** could be obtained. Based on microscopic and EDX/EPMA analysis alone, it was initially thought that the three samples placed in this region were in equilibrium, as they exhibited the β phase, Mo_3Si, and a 5-3 silicide with a composition that fit Mo_5Si_3. All three samples had phase compositions very close to each other, and no intersection with other tie triangles or tie lines was observed,

reinforcing the assumption that the samples were in thermodynamic equilibrium. However, phase analysis by XRD revealed that the 5-3 silicide does not have the crystal structure of Mo_5Si_3, but corresponds exactly to the structure of Ti_5Si_3. Even by shifting the lines of the pattern belonging to Mo_5Si_3, it is not possible to reconstruct the diffractogram of the samples. Therefore, it was concluded that the phases present are in fact β, Mo_3Si and Ti_5Si_3. Such an equilibrium cannot exist considering all available data, because it would intersect the experimentally confirmed region β+Mo_5Si_3+Ti_5Si_3. The reason for the presence of the observed phases is most likely due to the solidification process. Scheil solidification calculations show that all three phases found in the samples are formed during solidification. Therefore, it can be concluded that, similar to the adjacent two-phase region discussed above, the phases remain stable at the temperature of 1573 K for quite a long time. In fact, the diffractograms show no traces of Mo_5Si_3 at all, indicating that even after 330 h this phase has not started to form. Even if the corners of the triangle do not fall where the dataset suggests, or the samples are not in the triangle at all, the specimens can be expected to exhibit Mo_5Si_3 in equilibrium because all adjacent equilibria contain this phase. The fact that no fraction can be detected by powder XRD indicates that the sample is still extremely far from equilibrium, or possibly that the barrier to phase transformation is so high that it cannot be overcome at all at this temperature. One argument that has been investigated is the stabilization of the structure of Ti_5Si_3 by impurities such as O or C. As a Nowotny phase it can solve up to 11.1 at.% of such impurities and the barrier to dissolving such phases once formed is very high [141]. However, chemical analyses of these samples show that the impurity content is far too low to expect such strong stabilization as observed here.

The conclusions drawn from the samples of this work lead to further questions regarding the **thermodynamic equilibrium within the Mo-Si-Ti system**. First, while there are strong arguments for concluding that at least some of the samples are in equilibrium in the three-phase region β+Mo_5Si_3+Ti_5Si_3, definitive proof of this is not yet available. It is quite possible that the samples show these three phases in similar compositions purely by coincidence, just as the phase compositions of samples ITS4-ITS6 were very similar to each other despite not being in equilibrium. This may even lead to the conclusion that the equilibrium is not stable after all, if the samples are annealed for a sufficient amount of time and the previous experiments only gave the current state of the samples after 330 h. In addition, the validity of the existing Mo-Si-Ti dataset must be carefully evaluated based on the results of this work. As discussed above, many of the samples investigated here are extremely far from equilibrium after annealing at 1573 K for typically 330 h, and in one case as long as 708 h. While Yang et al. [16] chose slightly higher temperatures with 1698 and 1873 K, at least for the former temperature it seems highly unlikely that this would make a significant difference. As the examples in the two-phase region β+Mo_5Si_3 and the three-phase region β+Mo_3Si+Mo_5Si_3 demonstrate, the samples at 1573 K are not close to equilibrium after 330 h, and Yang et al. annealed for only a maximum of 300 h. Therefore, it seems quite likely that Yang et al. also observed "current" states of the

samples rather than true, stable equilibria, and based their optimization on them. At 1873 K it seems more likely that the samples reach thermodynamic equilibrium within the given time, but this is difficult to judge since no micrographs of such samples are provided. In addition, the annealing time at this temperature was only 150 h, which seems rather low given the results of this work. Furthermore, even if the the data at 1873 K is reliable, if the data at 1698 K is faulty or incomplete, the temperature-dependent parameters are likely to be inaccurate. Therefore, given how extremely difficult it is to equilibrate Mo-Si-Ti samples, and how challenging it can be to determine whether or not they are in equilibrium at all, the question arises as to whether any data in this system is reliable enough to form the basis of a predictive CALPHAD dataset. Of all the data, the binary equilibria β+Mo_3Si, Mo_3Si+Mo_5Si_3, and β+Ti_5Si_3 can be considered the most credible. These equilibria are direct extensions from their respective binary systems, and thus can be expected to extend into the ternary regions, and they have been observed in ternary samples as well. These samples are, at least often, very likely to be in equilibrium, which can be inferred from the fact that the sample compositions typically lie on a tie line connecting the phase compositions. If these three equilibria are accepted, the question remains which equilibria are stable between them. The only data available in the literature are those of Yang et al, who postulated the two phase region β+Mo_5Si_3 between the three phase regions β+Mo_5Si_3+Ti_5Si_3 and β+Mo_3Si+Mo_5Si_3 for the experimentally investigated temperatures. However, no micrographs or diffractograms were provided to prove this conclusively. In this work, samples containing the phases β+Mo_5Si_3+Ti_5Si_3 were also found, but it is not conclusively proven that these samples are in a stable equilibrium. Furthermore, it was shown that the samples expected to consist of β+Mo_5Si_3 and β+Mo_3Si+Mo_5Si_3 were definitely not in equilibrium after annealing at 1573 K for 330 h, because the phase Ti_5Si_3 formed during solidification remained (meta)stable. It seems unlikely that the annealing temperature selected by Yang et al., 1698 K, is sufficiently high to expect significantly different results. However, the higher annealing temperature chosen, 1873 K, could reasonably be expected to be sufficient to equilibrate the samples, which would tentatively prove the existence of the postulated regions. There is another datum in favor of the stability of the postulated equilibria, namely the sample SSC6/QE2 discussed in section 6.4.4. After 708 h heat treatment it shows the phases β+Mo_5Si_3+Ti_5Si_3, while after casting it additionally shows Mo_3Si. By analyzing after 330 h and 378 h, it could be shown that the amount of Mo_3Si decreases with increasing time. While it is unclear whether the sample is in equilibrium or not (according to the dataset of Yang et al., it is expected to be in the two-phase region β+Mo_5Si_3), its microstructural evolution over time suggests that the sample will eventually consist of either β+Mo_5Si_3 or β+Mo_5Si_3+Ti_5Si_3. In either case, the stability of one of these crucial equilibria is proven by this example, and for one of these two equilibria to exist, the adjacent one must also be stable. Finally, the last remaining tie triangle that must exist in the system according to the laws of heterogeneous equilibria must indeed be the postulated region β+Mo_3Si+Mo_5Si_3. This shows that despite the fact that much is still unknown in this system, there is enough data to determine

the stable equilibria even in regions that are not yet experimentally clear.
It should be noted that this work has provided several relevant new insights beyond the discovery that many, if not all, metal-rich Mo-Si-Ti samples in the literature are possibly not in thermodynamic equilibrium. For once, the Si deficiency of the Mo_3Si phase, which is fairly well studied in the binary system, was confirmed in the ternary system. While this has been reported before, e.g. by Schliephake et al. [12], now several samples with known composition and impurity content both before and after annealing confirm the finding. In addition, a significant solubility for Si in the β phase was found. This is particularly relevant because this phase is present in all equilibria except one in the metal-rich region. Because of its relatively high ductility it will be used in all parts and components that may eventually be made from Mo-Si-Ti based alloys. The different Si content of the β phase affects the predicted Si distribution in the microstructure (more Si is dissolved in β grains than previously assumed), which in turn affects the estimated oxidation and corrosion resistance. In addition, the mechanical properties of the β phase may change as a function of Si content, and the stable, single-phase β samples required to study this can now be prepared with greater accuracy. However, it is possible that this is also just an effect of the metastability of the system and that the Si solubility in β is actually lower in equilibrium. In terms of the practical application of potential Mo-Si-Ti alloys, the observation that diffusion in the system is so slow that some microstructures do not change even after prolonged annealing may even be beneficial. This fact can be exploited to take advantage of certain metastable microstructures formed during casting that may have favorable mechanical or corrosive properties, but would not be expected to be stable. However, as shown in this work, such structures can be stable at turbine operating temperatures, potentially opening up new avenues for alloy design. Finally, assuming that the three-phase region β+Mo_5Si_3+Ti_5Si_3 is indeed stable and in equilibrium, slightly different solubilities of Mo in Ti_5Si_3 and of Ti in Mo_5Si_3 were observed, as well as a higher stable Mo content of the corresponding β phase of this triangle. The differences between the calculation with the dataset from Yang et al. and the samples from this series of experiments which are most likely in thermodynamic equilibrium are shown in Figure 6.74.

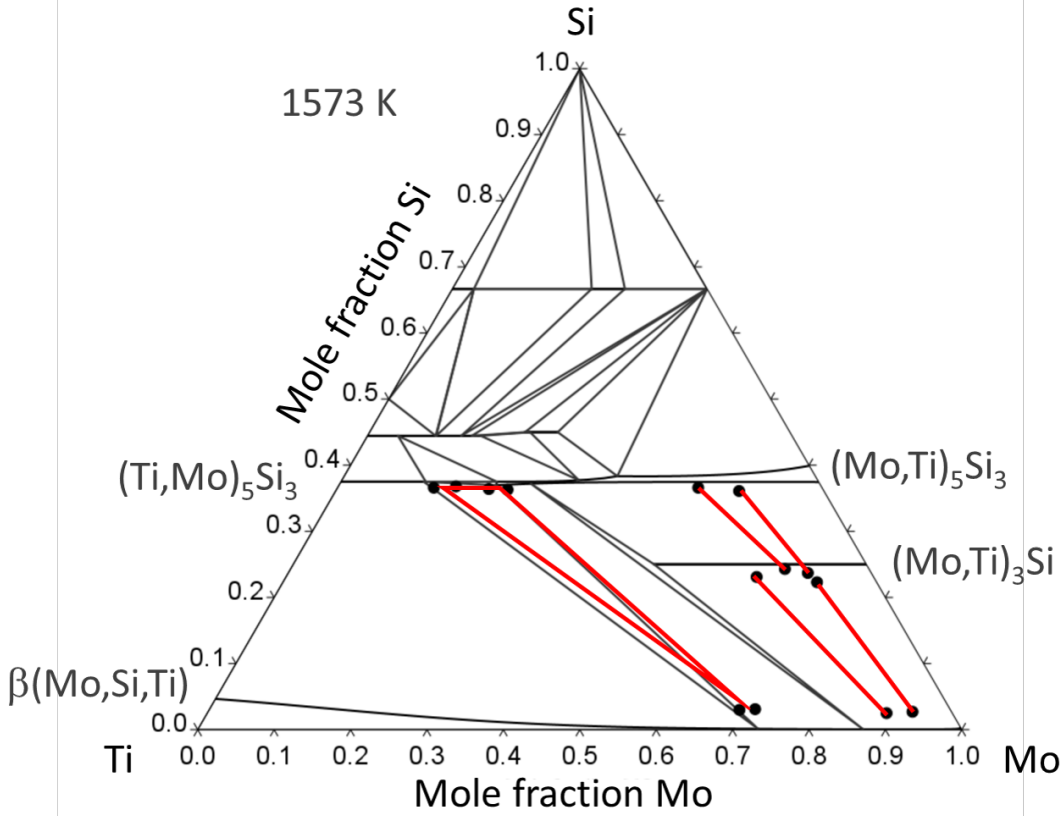

Figure 6.74.: The experimental phase compositions of the samples investigated after annealing at 1573 K for 330 h and subsequent water quenching, superimposed on the isothermal section of the Mo-Si-Ti system at this temperature. The isothermal section was calculated using the dataset of Yang et al. [16]. The equilibria found in this work are shown in red, with the circles indicating each phase composition.

7. Thermodynamic modelling and optimization

7.1. The Mo-Si system

As described in section 4.1, none of the available datasets of the Mo-Si system were entirely satisfactory. Therefore, a reassessment of the system based on both the literature data and the experimental data given in section 6.3 was performed. The results are published in [33]. The following section summarizes the assessment procedure as well as the computational results.

7.1.1. Thermodynamic models and phase descriptions

SGTE data compiled by Dinsdale [72] were used for the pure elements. Both the liquid and the β phase were described as solution phases. The phase $MoSi_2$ was described as stoichiometric phase. The compound Mo_5Si_3 was described by a sublattice model expressed in the Compound Energy Formalism [26, 24]. Two competing descriptions were used for the phase Mo_3Si. For once, it was simplified as a stoichiometric phase with the experimentally observed composition of 23 at.% Si. Alternatively, the phase was modelled in three sublattices; one containing Mo, one containing Si and one containing Si and vacancies. The following section explains the reasoning behind each model based on the crystallography of each respective phase.

7.1.1.1. $MoSi_2$

The space group of the phase $MoSi_2$ is *I4/mmm*. Si atoms occupy the Wyckoff position 4e on the lattice while Mo atoms occupy the position 2a. There is no significant substitution reported. Therefore, the phase is described as a line compound and no interaction parameters are used to describe the molar Gibbs energy of this phase. The model is thus: $(Mo)_1(Si)_2$.

7.1.1.2. Mo_5Si_3

The space group of the phase Mo_5Si_3 is *I4/mcm*. At stoichiometric composition (x(Si)=37.5 at.%), the Mo atoms occupy the Wyckoff positions 16k and 4b and the Si atoms occupy the 4a and

8h positions [142]. In case of Si deficiency, the Si atoms at the 4a positions are substituted by Mo, while in case of Si excess, the Mo atoms at the 4b positions are substituted by Si [143]. To describe this behavior, this phase was modeled with four sublattices, with each Wyckoff position corresponding to one sublattice: $(Mo)_{0.5}(\underline{Mo},Si)_{0.125}(Mo,\underline{Si})_{0.125}(Si)_{0.25}$. The majority atom is underlined, where applicable.

7.1.1.3. Mo_3Si

The crystal structure of Mo_3Si was determined by Templeton and Dauben [144] from powder XRD. It is isostructural with Cr_3Si and has the space group $Pm\overline{3}n$ (#223). This means that Si occupies Wyckoff position 2a while Mo atoms occupy Wyckoff position 6c. In 2006, Aindow et al. [145] found so-called "forbidden reflections" in the electron diffraction patterns of several other compounds with an A15 structure (Nb_3Al, Cr_3Si, V_3Si), indicating a superstructure in these crystals. These compounds typically have solubility ranges that extend particularly toward the excess component side. Therefore, they concluded that the inclusion of defects at only one of the two minority atom positions reduces the symmetry of the crystals (space group $Pm\overline{3}$, #200) and the reflections in question are now allowed. However, no decision could be made whether the underlying defects were antistructure atoms or vacancies. Information about this can be derived from diffusion experiments as reported by Prasad and Paul [146]. In this work, the growth of Mo silicides in diffusion pairs was examined. From the evaluation of the diffusion coefficients it was concluded that in Mo_3Si, the concentration of both antistructure atoms and vacancies must be significant.
For the sake of modeling, simplifications must be made, as a full model with both vacancies and antistructure atoms leads to an unreasonable number of end members for which no Gibbs energy data are available, while adding little value to the dataset and the calculations themselves. Therefore, it was decided to use two different descriptions of the Mo_3Si phase with different degrees of simplification. First, it was modeled as a simple line compound with the experimentally observed composition: $(Mo)_{0.77}(Si)_{0.23}$. Second, the defects were treated as if they were exclusively vacancies. Therefore, this model allows for a homogeneity range. This may be relevant in higher order systems such as Cr-Mo-Si, which have a continuous A15 phase and some homogeneity range in the ternary space. To best reflect the occupation of the Wyckoff positions, this model uses three sublattices: $(Mo)_6(Si)(Si,Va)$. It must be noted that this model has the distinct disadvantage that the phase is unstable at its stoichiometric composition. Since the phase was never reported at the stoichiometric composition however, but always with a Si deficiency (which the model is able to reflect well), this shortcoming was considered acceptable.

7.1.2. Assessment procedure

The first step of the optimization was to fit the heat capacity data. The parameters of each phase were optimized separately. Then all phases were optimized simultaneously to fit the invariant reaction data as well as the liquidus, solidus and solvus lines. Then the parameters of the phase Mo_5Si_3 were optimized. The parameter $G_{Mo:Mo:Si:Si}$, corresponding to the stoichiometric composition, was fitted first to match the congruent melting point of the compound. All other parameters corresponding to this compound were set to zero in this step. In this way, the model can be optionally simplified to treat this phase as a line compound by simply setting all other parameters of this phase to zero in the final dataset. Next, the parameter $G_{Mo:Si:Si:Si}$ was adjusted to reflect the Si-rich boundary of the homogeneity range, while the parameter $G_{Mo:Mo:Mo:Si}$ was adjusted to reflect the Mo-rich boundary. A similar approach was chosen for the version of the dataset where Mo_3Si was expressed in a sublattice model. It should be noted that, to the best of the authors knowledge, no DFT data exists for the enthalpies of formation of the unstable end members of either compound, so the best approach was to optimize the values in a way that yielded realistic results. Finally, all thermochemical and compositional data were optimized together.
The following section lists the experimental data used in the optimization. The heat capacity and enthalpy data were taken from the publications of King and Christensen [57], Douglas and Logan [60], Walker et al. [58], Callanan et al. [47], Mezaki et al. [75] and Bondarenko et al. [54]. The liquidus and solidus temperatures of the system were taken from Svechnikov et al. [37]. The same publication was used for the invariant reaction temperatures and composition, as well as for the homogeneity range of Mo_5Si_3. For the Si solubility of the β phase the data of Ham [35] were used additionally. For the enthalpies of formation of the intermetallic phases, the data of Chart [53] were used. Even though other experimental data and DFT data from several authors agree well with the data from Chart, they were not used for the optimization to avoid redundancy. Data for the enthalpy of mixing of the liquid phase were accepted from Arpaci and Frohberg [50].

7.1.3. Thermodynamic calculations

Figures 7.1 and 7.2 show the calculated phase diagrams of the Mo-Si system resulting from this optimization together with the corresponding experimental data. Data accepted for optimization are shown in black, while available data that were not considered for reasons explained in section 4.1.1 are shown as hollow symbols. Figure 7.1 shows the version where the Mo_3Si phase is modeled as a stoichiometric compound, while Figure 7.2 shows the version where this phase includes vacancies on one sublattice. In both variations of the dataset the agreement between the experimental data of the liquidus and solidus lines and the calculation is high.

Table 7.1.: Comparison between the experimentally determined values of the temperatures and Si concentrations of the liquid phase for the invariant reactions in the Mo-Si system with the calculated values.

Reaction	Temperature / K		x(Si)	
	This work	Experimental [37]	This work	Experimental [37]
$\beta + L \rightleftarrows Mo_3Si$	2301	2298 ±20	0.248	0.257
$L \rightleftarrows Mo_3Si + Mo_5Si_3$	2301	2293 ±20	0.250	0.264
$L \rightleftarrows Mo_5Si_3$	2452	2453 ±20	0.375	0.375
$L \rightleftarrows Mo_5Si_3 + MoSi_2$	2181	2173 ±20	0.543	0.540
$L \rightleftarrows MoSi_2$	2292	2293 ±20	0.666	0.666
$L \rightleftarrows Si + MoSi_2$	1674	1673 ±10	0.975	0.985

The liquidus line is in good agreement with the available experimental data. However, there is little reliable experimental information available at the boundaries of the system. The solidus lines are well represented throughout the system. The calculated maximum solubility for Si in the β phase is 4.1 at%, which is in good agreement with the DFT calculation by Lenchuk et al. [147]. For the solvus line of the β phase there are a few experimental data points that deviate from the calculation, but not by an unacceptably large margin. Beyond the temperature shown, no problems were found that would invalidate the dataset. It should be noted that an unrealistic miscibility gap in the liquid phase opens at about 4500 K. However, this problem is negligible due to the practical irrelevance of such temperatures. Another noteworthy point is the homogeneity range of the phase Mo_3Si. It increases with decreasing temperature, which is thermodynamically highly improbable. However, since no experiments in the Mo-Si system have shown the existence of a homogeneity range, and the solubility in the calculation is rather low, this point was considered acceptable. The homogeneity range has little relevance for the binary system, but can be optimized for ternary systems such as Mo-Si-Cr, where it is strongly pronounced.

Table 7.1 compares the experimental data and the calculated results for the invariant reactions. The agreement between the calculated and the experimentally determined reaction temperatures is very good, with a maximum deviation of only 3 K. The calculated concentrations also agree very well with the experimentally determined values in most cases. Only the eutectic reaction L $\rightleftarrows$ Si + $MoSi_2$ shows a noticeable deviation (1 at%), but given the excellent agreement of all other data throughout the system, this small difference was considered acceptable.

Table 7.2 compares the previously reported enthalpies of formation of the intermetallic compounds with the results calculated by this dataset. All values refer to a temperature of 298 K. The calculated enthalpies of formation at 298 K are -29.3 kJmol^{-1} for Mo_3Si, -38.2 kJmol^{-1} for

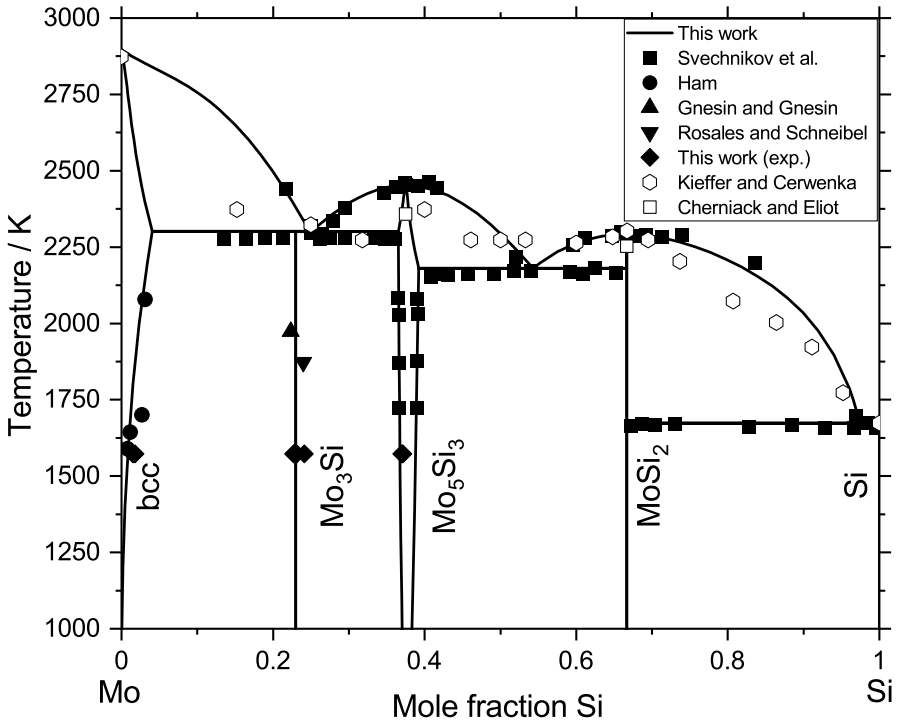

(a)

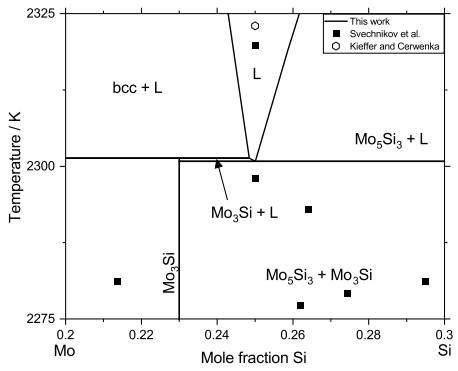

(b)

Figure 7.1.: The calculated phase diagram, with the phase Mo_3Si modelled as a stoichiometric compound. The data are the reported experimental values by Ham [35], Svechniknov et al. [37], Gnesin and Gnesin [43], Rosales and Schneibel [41], Kieffer and Cerwenka [36], Cherniak and Elliot [38] and the experimental data from this work. Black points were used in the optimization, white points were disregarded. a) The entire phase diagram, b) the section of the phase diagram from 20 to 30 at% Si.

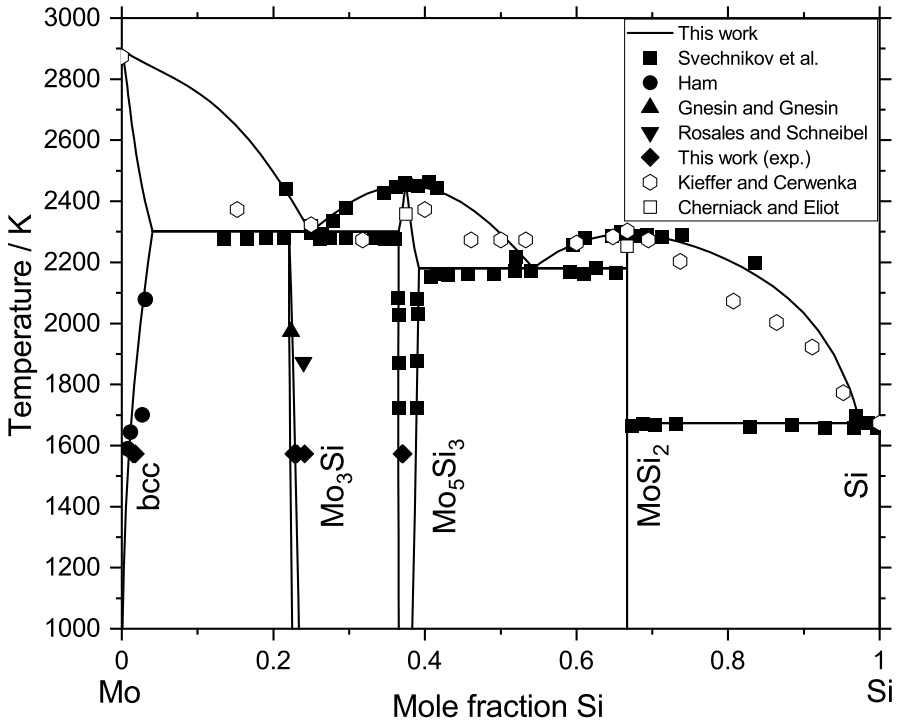

(a)

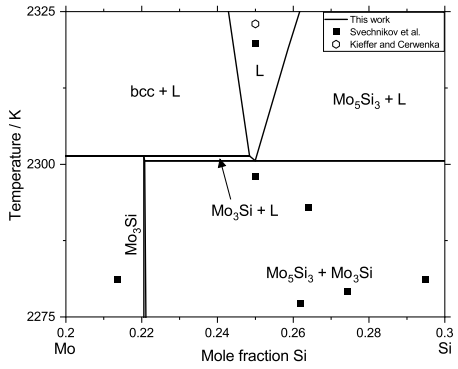

(b)

Figure 7.2.: The calculated phase diagram, with the phase Mo_3Si described by a sublattice model. The data are the reported experimental values by Ham [35], Svechniknov et al. [37], Gnesin and Gnesin [43], Rosales and Schneibel [41], Kieffer and Cerwenka [36], Cherniak and Elliot [38] and the experimental data from this work. Black points were used in the optimization, white points were disregarded. a) The entire phase diagram, b) the section of the phase diagram from 20 to 30 at% Si.

Mo_5Si_3 and -43.7 kJmol^{-1} for $MoSi_2$. The values stated by Chart, which are considered highly reliable as explained in section 4.1.2.1, are -29.1±3 kJmol^{-1} for Mo_3Si, -38.7±3 kJmol^{-1} for Mo_5Si_3 and -43.9±3 kJmol^{-1} for $MoSi_2$. The agreement between experimentally derived data and calculated results is equally good at 1500 K: -28.8 kJmol^{-1} for Mo_3Si, -39.3 kJmol^{-1} for Mo_5Si_3 and -44.5 kJmol^{-1} for $MoSi_2$ for the calculations versus -30.1±3 kJmol^{-1} for Mo_3Si, -38.9±3 kJmol^{-1} for Mo_5Si_3 and -45.0±3 kJmol^{-1} for $MoSi_2$ according to Chart.

Table 7.2.: Comparison of the enthalpies of formation of the intermetallic compounds at 298 K in different thermodynamic assessments, calculations and experimental measurements. All values in kJmol^{-1} and referred to one mole of atoms.

Literature	Phase			Method
	Mo_3Si	Mo_5Si_3	$MoSi_2$	
This work	-29.3	-38.2	-43.7	Assessment
Zhong et al. [62]	-35.83 -32.28			Local density approximation Generalized gradient approximation
Colinet and Tedenac [63]	-29.5	-38.44	-47.89	DFT
Guo et al. [83]	-29.3	-39.0	-38.3	Assessment
Geng et al. [81]	-29.3	-39.0	-43.8	Assessment
Fujiwara and Ueda [44]	-30.5 ±1.5	-39.2 ±1.5	-45.3 ±1.5	EMF
Liu et al. [80]	-27.9	-39.0	-45.2	Assessment
Meschel and Kleppa [45]		-38.2 ±1.6	-47.9 ±2.1	Direct synthesis calorimetry
Tomaszkiewicz et al. [46]		-39.3 ±1.1		Combustion calorimetry
Tomaszkiewicz et al. [48]	-31.3 ±1.5			Combustion calorimetry
Costa e Silva [77]	-31.8	-39.2	-45.7	Assessment
Bhaduri et al. [64]		-38.48	-43.7	Calculation
O'Hare [49]			-45.7 ±1.5	Combustion calorimetry

Chandrasekharaiah et al. [69]			-45.7 ±1.3	Assessment
Ohmori et al. [51]		-37.4 ±0.1		EMF
Niessen and de Boer [66]	-26		-16.0	Prediction with Miedema Model
Machlin [67]	-29.6			Calculation similar to Miedema
Kaufman [68]	-39.5	-55.3	-72.1	Prediction
Maslov et al. [52]			-47.4 ±1.0	Direct synthesis calorimetry
Chart [53]	-29.1 ±3	-38.7 ±3	-43.9 ±3	Knudsen effusion
Searcy and Tharp [56]	-24.4 ±4.2	-35.5 ±7.9	-36.3 ±13.9	Knudsen effusion
Robins and Jenkins [59]		(-40.1 ±1.6)	-43.8 ±3.3	Combustion calorimetry

Table 7.3 compares the entropies of formation reported in the literature with the values calculated by the optimized dataset. As explained in section 4.1.2.2, most of these values are derived from assessments and in no way experimentally determined. The only two sources of experimental data, Chart [53] and Fujiwara and Ueda [44], reported very different results. Chart found values of 0.42±1.3 $Jmol^{-1}K^{-1}$ for Mo_3Si, 1.0±1.3 $Jmol^{-1}K^{-1}$ for Mo_5Si_3 and -0.42±1.3 $Jmol^{-1}K^{-1}$ for $MoSi_2$. While no values are given directly by Fujiwara and Ueda, the values -0.76 $kJmol^{-1}K^{-1}$ for Mo_3Si, 0.55 $Jmol^{-1}K^{-1}$ for Mo_5Si_3 and 8.54 $Jmol^{-1}K^{-1}$ for $MoSi_2$ can be calculated from their data. For this reason, and due to the extreme scatter of the data in previous CALPHAD assessments, the entropies of formation were not considered at all in the optimization of the system. Nevertheless, for Mo_3Si and $MoSi_2$, the entropies of formation calculated from the optimized dataset agree fairly well with the data from Chart. For Mo_5Si_3, the calculated value is slightly lower than the value from Chart. However, the magnitude of the calculated value is not so high as to make the value implausible.

Figure 7.3 compares the mixing enthalpy of the liquid phase as reported by Arpaci and Frohberg [50] with the results calculated with the optimized dataset. The agreement between calculation and experiment is very high, as the entire curve lies within the stated uncertainty.

Figure 7.4 shows all heat capacity data for the Mo silicides. The lines are calculated with the optimized dataset, while the symbols are data taken from the literature [57, 54, 58, 60, 47, 75, 55]. The left column shows the heat capacities of the compounds, the right column their enthalpy

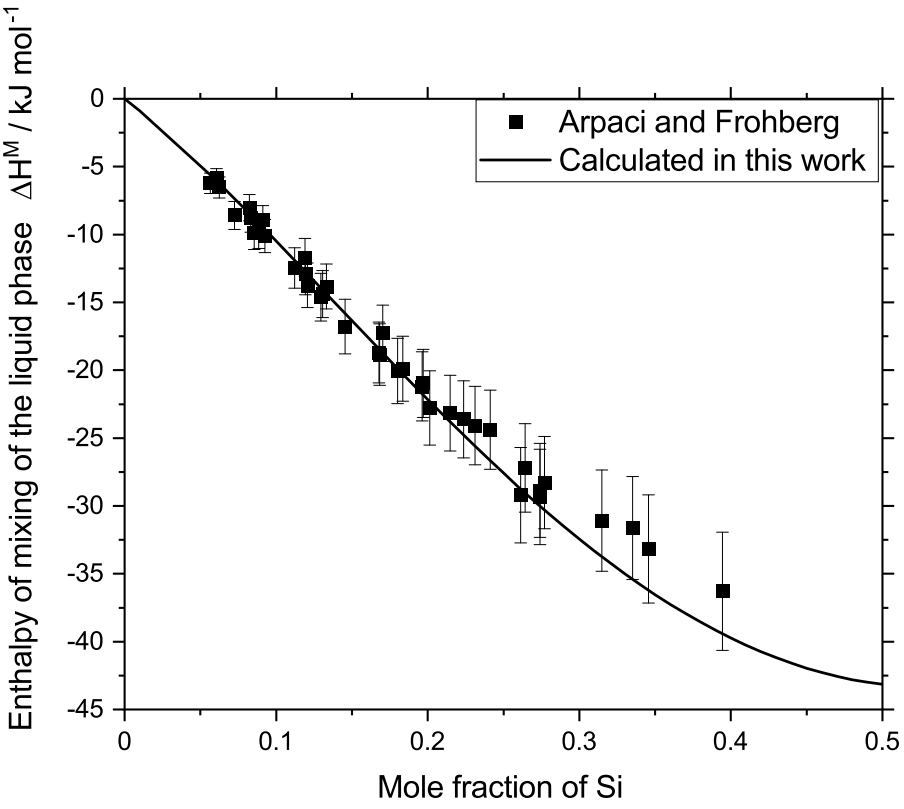

Figure 7.3.: The enthalpy of mixing of the liquid state at a mean temperature of 3087 K. The data points are taken from Arpaci and Frohberg [50], the line results from the calculation in this work.

increments. The agreement between calculations and experiments is very good. Only the early experiments of Bondarenko et al. (heat capacities in the temperature range 400 - 1200 K) differ strongly from the calculation. However, as discussed in section 4.1.2.4, this data is not very reliable and was therefore not considered for the optimization.

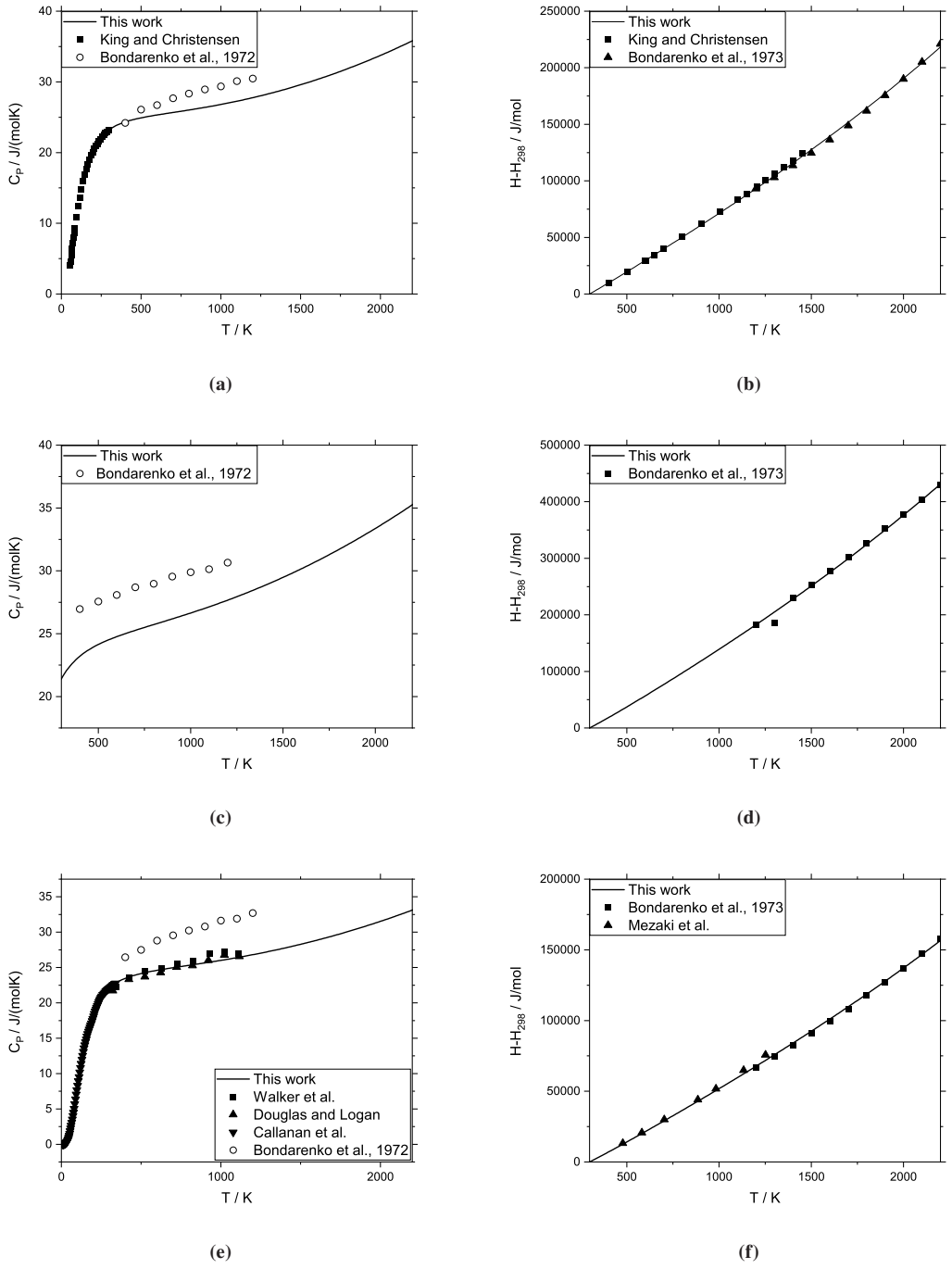

Figure 7.4.: Heat capacities (left column) and enthalpy increments (right column) of the three intermetallic phases. The black points are the data used in the optimization [58, 60, 47, 54, 75, 57], the white points correspond to the disregarded experimental data [55]. a) Heat capacity of Mo_3Si, b) enthalpy increments of Mo_3Si, c) Heat capacity of Mo_5Si_3, d) enthalpy increments of Mo_5Si_3, e) Heat capacity of $MoSi_2$, f) enthalpy increments of $MoSi_2$.

Table 7.3.: Comparison of the entropies of formation of the intermetallic compounds at 298 K in different thermodynamic assessments and experimental measurements. All values in $Jmol^{-1}K^{-1}$ and referred to one mole of atoms.

Literature	Phase			Method
	Mo_3Si	Mo_5Si_3	$MoSi_2$	
This work	0.284	3.214	0.148	Assessment
Guo et al. [83]	-1.3008	-3.5536	-4.29	Assessment
Geng et al. [81]	-1.3007	-3.545	-1.84786	Assessment
Fujiwara and Ueda [44]	-0.7589	0.55	8.54	EMF
Liu et al. [80]	0.28	4.349	-0.223	Assessment
Costa e Silva [77]	-2.5	-5.745	-4.2533	Assessment
Vahlas et al. [76]	-0.5096	-3.78675	-2.83236	Assessment
Chart [53]	0.42 $\pm$ 1.3	1.0 $\pm$ 1.3	-0.42 $\pm$ 1.3	Knudsen effusion
Hultgren et al. [148]	0.1 $\pm$0.3	-0.8 $\pm$1.3	-2.6 $\pm$4.2	Assessment

7.2. The Mo-Si-Ti system

Following the conclusions drawn in chapter 6, an attempt has been made to improve the Mo-Si-Ti dataset based on both the revised Mo-Si binary system [33] and the new experimental results described in this work and in the literature since the publication by Yang et al. [16]. Regardless of the fact that many samples, both in this study and presumably in the literature, are not in thermodynamic equilibrium, this can be done by extracting as much information as possible from the samples that are most likely in equilibrium and combining this with high quality ab initio data and the general rules of heterogeneous equilibria. In this way, reasonable arguments can be made for the existence of certain tie triangles in regions where reliable experimental data are scarce. The following section explains what data were used, what conclusions were drawn, and what parts of the system warrant further analysis. The results of the calculation with the revised dataset are then presented and compared with experimental results where applicable. It should be noted that the scope of this refinement is limited to the metal-rich region of the system (e.g., a Si content below 37.5 at.%); no effort has been made to optimize the dataset for higher Si contents.

7.2.1. Accepted binary systems, thermodynamic models and phase descriptions

The binary systems for Ti-Si, Mo-Ti, and Mo-Si were accepted from Seifert et al. [22], Ansara et al. [117], and Czerny et al. [33], respectively. The reasons why these descriptions were considered appropriate in the case of the first two systems are explained in detail in section 4. The Mo-Si evaluation was published as part of this work and is also discussed in detail in this section. From the work of Seifert et al. the model was chosen that simplifies Ti_5Si_3 as a line compound. Similarly, the version of the Mo-Si system by Czerny et al. was chosen that treats the phase Mo_3Si as a line compound. Furthermore, the phase Mo_5Si_3 was also simplified as a line compound. As explained in subsection 7.1.2, this is easily possible by setting all parameters of the non-stoichiometric end members to zero, without affecting the results in terms of melting point or enthalpy of formation etc. of the stable compound at stoichiometric composition. As discussed in subsection 4.4, the Mo-Si-Ti system contains two true ternary phases, $(Mo,Ti)Si_2$ and $(Mo,Ti)_6Si_5$. Both were described by a sublattice model expressed in the Compound Energy Formalism. The following section briefly describes the models chosen for the ternary phases.

7.2.1.1. (Mo,Ti)Si_2

The space group of the phase (Mo,Ti)Si_2 is $P6_222$ or $P6_422$. The Si atoms occupy the Wyckoff position 6i, whereas the Mo and Ti atoms occupy the position 3c. The stability range of the phase can be given by the formula $(Ti_{1-x}Mo_x)Si_2$, with $0.26 < x < 0.89$). No solubility range was reported for Si. Therefore, the compound was modeled as a strictly stoichiometric line compound with respect to Si, while Mo and Ti can substitute each other. The corresponding model chosen is therefore $(Mo,Ti)_1(Si)_2$.

7.2.1.2. (Mo,Ti)$_6Si_5$

The space group of the phase $(Mo,Ti)_6Si_5$ is Ibam, according to the DFT investigation by Colinet et al. [120]. In the isostructural phase V_6Si_5, Si occupies the Wyckoff positions 8j and 4a, while V occupies the positions 8j and 8g. While Svechnikov et al. [17] reported a homogeneity range both for the two metallic atoms as well as for Si, Yang et al. [16] reported the phase as a line compound with respect to Si. For the sake of simplicity, and because the phase is well outside the scope of this investigation, the data from Yang et al. was trusted and the phase was modelled as a line compound. In disagreement with Yang et al. however, who reported the phase to have the stoichiometry $(Ti,Mo)_{11}Si_9$, the results of the study by Colinet et al. were accepted regarding the composition of the phase. Therefore, the model of this phase is $(Mo,Ti)_{0.545}(Si)_{0.455}$.

7.2.2. Assessment procedure

Following the conclusions of the experimental chapter of this thesis, 6.4.6.8, the most difficult step of the ternary evaluation was to assess which data are reliable with respect to the exact positions of the tie triangles. As explained in section 6.4.6.8, these data are not very reliable at relatively low temperatures (1573 K from this work and 1698 K from Yang et al.). The results of this work show that at least the samples in the β+Mo_3Si+Mo_5Si_3 region are not in equilibrium, and the publication by Yang et al. does not provide sufficient evidence to conclude that the data they obtained at 1698 K are unquestionably reliable. The same is not necessarily true for the Yang et al. data at 1873 K however. This temperature is sufficiently high that it can be reasonably argued that diffusion is significantly faster, and that an energy barrier stabilizing Ti_5Si_3 could be overcome. For this reason, the data of Yang et al. at 1873 K were accepted. For lower temperatures, the phase compositions of the tie triangle β+Mo_5Si_3+Ti_5Si_3 were accepted, since it is only a conjecture that the samples located there might not be in equilibrium and no factual reason exists to doubt the measurements. For the tie triangle β+Mo_3Si+Mo_5Si_3, the existence was accepted based on the explanation above, but no phase composition was specified. This

was necessary because there is no conclusively reliable data for this region. For all two-phase regions, the results of this work were accepted.
In addition to these experimental data, the DFT data of Colinet et al. [120] were accepted for the enthalpies of formation of the unstable end members of the compounds $(Mo,Ti)_3Si$, $(Mo,Ti)_5Si_3$ and $(Ti,Mo)_5Si_3$. Since it is necessary to have data beyond 37.5 at.% Si in the dataset, despite the fact that this is beyond the scope of this work, the parameters of Yang et al. were used in this range. It should be noted that this inevitably leads to problems because the parameters were not adjusted for the changed Mo-Si system. Consequently, all equilibria beyond 37.5 at.% Si may not be supported by experimental evidence from either Svechnikov et al. or Yang et al. and are omitted from the figures in the following section. In a later work, this section of the phase diagram should be revisited experimentally and the dataset revised based on new results.
Regarding the liquidus projection of the system, the monovariant lines in the metal-rich region proposed by Yang et al. were accepted and reproduced in terms of reaction type, but not their compositions or temperatures. As shown in section 6.4.4, the liquidus projection of Yang et al. is largely reliable, except for their exact compositions. Since the experimental determination of the lines of double saturation require an effort far beyond the scope of this work, it must be part of a dedicated investigation. However, it will be shown below that the revised liquidus projection is just as capable of predicting the microstructures of samples as that of Yang et al. for several samples.
During the optimizitation, the isothermal section for which experimental data exist were optimized first. Then, increasingly higher temperatures were checked for unreasonable features, such as unlikely miscibility gaps, which were corrected as neccessary. The same was subsequently done for lower temperatures down to 1000 K. Finally, when all other calculations looked reasonable, care was taken to ensure that the liquidus projection qualitatively agrees with the features observed during solidification. Due to a lack of liqudus data for the system, however, corrections were only made whenever obvious mistakes occured in the lines of double saturation.
To describe $(Mo,Ti)_5Si_3$ and $(Ti,Mo)_5Si_3$ satisfactory, only one interaction parameter was necessary. A single interaction parameter for $(Mo,Ti)_3Si$ on the other hand typically led to the formation of unreasonable immiscibility at high temperatures, which was fixed by adding a second interaction parameter. The values of this parameter was adjusted by hand to avoid the formation of the miscibility gap, after all other parameters were optimized.

7.2.3. Thermodynamic calculations

The isothermal section of the Mo-Si-Ti system at 1573 K as a result of the calculation with the reassessed data set is shown in Figure 7.5. In addition, the phase compositions of the samples discussed in section 6.4.6 for the tie triangle β+Mo_5Si_3+Ti_5Si_3, as well as for the two-phase

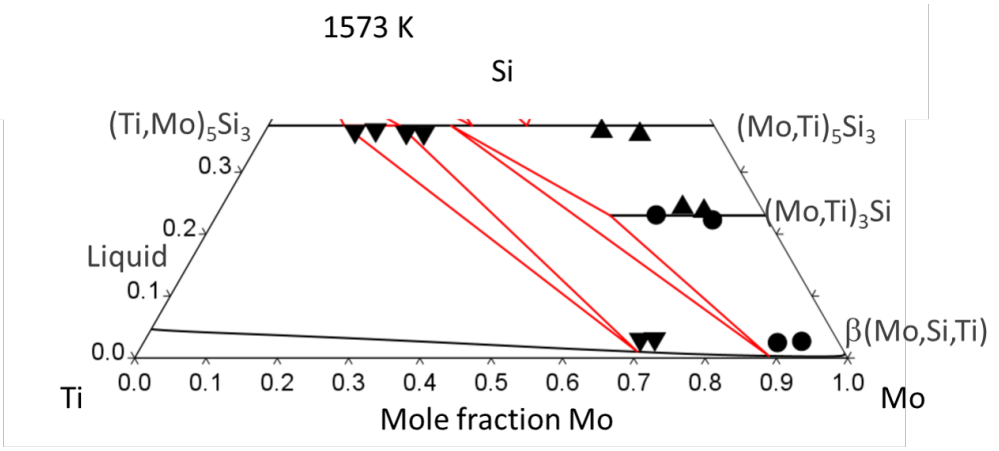

Figure 7.5.: The isothermal section of the Mo-Si-Ti system at 1573 K, calculated with the reassessed dataset. Indicated are the experimental results from this work, with the downward triangles representing the tie triangle β+Mo_5Si_3+Ti_5Si_3, the dots representing the region β+Mo_3Si and the upwards triangles representing the region Mo_3Si+Mo_5Si_3.

regions β+Mo_3Si and Mo_3Si+Mo_5Si_3. It can be seen that the agreement between the experiments and the calculation is very high. The tie triangle corresponds almost perfectly to the experimental data, and the composition of the phase Mo_3Si is in good agreement with the experiments. The simplification of Mo_5Si_3 as a line compound has no significant negative effect on the results. The Si content of the β phase is also quite good, although it is still somewhat underestimated for very high Mo contents. For the region β+Ti_5Si_3 no experimental data are given due to the presence of pure Ti in all samples. For the regions β+Mo_5Si_3 and β+Mo_3Si+Mo_5Si_3, no data were used in the optimization for the reasons discussed above. The exact position of this tie triangle is therefore uncertain, but the results of this calculation appear very reasonable based on the available data.

The isothermal section at 1873 K is shown in Figure 7.6. Also shown are the data from Yang et al. [16] that were used to optimize the tie triangles. The agreement between experiment and calculation is extremely high. Both tie triangles fit the reported experimental data very well, and the solubility of the β phase for Si is significantly better than in the original dataset. As in the dataset by Yang et al., liquid has started to form in the Ti-rich corner of the system, as expected from the binary system.

The enthalpies of formation of the unstable endmembers calculated with this dataset, together with the data calculated by Colinet et al. [120], are listed in Table 7.4. The agreement for the unstable Ti-endmembers of the Mo silicides is quite high, especially in the case of Ti_5Si_3 in the $D8_m$ structure. For Ti_3Si in the A15 structure, Colinet et al. reported a value of -42.41 kJmol^{-1}, while the dataset created in this work calculates a value of -39.28 kJmol^{-1}, which is reasonably close. It should be noted that the weight of the DFT data was less than that of the experimental

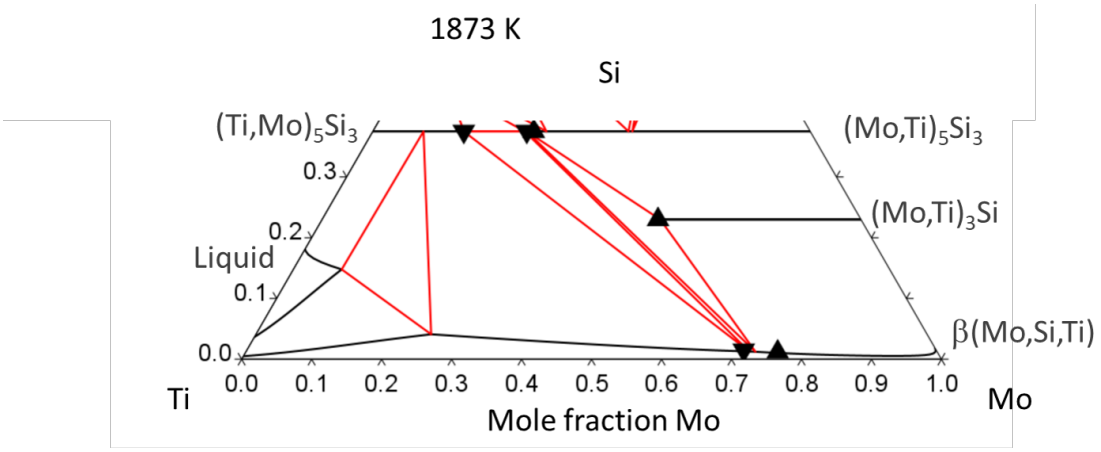

Figure 7.6.: The isothermal section of the Mo-Si-Ti system at 1873 K, calculated with the reassessed dataset. Indicated are the relevant experimental results from Yang et al. [16], with downward triangles represening the tie triangle β+Mo_5Si_3+Ti_5Si_3 and upwards triangles representing β+Mo_3Si+Mo_5Si_3.

Table 7.4.: A comparison of the enthalpies of formation of the unstable endmembers of the compounds Mo_3Si, Mo_5Si_3 and Mo_5Si_3 as calculated by Colinet et al. [120] and this work.

Compound	Type	Pearson Symbol	Space Group	ΔfE /kJmol^{-1} Colinet et al. [120]	ΔfE /kJmol^{-1} This work
A15-Ti_3Si	Cr_3Si	cP8	$Pm\bar{3}n$	-42.41	-39.28
$D8_m$-Ti_5Si_3	W_5Si_3	tI32	I4/mcm	-71.93	-72.15
$D8_8$-Mo_5Si_3	Mn_5Si_3	hP16	$P6_3$/mcm	-29.71	-14.73

values, since the experimental values were ultimately considered more reliable. Therefore, this order of magnitude can be expected for the discrepancy between the literature value and the calculated value. For Ti_5Si_3 in the $D8_m$ structure, the value calculated by Colinet et al. is -71.93 kJmol^{-1} and -72.15 kJmol^{-1} for this dataset, which is remarkably close. In the case of Mo_5Si_3 in the $D8_8$ structure the discrepancy between the DFT value of Colinet et al. and the one calculated with this dataset is quite large. While Colinet et al. reported a value of -29.71 kJmol^{-1}, this dataset calculates -14.73 kJmol^{-1}. Ultimately, this was deemed acceptable because a higher negative value for this compound stabilized it rather dramatically at the expense of all other data. It was not possible to get good agreement for all equilibria and DFT data if this compound was too stable, so the weight of this parameter was set fairly low.

The liquidus projection of the system is shown in Figure 7.7. It is not fundamentally different from that of Yang et al. in terms of the reactions taking place and the lines of double saturation present in the system. Again, there are two saddle points, each with a peritectic line on one side and a eutectic trough on the other. The exact composition and temperatures where the transitions from the peritectic to the eutectic characters happen were not investigated in this study. There

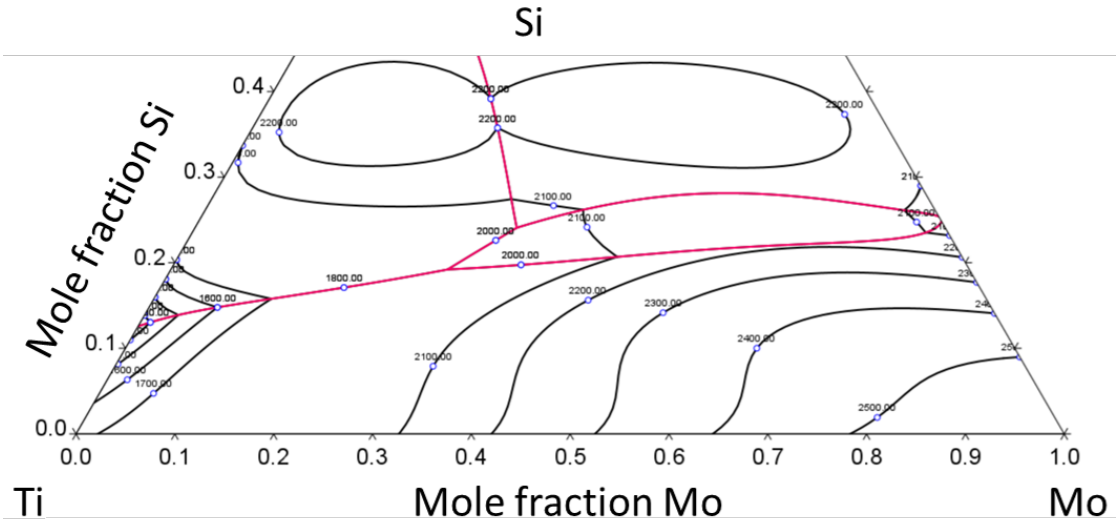

Figure 7.7.: The liquidus projection of the Mo-Si-Ti system, calculated with the reassessed dataset.

are also two transition reactions, but the trough L $\rightleftarrows$ Mo_3Si + Ti_5Si_3 is longer in this iteration of the projection. The most significant difference is the increased size of the region of primary solidification of Mo_3Si, which is much narrower in the version by Yang et al. As explained above, no attempt has been made to fit the reaction temperatures or compositions in the ternary space to any specific value, as no measurements are yet available.

The Scheil reaction scheme of the metal-rich area of the Mo-Si-Ti system, calculated with this dataset, is shown in Figure 7.8. This reaction scheme is remarkably similar to the one that results from the dataset of Yang et al., discussed in detail in section 4.4.1. All reactions are identical between the two datasets and vary only in their respective temperatures. The only noteworthy difference is in the maxima p_1 and e_2. In the dataset from Yang et al., the temperature of the maximum of the peritectic reaction is higher than that of the eutectic reaction (2399.5 K and 2396.0 K, respectively), while the opposite is true for this dataset (2458.7 K for the maximum of the eutectic reaction and 2437.6 K for the maximum of the peritectic reaction). Consequently, the evolution of the equilibria is slightly different at very high temperatures. Instead of the triangles on the Si-richer side of the region, L+Mo_3Si+Mo_5Si, remaining stable as calculated by Yang et al.'s dataset , those on the Si-lean side, β+L+Mo_3Si, are stable after the disappearance of the former equilibria. This is exemplarily depicted at a temperature of 2450 K in Figure 7.9. Since there is no experimental evidence of which reaction takes place, no conclusion can be drawn as to which dataset, if any, is correct in this case.

The equilibrium concentrations of all phases for the ternary invariant reactions in the metal-rich area of the system are listed in Table 7.5.

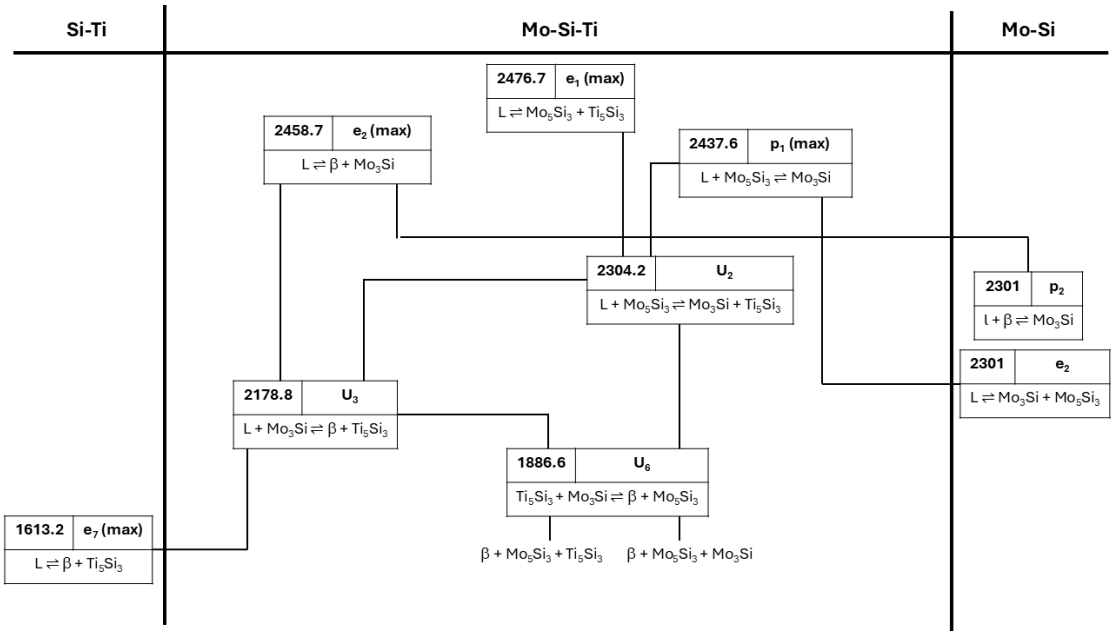

Figure 7.8.: The Scheil reaction scheme of the metal-rich area of the Mo-Si-Ti system, calculated with the reassessed dataset.

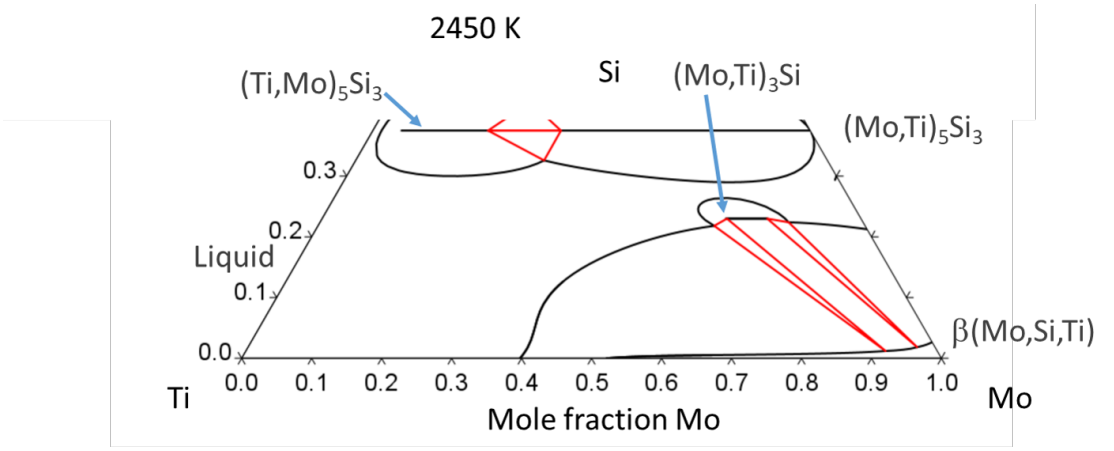

Figure 7.9.: The isothermal section of the Mo-Si-Ti system at 2450 K, calculated with the reassessed dataset.

Table 7.5.: Phase compositions of each phase in the ternary invariant reactions of the metal-rich area of the Mo-Si-Ti system, calculated with the reassessed dataset.

Reaction	**T / K**	**Type**	**Phase**	**Composition / at.%**		
				Mo	Si	Ti
$L \rightleftarrows Mo_5Si_3 + Ti_5Si_3$	2476.7	e_1	L	23.5	37.5	39.0
			Mo_5Si_3	27.0	37.5	35.5
			Ti_5Si_3	16.4	37.5	46.1
$L \rightleftarrows \beta + Mo_3Si$	2458.7	e_2	L	62.0	22.1	15.9
			β	93.9	1.4	4.7
			Mo_3Si	60.7	23.0	16.3
$L + Mo_5Si_3 \rightleftarrows Mo_3Si$	2437.6	p_1	L	53.7	28.4	17.9
			Mo_5Si_3	41.0	37.5	21.5
			Mo_3Si	61.0	23.0	16
$L + Mo_5Si_3 \rightleftarrows Mo_3Si + Ti_5Si_3$	2304.2	U_2	L	32.5	24.1	43.4
			Mo_3Si	48.5	23.0	28.5
			Mo_5Si_3	25.6	37.5	36.9
			Ti_5Si_3	15.7	37.5	46.8
$L + Mo_3Si \rightleftarrows \beta + Ti_5Si_3$	2178.8	U_3	L	28.0	19.2	52.8
			β	64.2	1.8	34
			Mo_3Si	44.6	23.0	32.4
			Ti_5Si_3	13.4	37.5	49.1
$Ti_5Si_3 + Mo_3Si \rightleftarrows \beta + Mo_5Si_3$	1886.6	U_6	β	72.0	1.3	26.7
			Mo_3Si	48.6	23.0	28.4
			Mo_5Si_3	21.7	37.5	40.8
			Ti_5Si_3	13.1	37.5	49.4

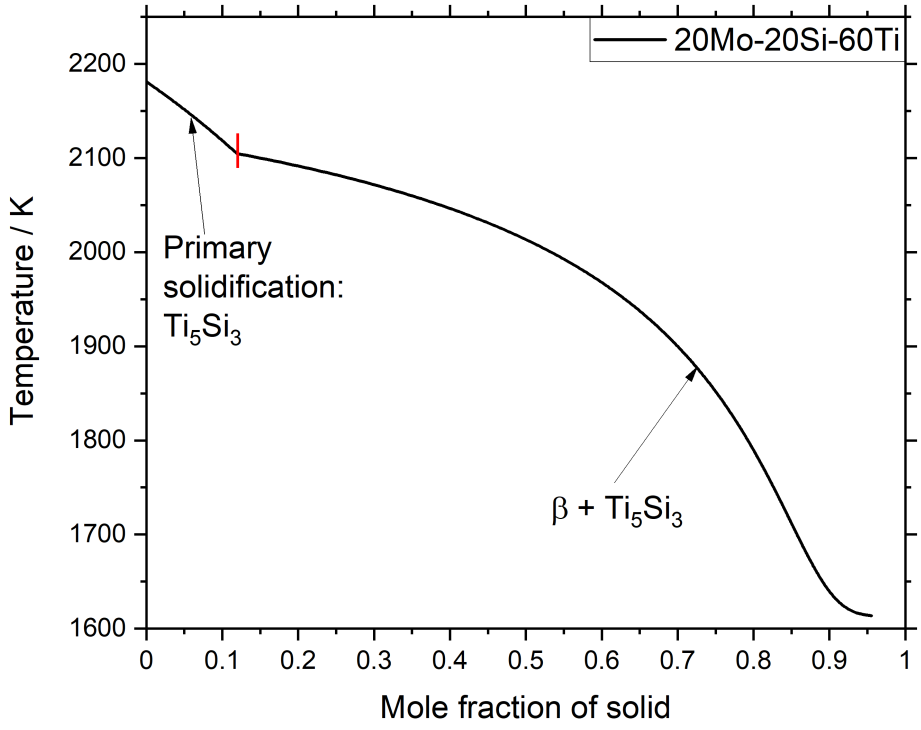

Figure 7.10.: The Scheil solidifcation calculation of the sample 20Mo-20Si-60Ti, calculated with the reassessed dataset.

The principle practical applicability of the liquidus projection is demonstrated with a few selected examples from section 6.4.3. It should be noted that the micrographs and the discussion of the microstructure evolution will not be discussed again here; the interested reader will find these topics in the appropriate section. The point of this section is to show that the new liquidus projection is equally capable of predicting the microstructures of Mo-Si-Ti alloys.

The first example is SSC9 with the composition 20Mo-20Si-60Ti. The micrograph of the sample, along with the discussion of the calculation using the dataset by Yang et al. can be found in section 6.4.3.9, starting at page 126. While it has a fairly simple microstructure, consisting entirely of eutectic β+Ti_5Si_3 except for a small amount of primary solidified Ti_5Si_3, it is in a potentially technologically relevant region of the phase diagram. As the Scheil solidification calculation in Figure 7.10 shows, the new dataset predicts the microstructure of this alloy perfectly.

The second example alloy to be discussed here is SSC13 with the composition 45Mo-21Si-34Ti. The SEM image of the sample, as well as the discussion of the Scheil solidification calculation

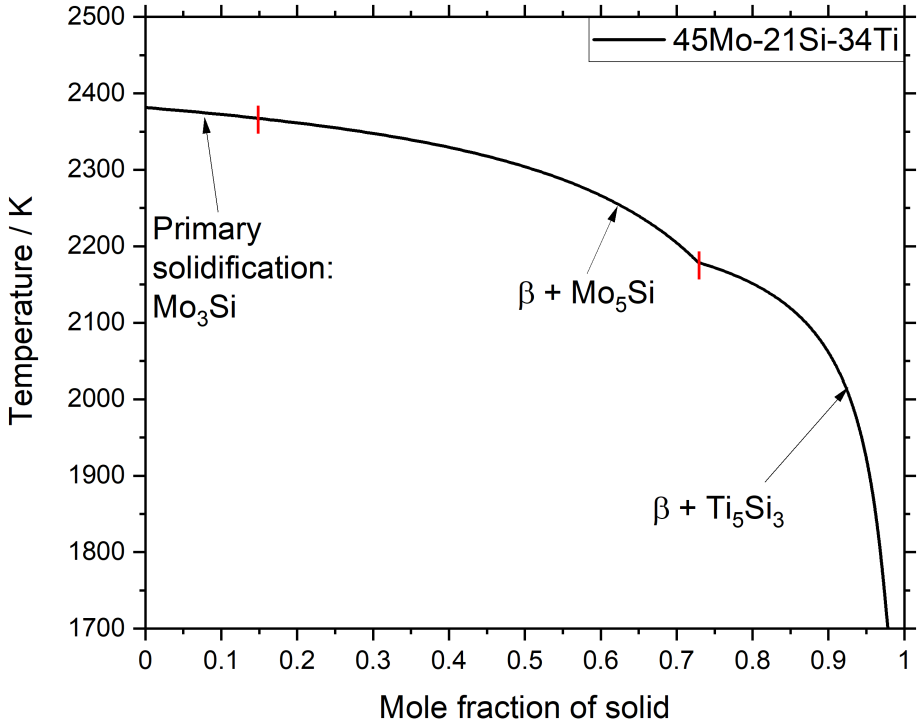

Figure 7.11.: The Scheil solidifcation calculation of the sample 45Mo-21Si-34Ti, calculated with the reassessed dataset.

using the dataset by Yang et al. can be found in section 6.4.3.13, starting at page 133. It has a very complex microstructure consisting of primary solidified β as well as the two eutectics β+Mo_3Si and β+Ti_5Si_3. As shown in Figure 7.11, the reassessed liquidus projection is basically able to predict all features of this microstructure.

In conclusion, the reassessed dataset reflects the available experimental data quite well. Both the isothermal section at 1573 K, where reliable data are available, and the one at 1873 K agree very well with the experimental compositions. At higher temperatures up to melting, the equilibria appear to be thermodynamically very reasonable. There are some minor discrepancies with the dataset by Yang et al., both in the reaction temperatures and in the stability of certain tie triangles at very high temperatures, but due to lack of data it is not possible to decide which version of the calculation, if any, is correct. Given the available evidence, the dataset is considered valid and reasonable. The liquidus projection of the re-evaluated data set is also reasonable. It is quite capable of predicting microstructures of cast alloys. However, like the dataset of Yang et al. [16], it suffers from a lack of experimental liquidus data. For this reason, little emphasis has

been placed at this point on perfecting the available microstructure predictions. Rather, it should be revisied as experimental data for reaction and liquidus temperatures in the system become available.

8. Conclusion and outlook

The metal-rich area of the Mo-Si-Ti system was experimentally investigated. An existing thermodynamoc dataset by Yang et al.[16] was used to calculate the liquidus projection, isothermal sections and solidification paths of several samples within the system. Samples were prepared and analysed by several methods to assess the accuracy of the dataset for the region of interest and to elucidate which aspects required refinement.

By comparing the microstructures of the as-cast samples with Scheil solidification calculations, it was concluded that the liquidus projection and the Scheil reaction scheme of the system are generally satisfactory. The most important aspects, such as the different regions of primary solidification and several edges of double saturation, could be verified. While several discrepancies were found, most were attributed to minor differences in temperatures and compositions of invariant reactions or saddle points of edges of double saturation. However, a small number of samples exhibited features that could not be explained by the current dataset. This suggests that some aspects of the liquidus project may need to be refined.

To investigate the influence of the cooling rate on the microstructure, samples were annealed at 1573 K for 330 h and cooled in the furnace prior to analysis. The same samples were then annealed at the same temperature for a further 48 hours and quenched in water before repeated analysis. In this way, the effect of the second annealing step was intended to be small due to the short duration, so that mainly the effect of slow vs. rapid cooling could be investigated. It was found that for most samples the cooling rate had little or no effect. Both microstructure and phase composition did not change significantly (or in most cases not at all) with cooling rate. One notable exception was a phase whose nature is not yet well understood. In many of the Ti-rich samples of the system, precipitates of pure or nearly pure Ti were found that do not fit any known phase diagram or the literature in general. These precipitates often took the form of dendritic structures and appeared to have more clearly defined grain boundaries when the sample has been quenched. They were found both in the cast state and after annealing. These facts suggest that they are formed during solidification and remain despite the heat treatment. The fact that in at least one sample the precipitates appear to have diffuse boundaries after furnace cooling, but sharply defined boundaries after subsequent repeated annealing and quenching, suggests that they are not dissolved at the chosen temperature, but are stable or metastable. However, their exact nature or mechanism of formation could not be elucidated during this work. It was theorized that

a local excess of Ti, that is not incorporated into the formed phases, leads to the segregation of extremly Ti-rich β phase, but this hypothesis was not yet tested.
Since, with one exception, the same samples that were used to investigate the influence of the cooling rate on the microstructure were also used to analyse the as-cast state, the overall effect of the heat treatment procedure chose could be studied. For most samples, some changes occured, either with regards to microstructural changes, or regarding the composition of the phases. However, in many cases, the effects were quite small. In particular, the compositions of the silicides never changed very significantly, aside from the fact that the standard deviation was typically larger in the as-cast state than after annealing. This fact can tentatively be interpreted as the presence of concentration gradients after solidification, but no dedicated investigation to measure such gradients has been conducted in the course of this work. If compositional changes did occur, it was typically only in the β phase, which indicate that diffusion in this phase is considerably faster than in the silicides. Another observation was that the presence of Ti_5Si_3 after solidification was usually associated with particularly small changes of the samples during annealing. This may indicate that this phase is so (meta)stable that equilibration may require more time or activation energy than can be provided under the selected heat treatment conditions.
Following the quenching experiments, the isothermal section of the Mo-Si-Ti system at 1573 K was investigated in the metal-rich region (x(Si) < 37.5 at.%). While some of the two-phase and one of the three-phase regions reported by Yang et al. and calculated with their dataset could be confirmed, other samples raised doubts about the validity of the dataset itself. To ensure that the results were as accurate as possible, the compositions of the samples were investigated by ICP-OES and CGHE before and after annealing. In this way the exact composition is known, which is relevant for assessing whether the sample is in equilibrium (i.e. lies on the tie line in a two-phase region) and for analysing how many impurities, such as O and C, it has incorporated. All samples were analysed by EDX and/or EPMA. It has been shown that for Mo-Si-Ti there is no difference in principle between these two methods. Selected samples were additionally analysed by XRD. The regions β+Mo_5Si_3+Ti_5Si_3, β+Mo_3Si and Mo_3Si+Mo_5Si_3 could be confirmed. However, the three-phase region is shifted to slightly higher Mo concentrations than the dataset calculated at this temperature. Furthermore, the solubility of the β phase for Mo was found to be significantly higher than calculated. The dataset assumed no solubility for Mo concentrations above about 50 at.%, whereas experimentally about 2-3 at.% of Si can be dissolved in β even for pure Mo.
In addition, the phase Mo_3Si was found to be consistently Si deficient. Instead of the stoichiometric composition, the Si content of this phase was about 23 at.% in each sample analysed. The two-phase region β+Ti_5Si_3 could only be partially confirmed. All samples in this region also showed the presence of the poorly understood pure Ti precipitates mentioned above. As this is most likely not a stable phase, no conclusions could be drawn regarding the tie lines of these samples. Samples in the β+Mo_5Si_3 and β+Mo_3Si+Mo_5Si_3 regions were not in equilibrium

after annealing. They exhibited either up to five phases simultaneously or a combination of phases that would intersect with another tie triangle. By comparing the microstructure with Scheil solidification calculations, it could be shown that the most likely explanation is that the microstructure formed during solidification is retained and does not change significantly or at all under the chosen conditions. Therefore, no experimental information could be obtained over large areas of the isothermal section. This finding also raised the question of whether the other samples are indeed in equilibrium or not. For the two Mo_3Si containing two-phase regions, several sample compositions fall on the tie line, which makes it very likely that equilibrium has been reached, but this is not true for all samples investigated. For the tie triangle β+Mo_5Si_3+Ti_5Si_3, the scatter between different phase compositions is quite small, which could also indicate that equilibrium has been reached. However, the samples which nominally fall within the β+Mo_3Si+Mo_5Si_3 tie triangle also show little scatter, but these were clearly shown by XRD not to be in equilibrium. Furthermore, the same conclusion that the as-cast microstructure does not change significantly during heat treatment could possibly be applied to the other tie triangle. It is therefore unclear whether there is any data on equilibrium samples at all. It could even be argued that the experiments of Yang et al. are not necessarily in equilibrium. At least one of the temperatures they chose, 1698 K, is not significantly higher than the temperature used in this work. It is therefore unlikely that significant diffusion took place in these experiments. If this were true, the entire dataset would be based on metastable data.

Based on the experimental results, it was decided to reassess the binary system Mo-Si. This was the only way to include the off-stoichiometry of the Mo_3Si phase. There are more recent evaluations of this system than the one accepted by Yang et al., but neither was entirely satisfactory. Therefore, literature data on invariant reaction temperatures and compositions, enthalpies of formation, heat capacities, enthalpy of mixing of the liquid phase, solvus, solidus and liquid lines, and homogeneity ranges were used to optimise a new dataset. The phase Mo_3Si was modelled in two different ways. In one dataset it was simplified as a line compound of the experimentally determined compositions. In the other dataset it was modelled to reflect the actual defect structure in a sublattice model. The model of the phase Mo_5Si_3 was chosen to best reflect the crystallography of the phase, with one sublattice per Wyckoff position. The phase $MoSi_2$ was modelled as a simple line compound, while β and the liquid phase were treated as solution phases. It was shown that all reliable experimental values could be accurately calculated with the new dataset. For the first time, this included the heat capacities of the Mo silicides, which had been disregarded in all previous assessments of the system.

Based on the new experiments and a thorough discussion of the available literature data, a reassessment of the Mo-Si-Ti system was performed. This evaluation took into account the optimized binary Mo-Si system from this work. It focused only on the metal-rich region of the ternary system up to a Si concentration of 37.5 at.%. For data with higher Si contents, two competing descriptions exist (that of Yang et al. [16] and that of Svechnikov et al. [17]), and

it is not possible to decide which of these publications, if any, is more reliable. Since only the metal-rich region of the system is relevant to the research question of this thesis, the decision was made to ignore higher Si contents altogether. For the metal-rich region, it has been shown that the agreement between calculations with the new dataset and experiments is very high. All reliable data can be accurately calculated, and the areas of the system where little information is available do not look unreasonable or improbable. The invariant reactions that occur in this region of the system have been plotted as well. Although there is no experimental evidence at all at the temperatures where they are proposed to occur, they all look thermodynamically reasonable. It was also shown that the liquidus projection calculated from the new dataset is as capable of predicting the microstructure of selected samples as that of Yang et al., although more dedicated research is urgently needed to be able to model the liquidus projection quantitatively correctly.

In order to further improve the dataset and answer the questions that have been identified in the course of this thesis, more data is needed. The first step should be to ensure that the samples to be analysed are in equilibrium. This can be done, for example, by annealing a sample and analysing it by XRD. Then the same sample, or the remaining material if powder XRD was used, would be annealed and analysed again. This process is repeated until the diffractogram no longer changes, indicating that equilibrium has been reached. However, given the affinity of the material for O and the slow diffusion of its elements, it is quite possible that equilibrium cannot be reached before the sample has incorporated too many impurities to be reasonably analysed. It is also possible that the phases initially formed during solidification are so metastable that they do not dissolve at all during annealing. In these cases, different methods of sample preparation could be explored. For example, powder metallurgy in an inert atmosphere might be feasible. When sintering specimens from elemental powders, there should be virtually no stable phases formed prior to annealing, significantly lowering the barrier to equilibrium. Ensuring that sample preparation is carried out under inert conditions would avoid the oxygen contamination that rendered the powdered samples unusable in this work. However, it is also possible that diffusion in a random powder sample is even slower than in a bulk sample, which would hinder equilibration. In this case, annealing would either have to be carried out at higher temperatures or for a much longer period of time.

A. Appendix

A.1. The optimized parameters of the dataset for the Mo-Si system

Table A.1.: Optimized thermodynamic parameters of the Mo-Si system as a result of this thesis. All temperature ranges are from 298.15 to 6000 K. See the publication [33] for more details.

Phase	Thermodynamic parameters
liquid	Model: (Mo,Si) $^{0}\mathbf{L}_{\mathbf{Mo,Si}}= -172591.2920 + 27.6145T$ $^{1}\mathbf{L}_{\mathbf{Mo,Si}}= 26612.6661 - 20.6586T$ $^{2}\mathbf{L}_{\mathbf{Mo,Si}}= 38731.7034$ $^{3}\mathbf{L}_{\mathbf{Mo,Si}}= 19624.2756$
bcc	Model: (Mo,Si) $^{0}\mathbf{L}_{\mathbf{Mo,Si}}= -114632.1170 + 26.9372T$
Mo_3Si	Model: $(Mo)_{0.77}(Si)_{0.23}$ $\mathbf{G}_{\mathbf{Mo:Si}}= -37759.2536 + 149.3282T - 26.059T\ln(T) + 9.6142 \cdot 10^{-4}T^2 - 4.8262 \cdot 10^{-7}T^3 + 113220T^{-1}$ - OR - Model: $(Mo)_{0.75}(Si)_{0.125}(Si,Va)_{0.125}$ $\mathbf{G}_{\mathbf{Mo:Si:Si}}= -37759.2536 + 149.3282T - 26.059T\ln(T) + 9.6142 \cdot 10^{-4}T^2 - 4.8262 \cdot 10^{-7}T^3 + 113220T^{-1}$ $\mathbf{G}_{\mathbf{Mo:Si:Va}}= -21414.3469 + 129.4122T - 22.8016T\ln(T) + 8.4124E \cdot 10^{-4}T^2 - 4.2229 \cdot 10^{-7}T^3 + 99067.5T^{-1}$ $^{0}\mathbf{L}_{\mathbf{Mo:Si:Si,Va}}= 0.0$ $^{1}\mathbf{L}_{\mathbf{Mo:Si:Si,Va}}= -10750 + 2.5T$

Phase	Thermodynamic parameters
Mo_5Si_3	Model: $(Mo)_{0.5}(Mo,Si)_{0.125}(Mo,Si)_{0.125}(Si)_{0.25}$ $\mathbf{G_{Mo:Mo:Si:Si}}= -46722+143T-25.2693T\ln(T)+3.2382\cdot10^{-4}T^2-3.9528\cdot10^{-7}T^3+1.7454\cdot10^{5}T^{-1}$ $\mathbf{G_{Mo:Si:Si:Si}}= -47765+147T-25.2693T\ln(T)+3.2382\cdot10^{-4}T^2-3.9528\cdot10^{-7}T^3+1.7454\cdot10^{5}T^{-1}$ $\mathbf{G_{Mo:Mo:Mo:Si}}= -37313+146T-25.2693T\ln(T)+3.2382\cdot10^{-4}T^2-3.9528\cdot10^{-7}T^3+1.7454\cdot10^{5}T^{-1}$ $\mathbf{G_{Mo:Si:Mo:Si}}= -34401+140T-25.2693T\ln(T)+3.2382\cdot10^{-4}T^2-3.9528\cdot10^{-7}T^3+1.7454\cdot10^{5}T^{-1}$
$MoSi_2$	Model: $(Mo)_1(Si)_2$ $\mathbf{G_{Mo:Si}}= -156216.6066+444.2883T-75.7102T\ln(T)+1.6413\cdot10^{-3}T^2-1.0682\cdot10^{-6}T^3+402589.974T^{-1}$

A.2. The .tdb file for the Mo-Si system

```
$ alternative Mo3Si with 3 sublattices -> phase S611
$ 2024-01-08

 ELEMENT /-   ELECTRON_GAS              0.0000E+00  0.0000E+00  0.0000E+00!
 ELEMENT VA   VACUUM                    0.0000E+00  0.0000E+00  0.0000E+00!
 ELEMENT MO   BCC_A2                    9.5940E+01  4.5890E+03  2.8560E+01!
 ELEMENT SI   DIAMOND_A4                2.8085E+01  3.2170E+03  1.8810E+01!

 TYPE_DEFINITION % SEQ *!
 DEFINE_SYSTEM_DEFAULT ELEMENT 2 !
 DEFAULT_COMMAND DEF_SYS_ELEMENT VA /- !


 PHASE LIQUID  %  1  1.0  !
 CONSTITUENT LIQUID  :MO,SI :  !
 PARAMETER G(LIQUID,MO;0)  298.15  +34085.045+117.224788*T
   -23.56414*T*LN(T)-.003443396*T**2+5.66283E-07*T**3+65812*T**(-1)
   -1.30927E-10*T**4+4.24519E-22*T**7;  2896.0  Y
   +3538.963+271.6697*T-42.63829*T*LN(T);  5000.0  N 91Din !
 PARAMETER G(LIQUID,SI;0)  298.15  +42533.751+107.13742*T
   -22.8317533*T*LN(T)-.001912904*T**2-3.552E-09*T**3+176667*T**(-1)
   +2.09307E-21*T**7;  1687.0  Y
   +40370.523+137.722298*T-27.196*T*LN(T);  3.60000E+03  N 91Din !
 PARAMETER L(LIQUID,MO,SI;0) 298.15 -172591.2920+27.6145*T; 6000.0 N !
 PARAMETER L(LIQUID,MO,SI;1) 298.15 26612.6661-20.6586*T; 6000.0 N !
 PARAMETER L(LIQUID,MO,SI;2) 298.15 38731.7034; 6000.0 N !
 PARAMETER L(LIQUID,MO,SI;3) 298.15 19624.2756; 6000.0 N !


 TYPE_DEFINITION & GES A_P_D BCC_A2 MAGNETIC  -1.0    4.00000E-01 !
 PHASE BCC_A2  %&  2 1   3 !
 CONSTITUENT BCC_A2  :MO,SI : VA :  !
 PARAMETER G(BCC_A2,MO:VA;0)  298.15  -7746.302+131.9197*T
   -23.56414*T*LN(T)-.003443396*T**2+5.66283E-07*T**3+65812*T**(-1)
   -1.30927E-10*T**4;  2896.0  Y
```

```
   -30556.41+283.559746*T-42.63829*T*LN(T)-4.849315E+33*T**(-9);
   5000.0 N 91Din !
 PARAMETER G(BCC_A2,SI:VA;0) 298.15 +38837.391+114.736859*T
   -22.8317533*T*LN(T)-0.001912904*T**2-3.552E-09*T**3+176667*T**(-1);
   1687.0  Y
   +37542.358+144.781367*T-27.196*T*LN(T)-4.20369E+30*T**(-9);
   3600.0 N 91Din !
 PARAMETER L(BCC_A2,MO,SI:VA;0)  298.15 -114632.1170
 +26.9372*T;  6000.0 N  !


 PHASE DIAMOND_A4  %  1  1.0  !
 CONSTITUENT DIAMOND_A4  :SI :  !
 PARAMETER G(DIAMOND_A4,SI;0) 298.15 -8162.609+137.236859*T
   -22.8317533*T*LN(T)-0.001912904*T**2-3.552E-09*T**3+176667*T**(-1);
   1687.0  Y
   -9457.642+167.281367*T-27.196*T*LN(T)-4.20369E+30*T**(-9);
   3600.0 N 91Din !


 FUNCTION GS611 298.15 -37759.2536+149.3282*T-26.059*T*LN(T)
   +9.6142E-4*T**2-4.8262E-7*T**3+113220*T**(-1);  6000.0 N !
$ select either S611 or Mo3Si, not both together!
 PHASE S611  % 3 6 1 1 !
 CONSTITUENT S611 : MO : SI : SI%, VA : !
 PARAMETER G(S611,MO:SI:SI;0) 298.15 8*GS611; 6000.0 N !
 PARAMETER G(S611,MO:SI:VA;0) 298.15 7*GS611+93000-10*T; 6000.0 N !
 PARAMETER L(S611,MO:SI:SI,VA;0) 298.15 0.0; 6000 N !
 PARAMETER L(S611,MO:SI:SI,VA;1) 298.15 -86000+20*T; 6000 N !


$ PHASE MO3SI  %  2  0.77  0.23 !
$ CONSTITUENT MO3SI  :MO : SI :  !
$ PARAMETER G(MO3SI,MO:SI;0) 298.15  GS611; 6000 N !
$ PARAMETER G(MO3SI,MO:SI;0) 298.15  -37759.2536+149.3282*T-26.059*T*LN(T)
$   +9.6142E-4*T**2-4.8262E-7*T**3+113220*T**(-1);  6000.0 N !
```

```
FUNCTION GD8M 298.15
-46865+143*T-25.269*T*LN(T)+3.2382E-04*T**2-3.9528E-07*T**3+174540*T**(-1);
 6000 N !
$ select either D8M or Mo5Si3, not both together!
PHASE D8M % 4 0.5 0.125 0.125 0.25 !
CONSTITUENT D8M : MO : MO%,SI : MO,SI% : SI : !
PARAMETER G(D8M,MO:MO:SI:SI;0) 298.15  +GD8M; 6000 N !
PARAMETER G(D8M,MO:SI:SI:SI;0) 298.15  -1043+4*T+GD8M; 6000 N !
PARAMETER G(D8M,MO:MO:MO:SI;0) 298.15  9409+3*T+GD8M; 6000 N !
PARAMETER G(D8M,MO:SI:MO:SI;0) 298.15  +12321-3*T+GD8M; 6000 N !

 PHASE MOSI2  %  2 1 2 !
 CONSTITUENT MOSI2  :MO : SI :  !
 PARAMETER G(MOSI2,MO:SI;0) 298.15 -156216.6066+444.2883*T
 -75.7102*T*LN(T)
   +1.6413E-03*T**2-1.0682E-06*T**3
   +402589.974*T**(-1);  6000.0 N !

 LIST_OF_REFERENCES
 NUMBER  SOURCE

  91Din   'A T Dinsdale, SGTE Data for Pure Elements,
           Calphad 15(1991)4 p 317-425; and updates 2001'
  !
```

A.3. The .tdb file for the Mo-Si-Ti system

```
$***************************************************************************
$ Thermodynamic Database of Mo-Si-Ti  system
$***************************************************************************
$ Binaries
$---------------------------------------------------------------------------
$ Mo-Si: remodeled from Czerny et al. 2024
$ Mo-Ti: from N. Saunders 1995, COST
$ Si-Ti from Hans Jurgen Seifert, Hans Leo Lukas and Gunter Petzow (1999)
$---------------------------------------------------------------------------
$--Define element
 ELEMENT /-   ELECTRON_GAS              0.0000E+00  0.0000E+00  0.0000E+00!
 ELEMENT VA   VACUUM                    0.0000E+00  0.0000E+00  0.0000E+00!
 ELEMENT MO   BCC_A2                    9.5940E+01  4.5890E+03  2.8560E+01!
 ELEMENT SI   DIAMOND_FCC_A4            2.8086E+01  3.2175E+03  1.8820E+01!
 ELEMENT TI   HCP_A3                    4.7880E+01  4.8100E+03  3.0648E+01!

 FUNCTION GHSERMO    2.98140E+02  -7746.302+131.9197*T-23.56414*T*LN(T)
     -.003443396*T**2+5.66283E-07*T**3+65812*T**(-1)-1.30927E-10*T**4;
     2.89600E+03  Y
      -30556.41+283.559746*T-42.63829*T*LN(T)-4.849315E+33*T**(-9);
     5.00000E+03  N !

 FUNCTION GMOFCC     2.98150E+02  +15200+.63*T+GHSERMO#;   6.00000E+03   N !

 FUNCTION GMOHCP     2.98150E+02  +11550+GHSERMO#;   6.00000E+03   N !

 FUNCTION GHSERSI    2.98140E+02  -8162.609+137.236859*T-22.8317533*T*LN(T)
     -.001912904*T**2-3.552E-09*T**3+176667*T**(-1);  1.68700E+03  Y
      -9457.642+167.281367*T-27.196*T*LN(T)-4.20369E+30*T**(-9);
     3.60000E+03  N !

 FUNCTION GHSERTI    2.98140E+02  -8059.921+133.615208*T-23.9933*T*LN(T)
     -.004777975*T**2+1.06716E-07*T**3+72636*T**(-1);  9.00000E+02  Y
      -7811.815+132.988068*T-23.9887*T*LN(T)-.0042033*T**2-9.0876E-08*T**3
     +42680*T**(-1);  1.15500E+03  Y
```

```
      +908.837+66.976538*T-14.9466*T*LN(T)-.0081465*T**2+2.02715E-07*T**3
     -1477660*T**(-1);  1.94099E+03  Y
      -124526.786+638.806871*T-87.2182461*T*LN(T)+.008204849*T**2
     -3.04747E-07*T**3+36699805*T**(-1);  4.00000E+03  N !

 FUNCTION GTIFCC     2.98150E+02  +6000-.1*T+GHSERTI#;   6.00000E+03   N !

 TYPE_DEFINITION % SEQ *!
 DEFINE_SYSTEM_DEFAULT SPECIE 2 !
 DEFAULT_COMMAND DEF_SYS_ELEMENT VA !

$**************************************************************************
$LIQUID
$**************************************************************************
PHASE LIQUID  %  1  1.0  !
CONSTITUENT LIQUID  :MO,SI,TI :  !

PARAMETER G(LIQUID,MO;0)  2.98140E+02  +41831.347-14.694912*T+GHSERMO#
  +4.24519E-22*T**7;  2.89600E+03  Y
   +3538.963+271.6697*T-42.63829*T*LN(T);  5.00000E+03  N REF0 !
PARAMETER G(LIQUID,SI;0)  2.98140E+02  +50696.36-30.099439*T+GHSERSI#
  +2.09307E-21*T**7;  1.68700E+03  Y
   +40370.523+137.722298*T-27.196*T*LN(T);  3.60000E+03  N REF0 !
PARAMETER G(LIQUID,TI;0)  2.98140E+02  +12194.415-6.980938*T+GHSERTI#;
  9.00000E+02  Y
   +12194.416-6.980938*T+GHSERTI#;  1.30000E+03  Y
   +369519.198-2554.0225*T+342.059267*T*LN(T)-.163409355*T**2
  +1.2457117E-05*T**3-67034516*T**(-1);  1.94099E+03  Y
   -19887.066+298.7367*T-46.29*T*LN(T);  4.00000E+03  N REF0 !

$------------MO-SI-----------------------------------------------
PARAMETER L(LIQUID,MO,SI;0) 298.15 -172591.2920+27.6145*T; 6000.0 N !
PARAMETER L(LIQUID,MO,SI;1) 298.15 26612.6661-20.6586*T; 6000.0 N !
PARAMETER L(LIQUID,MO,SI;2) 298.15 38731.7034; 6000.0 N !
PARAMETER L(LIQUID,MO,SI;3) 298.15 19624.2756; 6000.0 N !

$---------------MO-TI-----------------------------------------
   PARAMETER G(LIQUID,MO,TI;0)  2.98150E+02  -9000+2*T;
```

```
                                6.00000E+03   N  REF0 !

$----------------SI-TI-------------------------------------------
PARAMETER G(LIQUID,SI,TI;0)  2.98150E+02  -242611.79+17.57906*T;
  6.00000E+03   N REF0 !
PARAMETER G(LIQUID,SI,TI;1)  2.98150E+02  +26753.36-2.14028*T;
  6.00000E+03   N REF0 !
PARAMETER G(LIQUID,SI,TI;2)  2.98150E+02  +76881.7-6.15055*T;
  6.00000E+03   N REF0 !

$---------------Mo-Si-Ti-----------------------------------------
PARAMETER G(LIQUID,MO,SI,TI;0) 298.15 6209.9323
+43.5478*T; 3000 N REF0 !
PARAMETER G(LIQUID,MO,SI,TI;1) 298.15 726592.0090
-538.4830*T; 3000 N REF0 !
PARAMETER G(LIQUID,MO,SI,TI;2) 298.15 156346.7880
-4.7023*T; 3000 N REF0 !

$***************************************************************
$BCC_A2
$***************************************************************
TYPE_DEFINITION A GES A_P_D BCC_A2 MAGNETIC  -1.0    4.00000E-01 !
PHASE BCC_A2  %A  2 1   3 !
    CONSTITUENT BCC_A2  :MO,SI,TI :VA :  !

PARAMETER G(BCC_A2,MO:VA;0)  298.15  -7746.302+131.9197*T
   -23.56414*T*LN(T)-.003443396*T**2+5.66283E-07*T**3+65812*T**(-1)
   -1.30927E-10*T**4;  2896.0  Y
   -30556.41+283.559746*T-42.63829*T*LN(T)-4.849315E+33*T**(-9);
   5000.0 N !
PARAMETER G(BCC_A2,SI:VA;0) 298.15 +38837.391+114.736859*T
   -22.8317533*T*LN(T)-0.001912904*T**2-3.552E-09*T**3+176667*T**(-1);
   1687.0  Y
   +37542.358+144.781367*T-27.196*T*LN(T)-4.20369E+30*T**(-9);
   3600.0 N !
   PARAMETER G(BCC_A2,TI:VA;0)  2.98140E+02 -1272.064+134.71418*T
   -25.5768*T*LN(T)-6.63845E-04*T**2-2.78803E-07*T**3+7208*T**(-1);
  1.15500E+03  Y
```

```
   +6667.385+105.366379*T-22.3771*T*LN(T)+.00121707*T**2-8.4534E-07*T**3
  -2002750*T**(-1);  1.94099E+03  Y
   +26483.26-182.426471*T+19.0900905*T*LN(T)-.02200832*T**2
  +1.228863E-06*T**3+1400501*T**(-1);  4.00000E+03  N REF0 !

$-----------------MO-SI--------------------------------------
PARAMETER L(BCC_A2,MO,SI:VA;0)  298.15 -114632.1170
 +26.9372*T;  6000.0 N  !

$------------------MO-TI-----------------------------------------------------
PARAMETER G(BCC_A2,MO,TI:VA;0)  2.98150E+02  -2000;   6.00000E+03  N REF0 !
PARAMETER G(BCC_A2,MO,TI:VA;1)  2.98150E+02  -2000;  6.00000E+03  N REF0 !

$----------------------SI-TI-----------------------------------------
PARAMETER G(BCC_A2,SI,TI:VA;0)  2.98150E+02  -262502.74+38.81506*T;
  6.00000E+03   N REF0 !
PARAMETER G(BCC_A2,SI,TI:VA;1)  2.98150E+02  +26753.36-2.14028*T;
  6.00000E+03   N REF0 !
PARAMETER G(BCC_A2,SI,TI:VA;2)  2.98150E+02  +76881.7-6.15055*T;
  6.00000E+03   N REF0 !

$----------------------MO-SI-TI--------------------------------------
PARAMETER G(BCC_A2,MO,SI,TI:VA;0) 298.15 -325906.1660
+145.2600*T; 3000 N REF0 !
PARAMETER G(BCC_A2,MO,SI,TI:VA;1)  2.98150E+02  -1000;
  6.00000E+03   N REF0 !
PARAMETER G(BCC_A2,MO,SI,TI:VA;2)  2.98150E+02  -1000;
  6.00000E+03   N REF0 !

$***********************************************************************
$CBCC_A12
$***********************************************************************
PHASE CBCC_A12  %  2 1   1 !
CONSTITUENT CBCC_A12  :SI,TI : VA :  !

PARAMETER G(CBCC_A12,SI:VA;0)  2.98140E+02  +50208-20.377*T+GHSERSI#;
  3.60000E+03  N REF0 !
PARAMETER G(CBCC_A12,TI:VA;0)  2.98140E+02  +4602.2+GHSERTI#;
```

```
  4.00000E+03  N REF0 !
$**********************************************************************
$CUB_A13
$**********************************************************************
PHASE CUB_A13  %  2 1   1 !
CONSTITUENT CUB_A13  :SI,TI : VA :  !

PARAMETER G(CUB_A13,SI:VA;0)  2.98140E+02  +47279-20.377*T+GHSERSI#;
  3.60000E+03  N REF0 !
PARAMETER G(CUB_A13,TI:VA;0)  2.98140E+02  +7531.2+GHSERTI#;  4.00000E+03
   N REF0 !
$**********************************************************************
$DIAMOND_A4
$**********************************************************************
PHASE DIAMOND_A4  %  1  1.0  !
CONSTITUENT DIAMOND_A4  :SI,TI :  !

PARAMETER G(DIAMOND_A4,SI;0)  2.98140E+02  +GHSERSI#;  3.60000E+03 N REF0 !
PARAMETER G(DIAMOND_A4,TI;0)  2.98140E+02  +25000+GHSERTI#;  4.00000E+03
      N REF0 !
PARAMETER G(DIAMOND_A4,SI,TI;0)  2.98150E+02  +80*T;   6.00000E+03   N
  REF0 !
$**********************************************************************
$FCC_A1
$**********************************************************************
PHASE FCC_A1  %  2 1   1 !
CONSTITUENT FCC_A1  :MO,SI,TI : VA :  !

PARAMETER G(FCC_A1,MO:VA;0)  2.98140E+02  +GMOFCC#;  5.00000E+03
   N REF0 !
PARAMETER G(FCC_A1,SI:VA;0)  2.98140E+02  +51000-21.8*T+GHSERSI#;
  3.60000E+03  N REF0 !
PARAMETER G(FCC_A1,TI:VA;0)  2.98140E+02  +GTIFCC#;  4.00000E+03 N REF0 !
$**********************************************************************
$HCP_A3
$**********************************************************************
TYPE_DEFINITION B GES A_P_D HCP_A3 MAGNETIC  -3.0    2.80000E-01 !
PHASE HCP_A3  %B  2 1   .5 !
```

```
CONSTITUENT HCP_A3  :MO,SI,TI :VA :  !

$----------END MEMBER-------------------------------------------------------
PARAMETER G(HCP_A3,MO:VA;0)  2.98140E+02  +GMOHCP#;  5.00000E+03
   N REF0 !
PARAMETER G(HCP_A3,SI:VA;0)  2.98140E+02  +49200-20.8*T+GHSERSI#;
   3.60000E+03  N REF0 !
PARAMETER G(HCP_A3,TI:VA;0)  2.98140E+02  +GHSERTI#;  4.00000E+03
   N REF0 !

$------------MO-TI-----------------------------------------------------------
PARAMETER G(HCP_A3,MO,TI:VA;0)  2.98150E+02  +22760-6*T;   6.00000E+03
  N REF0 !

$-----------------SI-TI-----------------------------------------------------
PARAMETER G(HCP_A3,SI,TI:VA;0)  2.98150E+02  -302072.2+77.76859*T;
   6.00000E+03   N REF0 !
PARAMETER G(HCP_A3,SI,TI:VA;1)  2.98150E+02  +26753.36-2.14028*T;
   6.00000E+03   N REF0 !
PARAMETER G(HCP_A3,SI,TI:VA;2)  2.98150E+02  +76881.7-6.15055*T;
   6.00000E+03   N REF0 !


$***************************************************************************
$                         INTERMETALLIC COMPOUNDS
$***************************************************************************
$FORM FROM MO-SI BINARY
$***************************************************************************
$ Mo3Si-cP8
$***************************************************************************
PHASE MO3SI  %  2  0.77  0.23 !
CONSTITUENT MO3SI  :MO, TI : SI :  !
PARAMETER G(MO3SI,MO:SI;0) 298.15  -37759.2536+149.3282*T-26.059*T*LN(T)
  +9.6142E-4*T**2-4.8262E-7*T**3+113220*T**(-1);  6000.0 N !

PARAMETER G(MO3SI,TI:SI;0) 298.15 0.77*GHSERTI+0.23*GHSERSI-42400-1.46*T;
 3000 N REF0 !
```

```
$----------------------MO-TI-SI-----------------------------------------
PARAMETER G(MO3SI,MO,TI:SI;0) 298.15 6000-11.4*T;
 3000 N REF0 !
PARAMETER G(MO3SI,MO,TI:SI;1) 298.15 -30500;
 3000 N REF0 !

$**************************************************************************
$ Mo5Si3-tI38
$**************************************************************************
PHASE MO5SI3  %  2 0.625   0.375 !
CONSTITUENT MO5SI3  :MO,TI : SI :  !
$---------------
$END MEMBERS
$---------------
PARAMETER G(MO5SI3,MO:SI;0)  2.98140E+02 -46865+143*T-25.269*T*LN(T)
  +3.2382E-04*T**2
  -3.9528E-07*T**3+174540*T**(-1);
 6000 N !

PARAMETER G(MO5SI3,TI:SI;0) 298.15 -72148.8562
+1.3271*T+0.375*GHSERSI+0.625*GHSERTI; 3000 N REF0 !
$--------------------------------------------------------------------------
$L-PARAMETERS
$-------------------------------------MO-SI-TI---------------------------
PARAMETER G(MO5SI3,MO,TI:SI;0) 298.15 -26572.6461-1.5883*T; 3000 N REF0 !

$**********************************************************
$ MoSi2-tI6
$**********************************************************
PHASE MOSI2  %  2 1   2 !
CONSTITUENT MOSI2  :MO,TI : SI :  !

PARAMETER G(MOSI2,MO:SI;0) 298.15 -156216.6066+444.2883*T
-75.7102*T*LN(T)
+1.6413E-03*T**2-1.0682E-06*T**3
+402589.974*T**(-1);  3.60000E+03  N REF0 !

PARAMETER G(MOSI2,TI:SI;0) 298.15 0+0*T
```

```
+GHSERTI#+2*GHSERSI#;  3.60000E+03  N REF0 !

PARAMETER G(MOSI2,MO,TI:SI;0) 298.15 0+0*T;  3.60000E+03  N REF0 !

$***************************************************************************
$FROM SI-TI BINARY
$***********************************************************
$SI2TI-oF24
$***********************************************************
PHASE SI2TI  %  2 2   1 !
CONSTITUENT SI2TI  :SI : MO,TI :  !

PARAMETER G(SI2TI,SI:MO;0)  2.98150E+02  6.98725329E+04+GHSERMO#
   +2*GHSERSI#; 6.00000E+03   N REF0 !
PARAMETER G(SI2TI,SI:TI;0)  2.98150E+02  -175619.85+7.401*T+GHSERTI#
  +2*GHSERSI#;   6.00000E+03   N REF0 !
PARAMETER G(SI2TI,SI:MO,TI;0)  2.98150E+02  -1.66771452E+05
  -26.5420792*T; 6.00000E+03   N REF0 !
$***********************************************************
$SI3TI5-hP16
$***********************************************************
PHASE SI3TI5  %  2 .375   .625 !
CONSTITUENT SI3TI5  :SI : MO,TI :  !

PARAMETER G(SI3TI5,SI:MO;0) 298.15 -14725.7550
+6.2306*T+0.625*GHSERMO
+0.375*GHSERSI; 3000 N REF0 !

PARAMETER G(SI3TI5,SI:TI;0)  2.98150E+02  -72410.31+.29282*T
  +.375*GHSERSI#+.625*GHSERTI#;   6.00000E+03   N REF0 !


PARAMETER G(SI3TI5,SI:MO,TI;0) 298.15 -33231.3922
-22.3379*T; 3000 N REF0 !

$***********************************************************
$SI4TI5-tP36
$***********************************************************
```

```
PHASE SI4TI5  %  2 4   5 !
CONSTITUENT SI4TI5  :SI : MO,TI :  !

PARAMETER G(SI4TI5,SI:MO;0)  2.98150E+02  -3.5E5+5*GHSERMO#
  +4*GHSERSI#;   6.00000E+03   N REF0 !
PARAMETER G(SI4TI5,SI:TI;0)  2.98150E+02  -711000+26.79246*T+4*GHSERSI#
  +5*GHSERTI#;   6.00000E+03   N REF0 !
PARAMETER G(SI4TI5,SI:MO,TI;0)  2.98150E+02  -9.4929063E+04;
   6.00000E+03   N REF0 !
$*******************************************************************
$SITI1-oP8
$*******************************************************************
PHASE SITI1  %  2 1   1 !
CONSTITUENT SITI1  :SI : TI,MO :  !

PARAMETER G(SITI1,SI:TI;0)  2.98150E+02  -156888.96+9.74346*T+GHSERSI#
  +GHSERTI#;   6.00000E+03   N REF0 !

PARAMETER G(SITI1,SI:MO;0)  2.98150E+02  0+0*T+GHSERSI#
  +GHSERMO#;   6.00000E+03   N REF0 !

PARAMETER G(SITI1,SI:MO,TI;0)  2.98150E+02  0+0*T;   6.00000E+03   N REF0 !
$*******************************************************************
$SITI3-tP32
$*******************************************************************
PHASE SITI3  %  2 1   3 !
CONSTITUENT SITI3  :SI : TI, MO :  !

PARAMETER G(SITI3,SI:TI;0)  2.98150E+02  -200000+4.38996*T+GHSERSI#
  +3*GHSERTI#;   6.00000E+03   N REF0 !

PARAMETER G(SITI3,SI:MO;0) 298.15 -273.8405
+3426.1458*T+GHSERMO+3*GHSERSI; 3000 N REF0 !

PARAMETER G(SITI3,SI:MO,TI;0) 298.15 -209.8544
-156.1512*T; 3000 N REF0 !

$*******************************************************************
```

```
$FROM MO-SI-TI TERNARY
$***************************************************************************
$T-Phase
$***************************************************************************
PHASE MOTI6SI5  %  2 .545   .455 !
CONSTITUENT MOTI6SI5  :MO,TI : SI :  !

PARAMETER G(MOTI6SI5,MO:SI;0)  2.98150E+02  -3.29186E+04+.545*GHSERMO#
  +.455*GHSERSI#;   6.00000E+03   N REF0 !
PARAMETER G(MOTI6SI5,TI:SI;0)  2.98150E+02  -6.81261E+04+.545*GHSERTI#
  +.455*GHSERSI#;   6.00000E+03   N REF0 !
PARAMETER G(MOTI6SI5,MO,TI:SI;0)  2.98150E+02  -3.7155041E+04;
  6.00000E+03   N REF0 !
$***************************************************************************
$MOTISI2
$***************************************************************************
PHASE MOTISI2  %  2 1   2 !
CONSTITUENT MOTISI2  :MO,TI : SI :  !

PARAMETER G(MOTISI2,MO:SI;0)  2.98150E+02  -117586.90-5.1670658*T
   +GHSERMO#+2*GHSERSI#;   6.00000E+03   N REF0 !
PARAMETER G(MOTISI2,TI:SI;0)  2.98150E+02  -126474.57-19.25956*T
   +GHSERTI#+2*GHSERSI#;   6.00000E+03   N REF0 !
PARAMETER G(MOTISI2,MO,TI:SI;0)  2.98150E+02  0+0*T; 6.00000E+03   N REF0 !

LIST_OF_REFERENCES
NUMBER  SOURCE
REF0 'Placeholder'
!
```

A.4. Comparison of samples with identical compositions

Note: Unless otherwise noted, annealed specimens were heat treated at 1573 K for 330 h. Furnace cooling is abbreviated as fc, water quenching is abbreviated as wq, and as-cast is abbreviated as ac. The images shown here are identical to those discussed in the text, but are printed together for easier comparison of the microstructures after the different treatments.

A.4.1. 22Mo-33Si-44Ti

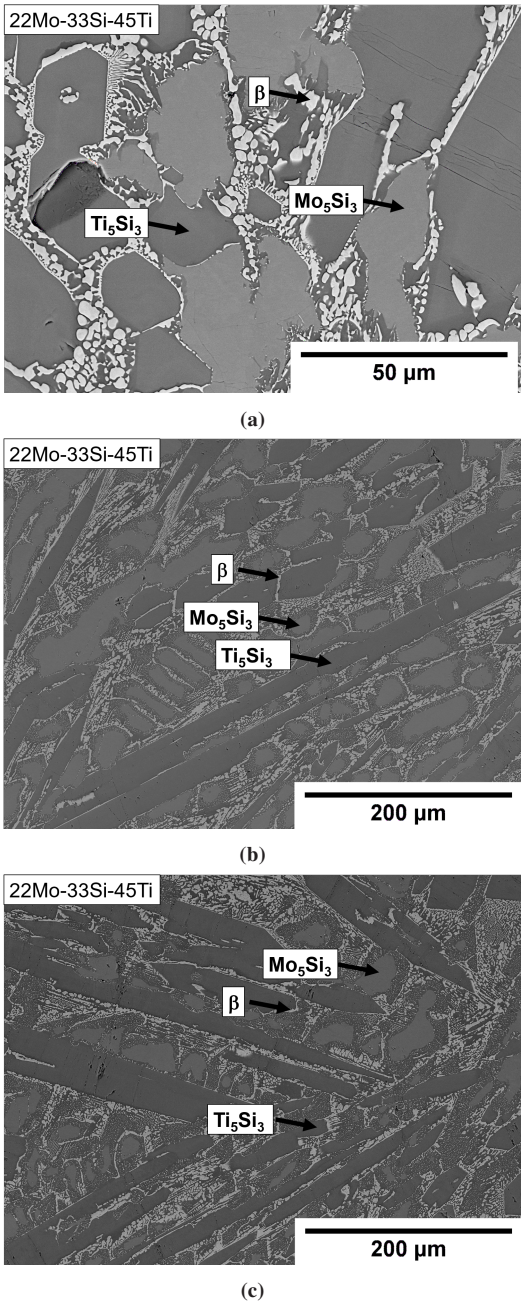

Figure A.1.: The microstructures of all samples with the composition 22Mo-33Si-45Ti. a) SSC5, ac. b) QE1, fc. c) QE1, wq.

A.4.2. 44.5Mo-23.5Si-32Ti

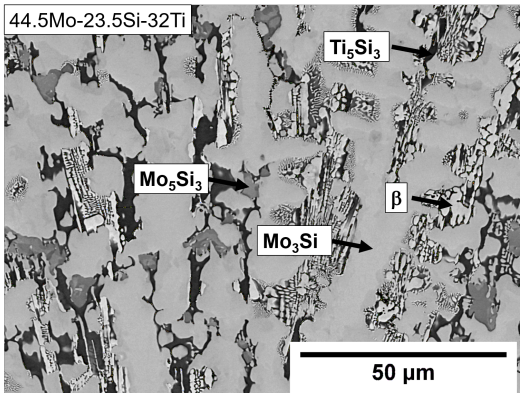

(a)

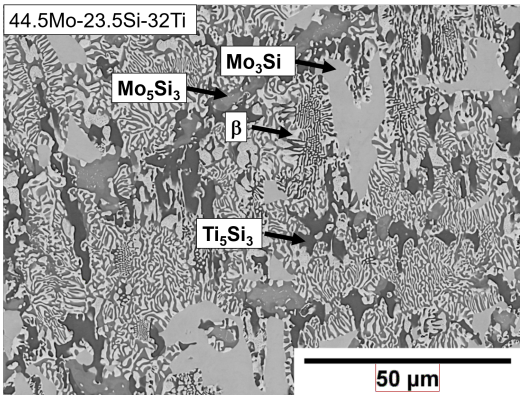

(b)

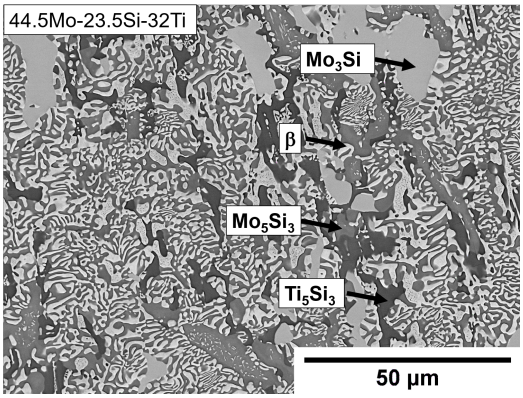

(c)

Figure A.2.: The microstructures of all samples with the composition 44.5Mo-23.5Si-32Ti. a) SSC6, ac. b) QE2, fc. c) QE2, wq.

A.4.3. 53Mo-32Si-15Ti

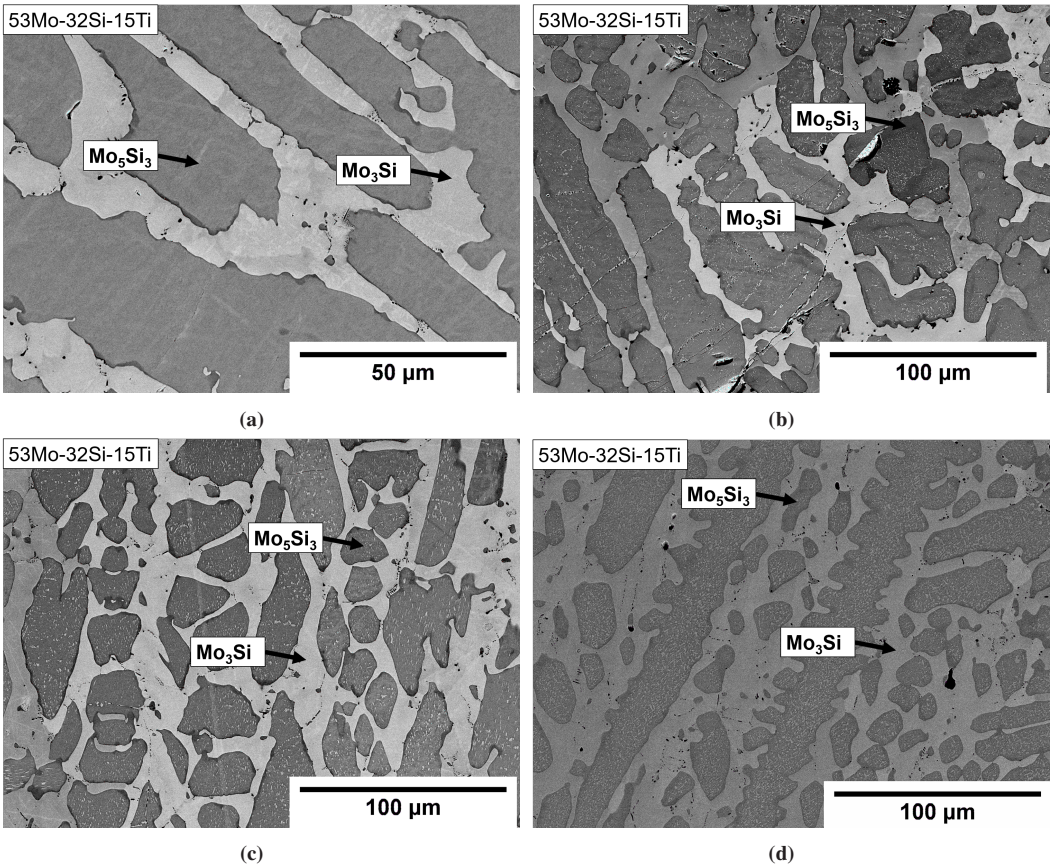

Figure A.3.: The microstructures of all samples with the composition 53Mo-32Si-15Ti. a) SSC7, ac. b) QE3, fc. c) QE3, wq. d) ITS10, wq.

A.4.4. 75Mo-15Si-10Ti

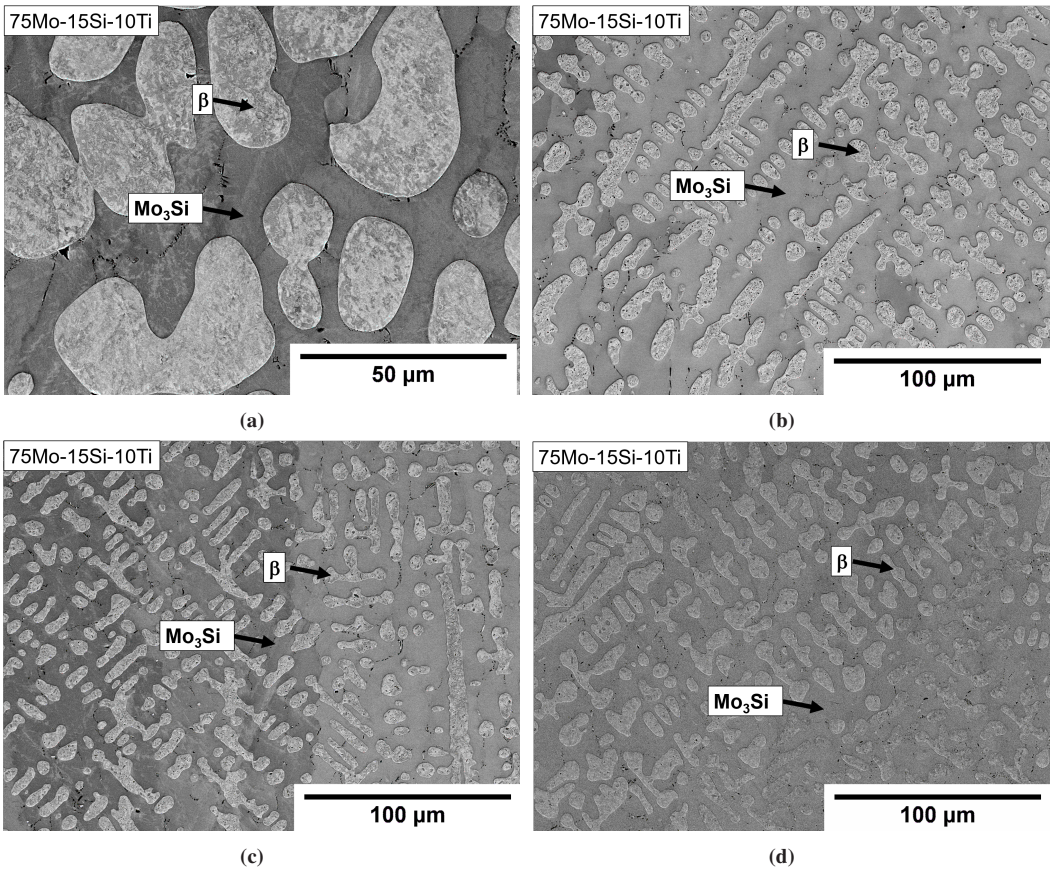

Figure A.4.: The microstructures of all samples with the composition 75Mo-15Si-10Ti. a) SSC8, ac. b) QE4, fc. c) QE4, wq. d) ITS7, wq.

A.4.5. 50Mo-38Si-12Ti

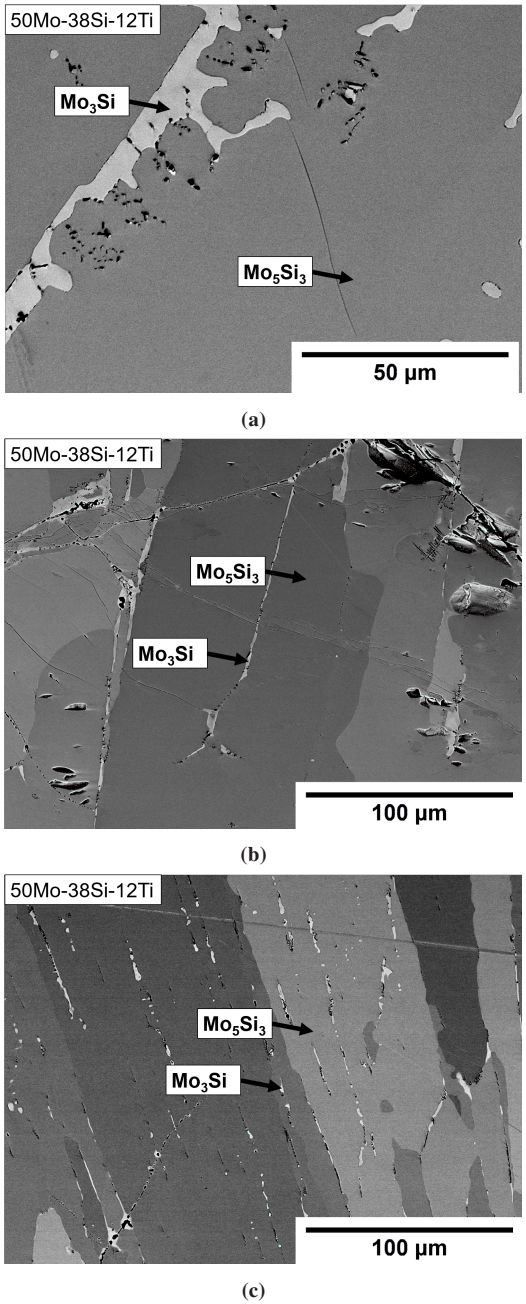

Figure A.5.: The microstructures of all samples with the composition 50Mo-38Si-12Ti. a) SSC10, ac. b) QE5, fc. c) QE5, wq.

A.4.6. 20Mo-37.5Si-42.5Ti

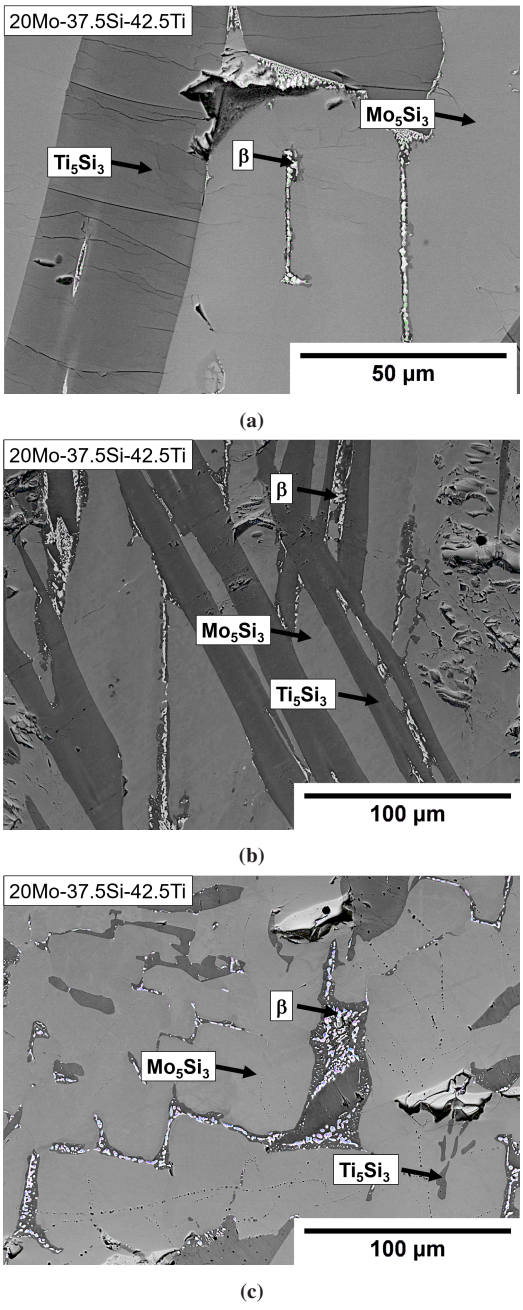

Figure A.6.: The microstructures of all samples with the composition 20Mo-37.5Si-42.5Ti. a) SSC11, ac. b) QE6, fc. c) QE6, wq.

A.4.7. 47.5Mo-12.5Si-40Ti

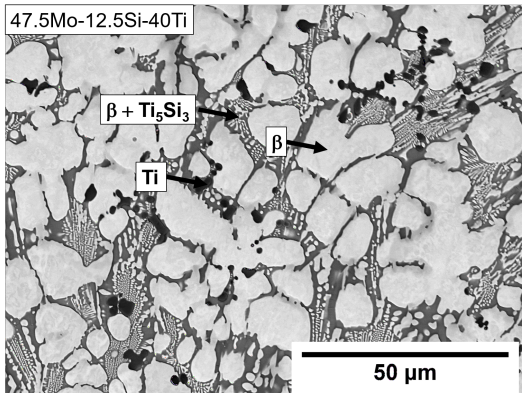

(a)

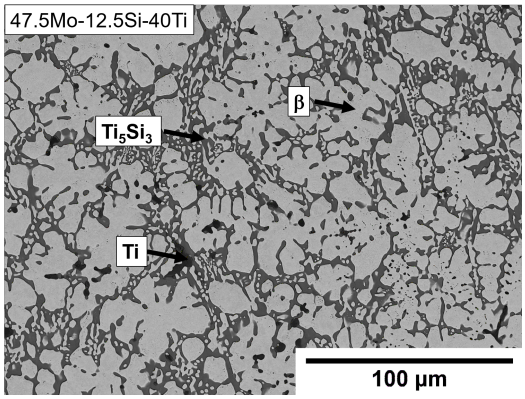

(b)

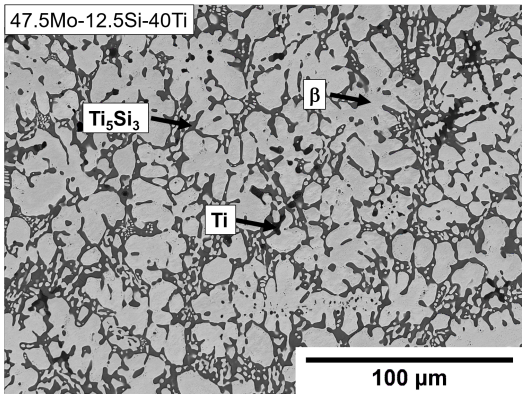

(c)

Figure A.7.: The microstructures of all samples with the composition 47.5Mo-12.5Si-40Ti. a) SSC12, ac. b) QE7, fc. c) QE7, wq.

A.4.8. 45Mo-21Si-34Ti

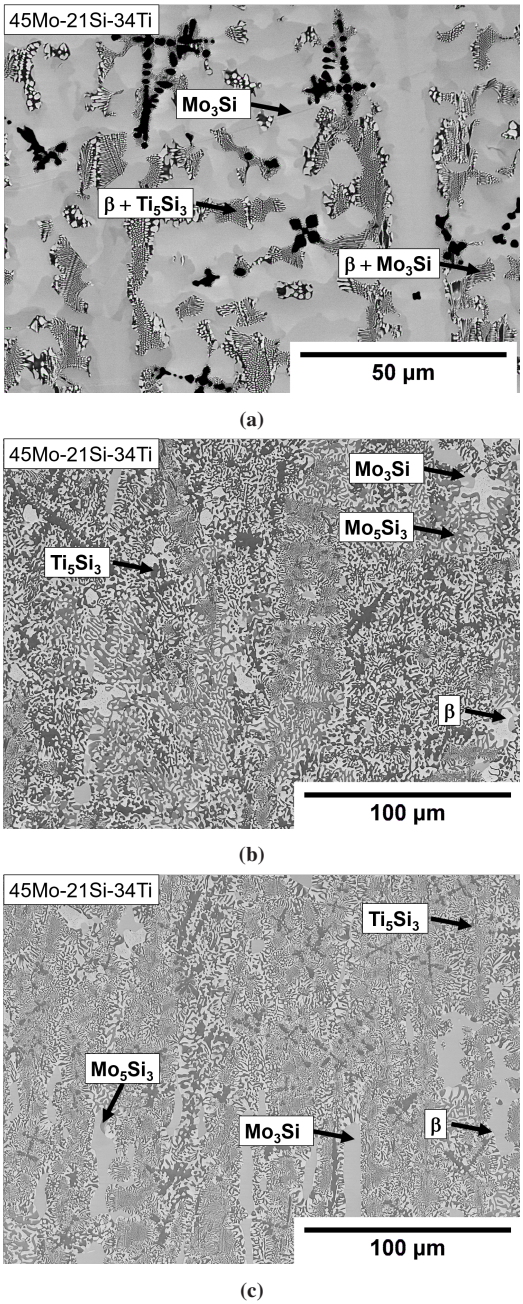

Figure A.8.: The microstructures of all samples with the composition 45Mo-21Si-34Ti. a) SSC13, ac. b) QE8, fc. c) QE8, wq.

A.4.9. 25Mo-33Si-42Ti

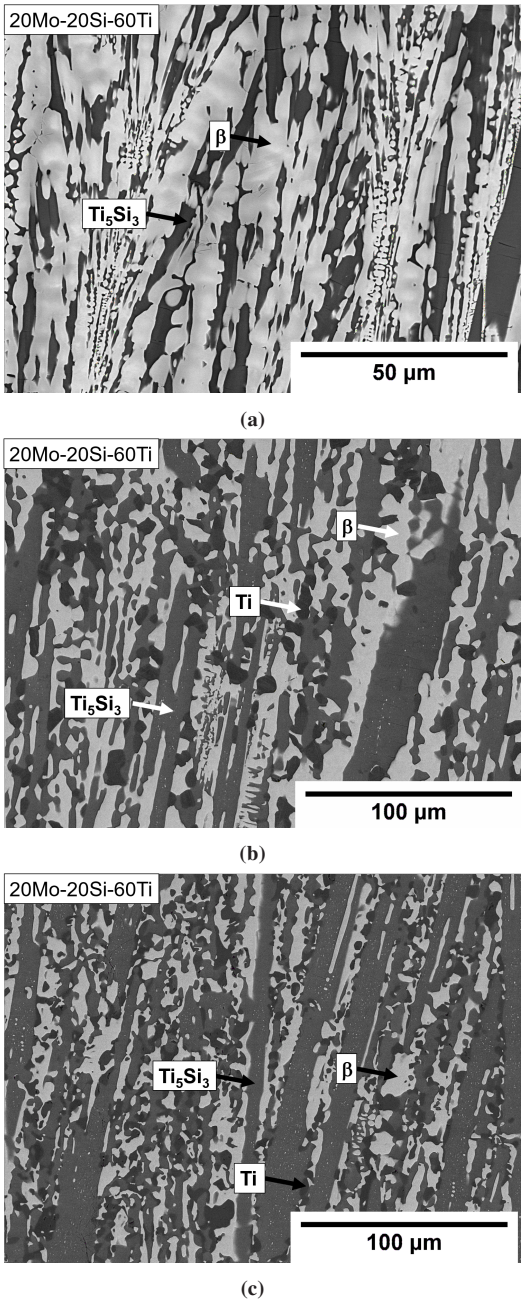

Figure A.9.: The microstructures of all samples with the composition 25Mo-33Si-42Ti. a) SSC9, ac. b) ITS12, fq. c) ITS13, wq.

A.4.10. 60Mo-30Si-10Ti

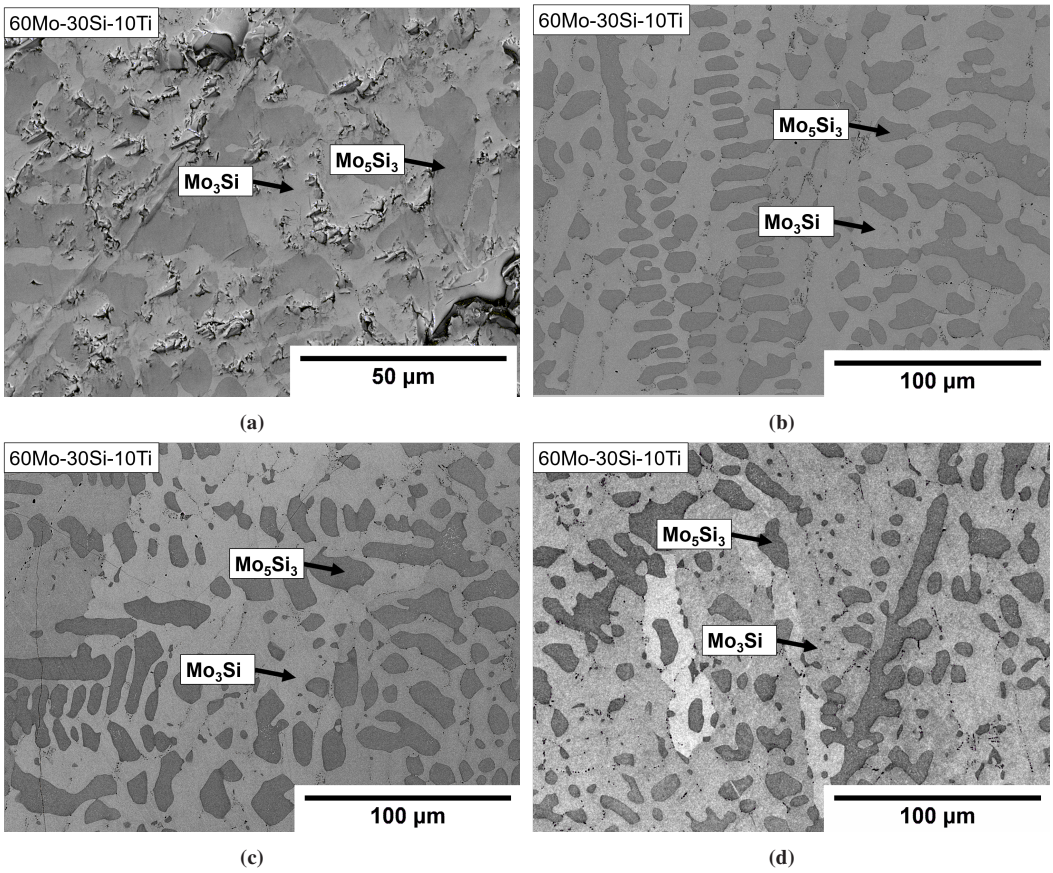

Figure A.10.: The microstructures of all samples with the composition 60Mo-30Si-10Ti. a) SSC14, ac. b) QE10, fc. c) QE10, wq. d) ITS9, wq.

A.5. Chemical analysis post annealing

Table A.2.: The original data of the samples ITS1-ITS3 and ITS5-ITS10 after annealing for 330 h at 1573 K and water quenching. The only changes made are the sample designations, which originally deviated from those chosen in this document, and the translation of the table from German to English.

Analysis no.			305 / 2024			306 / 2024			307 / 2024		
Designation			ITS1			ITS2			ITS3		
	Unit	LoQ	MV	SD	±	MV	SD	±	MV	SD	±
O	(wt. %)	0.0049	0.228	0.098	0.046	0.143	0.091	0.029	0.189	0.106	0.038
Si	(wt. %)	0.31	19.2	0.2	0.6	18.0	0.1	0.6	10.8	0.1	0.35
Ti	(wt. %)	0.14	45.6	0.2	1.3	41.0	0.2	1.2	32.2	0.1	0.9
Mo	(wt. %)	1.6	34.0	0.3	0.7	40.4	0.2	0.9	55.8	0.1	1.2
Sum	(wt. %)		99.028			99.543			98.989		
Analysis no.			308 / 2024			309 / 2024			310 / 2024		
Designation			ITS5			ITS6			ITS7		
	Unit	LoQ	MV	SD	±	MV	SD	±	MV	SD	±
O	(wt. %)	0.0049	0.316	0.213	0.064	0.0850	0.0941	0.0171	0.250	0.190	0.050
Si	(wt. %)	0.31	9.21	0.05	0.29	6.85	0.33	0.22	5.07	0.05	0.16
Ti	(wt. %)	0.14	18.8	0.2	0.5	16.6	0.5	0.5	5.82	0.10	0.17
Mo	(wt. %)	1.6	70.2	0.4	1.5	75.2	0.7	1.7	87.6	0.2	1.9
Sum	(wt. %)		98.526			98.7350			98.740		
Analysis no.			311 / 2024			312 / 2024			313 / 2024		
Designation			ITS8			ITS9			ITS10		
	Unit	LoQ	MV	SD	±	MV	SD	±	MV	SD	±
O	(wt. %)	0.0049	0.0595	0.0302	0.0120	0.0606	0.0717	0.0122	0.0497	0.0177	0.0100
Si	(wt. %)	0.31	3.00	0.13	0.10	10.7	0.1	0.3	12.5	0.10	0.40
Ti	(wt. %)	0.14	8.12	0.29	0.24	6.79	0.04	0.20	10.8	0.1	0.3
Mo	(wt. %)	1.6	85.7	0.5	1.9	80.7	0.5	1.8	75.8	0.6	1.7
Sum	(wt. %)		96.8795			98.2506			99.1497		
LoQ: Limit of Quantification; MV: sean value; SD: standard deviation; ±: inaccuracy of measurement											

List of figures

List of tables

List of publications

Peer-reviewed articles

[1] Beck, K. ; Ulrich, A. S. ; Czerny, A. K. ; White, E. M. ; Heilmaier, M. ; Galetz, M. C.: Aluminide diffusion coatings for improving the pesting behavior of refractory metals. In: *Surface and Coatings Technology* 476 (2024), S. 130205. – ISSN 0257–8972

[2] Czerny, A. K. ; Ma, W. ; Hausner, C. S. ; Franke, P. ; Rohde, M. ; Seifert, H. J.: Thermodynamic Assessment of the Mo–Si System. In: *Advanced Engineering Materials* (2024), S. 2302085. – ISSN 1438–1656

[3] Winkens, G. ; Kauffmann, A. ; Herrmann, J. ; Czerny, A. K. ; Obert, S. ; Seils, S. ; Boll, T. ; Baruffi, C. ; Rao, Y. ; Curtin, W. A. ; Schwaiger, R. ; Heilmaier, M.: The influence of lattice misfit on screw and edge dislocation-controlled solid solution strengthening in Mo-Ti alloys. In: *Communications Materials* 4 (2023), Nr. 1, S. 26. – ISSN 2662–4443

[4] Y., Cai ; Wang, F. ; Czerny, A. K. ; Seifert, H. J. ; Nestler, B.: Phase-field investigation on the microstructural evolution of eutectic transformation and four-phase reaction in Mo-Si-Ti system. In: *Acta Materialia* 258 (2023), S. 119178. – ISSN 1359–6454

MSIT (Materials Science International Team) System Reports

[1] Bondar, A. ; Lukas, H. L. ; Czerny, A. K. ; Romaka, V.: *Mo-Si-Ti Ternary Phase Diagram Evaluation*. Stuttgart, 2023 (Ternary Evaluations)

[2] Czerny, A. K.: *Mo-Si Binary Phase Diagram Evaluation*. Stuttgart, 2024 (Binary Evaluations)

Conference presentations

[1] Czerny, A. K. ; Franke, P. ; Seifert, H. J.: *Thermodynamic assessment of the systems Mo-Si and Mo-Si-Ti.* CALPHAD LI, 27-31 May 2024, Mannheim, Germany, 2024

[2] Czerny, A. K. ; Rohde, M. ; Hausner, C. ; Seifert, H. J.: *Heterogeneous equilibria in the systems Mo-Si-Ti and Mo-Si-Ti-B.* Intermetallics Conference 2021, 04-08 October 2021, Bad Staffelstein, Germany, 2021

[3] Czerny, A. K. ; Rohde, M. ; Hausner, C. ; Seifert, H. J.: *Heterogeneous phase equlibria in the Mo-Si-Ti system.* Euromat, 12-16 September 2021, Online, 2021

[4] Czerny, A. K. ; Rohde, M. ; Seifert, H. J.: *Heterogeneous phase equilibria in the Mo-Si-Ti system at 1300 °C.* 18th Discussion Meeting on Thermodynamics of Alloys (TOFA), 12-16 September 2022, Kraków, Poland, 2022

[5] Czerny, A. K. ; Rohde, M. ; Seifert, H. J.: *Heterogeneous phase equilibria in the Mo-Si-Ti system at 1300 °C.* Materials Science and Engineering (MSE) 2022, 24-26 September 2022, Darmstadt, Germany, 2022

[6] Czerny, A. K. ; Rohde, M. ; Seifert, H. J.: *Heterogeneous phase equilibria in the Mo-Si-Ti system at 1300 °C.* Euromat 2023, 03-07 September 2023, Frankfurt, Germany, 2023

Bibliography

[1] J. H. Perepezko. The Hotter the Engine, the Better. *Science*, 326(5956):1068–1069, 2009.

[2] M. A. Gonzalez-Salazar, T. Kirsten, and L. Prchlik. Review of the operational flexibility and emissions of gas- and coal-fired power plants in a future with growing renewables. *Renewable and Sustainable Energy Reviews*, 82:1497–1513, 2018.

[3] M. A. Nazari, M. F. Alavi, M. Salem, and M. El Haj Assad. Utilization of hydrogen in gas turbines: a comprehensive review. *International Journal of Low-Carbon Technologies*, 17:513–519, 2022.

[4] E. Stefan, B. Talic, Y. Larring, A. Gruber, and T. A. Peters. Materials challenges in hydrogen-fuelled gas turbines. *International Materials Reviews*, 67(5):461–486, 2022.

[5] J.J. Petrovic and A. K. Vasudevan. Key developments in high temperature structural silicides. *Materials Science and Engineering: A*, 261(1):1–5, 1999.

[6] T. C. Chou and T. G. Nieh. Pesting of the high-temperature intermetallic $MoSi_2$. *JOM*, 45(12):15–21, 1993.

[7] U. V. Waghmare, V. Bulatov, E. Kaxiras, and M. S. Duesbery. Microalloying for ductility in molybdenum disilicide. *Materials Science and Engineering: A*, 261(1):147–157, 1999.

[8] G.-J. Zhang, X.-H. Lin, R.-H. Wang, G. Liu, and J. Sun. Tensile properties and strengthening mechanisms of Mo–Si alloy. *International Journal of Refractory Metals and Hard Materials*, 29(5):608–613, 2011.

[9] D. M. Dimiduk and J. H. Perepezko. Mo-Si-B Alloys: Developing a Revolutionary Turbine-Engine Material. *MRS Bulletin*, 28(9):639–645, 2003.

[10] J. A. Lemberg and R. O. Ritchie. Mo-Si-B Alloys for Ultrahigh-Temperature Structural Applications. *Advanced Materials*, 24(26):3445–3480, 2012.

[11] D. Schliephake, M. Azim, K. von Klinski-Wetzel, B. Gorr, H.-J. Christ, H. Bei, E. P. George, and M. Heilmaier. High-Temperature Creep and Oxidation Behavior of Mo-Si-B Alloys with High Ti Contents. *Metallurgical and Materials Transactions A*, 45(3):1102–1111, 2014.

[12] D. Schliephake, A. Kauffmann, X. Cong, C. Gombola, M. Azim, B. Gorr, Ha.-J. Christ, and M. Heilmaier. Constitution, oxidation and creep of eutectic and eutectoid Mo-Si-Ti alloys. *Intermetallics*, 104:133–142, 2019.

[13] S. Obert, A. Kauffmann, and M. Heilmaier. Characterisation of the oxidation and creep behaviour of novel Mo-Si-Ti alloys. *Acta Materialia*, 184:132–142, 2020.

[14] S. Obert, A. Kauffmann, R. Pretzler, D. Schliephake, F. Hinrichs, and M. Heilmaier. The creep and oxidation behaviour of pesting-resistant $(Mo,Ti)_5Si_3$-containing eutectic-eutectoid Mo-Si-Ti alloys. *Metals*, 11(169), 2021.

[15] L. Kaufman and H. Bernstein. *Computer calculation of phase diagrams With special reference to refractory metals*, volume 4. Academic Press Inc, New York, 1970.

[16] Y. Yang, Y. Chang, L. Tan, and Y. Du. Experimental investigation and thermodynamic descriptions of the Mo–Si–Ti system. *Materials Science and Engineering A*, 361:281–293, 11 2003.

[17] V. Svechnikov, Y. A. Kocherzhinsky, and L. Yupko. Investigation of Phase Equilibria in Alloys of Silicon with Molybdenium and Titanium. A6, 1972.

[18] H. L. Lukas, S. G. Fries, and B. Sundman. *Computational Thermodynamics - The Calphad Method*. Cambridge University Press, New York, USA, 2007.

[19] P. J. Spencer. A brief history of CALPHAD. *Calphad*, 32(1):1–8, 2008.

[20] J. J. van Laar. Melting or solidification curves in binary systems (in German). *Zeitung für Physikalische Chemie*, 63:216–253, 1908.

[21] J. J. van Laar. Melting or solidification curves in binary systems (in German). *Zeitung für Physikalische Chemie*, 64:257–297, 1908.

[22] H. J. Seifert and F. Aldinger. Applied phase studies. *Zeitschrift fuer Metallkunde*, 87(11):841–853, 1996.

[23] O. Redlich and A. T. Kister. Algebraic Representation of Thermodynamic Properties and the Classification of Solutions. *Industrial & Engineering Chemistry*, 40(2):345–348, 1948.

[24] M. Hillert. The compound energy formalism. *Journal of Alloys and Compounds*, 320(2):161–176, 2001.

[25] B. Sundman and J. Ågren. A regular solution model for phases with several components and sublattices, suitable for computer applications. *Journal of Physics and Chemistry of Solids*, 42(4):297–301, 1981.

[26] M. Hillert and L. I. Staffansson. Regular-solution model for stoichiometric phases and ionic melts. *Acta Chemica Scandinavica*, 24(10):3618–3626, 1970.

[27] D. W. Marquardt. An Algorithm for Least-Squares Estimation of Nonlinear Parameters. *Journal of the Society for Industrial and Applied Mathematics*, 11(2):431–441, 1963.

[28] W. Zhou, R. Apkarian, Z. L. Wang, and D. Joy. *Fundamentals of Scanning Electron Microscopy (SEM)*, chapter 1, pages 1–40. Springer New York, New York, NY, 2007.

[29] M. Dunlap and J. E. Adaskaveg. *Introduction to the Scanning Electron Microscope - Theory, Practice, & Procedures*. Facility for Advanced Intrumentation, U. C. Davis, 1997.

[30] P. F. Schmidt. *Praxis der Rasterelektronenmikroskopie und Mikrobereichsanalyse (in German)*. Kontakt & Studium: Messtechnik. expert-Verlag GmbH, Fachverlag für Wirtschaft und Technik, 1998.

[31] E. Zolotoyabko. *Basic Concepts of X-Ray Diffraction*. Wiley-VCH, Weinheim, 2014.

[32] Y. Waseda, K. Shinoda, and E. Matsubara. *X-Ray Diffraction Crystallography - Introduction, Examples and Solved Problems*. Springer Berlin, Heidelberg, 2011.

[33] A. K. Czerny, W. Ma, C. S. Hausner, P. Franke, M. Rohde, and H. J. Seifert. Thermodynamic Assessment of the Mo–Si System. *Advanced Engineering Materials*, page 2302085, 2024.

[34] A. K. Czerny. Mo-Si Binary Phase Diagram Evaluation, 2024.

[35] J. L. Ham. An introduction to arc-cast Molybdenum and its alloys. *Transactions of the American Society of Mechanical Engineers*, 73:723–731, 1951.

[36] R. Kieffer and E. Cerwenka. Beitrag zum System Molybdän-Silizium (in German). *Zeitschrift für Metallkunde*, 43(4):101 – 105, 1952.

[37] V. N. Svechnikov, Y. A. Kocherzhinskii, and L. M. Yupko. *Diagrammy sostojanija metalliceskich sistem*. Nauka, 1971.

[38] G. B. Cherniak and A. G. Elliot. High-Temperature Behavior of $MoSi_2$ and Mo_5Si_3. *Journal of the American Ceramic Society*, 47(3):136–141, 1964.

[39] A. B. Gokhale and G. J. Abbaschian. The Mo-Si (Molybdenum-Silicon) system. *Journal of Phase Equilibria*, 12(4):493–498, 1991.

[40] P. S. Frankwicz and J. H. Perepezko. Phase stability of $MoSi_2$ in the $C11_b$ and C40 structures at high temperatures. *Materials Science and Engineering: A*, 246:199–206, 05 1998.

[41] I. Rosales and J. H. Schneibel. Stoichiometry and mechanical properties of Mo_3Si. *Intermetallics*, 8:885–889, 2000.

[42] A. Gulec, X. Yu, M. Taylor, J. H. Perepezko, and L. Marks. Direct observation of incommensurate structure in Mo_3Si. *Acta Crystallographica A*, 72:660–666, 2016.

[43] I. Gnesin and B. Gnesin. Composition of the Mo-Mo_3Si alloys obtained via various methods. *International Journal of Refractory Metals and Hard Materials*, 88:105188, 2020.

[44] H. Fujiwara and Y. Ueda. Thermodynamic properties of molybdenum silicides by molten electrolyte EMF measurements. *Journal of Alloys and Compounds*, 441:168–173, 2007.

[45] S. V. Meschel and O. J. Kleppa. Standard enthalpies of formation of some 4d transition metal silicides by high temperature direct synthesis calorimetry. *Journal of Alloys and Compounds*, 274:193–200, 1998.

[46] I. Tomaszkiewicz, G. A. Hope, C. M. Beck II, and P. A. G. O'Hare. Thermodynamic properties of silicides VI. Pentamolybdenum trisilicide (Mo_5Si_3). Fluorine-combustion calorimetric determination of the standard molar enthalpy of formation at the temperature 298.15 K. *The Journal of Chemical Thermodynamics*, 29:87–98, 1997.

[47] J. E. Callanan, R. D. Weir, and E. F. Westrum Jr. Transition metal silicides and tellurides: crystal structure, heat capacities, and derived thermodynamic properties from absolute zero to 2200 K. *Pure & Applied Chemistry*, 69(11):2289 – 2294, 1997.

[48] I. Tomaszkiewicz, G. A. Hope, C. M. Beck II, and P. A. G. O'Hare. Thermodynamic properties of silicides V. Fluorine-combustion calorimetric determination of the standard molar enthalpy of formation at the temperature 298.15 K of trimolybdenum monosilice Mo_3Si, and a critical assessment of its thermodynamic properties. *The Journal of Chemical Thermodynamics*, 28:29–42, 1996.

[49] P. A. G. O'Hare. Thermodynamic properties of silicides III. Specific energy of combustion in fluirine of a hyperstoichiometric molybdenum disilicide. The standard molar enthalpy of formation $\Delta_f H^o_m$ of $MoSi_{2.067\pm0.002}$ at the temperature 298.15 K. *The Journal of Chemical Thermodynamics*, 25:1333–1343, 1993.

[50] E. Arpaci and M. G. Frohberg. Experimental determination of the mixing enthalpies of liquid Molybdenum-Silicon alloys. *Zeitschrift für Metallkunde*, 76:440 – 444, 1985.

[51] S. Ohmori, Y. Hashimoto, and K. Kohyama. Standard free energy of formation of Mo_3Si and Mo_5Si_3 by EMF measurement. *Journal of High Temperature Society Japan*, 8:113–118, 1982.

[52] V. M. Maslov, A. S. Neganov, I. P. Borovinskaya, and A. G. Merzhanov. Self-propagating high-temperature synthesis as a method for determination of the heat of formation of refractory compounds. *Combustion, Explosion, and Shock Waves*, 14:759–767, 1978.

[53] T. G. Chart. Thermodynamic properties of the system Molybdenum-Silicon. *Metal Science*, 8:344–348, 1974.

[54] V. P. Bondarenko, E. N. Fomichev, and A. A. Kalashnik. Enthalpy of Molybdenum and Tungsten silicides at 1200-2200°K. *Heat Transfer-Sov. Res.*, 5(2):76 – 78, 1973.

[55] V. P. Bondarenko, P. N. V'yugov, V. I. Zmii, and A. S. Knyazhev. Thermodynamic characteristics of molybdenum silicides in the temperature range 400 - 1200 °K. *Teplofizika Vysokikh Temperatur (in Russian)*, 10(5):1013–1017, 1972.

[56] A. W. Searcy and A. G. Tharp. The dissociation pressures and the heats of formation of the molybdenum silicides. *The Journal of Physical Chemistry*, 64:1539–1542, 1960.

[57] E. G. King and A. U. Christensen, Jr. Low temperature heat capacity, entropy at 298.15°K and high temperature heat content of Mo_3Si. *The Journal of Physical Chemistry*, 62:499–500, 1958.

[58] B. E. Walker, J. A. Grand, and R. R. Miller. High temperature heat content and heat capacity of Al_2O_3 and $MoSi_2$. *The Journal of Physical Chemistry*, 60:231–233, 1956.

[59] D. A. Robins and I. Jenkins. The heats of formation of some transition metal silicides. *Acta Metallurgica*, 3:598–604, 1955.

[60] T. B. Douglas and W. M. Logan. Heat content of Molybdenum disilicide from 0° to 900° C. *Journal of Research of the National Bureau of Standards*, 53(2):91–93, 1954.

[61] Y. Pan. First-principles investigation of the new phases and electrochemical properties of $MoSi_2$ as the electrode materials of lithium ion battery. *Journal of Alloys and Compounds*, 779:813–820, 2019.

[62] S. Zhong, Z. Chen, M. Wand, and D. Chen. Structural, elastic and thermodynamic properties of Mo_3Si and Mo_3Ge. *European Physical Journal B*, 89(6), 2016.

[63] C. Colinet and J.-C. Tedenac. Enthalpies of formation of TM-X compounds (X=Al, Ga, Si, Ge, Sn). Comparison of ab-initio values and experimental data. *CALPHAD*, 54:16–34, 2016.

[64] S. B. Bhaduri, Z. B. Qian, and R. Radhakrishnan. Further thermodynamic assessment for synthesizing transition metal silicides by the combustion synthesis process. *Scripta Metallurgica et Materialia*, 30:179–184, 1994.

[65] D Birnie, E. S. Machlin, L. Kaufman, and K. Taylor. Comparison of pair potential and thermochemical models of the heat of formation of bcc and fcc alloys. *CALPHAD*, 6(2):93 – 126, 1982.

[66] A. K. Niessen and F. R. de Boer. The enthalpy of formation of solid borides, carbides, nitrides, silicides and phosphides of transition and noble metals. *Journal of the Less-Common Metals*, 82:75–80, 1981.

[67] E. S. Machlin. Correction terms to pair potential model values of the energy of formation for transition element-polyvalent element phases. *CALPHAD*, 5(1):1–17, 1981.

[68] L. Kaufman. Coupled phase diagrams and thermochemical data for transition metal binary systems-VI. *CALPHAD*, 3(1):45–76, 1979.

[69] M. S. Chandrasekharaiah, J. L. Margrave, and P. A. G. O'Hare. The Disilicides of Tungsten, Molybdenum, Tantalum, Titanium, Cobalt, Nickel, and Platinum Monosilicide: a survey of their thermodynamic properties. *The Journal of Physical Chemistry Reference Data*, 22(5):1459–1468, 1993.

[70] A. R. Miedema, P. F. de Châtel, and F. R. de Boer. Cohesion in alloys — fundamentals of a semi-empirical model. *Physica B+C*, 100(1):1–28, 1980.

[71] I. Barin. *Thermochemical data of pure substances*. VCh Verlagsgesellschaft mbH, Weinheim, Germany, 1989.

[72] A. T. Dinsdale. SGTE data for pure elements. *CALPHAD*, 15(4):317–425, 1991.

[73] J. E. Callanan, R. D. Weir, and E. F. Westrum Jr. Thermodynamic properties of silicides IV. Molar heat capacity at temperatures from 7 K to 340 K and derived thermodynamic properties to T= 2200 K of molybdenum disilicide ($MoSi_{2.067 \pm 0.002}$). *The Journal of Chemical Thermodynamics*, 28(11):1233–1245, 1996.

[74] V. S. Sudavtsova, G. I. Batalin, and V. S. Tutevich. Thermodynamic properties of binary Si-(V, Nb, Mo) Melts. *Russian Journal of Physical Chemistry*, 59(9):1282 – 1283, 1985.

[75] R. Mezaki, E. W. Tilleux, T. F. Jambois, and J. L Margrave. *High-temperature thermodynamic functions for refractory compounds*. American Society of Mechanical Engineers, New York, 1965.

[76] C. Vahlas, P. Y. Chevalier, and E. Blanquet. A thermodynamic evaluation of four Si-M (M = Mo, Ta, Ti, W) binary systems. *CALPHAD*, 13(3):273–292, 1989.

[77] A. Costa e Silva. *Synthesis of Molybdenum disilicide composites using in situ reactions*. PhD thesis, University of Florida, Gainsville, FL, 1994.

[78] T. G. Chart. Thermochemical data for transition metal - silicon systems. *High temperatures - High pressures*, 5:241 – 252, 1973.

[79] L. Brewer, editor. *Atomic Energy Review, Special Issue No. 7 Molybdenum: Physico-chemical properties of its compounds and alloys*. International Atomic Energy Agency, Vienna, 1980.

[80] Y. Liu, G. Shao, and P. Tsakiropoulos. Thermodynamic reassessment of the Mo-Si and Al-Mo-Si systems. *Intermetallics*, 8:953–962, 2000.

[81] T. Geng, C. Li, X. Zhao, H. Xu, Z. Du, and C. Guo. Thermodynamic assessment of the Nb–Si–Mo system. *CALPHAD*, 34(3):363–376, 2010.

[82] P. B. Fernandes, G. C. Coelho, F. Ferreira, C. A. Nunes, and B. Sundman. Thermodynamic modeling of the Nb–Si system. *Intermetallics*, 10(10):993–999, 2002.

[83] C. Guo, C. Li, P. J. Masset, and Z. Du. A thermodynamic description of the Al-Mo-Si system. *CALPHAD*, 36:100–109, 2012.

[84] M. Hansen, H. Kessler, and D. McPherson. Ti-Si phase diagram. 44, 1952.

[85] V. Svechnikov, Y. Kocherzhinskii, L. Iupko, O. Kulik, and E. Shishkin. A Titanium-Silicon Phase Diagram. 193(2), 1970.

[86] W. J. J. Wakelkamp, F. J. J. van Loo, and R. Metselaar. Phase relations in the Ti-Si-C system. *Journal of the European Ceramic Society*, 8(3):135–139, 1991.

[87] D. A. Sutcliffe. Titanium-silicon alloys. *Metal Treatment and Drop Forging*, 4:181–197, 1954.

[88] E. N. Pylaeva and M. A. Volkova. 7:74–77, 1962.

[89] S. V. Meschel and O. J. Kleppa. Standard enthalpies of formation of some 3d transition metal silicides by high temperature direct synthesis calorimetry. *Journal of alloys and compounds*, 267(1-2):128–135, 1998.

[90] W. Sylla, S. Stillman, M. Sabella, and E. Cotts. The Heat Capacity of Titanium Disilicide. 76(5), 1994.

[91] L. Topor and O. J. Kleppa. Standard enthalpies of formation of $TiSi_2$ and VSi_2 by high-temperature calorimetry. *Metallurgical Transactions A*, 17:1217–1221, 1986.

[92] V. S. Sudavtsova, G. I. Batalin, and V. S. Titevich. Thermodynamic properties of alloys of Si-Ti (Zr) systems. *Izv. Akad. Nauk SSSR, Neorg. Mater.;(USSR)*, 21(5), 1985.

[93] Y. Yusin, M. G. Valishev, A. F. Ermakov, P. V. Gel'd, and M. S. Petrushevskii. Partial and Integral Enthalpies of Formation of Liquid Alloys of Titanium with Iron. *Russ. Metall.,*, 3:15–17, 1981.

[94] N. I. Sychev, P. V. Gel'd, and G. I. Kalishevich. Thermodynamic Characteristics of Scandium Silicide (Sc_5Si_3), Titanium Silicide (Ti_5Si_3), and Vanadium Silicide (V_5Si_3). *Zh. Fiz. Khim.*, 54:224 – 225, 1980.

[95] V. Bondarenko, L. A. Dvorina, V. I. Zmii, E. N. Fomichev, N. P. Slyusar, and A. D. Krivorotenko. Enthalpies and Heat Capacities of Titanium and Vanadium Disilicides at Temperatures Above 1200°K. 12(11), 1973.

[96] V. D. Savin. Thermographic determination of the thermochemical characteristics of processes and materials. *Russ. J. Phys. Chem.(Engl. Transl.)*, 47:1423–1426, 1973.

[97] L. D. Polyachenok, G. I. Novikov, and O. G. Polyachenok. Thermodynamic characteristics of lower titanium chlorides and titanium oxychloride. *Obshch. Prikl. Khim.*, pages 45–48, 1972.

[98] K. E. Yuck and F. E. Block. *Metallurgiya*, 170:84, 1965.

[99] P. Gel'd and Y. Gertman. About the First Heat of Solubility of Liquid Transition Metals in Liquid Silicon. 10, 1960.

[100] Y. M. Golutvin. Heat content and heat capacities in the system titanium-silicon. *Zhur. Fiz. Khim.*, 33, 1959.

[101] Y. M. Golutvin. O teplotakh obrazovaniya silitsidov titana. *Zh. Fiz. Khim*, 30(10):2251–2259, 1956.

[102] R. Kematick and C. Myers. Thermodynamics of the Phase Formation of the Titanium Silicides. 8(1), 1996.

[103] J. L. Murray. *Phase Diagrams of Binary Titanium Alloys*. Monograph series on alloy phase diagrams. ASM International, 1987.

[104] H. J. Seifert, H. L. Lukas, and G. Petzow. Thermodynamic Optimization of the Ti-Si System / Thermodynamische Optimierung des Systems Ti-Si. *International Journal of Materials Research*, 87(1):2–13, January 1996.

[105] F. R. de Boer, W. C. M. Mattens, R. Boom, A. R. Miedema, and A. K. Niessen. *Cohesion in metals. Transition metal alloys*, volume 1. Elsevier, 1988.

[106] M. Fiore, F. Beneduce, and Azevedo, C. R. de Farias. Assessment of the Ti-rich corner of the Ti-Si phase diagram using two sublattices to describe the Ti_5Si_3 phase. *REM: International Engineering Journal*, 70(2), 2017.

[107] M. Sabeena, S. Murugesan, R. Mythili, A. K. Sinha, M. N. Singh, M. Vijayalakshmi, and S. K. Deb. Studies on ω Phase Formation in Ti-Mo Alloys Using Synchrotron XRD. *Transactions of the Indian Institute of Metals*, 68(1):1–6, 2015.

[108] M. Hansen, E. L. Kamen, H. D. Kessler, and D. J. McPherson. Systems Titanium-Molybdenum and Titanium-Columbium. *JOM*, 3(10):881–888, 1951.

[109] E. Rudy. Part V. Compendium of Phase Diagram Data. 5, 1969.

[110] H. M. Flower, S. D. Henry, and D. R. F. West. The $\beta \rightleftarrows \alpha$ transformation in dilute Ti-Mo alloys. *Journal of Materials Science*, 9(1):57–64, 1974.

[111] S. Terauchi, H. Matsumoto, T. Sugimoto, and K. Kamei. Investigation of the Titanium-Molybdenum Binary Phase Diagram. 41(6), 1977.

[112] A. A. Kuz'min and L. S. Palatnik. Vapour Pressure of Titanium Over Ti- Mo Alloys. *Phys. Met. Metallogr.*, 14:142–144, 1962.

[113] M. Hoch and R. Viswanathan. Thermodynamics of titanium alloys: III. The Ti-Mo system. *Metallurgical Transactions*, 2:2765–2767, 1971.

[114] S. Barzilai, C. Toher, S. Curtarolo, and O. Levy. Molybdenum-titanium phase diagram evaluated from ab initio calculations. *Phys. Rev. Mater.*, 1:023604, Jul 2017.

[115] C. Jiang, R. D. Mariani, and C. A. Adkins. Ab initio investigation and thermodynamic modeling of the Mo–Ti–Zr system. *Materialia*, 10:100701, 2020.

[116] J. L. Murray. The Mo-Ti (Molybdenum-Titanium) system. *Bulletin of Alloy Phase Diagrams*, 2(2):185 – 192, 1981.

[117] I. Ansara, A. T. Dinsdale, and M. H. Rand. Mo-Ti. *COST 507 Thermochemical database for light metal alloys*, 2:249–252, 1998.

[118] S. Burk, B. Gorr, H.-J. Christ, D. Schliephake, M. Heilmaier, C. Hochmuth, and U. Glatzel. High-temperature oxidation behaviour of a single-phase $(Mo,Ti)_5Si_3$ (Mo–Si–Ti) alloy. *Scripta Materialia*, 66(5):223–226, 2012.

[119] A. Bondar, H. L. Lukas, A. K. Czerny, and V. Romaka. Mo-Si-Ti Ternary Phase Diagram Evaluation. 2023.

[120] C. Colinet, J.-M. Joubert, and J.-C. Tedenac. The T Phase with the V_6Si_5 Type Structure in the Mo-Si-Ti System Studied by Ab Initio Calculations and X-Ray Diffraction. *Scripta Materialia*, 159, 2019.

[121] E. Stroem, S. Eriksson, H. Rundloef, and J. Zhang. Effect of Site Occupation on Thermal and Mechanical Properties of Ternary Alloyed Mo_5Si_3. 53(2), 2005.

[122] E. Stroem, J. Zhang, S. Eriksson, C. Li, and D. Feng. The Influence of Alloying Elements on Phase Constitution and Microstructure of $Mo_3M_2Si_3$ (M = Cr, Ti, Nb, Ni or Co). 329-331, 2002.

[123] F. Wei, Y. Kimura, and Y. Mishima. Microstructure and Phase Stability in MoSi2-TSi2 (T = Cr, V, Nb, Ta, Ti) Pseudo-Binary Systems. 42(7), 2001.

[124] W. Boettinger, J. Peperezko, and P. Frankwicz. Application of Ternary Phase Diagrams to the Development of $MoSi_2$-Based Materials. A155(1), 1992.

[125] P. Frankwicz and J. H. Perepezko. Phase Stability and Solidification Pathways in $MoSi_2$-Based Alloys. 213, 1991.

[126] E. Vasilieva and V. Terentieva. Structure, Phase Composition, and Heat Resistance of Alloys of the System Si-Ti-Mo. 10(6), 1974.

[127] V. Svechnikov, Y. Kocherzhinsky, and L. Yupko. $MoSi_2$-$TiSi_2$ Diagram. 206(3), 1972.

[128] J. A. Kocherzhinsky. Differential Thermocouple up to 2450°C and Thermographic Investigation of Refractory Silisides. 1, 1971.

[129] M. Garfinkle and H. M. Davis. Reaction of liquid titanium with some refractory compounds. *Amer. Soc. Metals, Trans. Quart.*, 58, 1965.

[130] H. Kudielka and H. Nowotny. Disilizidsysteme (in German). 87, 1956.

[131] H. Schachner, E. Cerwenka, and H. Nowotny. Neue Silizide vom M_5Si_3-Typ mit $D8_8$-Struktur. 85(1), 1954.

[132] H. Nowotny, R. Kieffer, and H. Schachner. Strukturuntersuchungen an Disiliziden (in German). 83(5), 1952.

[133] E. Daufresne, M. Bechelany, Y. Le Petitcorps, and O. Dezellus. Computational Thermodynamics of Mo-Ti-Si-C system to develop new discontinuous Ceramic fiber reinforced-Intermetallic Matrix Composites. In *CALPHAD 50*, 2023.

[134] G. H. Gulliver. The quantitative effect of rapid cooling upon the constitution of binary alloys. *J. Inst. Met.*, 9, 1913.

[135] E. Scheil. Bemerkungen zur Schichtkristallbildung (in German). *Zeitschrift für Metallkunde*, 34(3):70–72, 1942.

[136] D. A. Porter, K. E. Easterling, and M. H. Sherif. *Phase Transformations in Metals and Alloys (Revised Reprint)*. CRC Press, Taylor & Francis Group, 2009.

[137] B. Cantor. The Scheil Equation: Solidification. In *The Equations of Materials*. Oxford University Press, 2020.

[138] E. Kozeschnik, W. Rindler, and B. Buchmayr. Scheil–Gulliver simulation with partial redistribution of fast diffusers and simultaneous solid–solid phase transformations. *Int. J. Mat. Res.*, 98(9):826–831, 2007.

[139] HTM Reetz GmbH. Homepage of the htm reetz gmbh, 2024. `https://www.htm-reetz.com/` (Accessed: 05.04.2024).

[140] J. J. Williams, M. J. Kramer, M. Akinc, and S. K. Malik. Effects of interstitial additions on the structure of Ti_5Si_3. *Journal of Materials Research*, 15(8):1773–1779, 2000.

[141] J. J. Williams, Y. Y. Ye, M. J. Kramer, K. M. Ho, L. Hong, C. L. Fu, and S. K. Malik. Theoretical calculations and experimental measurements of the structure of Ti_5Si_3 with interstitial additions. *Intermetallics*, 8(8):937–943, 2000.

[142] P. Villars and L. D. Calvert. Pearson's handbook of crystallographic data for intermediate phases. *American Society of Metals, Cleveland, OH*, 1985.

[143] H. L. Zhao, M. J. Kramer, and M. Akinc. Thermal expansion behavior of intermetallic compounds in the Mo–Si–B system. *Intermetallics*, 12(5):493–498, 2004.

[144] D. H. Templeton and C. H. Dauben. The Crystal Structure of Mo_3Si. *Acta Crystallographica*, 3:261–262, 1950.

[145] M. Aindow, L. S. Smith, J. Shyue, M. H. Loretto, and H. L. Fraser. On the origins of 'forbidden' 100-type spots in electron diffraction patterns from the A15 compounds Nb_3AI, Cr_3Si and V_3Si. *Philosophical Magazine Letters*, 69(1):23–30, 1994.

[146] S. Prasad and A. Paul. Growth mechanism of phases by interdiffusion and atomic mechanism of diffusion in the molybdenum–silicon system. *Intermetallics*, 19(8):1191–1200, 2011.

[147] O. Lenchuk, J. Rohrer, and K. Albe. Solubility of zirconium and silicon in molybdenum studied by first-principles calculations. *Scripta Materialia*, 97:1–4, 2015.

[148] R. Hultgren, P. D. Desai, D. T. Hawkins, M. Gleiser, and K. K Kelley. Selected values of the thermodynamic properties of the elements. Technical report, National Standard Reference Data System, 1973.

[149] B. Sundman, B. Jansson, and J.-O. Andersson. The Thermo-Calc databank system. *CALPHAD*, 9(2):153–190, 1985.

[150] M. E. Schlesinger. Thermodynamics of solid transition-metal silicides. *Chemical Reviews*, 90:607 – 628, 1990.

[151] V. P. Bondarenko. Chemical linkage in and enthalpy of transition-metal disilicides at temperatures above 1200°K. *Sov. Powder Metall. Met. Ceram. (Engl. Transl.)*, 15:938–941, 1976.

[152] D. R. Askeland. *The Science and Engineering of Materials*. Springer New York, NY, 2013.

[153] G. F. Harrington and J. Santiso. Back-to-Basics tutorial: X-ray diffraction of thin films. *Journal of Electroceramics*, 47(4):141–163, 2021.